THE ATMOSPHERIC CORROSION OF 304L AND 316L STAINLESS STEELS UNDER CONDITIONS RELEVANT TO THE INTERIM STORAGE OF INTERMEDIATE LEVEL NUCLEAR WASTE

by

ANGUS JAMES MCDONALD CHARTRES COOK

A thesis submitted to the University of Birmingham for the degree of DOCTOR OF PHILOSOPHY

Word count: 24,630

School of Metallurgy and Materials
College of Engineering and Physical Sciences
University of Birmingham
September 2017

ABSTRACT

The atmospheric corrosion of 304L and 316L austenitic stainless steels was investigated in conditions relevant to the storage of intermediate level nuclear waste (ILW). Thin electrolyte films were created via automated droplet deposition, allowing multiple tests to be conducted in parallel.

In-situ monitoring of droplet arrays on stainless steel samples was conducted with the use of a flat-bed document scanner, allowing large-scale, automated monitoring of corrosion processes. The initiation time for individual corrosion processes was established, showing that corrosion was slower to initiate under less aggressive conditions, and allowing ‘true’ corrosion site lifetimes to be recorded, and compared with their depths.

The presence of precipitated species within an electrolyte film was shown to affect the corrosion processes within that film. Both NaCl precipitates and glass shards acted as barriers to ion transport. This affected both the propagation of corrosion, and the electrochemical potential within the droplets; a higher precipitate content decreased the average corrosion depth and the extent of corrosion.

The presence of nitrate and sulphate salts, both known corrosion inhibitors in full-immersion conditions, was shown to inhibit atmospheric corrosion when the inhibitor:chloride ratio was above a certain value. This was independent of the absolute amounts of salts, but dependent on the exposure humidity of the test.

For Zara, for my family,

and for Grandma

“I met a traveller from an antique land
Who said: Two vast and trunkless legs of stone
Stand in the desert... near them, on the sand,
Half sunk, a shattered visage lies, whose frown,
And wrinkled lip, and sneer of cold command,
Tell that its sculptor well those passions read
Which yet survive, stamped on these lifeless things,
The hand that mocked them and the heart that fed:

And on the pedestal these words appear:
'My name is Ozymandias, king of kings:
Look on my works, ye Mighty, and despair!'
Nothing beside remains. Round the decay
Of that colossal wreck, boundless and bare
The lone and level sands stretch far away.”

- ‘*Ozymandias*’, Percy Shelly[1]

“In Egypt's sandy silence, all alone,
Stands a gigantic Leg, which far off throws
The only shadow that the Desert knows:—
"I am great OZYMANDIAS," saith the stone,
"The King of Kings; this mighty City shows
"The wonders of my hand."— The City's gone,—
Nought but the Leg remaining to disclose
The site of this forgotten Babylon

We wonder,—and some Hunter may express
Wonder like ours, when thro' the wilderness
Where London stood, holding the Wolf in chace,
He meets some fragment huge, and stops to guess
What powerful but unrecorded race
Once dwelt in that annihilated place.”

- *‘Ozymandias’*, Horace Smith[2]

ACKNOWLEDGEMENTS

Although it will be judged as such, a Ph.D. is not the work of a single person, and there are many people to acknowledge for their extensive contributions.

Firstly, and most importantly, I wish to thank Professors Alison Davenport and Trevor Rayment for acting as my supervisors over the last 4 years. Their guidance and support have been truly invaluable, and I cannot adequately express my appreciation in this paragraph.

I also wish to thank the group members who helped me settle into Ph.D. life: Andrew du Plessis, Haval Mohammed-Ali, Liya Guo, Georgia Adams, Wayne Xu, Fei Yu, and particularly Steven Street, who taught me everything I know about metallurgy. Any errors in the thesis may be attributed to him.

I started, and now end, this Ph.D. alongside Sophie Zhang and Sarah Glanville, who it has been my great pleasure to work and learn alongside.

I wish to also thank William Rowley, Qi Wei, Flaviu Gostin, Berenika Syrek-Gersternkorn and Rowena Fletcher-Wood. All have helped keep me sane.

Dr Rob Winsley and particularly Dr Cristiano Padovani have been key in giving advice and support from the NDA perspective, and helping set the context of this work.

To all, thank you.

This project was funded by EPSRC grant EP/I036397/1, and Radioactive Waste Management Ltd. contract NPO004411A-EPS02.

CONTENTS

TABLE OF SYMBOLS

Abbreviations

ACS	American chemical society
AISCC	Atmospherically induced stress corrosion cracking
ASTM	American society for testing materials
CDD	Chloride deposit density
CCD	Charge coupled device
CIS	Contact imaging sensor
DI	De-ionised
DSLR	Digital single lens reflex
EPS	Encapsulated product stores
EPSRC	Engineering and physical sciences research council
GDF	Geological disposal facility
HFP	Humidity fixed point
IDD	Inhibitor deposit density
ILW	Intermediate level nuclear waste
LED	Light emitting diode
MSE	Mixed solvent electrolyte
NDA	Nuclear decommissioning authority
NDD	Nitrate deposit density
RH	Relative humidity
SCC	Stress corrosion cracking
SDD	Sulphate deposit density
SEM	Scanning electron microscope
SVET	Scanning vibrating electrode technique
TPB	Three phase boundary
UK	United Kingdom
UNS	Unified numbering system
UV	Ultra-violet

Equations

A	Area
$C_{(x, sat)}$	Concentration (at point x, at saturation)
$D_{(eff)}$	(Effective) diffusion constant
E_p	Pitting potential
F	Faraday constant
h	Depth of pit
i	Current density
$I^{(crit)}/C$	(Critical) inhibitor/chloride ratio
J	Flux
Λ	Likelihood of stable pitting
λ	Likelihood of metastable pitting
μ	Probability of transition to stability
m	Mass of metal
M	Molar mass of metal
n	Oxidation state of metal ions
Q	Total charge
ρ	Density of metal
τ	Survival period
t	Pit lifetime

1 INTRODUCTION

This thesis details work undertaken to investigate the corrosion of austenitic stainless steels under atmospheric conditions. The motivation for this work is the interim storage of intermediate level nuclear waste (ILW).

In the UK ILW is packaged in stainless steel containers, made with 304L and 316L stainless steel alloys, and stored in above-ground storage facilities. These waste packages are likely to remain in interim storage for a period of several decades before being moved to an underground facility for permanent disposal. Atmospheric aerosols will collect on the container surfaces, and may lead to atmospheric corrosion, and potential container failure through stress corrosion cracking. The work detailed within this thesis explores some key areas of interest for corrosion under these particular systems.

Firstly, a new methodology for the automated in-situ monitoring of atmospheric corrosion samples is presented, using a flat-bed document scanner. This method, combined with a high-throughput droplet deposition technique allows optical data to be gathered from multiple samples in parallel, delivering robust statistics on the effects of different salt types, contamination levels, and alloys on the initiation time for pitting corrosion to occur.

Next, the effect of precipitates within an atmospheric corrosion system on stainless steel is explored. Realistic chemical deposits within ILW stores are expected to be composed of a range of species, including species which may precipitate from solution, depending on the environment. NaCl precipitates or glass-shards in droplets of either $MgCl_2$ or $CaCl_2$ were analysed, and the effect on the morphology of corrosion sites in these droplets was recorded.

Lastly, the effect of binary chloride-inhibitor electrolytes on the atmospheric corrosion of stainless steels is demonstrated, using inhibiting salts (nitrates and sulphates) which are naturally present within ILW storage environments. The thermodynamics of these mixed-salt electrolytes in relation to the ambient humidity is also explored, with a view to establishing environmental domains where corrosion or inhibition are likely to occur, for a given electrolyte composition.

The thesis is presented as an ‘alternative format thesis’. The results chapters have either been formatted in preparation for submission to an academic journal, or have already been published in an academic journal. For all sections formatted in this manner Angus Cook was the lead author, undertaking the entirety of the experimental work and write-up. The contributions of other authors were mainly editorial, though specific contributions are detailed immediately before each relevant section.

2 LITERATURE REVIEW

2.1 Interim storage of intermediate level nuclear waste

2.1.1 Overview

The UK Government has committed to a policy of geological disposal for all civil higher activity nuclear waste.[3, 4] This is overseen by the Nuclear Decommissioning Authority (NDA) and will involve the creation of a Geological Disposal Facility (GDF) between 200 m and 1000 m below ground wherein all Intermediate Level Waste (ILW) and High Level Waste (HLW) will be placed. After a period of operation the facility will be backfilled with concrete and permanently sealed providing a stable and contained environment for the active lifetime of the waste.[5]

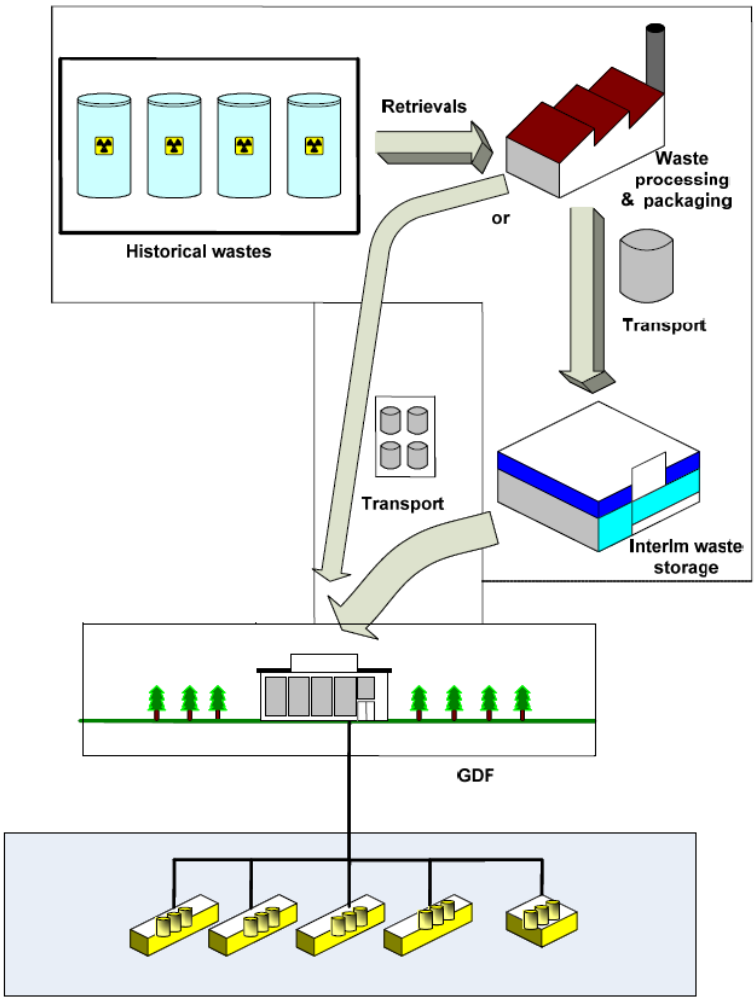

Figure 2-1 Schematic of the radioactive waste processing stream.[6]

At present there is no suitable site for a GDF identified within the UK. When such a site is identified it will still take several decades before the facility is able to accept waste packages for permanent storage. Current waste packages will face an extended (~100 year) interim storage period.[6] The integrity of these packages is under investigation as this storage period exceeds humanity's experience with modern day stainless steels. The grades of steel currently in use for ILW packages are 304L and 316L.[5]

The main failure mode of the containers in above-ground stores is expected to be brought about by the gradual deposition of aerosol contaminants including chloride,

nitrate and sulphate salts on the surface of the containers leading to atmospherically induced stress corrosion cracking (AISCC) and thus potential loss of container integrity.[7]

2.1.2 Conditions within stores

Determining the long-term integrity of ILW packages in surface stores relies on knowledge of the environment present within those stores. Surveys have been carried out to ascertain typical temperatures and humidities within these stores or within store analogues, as well as assessing the chemical species found within the stores and on the surfaces of test containers.[8-10]

2.1.2.1 Temperature and humidity

Current ILW stores are a mix of passively and actively ventilated sites. Stores such as the Encapsulated Product Stores (EPS) 1&2 at Sellafield are currently subject to environmental control to restrict the possibility of surface wetting of the containers through condensation, while other stores are passively ventilated, with perhaps the addition of heating in the winter period.[8] The conditions within stores with passive ventilation will be heavily influenced by the external environment and weather, though the buildings will naturally supress these fluctuations. The temperature of the container surface itself is not expected to be affected by the decay of the ILW within, the emission levels of which are insufficient to cause a heat build-up.[6] As such the container surfaces are expected to follow ambient temperature trends. Temperature and humidity trends for a number of stores are summarised in Table 2-1, and trends over a two year period for a single site are shown in Figure 2-2.

Table 2-1 Summary of environmental conditions within some stores and store analogues.

Store	Monitoring Period		Temperature (°C)		Humidity (%rh)	
	Start	End	Min	Max	Min	Max
Culham[8]	Sep 1998	Aug 2008	1.71	25.3	19.5	100.0
Harwell[8]	Apr 2009	Jun 2010	2.35	18.10	32.03	100.00
Trawsfynydd[11]	Oct 2008	Oct 2009	8	18	55	98
Sellafield[11]	Jul 2011	May 2012	4	20	50	95
Winfrith[12]	May 2008	March 2011	1	24	21	94
Total Range	**-**	**-**	**1**	**25.3**	**21**	**100**

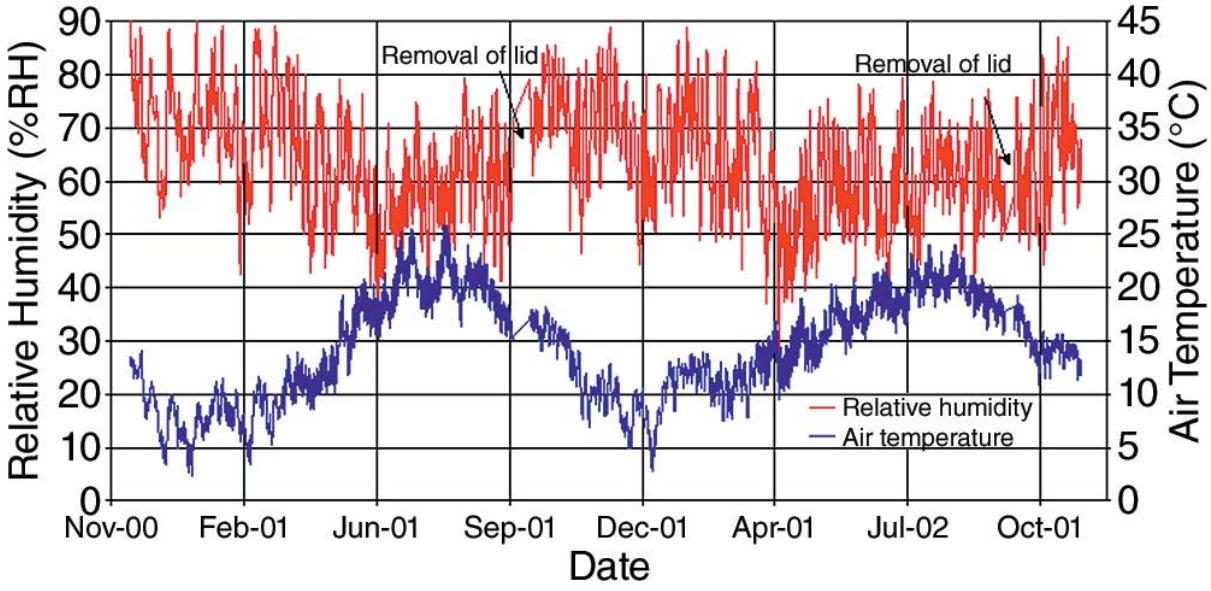

Figure 2-2 Temperature and humidity data from an inland warehouse in Culham, Oxfordshire, over the period November 2000 to October 2002.[10]

2.1.2.2 Aerosol deposition

The composition of chemical species present on the surfaces of the waste containers will play a key role in the initiation and propagation of local corrosion. While chloride is generally required for corrosion to take place on stainless steels,

there can be significant interaction with other chemical species to either promote or inhibit localised corrosion. The amounts of surface contaminant, both relative to each other and absolute, should also be considered.

Surface swab analysis has been carried out over a number of sites in the UK, in stores at Trawsfynydd, Sellafield, Hunterston, Dinorwig and a salt mine used as a deep store analogue. Values for the maximum levels of contamination, in terms of mass per unit area, are shown in Table 2-2.

Table 2-2 – Summary of surface swab results across surface stores and deep store analogue. Maximum surface concentrations across all surface stores are given. Deep store results have been kept separate as the concentrations of most surface species were much greater than those found in surface sites.[11]

Anion surface concentration (µg/cm^2)			Cation surface concentration (µg/cm^2)		
Species	**Surface Stores**	**Deep Store**	**Species**	**Surface Stores**	**Deep Store**
F^-	0.711	2.131	Li^+	0.012	3.008
$CH_3CO_2^-$	3.715	5.553	Na^+	16.060	588.963
HCO_2^-	0.567	1.243	NH_4^+	0.618	4.794
Cl^-	22.296	1024.351	K^+	14.426	7.573
NO_2^-	0.159	0.675	Mg^{2+}	1.947	3.830
Br^-	0.030	0.456	Ca^{2+}	23.540	74.734
NO_3^-	10.819	47.299			
PO_4^{3-}	0.254	-			
SO_4^{2-}	25.618	154.342			
$C_2O_4^{2-}$	1.788	15.803			

A separate study involving long term monitoring of a dummy container in Culham found a similar range and concentration of surface species as above. The bottom of the dummy container, however, exhibited an increase in chloride and metal species, which was attributed to road salt deposition during transport of the box during the monitoring period.[8] There is no representative combination of ions found common to all sample surfaces, with variations in composition between sample sites.[10, 11] As such there is likely to be significant differences in the phase and chemical behaviours of the chemicals on these surfaces between sites.

Deposition rates for chloride were also assessed, estimated to range from 3.8 to 0.14 µg cm^{-2} yr^{-1}.[8, 10] Chloride is an important ion to consider in this system, as it is a key promoter of corrosion.

2.2 Stainless steel

2.2.1 Composition and microstructure of austenitic stainless steels

Stainless steels are steel alloys containing at least 10.5 to 13 wt% chromium.[13] The addition of chromium allows the formation of a spontaneously passive layer at the surface of the metal, enriched in chromium and more resistant to corrosion than iron or mild steel.[14] Chromium encourages the formation of ferritic (body centred cubic) crystal structures in stainless steel. Nickel is commonly used as an austenite (face centred cubic) stabiliser. Common austenitic stainless steel grades, types 304 and 316, contain 18-20 wt% chromium, 8-12 wt% nickel; and 16-18 wt% chromium, 10-14 wt% nickel, 2-4 wt% molybdenum, respectively.[13] The molybdenum addition to type 316 stainless steels further enhances the resistance to corrosion, and will be discussed later.

Due to the presence of carbon in these steels, chromium carbide precipitates may be formed at grain boundaries in the alloy. These precipitates may act as preferential sites for corrosion of the alloy, due the local reduction in chromium surrounding the carbides, and the subsequent decrease in corrosion resistance at these sites. Solution treatment of the alloy will allow this carbon to be distributed throughout the matrix, but exposure to temperatures between 550-800 °C, such as when undergoing welding, may allow these carbides to form. Specifications for low carbon 'L' grades, with carbon contents <0.03 wt% to prevent this 'weld-decay' are therefore available.[13]

Other metallurgical inclusions may be present in these alloys, such as sulphur containing inclusions, which can also act as corrosion site initiators.[15-19] The role of inclusions on the initiation of corrosion will be discussed in detail in a later section.

2.3 Corrosion

2.3.1 General

The corrosion of metal refers to one half of an electrochemical redox reaction whereby metal ions are oxidised.[20] It requires the transport of both electrons and ions to complete the electrical circuit between the anode and cathode. The electron pathway is often provided by the metal in question, and the presence of a solvent, commonly water, may provide the ionic pathway. An example oxidation reaction for iron may be written as

$$Fe \leftrightarrow Fe^{2+} + 2e^{-} \qquad \textbf{Equation 2-1}$$

Counterpart to this is a reduction reaction which, in aqueous environments may involve the reduction of hydrogen ions to hydrogen gas, or if present in the system, the reduction of dissolved oxygen and water to hydroxide ions:

$$2H^+ + 2e^- \leftrightarrow H_2$$ **Equation 2-2**

$$2H_2O + O_2 + 4e^- \leftrightarrow 4OH^-$$ **Equation 2-3**

The electrochemical circuit is completed by the interactions between the oxidised metal species, and the reduced species to produce corrosion products. For corroding iron an example reaction may be

$$4Fe^{2+} + O_2 + 8OH^- \leftrightarrow 4FeOOH + 2H_2O$$ **Equation 2-4**

forming iron oxy-hydroxide, though there are many more different corrosion product species that may be formed.[21]

These reactions are reversible half-reactions, with the equilibrium point of the reaction dictated by the environment. As two key parameters of these reactions are the availability of electrons (the voltage potential) and the pH of the system (the balance of H^+ and OH^-) the thermodynamic stability of metals and metal oxides may be represented on a potential-pH diagram, or a Pourbaix diagram.[22]

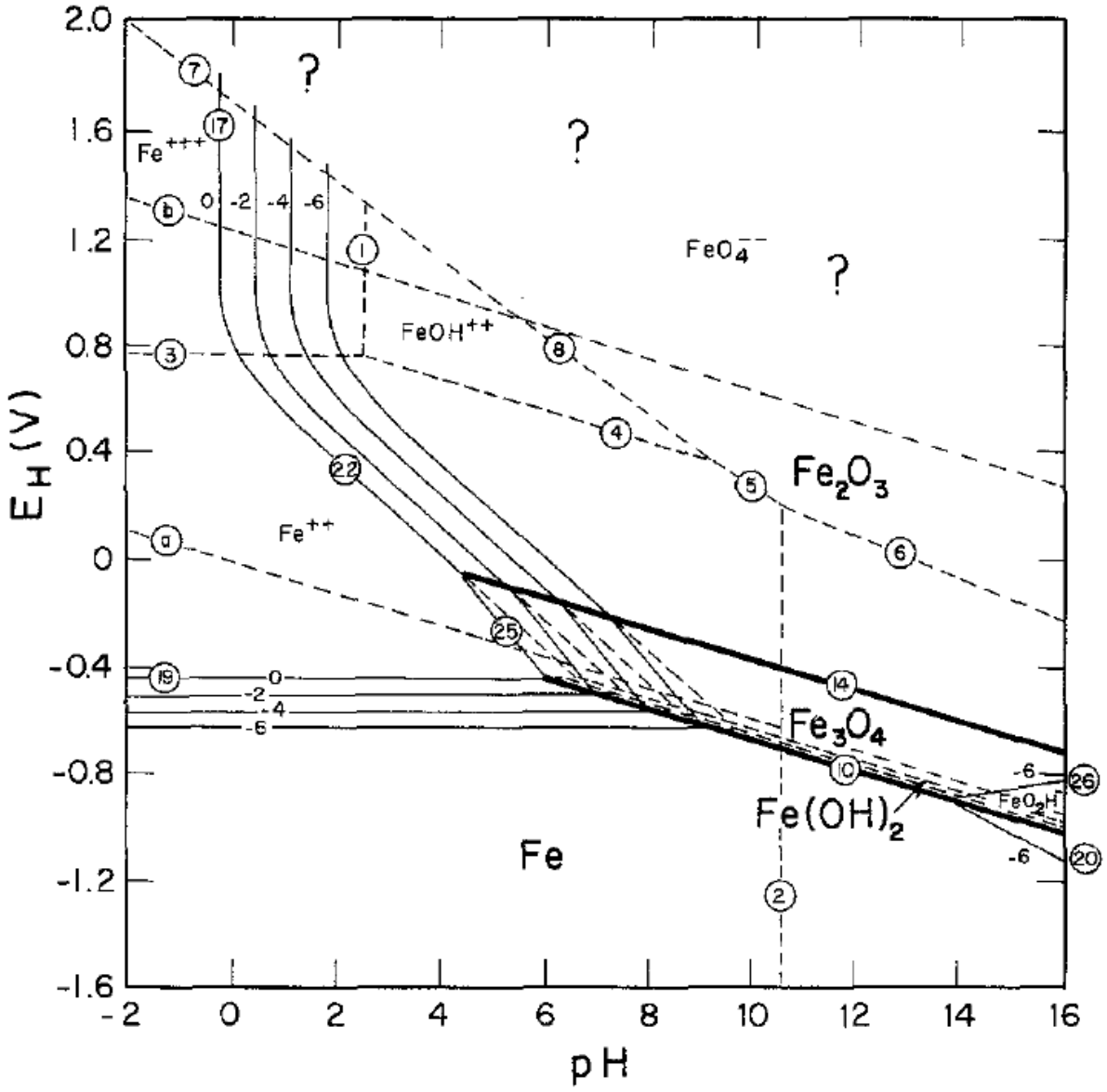

Figure 2-3 Potential-pH or 'Pourbaix' diagram of an iron-water system calculated at 25 °C, using the standard hydrogen electrode. Republished with permission of Electrochemical Society, Inc, from [23]; permission conveyed through Copyright Clearance Center, Inc.

These diagrams are useful tools in assessing regimes in which corrosion may or may not occur based on the surrounding environment.

2.3.2 Passivity

Thermodynamically there are situations where metals may be spontaneously passive rather than active, that is where the formation of an insoluble metal-oxide

or -hydroxide layer, which can protect the metal beneath it from contact with the environment.[24] For iron, for example, low potentials favour the formation of metallic iron; at high pH Fe_2O_3 or Fe_3O_4 are more thermodynamically stable than iron ions, and the metal is considered passive.

2.3.3 The role of chloride

While metals can undergo corrosion reactions in water, the presence of certain aggressive ions, such as halides, can cause corrosion to be more severe, or can allow corrosion to occur in a wider range of environments.[25] Chloride is typically the most considered halide in corrosion science, due to its ubiquity in the environment, and so its high likelihood of contact with metals.[26, 27] The pitting potential of iron and nickel exposed to chloride electrolytes has been shown to vary as

$$E_p = a + b \log[Cl] \qquad \textbf{Equation 2-5}$$

where E_p is the pitting potential, a and b are constants (where $b < 0$) and $[Cl]$ is the chloride concentration.[28, 29] As such an increase in the amount of chloride will decrease the potential required for stable pitting to occur.

The question of how chloride affects corrosion in a mechanistic sense has been long-standing.[26] For one, the motility of chloride is high, and so it is able to promptly move to a corroding area and charge-balance the production of positive metal and H^+ ions, thus allowing the oxidation reaction to be sustained.[30] Chloride is also thought to be able to disrupt the passive layers of metals, negating its protective effects.[31]

2.3.4 Pitting corrosion

Stainless steels are considered to have a higher resistance to corrosion than iron or mild steel, due the presence of chromium in the alloy, which enriches at the metal surface and forms a more thermodynamically stable passive layer than that found on pure iron, protecting the material underneath from corrosion.[32] Passive metals, however, are susceptible to localised corrosion due to local breakdowns or inhomogeneities in the passive layer. These local areas of dissolution can become autocatalytic, lowering the pH locally due to metal ion hydrolysis and preventing the passive layer from reforming.[33] For iron this reaction may progress as

$$Fe^{2+} + H_2O = Fe(OH)^{-} + H^{+} \qquad \textbf{Equation 2-6}$$

Due to the coupled cathodic reaction around this pitting site, the passive layer around the site is often maintained by a mixture of the lower potential (due to the production of electrons) and the formation of OH^- ions due to cathodic reduction of O_2. This protects the rest of the surface from further attack, but also drives the continued local pitting attack.[34] Pitting corrosion has been labelled an 'insidious' form of corrosion, in part due to the hidden nature of the sub-surface attack, as well as the difficulty in predicting its propagation and damage to the metal.[35]

2.3.4.1 Initiation of pitting corrosion

Due to the spontaneous passivity of the passive layer on stainless steels, pitting is most likely to occur at disruptions in the passive layer. Three key models for the breakdown of the passive layer are[31]: the penetration model, where aggressive ions such as halides enter the passive layer and increase its ionic conductivity[36]; the film breaking model, where a mechanical rupture in the passive layer exposes the unprotected metal underneath to the electrolyte[37]; and the adsorption model,

where again halide ions adsorb to the passive layer and increase the rate of metal dissolution, thinning and eventually removing the passive layer.[38, 39]

It is important to note that these models generally assume a homogeneous passive layer, and attempt to explain reasons for its spontaneous failure. For realistic alloys, however, metallurgical inclusions (such as MnS) are far more likely to be the reason for inhomogeneities in the passive layer, and are commonly held to be key initiation sites for pitting corrosion.[16-19, 40, 41] Inclusions which are not thermodynamically stable in situations where the rest of the passive layer is stable are likely to fully or partially dissolve, creating a cavity or occlusion in which an aggressive chemistry (build-up of metal ions leading to a decrease in the local pH due to hydrolysis) may more easily develop.[19, 40, 42, 43]

If sulphur is present in the inclusion, then sulphur compounds may further promote local corrosion. Elemental sulphur may be produced due to the dissolution of MnS inclusions, and has been seen to replace oxygen in the passive layer, allowing de-passivation to occur.[44, 45] Thiosulphate species have also been detected around dissolving inclusions, which have been shown to promote corrosion.[17, 46] Studies have also shown that the interface between some MnS inclusions and the steel matrix are more susceptible to corrosion due to a depletion of chromium, though this has not been observed for all such inclusions.[15, 47, 48]

2.3.4.2 Salt layers

For stable pitting to occur the rate of generation of metal ions must match or exceed the rate at which they are lost from the pit, otherwise the concentration of ions will decrease (and the pH increase) allowing the pit to re-passivate and cease growing.[33] If the rate of metal dissolution is greater than the rate of metal loss then

there will be a net increase in the concentration of metal ions over time, eventually leading to saturation and precipitation of the metal ions as a salt layer within the pit.[49-51]

The presence of a salt layer acts as a reservoir of metal ions within the pit, and may aid in the stability of the pit. A pit without a salt layer subject to a transient in the electrochemical potential (e.g. where the oxidation reaction is temporarily stopped) will continue to lose metal ions at a given rate until either the oxidation reaction is restarted, or the change in pH is sufficient to allow passivation, stopping the pit from re-activating. A pit which contains a salt layer, however, can survive a longer period of time before re-passivating, as it has a greater amount of metal ions to lose before re-passivation occurs, and is therefore more likely to survive transient events which affect the rate of corrosion.[52]

The salt layer also controls the electrochemical potential experienced at the corroding interface.[49] The electrochemical circuit involves the transport of both electrons through the metal, and ions through solution; the conductivity of metals is generally several orders of magnitude greater than the conductivity of electrolytes, and so the main source of resistance between anode and cathode arises within the electrolyte. The salt layer itself is one such source of resistance, leading to a potential drop as ions migrate through it. The resistance of the salt layer is proportional to its thickness, and this leads to a feedback mechanism whereby the rate of metal dissolution at the interface will always equilibrate to the rate of metal ion dissolution from the salt film, equivalent to the rate of diffusion from the pit.

2.3.4.3 Metastable pits

Electrochemical monitoring of stainless steel samples have shown evidence of transient current events in environments where stable pitting is not seen.[53, 54] These events have been attributed to the formation and rapid failure of small corrosion sites, named ‘metastable pits’. The existence of these metastable events shows that the conditions for the initiation of pitting, and the conditions for the stable propagation of pitting can be different. The failure of these metastable pits is attributed to their inability to produce at a sufficient rate (and so maintain) the high-concentration, low pH solution required to prevent the re-passivation of the alloy. Key to this interpretation is that the rate of the production of metal ions from the dissolving interface must be greater or equal to the rate of metal ion loss through the opening of the pit out into the bulk electrolyte solution.[33, 55]

Due to their small size metastable pits themselves do not present any real threat of material failure.[53] The metastable pits that manage to retain an aggressive pit solution however, may then propagate to stable pits. As such metastable pitting has been investigated in order to relate their formation to the formation of stable pits.

At the typical level of inspection of a metal surface the initiation of pits is usually regarded as stochastic, determined by factors which appear to be random in nature.[25] The rate of generation of metastable pits may be related to the likelihood of stable pitting by considering a transition probability; this expression may be written in the form

$$\Lambda = \lambda\, e^{-\mu\tau}, \qquad \textbf{Equation 2-7}$$

where the rate of formation of propagating, stable pits Λ is related to the rate of generation of metastable pits λ, which then must survive a critical period τ, with μ

representing the probability of re-passivation of the metastable pit before it can transition to a stable pit.[56] The term μ in Equation 2-7 is dependent on the system in question, and will be heavily influenced by the exposure environment.

2.3.4.4 Propagation of pits

The stabilisation of penetrative pit growth by the salt layer, and thus the linking of corrosion rate with ion escape rate allows the use of diffusion based calculations to describe the rate of pit growth.[57]

When considering a simple one dimensional (1D) system, Fick's first law may be written as

$$J = -D\frac{\delta C}{\delta x} \qquad \textbf{Equation 2-8}$$

where J is the flux of particles, D is the diffusion constant of those particles, and C is the concentration of particles. This describes the relation that the flux of particles from one region to another is proportional to the difference in concentration of those particles in the two regions.

This equation may be integrated, such that

$$J\int_0^h \delta x = -D\int_{C_0}^{C_h} \delta C \qquad \textbf{Equation 2-9}$$

$$J\,h = -D(C_h - C_0) \qquad \textbf{Equation 2-10}$$

$$J\,h = -D\Delta C \qquad \textbf{Equation 2-11}$$

where C_h and C_0 are the particle concentration at positions $x = h$ and $x = 0$, respectively, where h is an arbitrary distance from position 0.

If we now consider the system to be a 1D pit, of depth h, with metal ion concentration C_0 at the pit mouth (the top of the pit) and a metal ion concentration C_h at the bottom of the pit, we may express the electrochemical current associated with that pit using the relation

$$J = \frac{i}{nF} \quad \textbf{Equation 2-12}$$

where i is the current density (current per unit area), n is the average oxidation state of the metal ions, and F is the faraday constant. This gives

$$\frac{ih}{nF} = -D\Delta C \quad \textbf{Equation 2-13}$$

$$i = \frac{nFD\Delta C}{h} \quad \textbf{Equation 2-14}$$

where the negative term may be discarded as it is implicit that current flows from the pit bottom to the pit mouth, and out into the bulk solution. Equation 2-14 then gives the diffusion limited current density for a 1D model pit, showing that the current density is inversely proportional to the depth of the pit.[57]

The charge transfer given by a mass of metal oxidising can be expressed as

$$Q = \frac{mnF}{M} \quad \textbf{Equation 2-15}$$

Where Q is the total charge, m is the mass of the metal, and M is the molar mass of the metal. Considering a cylindrical volume of metal, with circular area A and height h, we may re-write Equation 2-15 as

$$Q = \frac{Ah\rho nF}{M} \quad \textbf{Equation 2-16}$$

where ρ is the density of the metal. Using the simplified relation $Q = It$, where I is current, and t is time, Equation 2-16 may be rearranged to

$$h = \frac{Mit}{\rho nF}$$ **Equation 2-17**

Now combining Equation 2-17 and Equation 2-14 we may show

$$h^2 = \frac{Mit}{\rho nF} \times \frac{nFD\Delta C}{i} = \frac{MD\Delta C}{\rho}\, t$$ **Equation 2-18**

Thus for pits propagating with a salt layer, the depth of the corrosion site may be expected to increase proportional to $\sqrt{t}$, if the term $D\Delta C$ is a constant.[58] This relation has been shown to hold for electrochemical tests with 1D 'lead-in-pencil' electrodes, 2D foils, and 3D pits.[51, 57-61]

2.3.5 Crevice corrosion

The fundamentals of crevice corrosion on stainless steel share many similarities with those of pitting corrosion. Both involve the development and retention of an aggressive, low pH, high chloride concentration electrolyte, though in the case of crevice corrosion the occlusion of the corroding area is not formed by the corrosion process itself, as it is in pitting corrosion, but by the presence of a physical barrier in contact with the metal.[62]

Crevice corrosion may initiate from a metallurgical inhomogeneity, like an inclusion. Due to the ready presence of a physical barrier, however, an aggressive electrolyte may also build-up from the passive dissolution and hydrolysis of metal ions from the passive film of the metal.[63, 64] In either case, as a barrier is already present to confine the metal ions within the crevice, the generation of an aggressive solution can destabilise the passive layer present within the creviced region and the surface may undergo active dissolution.

The corresponding cathode for crevice corrosion reactions is often located outside the crevice in aerobic systems where the reduction of O_2 is the primary cathodic reaction, though H_2 may also be produced within the crevice.[62, 65]

2.3.6 The effect of molybdenum on corrosion

As described earlier, the key difference between types 304 and 316 stainless steel is the addition of 2-3 wt% molybdenum into the 316 alloy, to improve its corrosion resistance. The exact mechanism (or perhaps more accurately, the key mechanism) by which molybdenum improves the corrosion resistance of type 316 stainless steel is debated.[66, 67] The two main mechanisms can be simplified to: molybdenum's effect on the passive layer of stainless steels, and molybdenum's effect on the active dissolution of stainless steels.

Molybdenum may bolster the passive layer of alloys either through its own enrichment in the passive layer [68], by encouraging the enrichment of chromium in the passive layer [69, 70], or both.[71-73] The presence of molybdenum may also counteract the deleterious effects of sulphur species on the passive layer, with Mo binding to adsorbed S on the surface, and removing it into solution by dissolution.[74, 75]

As well as being enriched in the passive state, molybdenum has been seen to become enriched in metals at sites undergoing active dissolution, lowering the corrosion rate, and making it more likely for a passive film to re-develop.[52, 76-80] This may be due to the formation of thermodynamically stable molybdenum-oxides or -hydroxides at active corrosion sites, though elemental molybdenum is expected to form at lower pH conditions.[80]

It is interesting to note that, although evidence of the importance of both regimes has been presented, under realistic, industrial type alloys with significant metallurgical inclusions it is arguable that molybdenum is more important in interrupting active corrosion processes, rather than due to preventing them from initiating in the first place.[67]

2.3.7 Atmospheric corrosion

2.3.7.1 Characteristics of atmospheric corrosion

Atmospheric corrosion may be broadly differentiated from ‘full immersion’ corrosion in three ways. Firstly, there is a greatly decreased volume of electrolyte involved with the corrosion reaction, usually taking place under a thin-film or droplet of electrolyte. This also affects the availability of oxygen for the electrochemical reaction, generally allowing much easier access of oxygen to the metal surface.[81] Secondly, atmospheric conditions tend to give rise to high solution concentrations, as the water activity of the electrolyte and of the surrounding atmosphere (i.e. the relative humidity) are in equilibrium. $MgCl_2$ solutions, for example, may reach a chloride concentration of 8 M at humidity or ~50 %rh (Figure 2-4).[82, 83]

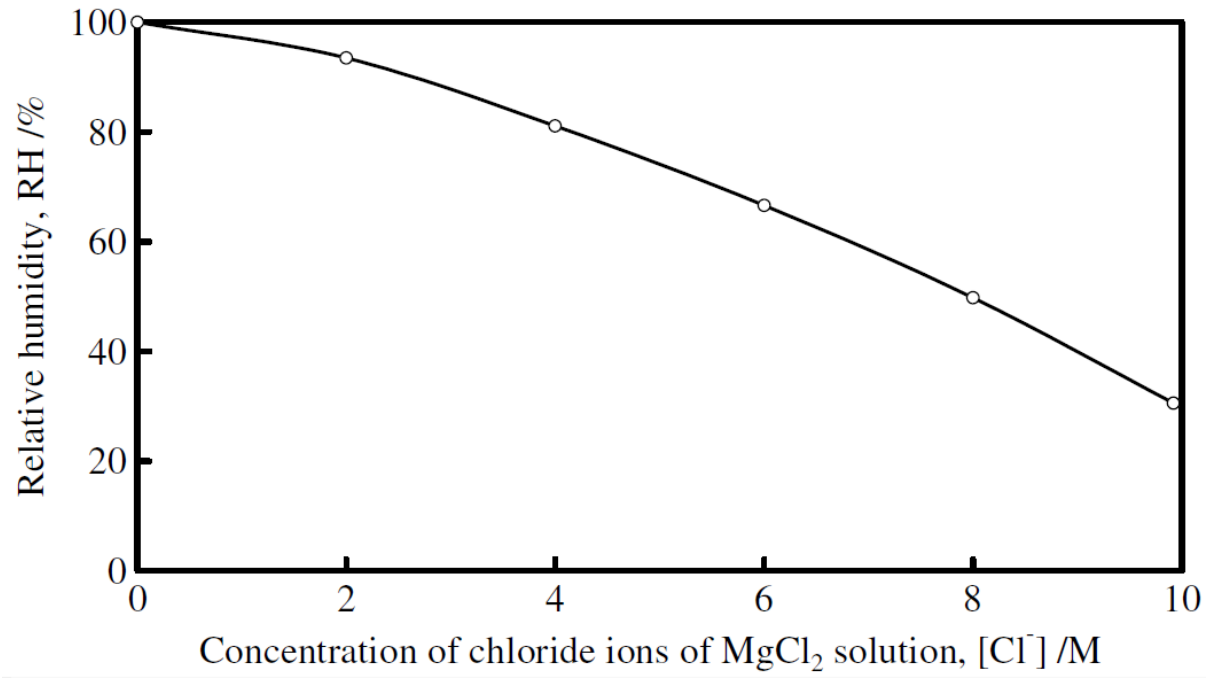

Figure 2-4 Relationship between equilibrium relative humidity and chloride concentration in a $MgCl_2$ solution.[82]

Lastly, and hinted at above, systems under atmospheric conditions are greatly influenced by their surrounding environment, such as temperature, humidity, and aerosol content. As such comprehensive consideration of atmospheric corrosion systems requires a consideration of the environments in which they are subjected to.

2.3.7.2 Evans' droplet and three phase boundary

The seminal work on droplet corrosion is arguably from Evans, and his analysis of the location of the anodic and cathodic areas formed during the corrosion of iron under a droplet of NaCl solution.[84] Evans observed that the cathode preferentially formed at the edge of the droplet, where the ingress of O_2 from the surrounding air was easiest, with the anode preferentially forming in the centre of the droplet. Subsequently the consideration of the three phase boundary (TPB) i.e. the area where metal, electrolyte and air meet as an important aspect of droplet corrosion has

been developed, and the properties of the TPB have been shown to influence the cathodic reactions under droplets.[85-87]

It is important to note that the significance of the TPB relies on a differential aeration cell being set up within a droplet due to the difference in diffusion path length between the air and different parts of the meal surface. For distances (or electrolyte thicknesses) below ~20 µm, however, the rate limiting step for the cathodic reduction of O_2 becomes the dissolution of O_2 into solution, rather than the diffusion to the metal surface.[88] As such, very small droplets, or very thin solution layers are unlikely to demonstrate a TPB in the same manner as larger droplets, and the location of the cathode in corrosion reaction is more likely to be determined by the proximity to the anode, and the solution resistance.[82]

2.3.7.3 Precipitation in atmospheric systems

As the water activity (and so concentration) of atmospheric electrolytes is dictated by the surrounding environment (humidity and temperature), there are very likely to be cases where the surrounding water activity is decreased below the saturation point of a given salt, causing that salt to precipitate from the electrolyte; Cook *et al.* have observed this with droplets of seawater.[89] Such precipitation has been predicted to have the effect of reducing both the solution conductivity, and the available cathodic area, due to the physical barriers presented by precipitates within the electrolyte.[90] The use of silica particles to create reproducible surface layers on 304 stainless steel to investigate the effects of precipitates on corrosion under thin-films has been reported, though silica particles may not fully replicate the effects of realistic salt-based precipitates.[91, 92]

2.3.7.4 Atmospheric corrosion of stainless steels

The onset of pitting corrosion of stainless steels has a strong dependence on the chloride concentration of the electrolyte solution. In tests where stainless steel samples cycled through wet-dry conditions over the testing period, Cruz *et al.* showed that pitting was seen to initiate preferentially just before the NaCl testing solution dried out, i.e. at the higher chloride concentrations, and that pits re-passivated during the dry, precipitation period.[93, 94] Tsutsumi *et al.* were able to show that pitting on type 304 stainless steel samples occurred after a chloride concentration of ~6 mol/L was achieved through the drying of $MgCl_2$ solution layers.[82, 95, 96] This critical chloride concentration was found to be ~4-4.5 mol/L for type 430 stainless steel, suggesting that different alloy compositions have a significant effect on this critical concentration.[97, 98] Similarly, Prosek *et al.* observed pitting under $CaCl_2$ droplets on both 304 and 316L stainless steels at 50 %rh, but none at 70 %rh.[99] Sensitised alloys have also been shown to initiate corrosion at higher humidities (and so lower chloride concentrations) than non-sensitised specimens of the same alloy.[100]

The thickness of solution layers and, when used, the dimensions of droplets have been shown to affect the corrosion behaviour of stainless steels. Tomashov related the corrosion rate of active metals (rather than stainless steels) to the thickness of the moisture layer present on the surface.[81] Changes in the electrolyte layer thickness change both the availability of atmospheric oxygen (thinner layers decrease the diffusion path for O_2, increasing the amount available for reduction reactions), as well as the conductance and interconnectivity of the electrolyte (affecting the electrochemical resistance between cathode and anode). While these were described for active metals, the same arguments can be made for passive

metals undergoing localised corrosion; indeed thinner solution layers, and less expansive solution layers have been shown to be less likely to initiate corrosion.[82, 95, 97] Once corrosion has initiated, pits have been shown to grow with larger diameters under larger, and thicker droplets, associated with the increase in the cathodic area, and a decrease in the ohmic drop between cathode and anode.[101]

Corrosion sites under atmospheric conditions tend to initiate as an initial area of shallow attack around an inclusion, which etches the metal surface.[82, 95, 97, 102, 103] After ~1 hour the attack becomes more localised. Street *et al.* showed that the morphology of continued attack depended heavily on the exposure humidity and droplet thickness, with small 'satellite' pits appearing around the shallow dish area at low humidity (33 - 38 %rh), spiral or 'lobe'-like attack seen at intermediate humidities (38 - 48 %rh), and continued deep attack of the original area at higher humidities (56 %rh).[102]

$MgCl_2$ is commonly used to investigate atmospheric corrosion systems. Shoji and Ohnaka demonstrated that it was the $MgCl_2$ content within seawater that was responsible for low-temperature cracking of austenitic stainless steels under seawater droplets.[104] Since this $MgCl_2$ has been commonly used as an analogue for marine-derived aerosols.[82, 95, 97, 99, 102, 103, 105-107] $MgCl_2$'s low deliquescence point (~33 %rh) also allows it to remain aqueous in a wide range of environmental conditions, and to reach a high chloride concentration (~10 M [Cl^-]) likely to initiate corrosion.[82] $CaCl_2$, which has similar deliquescence behaviour to $MgCl_2$, and NaCl, which is common in the environment are also used for corrosion testing.[99, 105]

2.3.7.5 Formation of atmospheric corrosion environments

The simple (though time-expensive) way to gather information on the atmospheric corrosion of metals is to expose metal samples in real conditions of interest for extended periods.[108-111] This has the benefit of giving truly representative results, though the downsides to this method include the many uncontrolled environmental factors affecting the test samples, as well as the extended testing periods required to give representative results.

Multiple techniques have been used to simulate the thin-film nature of atmospheric corrosion systems in a controlled, laboratory environment. Thin films may be formed by immersing a sample in a solution, then removing it, relying on surface tension effects (or sometimes a permeable covering) to keep any electrolyte in contact with the surface.[93] Thin films have also been formed by depositing an initially dilute solution layer onto a sample, and then allowing it to dry and thin to a given exposure humidity.[95]

Other methods involve immersing a sample within a solution, and then raising it up to the solution surface.[112, 113] This has the advantage of covering a large area in a homogeneous layer, which can be changed by altering the sample height, as well as ensuring that the thin-film is in contact with a larger reservoir of electrolyte to mediate concentration or composition changes.

Droplets deposited *via* micropipette may be used to accurately control electrolyte coverage over an area, as well as the composition of the electrolyte.[82, 89, 99, 103, 105, 106, 114, 115] Multiple droplets may be used on a single sample, allowing multiple tests to be conducted in parallel.[102]

Ink-jet style depositions have been used to create reproducible salt layers on samples, again allowing multiple tests to be conducted in parallel, while controlling electrolyte composition and coverage.[101, 116-118]

Ultrasonic deposition methods have also been explored to both deposit and hydrate aerosols on aluminium alloys.[119] This technique has the advantage of more accurately mimicking the deposition of aerosols, rather than assuming a ready-formed, continuous electrolyte.

2.3.7.6 In-situ monitoring of atmospheric corrosion

Atmospheric systems present specific challenges when attempting to monitor them during exposure. Electrochemical tests, for example, must find ways to introduce reference and counter electrodes into systems comprising thin electrolyte films, or droplets. Techniques to address this have included: the use of metal plates as electrodes, embedding every plate into the same resin block and covering the whole assembly with a thin electrolyte film;[93, 120] introducing reference and counter electrodes into a droplet using a micropipette tip as a Luggin probe;[115] and using a silver wire pulled taught through a droplet to act as a pseudo-reference electrode.[100, 114]

The distribution of electrochemical potentials under a corroding system (such as under an electrolyte layer or droplet) may be assessed using non-contact methods, such as with a Kelvin probe, or scanning vibrating electrode technique (SVET).[121-127] These methods may provide spatially resolved information on anodic and cathodic reactions occurring under atmospheric conditions.

In-situ x-ray tomography has been conducted on pin samples under droplets, allowing the development of corrosion site morphologies to be monitored in 3D over time.[128-130]

Optical methods have also provided insights into corrosion processes. The simple inclusion of an optical camera or microscope watching a corroding sample has provided insight into changes in electrolyte volume during pitting, caused by the generation of metal ions, as well as the development of corrosion site morphology in stainless steels under different humidities.[102, 131]

2.3.8 Corrosion inhibition

Just as corrosion processes can be promoted by certain chemicals (such as chlorides) corrosion may also be inhibited by the presence of certain chemicals in the electrolyte (such as chromates, or nitrates).[132-134] These chemicals may be purposefully included, such as inhibitors included in coating systems to protect from external corrosion, or additions to internal fluids to protect from internal corrosion.[135, 136] In other systems these inhibiting species may be naturally present in the environment, such as in certain atmospheric systems.[10]

2.3.8.1 Nitrates and sulphates

Nitrate and sulphate salts have long been recognised to have an inhibiting effect on the chloride-induced corrosion of stainless steels.[63, 133, 134, 137-144] These particular salts are likely to appear in corrosion systems due environmental factors, rather than due to their purposeful addition, especially in environmental systems. Work under full-immersion conditions has shown that the inhibiting effect occurs when a critical ratio of chloride and inhibitor is reached, and the ‘minimum ion activity necessary to inhibit [corrosion]’ may be expressed in the form

$$\log\{Cl^{-}\} = A\log\{I\} + B \qquad \textbf{Equation 2-19}$$

where I represents the inhibitor, and A and B are constants.[137]

There is evidence that nitrate requires the presence of a salt film before any inhibiting effects can occur, having no effect on the active dissolution of a pit.[133, 143] It has been proposed that the presence of NO_3^- within the salt film allows it to be reduced, consuming available H^+ ions, increasing the pH within the pit, and so promoting the re-passivation of the metal surface.[143] Nitrate also affects the formation of metastable-pits which are thought to contain salt-layers, with the addition of nitrate into solution eliminating slow-rise electrochemical transients, thought to be indicative of such metastable events.[139]

The inhibition mechanism of sulphate ions is thought to be one of competitive migration, where the aggressive effects of chloride ions (e.g. electromigration to a corrosion site) are reduced due to interactions with sulphate ions.[63] There is also evidence that sulphate may be present in the salt film found inside pits, increasing the required concentration of metal ions within a pit to maintain a stable aggressive electrolyte.[61]

2.4 Summary

As has been suggested above, there are a large number of variables which can impact the pitting corrosion of stainless steels. This, coupled with the stochastic nature of pitting corrosion (at least at the level at which it is usually observed) suggests that high-throughput, parallel testing techniques would be of benefit to assess these systems. Furthermore, methods to easily gather more data on corrosion processes in-situ on a large (i.e. more than one sample at a time) scale would help fill in gaps that may be left by extended inspection periods.

Discussions of crevice corrosion generally tend to focus on crevices formed by connections, fixings, or other component design choices. There is the likelihood, however, that under atmospheric systems precipitates will form which can act as crevice formers and crevice-corrosion may occur under these nominally un-occluded atmospheric conditions (as has been reported by Guo).[129] There is therefore benefit to a systematic study of systems likely to develop precipitates, and to study their effect on atmospheric corrosion.

Similarly, although the inhibiting effects of nitrates and sulphates on the corrosion of stainless steels are well known for full-immersion conditions, there is little information available on how these systems will behave under atmospheric conditions. This may be of particular importance, as nitrate and sulphate salts may be deposited alongside chloride salts under atmospheric conditions.

3 MATERIALS AND METHODOLOGY

3.1 Overview

Droplets of salt solutions were deposited onto stainless steel samples, which were then placed into controlled exposure environments with specified temperature and humidity. After a set exposure period the samples were removed and analysed.

3.2 Materials

The alloys investigated were commercial low carbon austenitic stainless steels, grades 304L (EN 1.4307, UNS S304003, X2CRNi18-9, BS 304S 11) and 316L (EN 1.4404, UNS S31603, X2CrNi18-9, BS 316S 11).[145] Both alloys were provided by Aperam – Stainless France, and were cold rolled plate, 3 mm thick, which was solution treated between 1040-1100 °C with subsequent cooling by forced air before receipt. A cast analysis of both alloys, provided by the foundry, is shown in Table 3-1. The plate was received in 250 x 250 mm squares, and was cut into samples first by mitre saw with a bi-metallic blade, then by alumina cutting disc.

Table 3-1 Cast analysis of 304L and 316L stainless steels, provided by the foundry.

	Element (wt%)	C	Si	Mn	Ni	Cr	Mo	N	S	P	Co
304L	Spec.	<0.030	<0.75	<2.00	8.00-10.50	18.00-19.50		<0.100	<0.0150	<0.045	
	Rec.	0.023	0.44	1.46	8.00	18.08		0.07	0.0033	0.032	0.171
316L	Spec.	<0.030	<0.75	<2.00	10.00-13.00	16.50-18.00	2.000-2.500	<0.100	<0.0150	<0.045	
	Rec.	0.024	0.38	1.25	10.04	16.55	2.000	0.044	0.0032	0.034	0.189

3.3 Microstructure

To assess the microstructure of the two stainless steels a 25 x 25 mm section of each alloy (304L and 316L) was cut and cold-mounted in resin (VARI-SET 20 powder with VARI-SET 10/20 liquid, Metprep). The samples were ground with SiC papers to P4000 grit, and then polished first with 3 µm diamond suspension (DiaPro3, Struers), and then a 0.02 µm OP-AN alumina suspension (Struers). The samples were ultrasonically cleaned in deionised (DI) water (>15 MΩ·cm Millipore), and imaged in a SEM (Joel 6060).

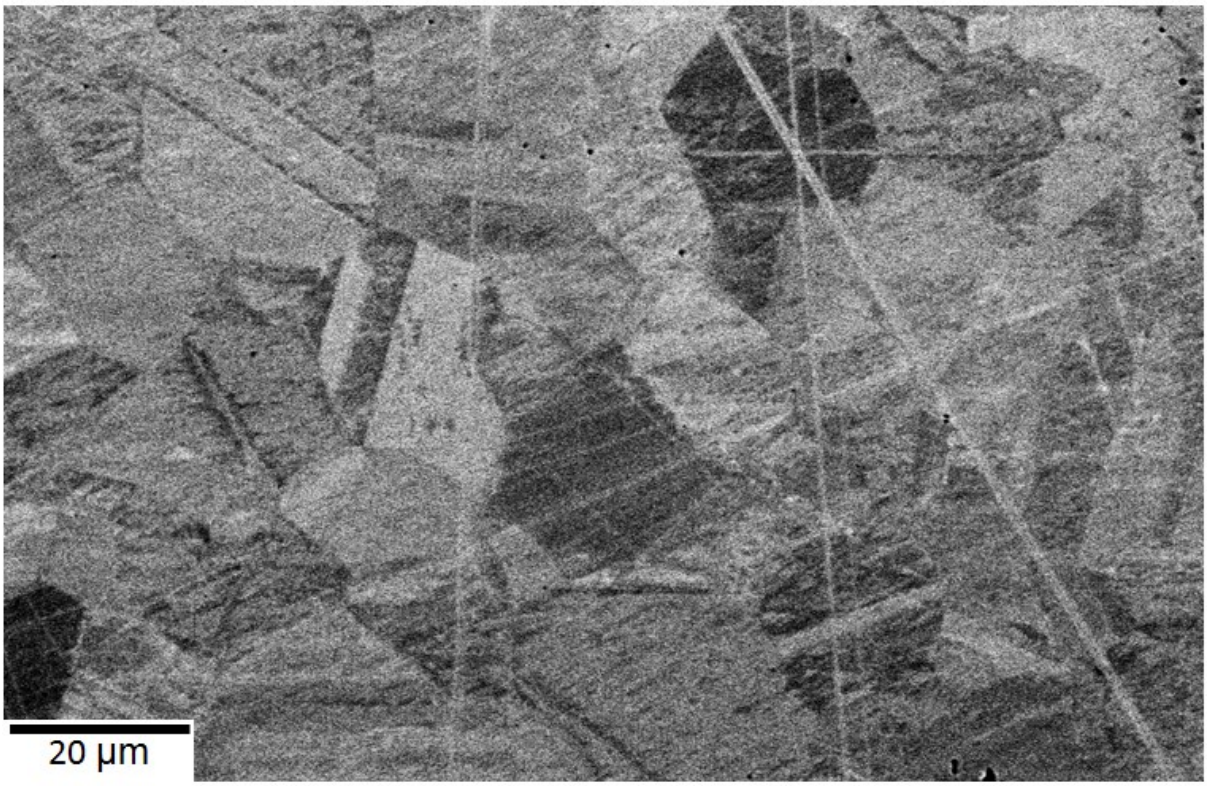

Figure 3-1 Backscattered electron image of 304L stainless steel, after mirror polish with 0.2 µm OP-AN suspension. Accelerating voltage at 20 keV.

The microstructure of both alloys was seen to consist of equiaxed grains, ~20 µm across, with inclusions throughout (Figure 3-1). An example manganese sulphide (MnS) inclusion is shown in Figure 3-2. Titanium-rich and aluminium-rich particles were also observed, though any aluminium rich particles may have been left over from the final polishing with an alumina-based polishing suspension.

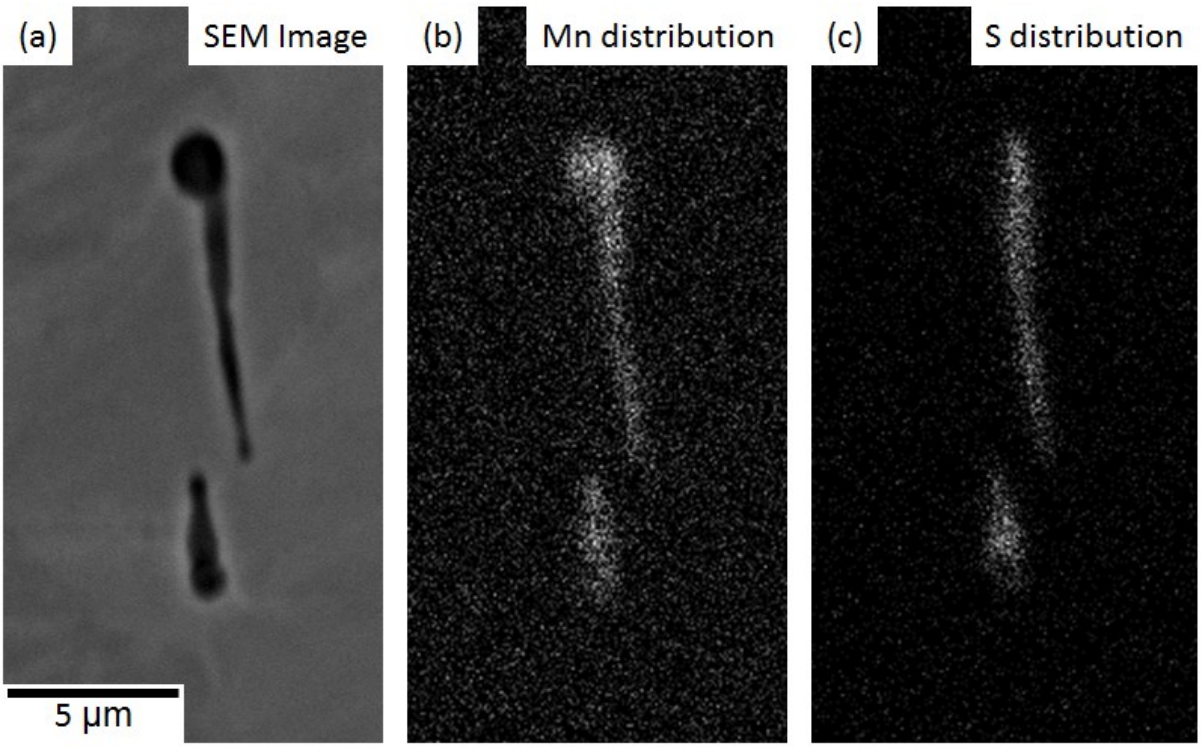

Figure 3-2 SEM secondary electron image (a) and EDX elemental maps (b,c) of an MnS inclusion found in 304L stainless steel. 20 keV accelerating voltage.

3.4 Mounting and grinding

Small samples (≤25 x 25 mm) were cold-mounted in resin (VARI-SET 20 powder with VARI-SET 10/20 liquid, Metprep). Larger samples were either cold-mounted in resin, as above, or mounted onto rubber bungs with epoxy (Araldite Rapid). The two types of sample are shown in Figure 3-3.

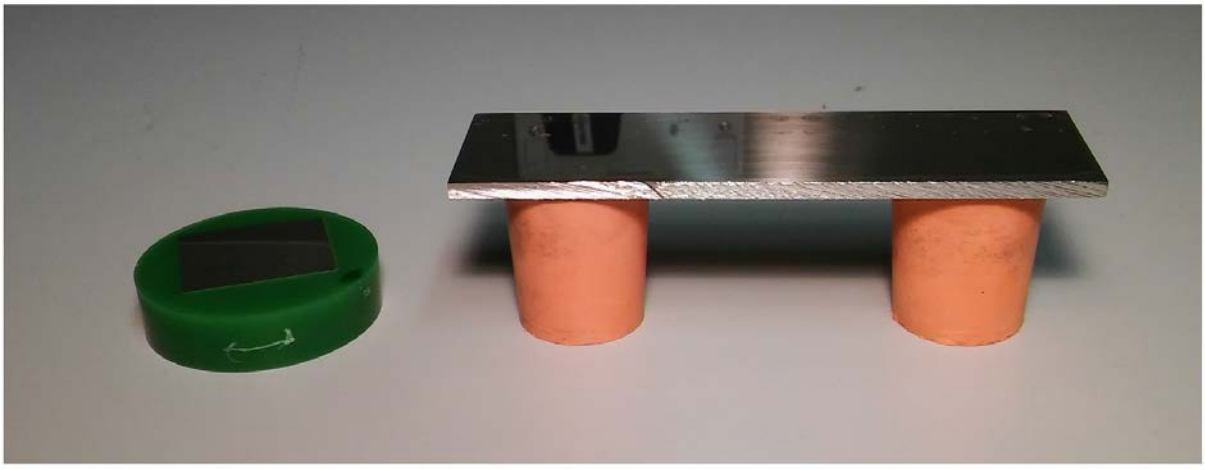

Figure 3-3 Examples of mounting techniques for small (25 x 25 mm, left) and larger (25 x 75 mm, right) stainless steel samples.

All samples used in atmospheric corrosion tests were wet-ground with mains water to P800 grit, using SiC papers. The final grinding direction was always perpendicular to the rolling direction of the sample. After grinding samples were ultrasonically cleaned with de-ionised (DI) water (>15 MΩ·cm, Millipore) to remove particulates left over from grinding. ~60 seconds of ultrasonic cleaning was sufficient to remove all visible particulates from the surface. Samples were dried using an empty wash bottle to blow the water film from the sample surface. Dried samples were placed in a covered container at ambient temperature and humidity to allow the passive layer to re-grow. Samples were generally left for ~24 hours before use.

3.5 Chemicals

All chemicals were ACS grade, unless otherwise stated. Solutions were made using de-ionised (DI) water (>15 MΩ·cm, Millipore).

3.5.1 Humidity control using saturated salts

Humidity control within sealed desiccators was carried out based on ASTM standard E104-02(2007), using quantities of saturated salt solutions to maintain set

humidities.[146] The solutions used and corresponding equilibrium relative humidities at 30 °C are shown in Table 3-2.

Table 3-2 Saturated salts used for humidity control, based on ASTM E104.[146]

Salt	Humidity fixed point designation	Relative humidity at 30 °C
$MgCl_2$	HFP 33	32.4 ± 0.2
K_2CO_3	HFP 43	43.2 ± 0.5
NaBr	HFP 59	56.0 ± 0.4
NaCl	HFP 75	75.1 ± 0.2

A saturated solution of each salt was made, and added to a quantity of dry salt within the bottom of a desiccator. The desiccator was then placed in the intended exposure environment for 24 hours so that the internal environment could equilibrate. The equilibration was verified using a temperature and humidity logger, placed inside the desiccator (EasyLog EL-USB-2-LCD, Lascar Electronics Ltd.).

3.5.2 Solutions for deposition

The salts used to make deposition solutions included: NaCl, $MgCl_2$, $CaCl_2$, $Mg(NO_3)_2$, $MgSO_4$ and $CaSO_4$. Solutions were made from NaCl, $MgCl_2{\cdot}6H_2O$, $CaCl_2{\cdot}2H_2O$, $Mg(NO_3)_2{\cdot}6H_2O$, $MgSO_4{\cdot}7H_2O$ and $CaSO_4{\cdot}2H_2O$ salts respectively. Salts were supplied from Sigma-Aldrich and Arcos Organics.

Stock solutions were mixed to a given molar concentration by weighing out a calculated mass of the desired salt, and dissolving it in a set volume of DI water. The accuracy of the balance scales for mass measurement was ±0.005 g, and the accuracy of the volumetric flasks was between ±0.1 mL for a 100 mL flask, and ±0.4 mL for a 1000 mL flask. Hygroscopic salts, such as $CaSO_4{\cdot}2H_2O$, which were

likely to take on water from the ambient laboratory humidity were kept in a dry desiccator before use, and weighed within ~10 minutes of removal in order to minimise any change in mass due to water uptake.

3.6 Apparatus

3.6.1 Droplet deposition

Two methods of droplet deposition were used: manual, and automatic. Manual droplet deposition was carried out by hand *via* micropipette, and was usually carried out on smaller samples (i.e. fewer than ~20 droplets per sample). Automated droplet deposition was usually used for larger samples, and carried out using an automated pipette.

3.6.1.1 Manual droplet deposition

For droplets up to 2 µL a micropipette with a 2 µL maximum capacity was used (Eppendorf). For droplets larger than 2 µL a micropipette with a 20 µL maximum capacity was used.

3.6.1.2 Automated droplet deposition

Automated droplet deposition was carried out with a MultiPROBE II Ex robotic liquid handling system (Packard Biosciences). The system consists of a robotic arm able to move a pipette tip over a sample deck (Figure 3-4(a,b)). The pipette tip is connected to an automated syringe and filled with a reservoir of system liquid (DI water). Through hydraulic action the pipette can aspirate and dispense aqueous solutions, transporting them around the sample deck.

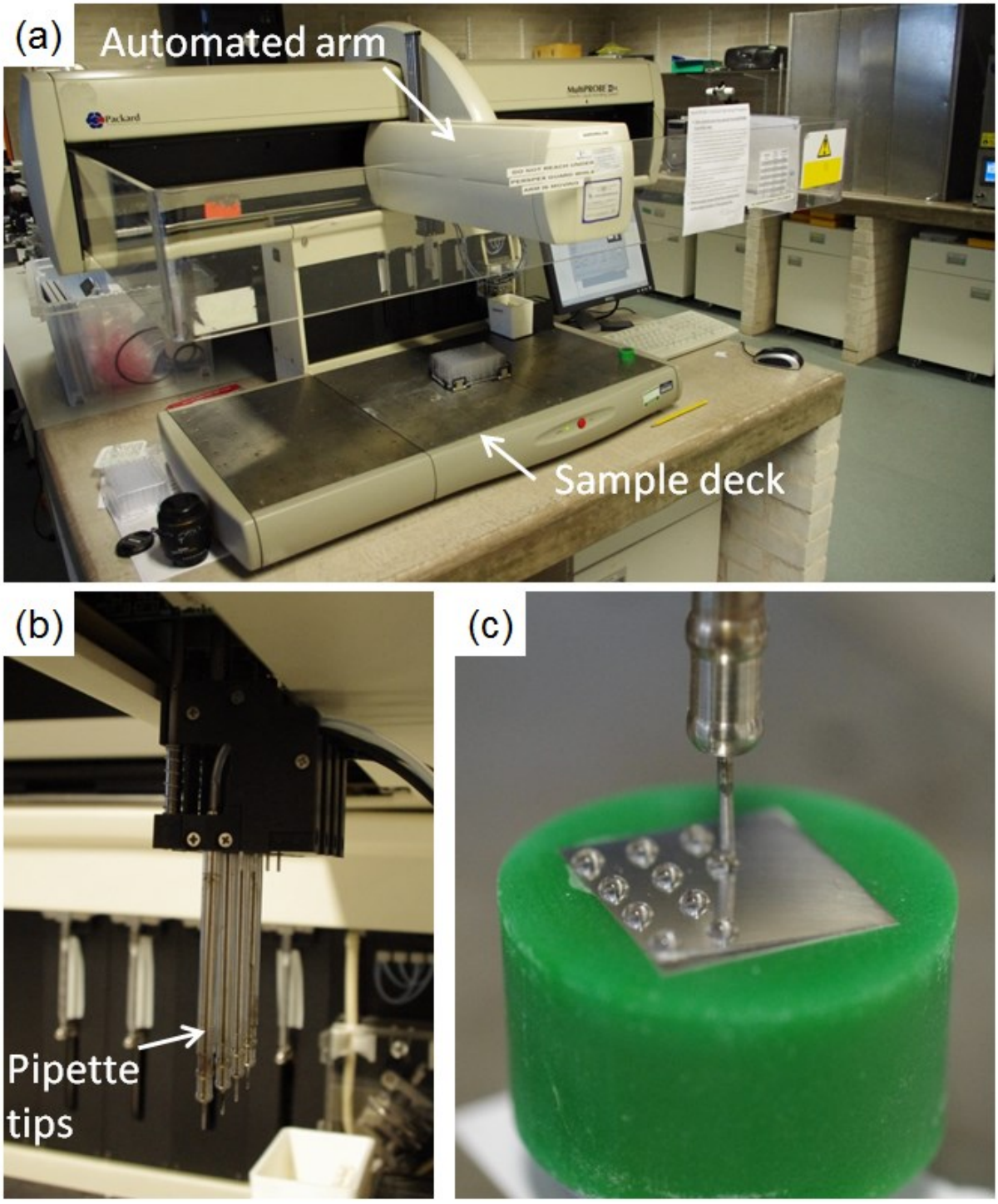

Figure 3-4 MultiPROBE II Ex automated liquid handler (Packard Biosciences), (a) whole system showing sample deck and automated arm, (b) pipette tips, (c) example of droplet deposition procedure.

The syringe volume was 500 µL, with the syringe plunger stepper motor able to move to 12000 unique positions along the syringe, resulting in a theoretical instrument accuracy of ~0.05 µL.

Droplets were deposited in arrays of different sizes, depending on the sample size (Figure 3-4(c)). For each droplet of a given volume the hanging height of the droplet from the pipette tip was measured. When depositing a droplet the pipette tip was moved to a height over the sample surface that was equivalent to 80% of the hanging droplet height. The deposition rate was 10 µL/second.

The pipette tips were automatically flushed through and rinsed when changing between different salt solutions, in order to prevent cross-contamination of solutions. When multiple droplets on a sample were of the same composition, these droplets were all deposited as part of the same sequence, with the pipette tip not needing to be flushed and washed until the end of the sequence.

3.6.2 Sample exposure

After droplet deposition, samples were placed in an exposure environment with controlled temperature and humidity. The exposure environment was controlled in one of two ways. The first method used saturated salt solutions to maintain a given humidity within desiccators, which were then placed into a temperature controlled oven (Temperature Applied Sciences Ltd.). For the second method the samples were placed directly into an environmental chamber, which actively controlled the temperature and humidity within (Temperature Applied Sciences Ltd.).

Samples were exposed alongside a datalogger which monitored the temperature and humidity of the exposure environment (EasyLog EL-USB-2-LCD, Lascar Electronics Ltd.). The accuracy of the logger was ±0.5 °C for temperature readings, and ±3.0 %rh for humidity readings. Data were recorded at 1 minute intervals.

Samples were generally exposed for a period of 7 days. Exceptions to this will be specified in the text.

3.6.3 Sample analysis

After the exposure period, samples and droplets were imaged using a DSLR camera and digital microscope. The DSLR camera (Pentax K-r) recorded 12 megapixel images in JPEG format, and was used to take overview photos of each sample. The digital microscope comprised a Leica DFC 420 digital camera on a Leica DMLM microscope, and was used to image individual droplets and corrosion sites.

Samples were imaged variously: directly after exposure, after the salt droplets had been washed off with DI water, and after having been ultrasonically cleaned in DI water.

Corrosion site depths were measured by using a differential focussing technique. On the optical microscope a magnification objective with a low depth-of-field was used to focus on the sample surface, and then the bottom of the corrosion site; the difference in z-stage position between the two planes was recorded. Measurements of select sites were verified using a confocal microscope (LEXT OLS3100, Olympus). The error of this technique was approximately ±3 µm.

3.7 Software

Image processing and digital image measurements were carried out using the FIJI software package.[147, 148] Measurements were made by manually outlining areas (i.e. droplet outlines) and recording properties of the outline.

Thermodynamic calculations were carried out using OLI Analyser, versions 9.2 and 9.3. The exact version used is specified where relevant. The mixed solvent electrolyte (MSE) database was used, with the H_3O^+ databank. The temperature was set to 30 °C, at a pressure of 1 atm, representative of common testing conditions.

Model inputs were given in terms of molar concentration (mol/L, M). Vapour phases were excluded from the calculations, as they were not deemed of interest.

The method used to calculate the eutectic behaviour of two-component salt solutions was to vary the concentrations of each salt separately, between 0 and their independent saturation concentrations in steps of 0.1 M. For each datapoint the quantity of any solid phase was recorded, as well as the water activity of the solution. Data where any solid phase was present were discarded, and the water activity was plotted against the molar fraction (A / (A + B)).

4 HI-THROUGHPUT IN-SITU OPTICAL MONITORING OF ATMOSPHERIC CORROSION USING A FLAT-BED SCANNER – PART 1: METHODOLOGY AND INITIAL OBSERVATIONS

Preface

The following chapter has been formatted in preparation for submission to an academic journal; the section contains its own list of references at the end, and the reference numbering for this section is self-contained. The section numbering, figure and table numbering, and pagination, however, has been continued from the main text of the thesis in order to aid readability and navigation in the context of the whole document.

Angus Cook is the lead author of the following paper, having conducted the entirety of the experimental and write-up work. Alison Davenport and Trevor Rayment provided editorial advice on the structure and clarity of the text and figures.

Hi-throughput *in-situ* optical monitoring of atmospheric corrosion using a flat-bed scanner – Part 1: Methodology and initial observations

Angus J. M. C. Cook[1], Trevor Rayment[2], Alison Davenport[1]

[1] School of Metallurgy and Materials, University of Birmingham, Edgbaston, Birmingham, UK, B15 2TT.

[2] School of Chemistry, University of Birmingham, Edgbaston, Birmingham, UK, B15 2TT

4.1 Abstract

A new cost-effective method for the in-situ monitoring of corrosion samples is presented, using a flatbed document scanner to capture images of the samples during exposure. As a test case $MgCl_2$ and $CaCl_2$ droplets were deposited on to stainless steel samples (304L and 316L), exposed to a constant environment of 30 °C, 43 %rh for 7 days, and monitored using the scanner. In Part 1 we present an assessment of the performance of the scanner in this experimental set-up, noting a suitable optical resolution, no significant thermal or optical output expected to interfere with corrosion processes, and good scalability for larger tests. We also highlight some observations of corrosion processes observed from this in-situ monitoring technique that would likely have been missed from an ex-situ 'post-mortem'. An analysis of the data gathered from this experiment, including factors effecting time to corrosion initiation, is presented in Part 2.

4.2 Introduction

A wide variety of corrosion tests, such as investigations into stress corrosion cracking, or long-term exposure tests, require extended experimental durations,

generally over a period of months or years. Inspection and analysis of samples is usually undertaken periodically, and it is common for weeks to pass between inspections.(1, 2) With such intervals, however, there is a risk of missing important events that occur on shorter timescales than the inspection interval.

This is well recognised within the field, and several methods and techniques have been developed for the in-situ monitoring different properties of thin-film and atmospheric corrosion systems. These include the use of Kelvin probes, silver-wire electrodes, thin-film Luggin probe techniques, in-situ optical cameras and synchrotron techniques (e.g.)(3-12). These have collectively allowed a variety of aspects of corrosion to be studied, such as the extent of the cathodic area from a corroding chloride droplet on aluminium, the relative humidities (RHs) at which corrosion will initiate and stop on stainless steel under chloride droplets, observation of solution volume increases due to ion production, and the progression of corrosion in an occluded, galvanically coupled cell.

While certainly useful and illuminating, some of these techniques have drawbacks in terms of requiring (sometimes highly) specialised equipment, and being confined to the study of, at most, a handful of corrosion systems per experimental run. High-throughput techniques to study the development of thin-film and atmospheric corrosion have been used previously, yet still rely on post-mortem inspection to gather relevant data.(13, 14) There is, therefore, a need to find methods for the in-situ monitoring of thin-film atmospheric corrosion samples which are both scalable to large sample sets, and readily accessible to the majority of researchers.

Modern flatbed scanners have been shown to provide inexpensive, high quality imaging data in a number of scientific fields, including inspection of growing plant

roots, digitisation of geological samples and inspection of optical layers for solar cells.(15-23) In theory a single scanner, with a platen area of ~200 x 300 mm, would be able to image ~2400 droplets, such as those used in (13, 14), in parallel. In this paper we demonstrate the viability of a flatbed scanner to monitor the progress of corrosion under deliquescent salt droplets on 304L and 316L stainless steels under atmospheric conditions.

4.3 Methodology

The flatbed scanner used for this experiment was an Epson Perfection v37, with a CCD imaging sensor. CCD imaging sensors tend to have better depth of field than the alternative contact imaging sensor (CIS). A comparison between the two sensor types is shown in Figure 4-1, where it can be seen that the CCD gives a clearer image up to working distances of 10 mm from the glass platen.

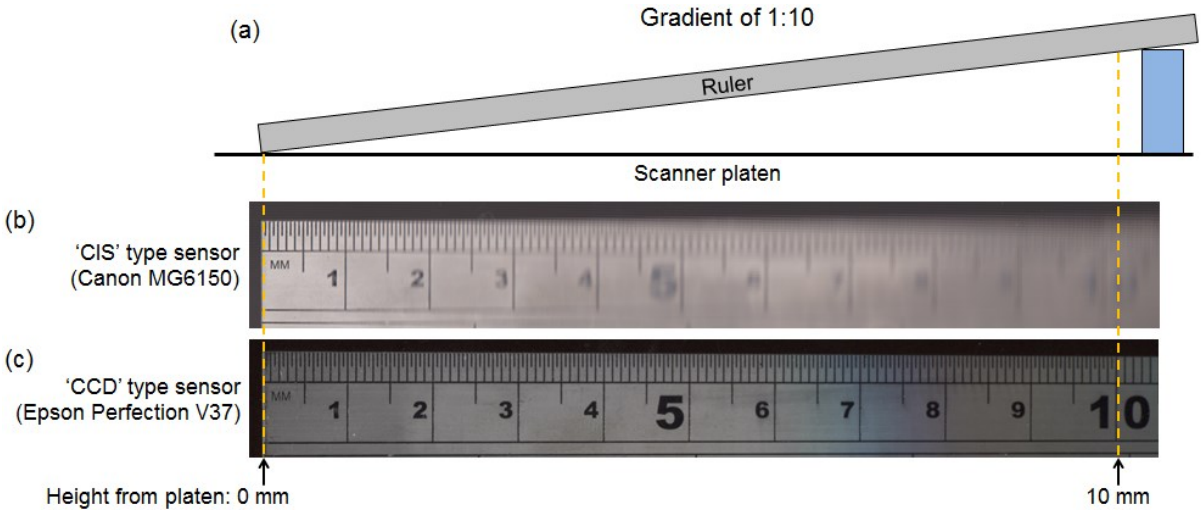

Figure 4-1 Comparison of the depth of field from a CIS type scanner (b) and a CCD type scanner (c). In both images the ruler is touching the glass platen at '0 mm', and at a distance of 10 mm from the platen at '10 cm' as read from the ruler.

The scanner was operated with VueScan (Hamrick Software), which can automate periodic scans and record unfiltered images so that automatic image processing (i.e. 'dust-removal') does not eliminate features of interest.

In order to test the sensitivity of the scanner in detecting localised corrosion sites, a 304L[1] stainless steel sample was wet ground to P800 grit with SiC discs, cleaned in an ultrasonic bath in de-ionised (DI) water (Millipore, >15 MΩ·cm) for ~30 seconds, dried under an air-stream, then kept in an ambient lab environment for ~1 hour to allow a passive layer to re-form. A 4 µL droplet of 0.5 M $MgCl_2$ solution ($MgCl_2 \cdot 6H_2O$, Sigma-Aldrich) was deposited onto the sample *via* micropipette (Eppendorf), and the droplet was monitored with an optical microscope until the onset of pitting. A timelapse recording of the droplet was taken at intervals of 1 minute using the optical microscope (Figure 4-2(c-d)), in order to accurately chart the initiation point of the pit. At the earliest opportunity after confirming the initiation of a pit (~4 minutes after initiation) the droplet was washed off the sample with DI water. The sample was then imaged using the flatbed scanner (Figure 4-2(g)).

It has been reported that, due to the semi-conductive properties of both the oxide layer on stainless steel and the corrosion products, incident light on stainless steel can have an effect on the corrosion properties of the material.(24-26) As such the act of periodic illumination of corrosion samples may have an effect on their response to the testing environment. A spectrometer (Ocean Optics) was used to record the wavelength profile of light emitted from the scanner's LEDs. Intensity data were collected from a wavelength of ~340 nm to ~1025 nm, with a changing step size of ~0.39 nm at the low wavelengths, decreasing to ~0.28 nm at the longer wavelengths.

[1] A cast analysis of the alloy is presented in Part 2.

Further tests were undertaken on 304L stainless steel samples, which were prepared as above, though allowed to re-passivate for 24 hours before droplet deposition. 4 µL droplets of $MgCl_2$ or $CaCl_2$ were deposited, and the sample was exposed to an environment of 30 °C, 43 %rh for 7 days, with an initial humidity of ~80 %rh for a period of one hour. Full experimental details for these samples are given in Part 2.

4.4 Assessment of flatbed scanner as an in-situ monitoring device

4.4.1 Test of scanner sensitivity

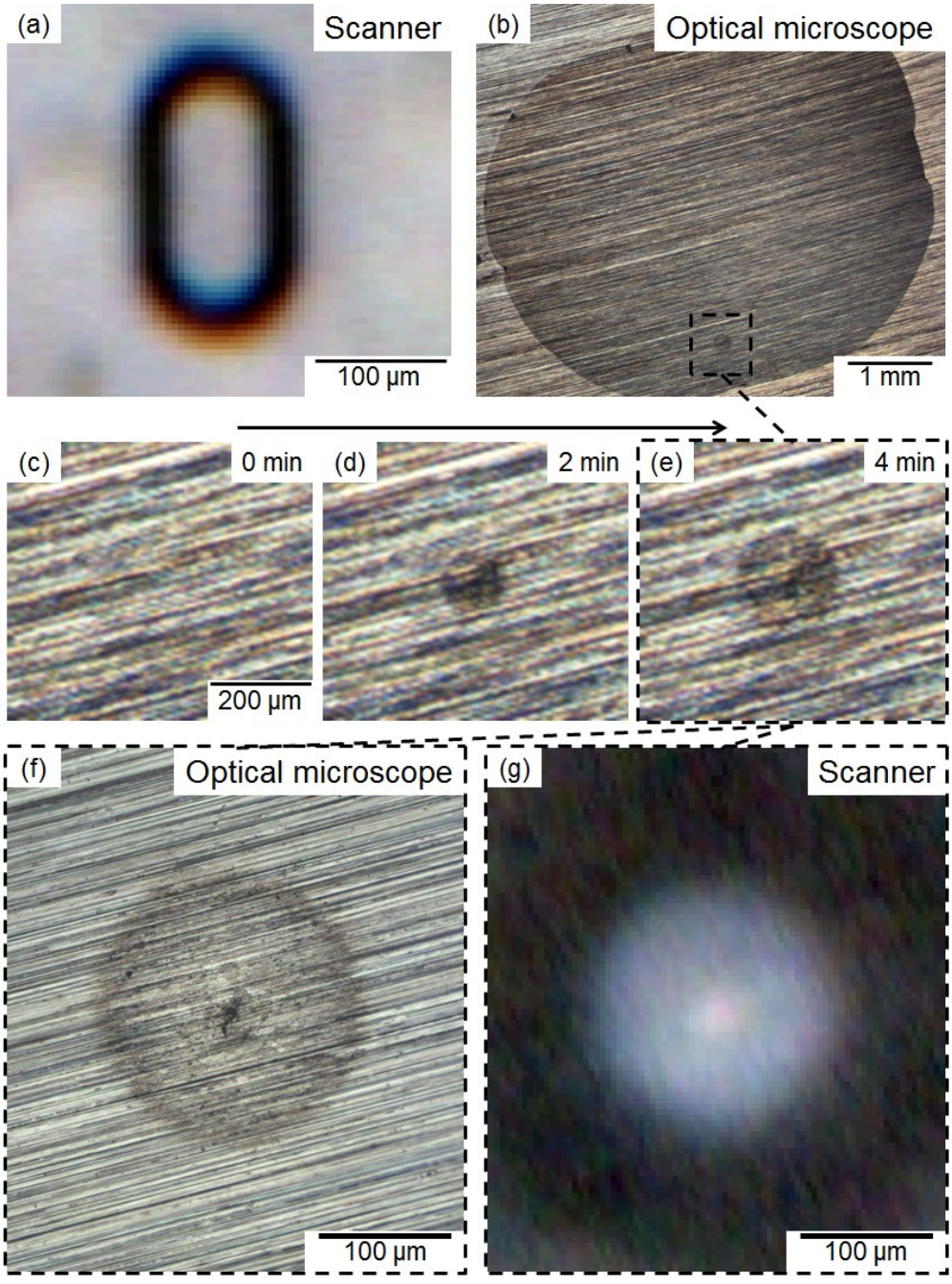

Figure 4-2 Demonstration of the resolution of the scanner. (a) scanner image of the numeral '0' from a microscope graticule. (b) Microscope image of a 4 µl $MgCl_2$ droplet at ~1000 µg/cm^2 on 304L stainless steel, exposed under ambient conditions. (c-e) close up of pitting area (c) immediately before pitting was observed, (d) 2 minutes after initiation, and (e) 4 minutes after initiation. (f) Optical microscope image of 4 minute old pit, (g) scanner image of the same site shown in (f).

Figure 4-2 shows images taken during the scanner verification process. Figure 4-2(a) indicates the optical resolution of a scanned image provided by this scanner, as well as indicating chromatic aberration of the recorded image (blue and red colour outlines at the top and bottom of the '0', respectively). In the current use (imaging corrosion pits) the scanner was judged to have sufficient resolution to gather meaningful data; the limitations in terms of optical resolution and chromatic aberration, however, should both be taken in to account when considering such a system for imaging systems with smaller feature sizes than corrosion pits.

A corrosion pit on stainless steel (304L) was monitored while growing under a $MgCl_2$ droplet with an optical microscope (Figure 4-2(b-e)). After ~4 minutes of growth the droplet was washed off to prevent further pit growth, and the pit was imaged using both the optical microscope (Figure 4-2(f)) and the flatbed scanner (Figure 4-2(g)). The pit can clearly be identified in from the scanner image, where the 4 minute-old pit created a feature ~40 pixels in diameter.

Although no images of 'younger' pits were obtained in this trial, the clarity of the 4 minute-old pit from the scanner suggests that pits as young as 2 minutes, or younger, would be able to be detected using this method. Therefore it is possible to have confidence that a pit such as the one shown above would be detected promptly after initiation by the scanner.

4.4.2 Optical output

An assessment of the optical output of the scanner LEDs is shown in Figure 4-3. The main outputs peak at ~440 nm (blue-violet) and ~550 nm (green). This is consistent with a blue emission LED with a phosphor coating which fluoresces in the green-yellow spectrum.(27) As such, even though the investigation of the optical profile did

not fully record wavelengths in the UV spectrum, it is unlikely that there will be significant UV emissions from the scanner LEDs, and so no significant corrosion effects are expected due to the presence of UV light.

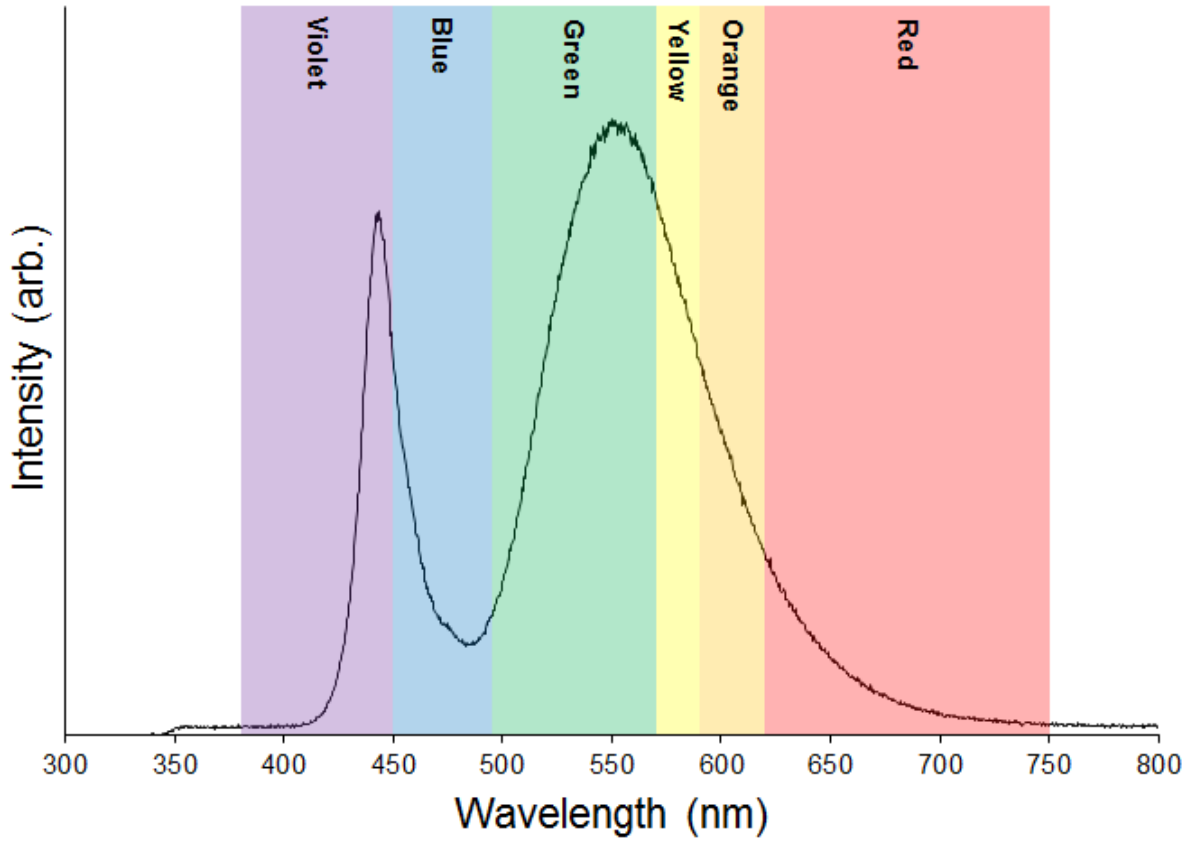

Figure 4-3 Optical profile of light emitted from the white LEDs in the scanner. Nominal colour ranges are indicated as a guide for the reader.

4.4.3 Thermal output

In order to assess any thermal output from the scanner during a scan, a thermocouple was taped to the glass platen, and a slow scan was conducted over the area. As the imaging bar passed over the thermocouple, a maximum transient of ~0.7 °C above average temperature was recorded. For samples which are not in direct contact with the glass platen it is likely that any heating effects will be reduced, and so are likely to be negligible for most applications.

4.4.4 Visual interference

Figure 4-4 shows an example of visual artefacts which were caused by the interaction between the light from the scanner, and the angle of the grinding lines present on the stainless steel samples. These ‘rainbow’ patterns were seen to be most apparent when the angle between the grinding lines, and the scanning direction was ~45°, and not noticeable when the grinding lines were approximately parallel to the direction of scan.

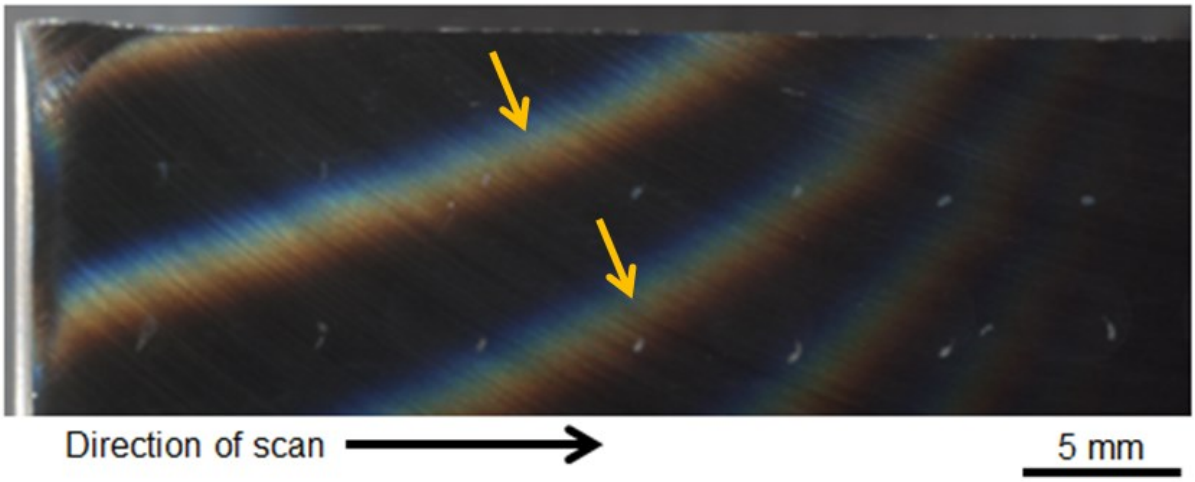

Figure 4-4 Example of ‘rainbow’ diffraction artefact (highlighted with arrows) due to interaction of scanner LEDs with grinding lines on sample.

Although in this experiment images were still able to be interpreted despite the ‘rainbow’ interference, it is recommended that future experiments attempt to reduce this interference by orienting the grinding lines on the sample perpendicular to the direction of scan.

4.5 Corrosion processes observed from in-situ data

While a more thorough analysis of data from this experiment is presented in Part 2, a selection of observations are presented here. The purpose of these examples is to demonstrate the types of data gathered by the scanner, and to highlight the new

insights into corrosion processes that the use of this method has allowed that would not be possible when relying only on ex-situ ‘post-mortem’ examination of samples.

Figure 4-5 shows an example of timelapse data captured by the scanner during sample exposure. The initiation of a corrosion site is clearly detectable from the image (Figure 4-5(b)), showing that this technique can be used to accurately capture the moment of initiation of corrosion under a thin film or droplet. Furthermore, the development and distribution of corrosion product is clearly recognisable from the images, and can be seen to develop with the exposure duration. The progression and precipitation of different phases (colours) of corrosion product may yield insights as to the corrosion processes occurring within the corrosion site, or to the development of local chemistry with time.

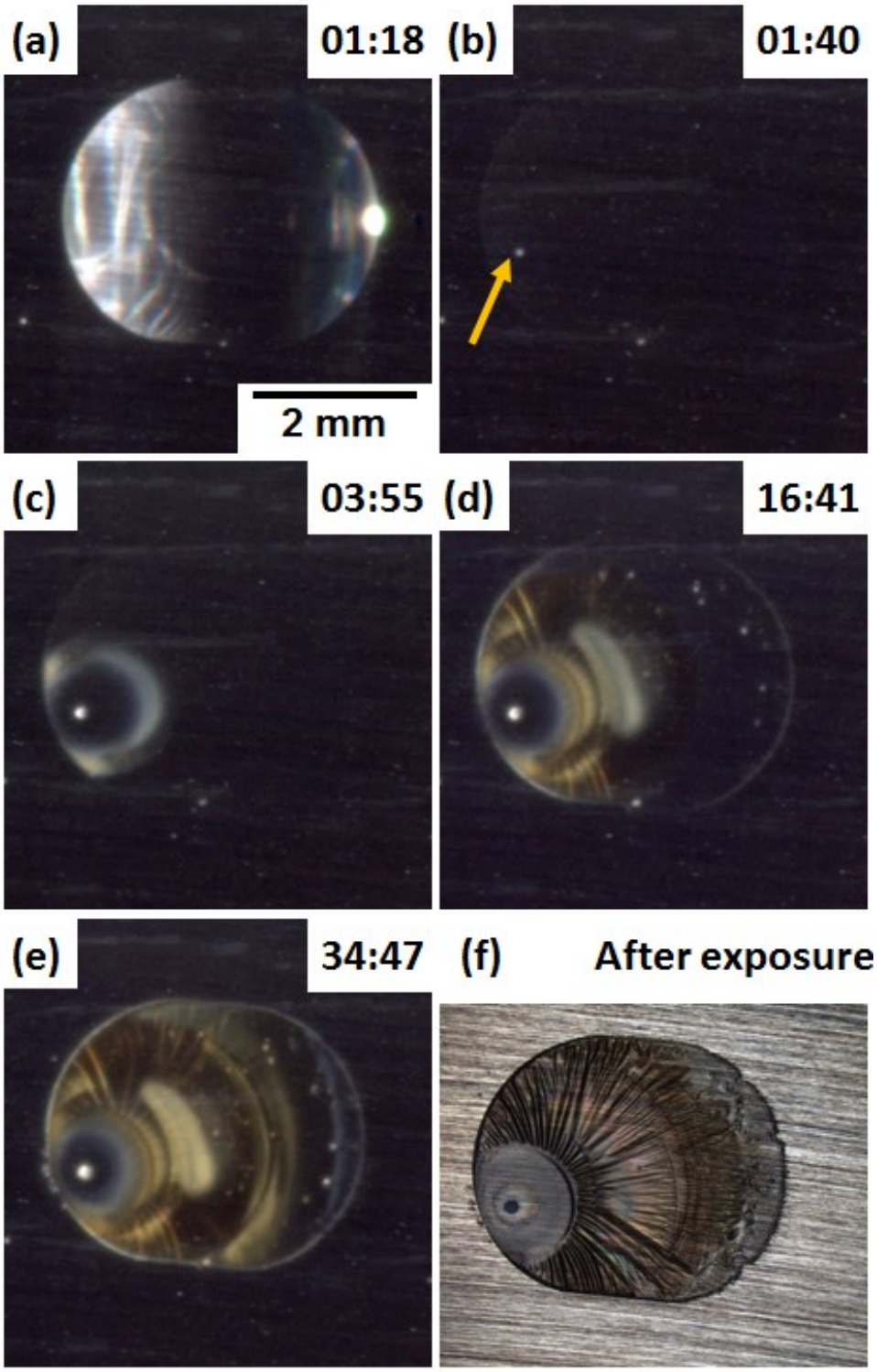

Figure 4-5 Timelapse of the development of corrosion under a 4 µL droplet of $CaCl_2$ on 304L stainless steel, exposed at a temperature of 30 °C and humidity of 43 %rh. CDD was ~1000 µg/cm^2. Time from deposition (hours:minutes) is shown in the top right of each image. The location of a pit initiating is shown by a yellow arrow in (b). Note that the droplet in (a) has been imaged during the initial hold at 80 %rh.

Figure 4-6 shows the development of a feature within the corrosion product produced by a corrosion site (highlighted in Figure 4-6(e)). A white-grey lenticular structure appears to develop from the original corrosion site, and over time moves away from the initiation site to settle a little further away. Figure 4-6(f) shows an optical micrograph of the same droplet at the end of the 7 day exposure period. This is included to highlight that the corrosion product structure observed with the scanner is difficult to distinguish using regular ex-situ techniques. Although this structure in the corrosion product has not been positively identified, the authors highlight that without the in-situ timelapse data provided by the scanner the existence of this particular feature (observed commonly from in-situ scanner images under $CaCl_2$ droplets with CDDs of ~1000 µg/cm^2) would likely have been overlooked.

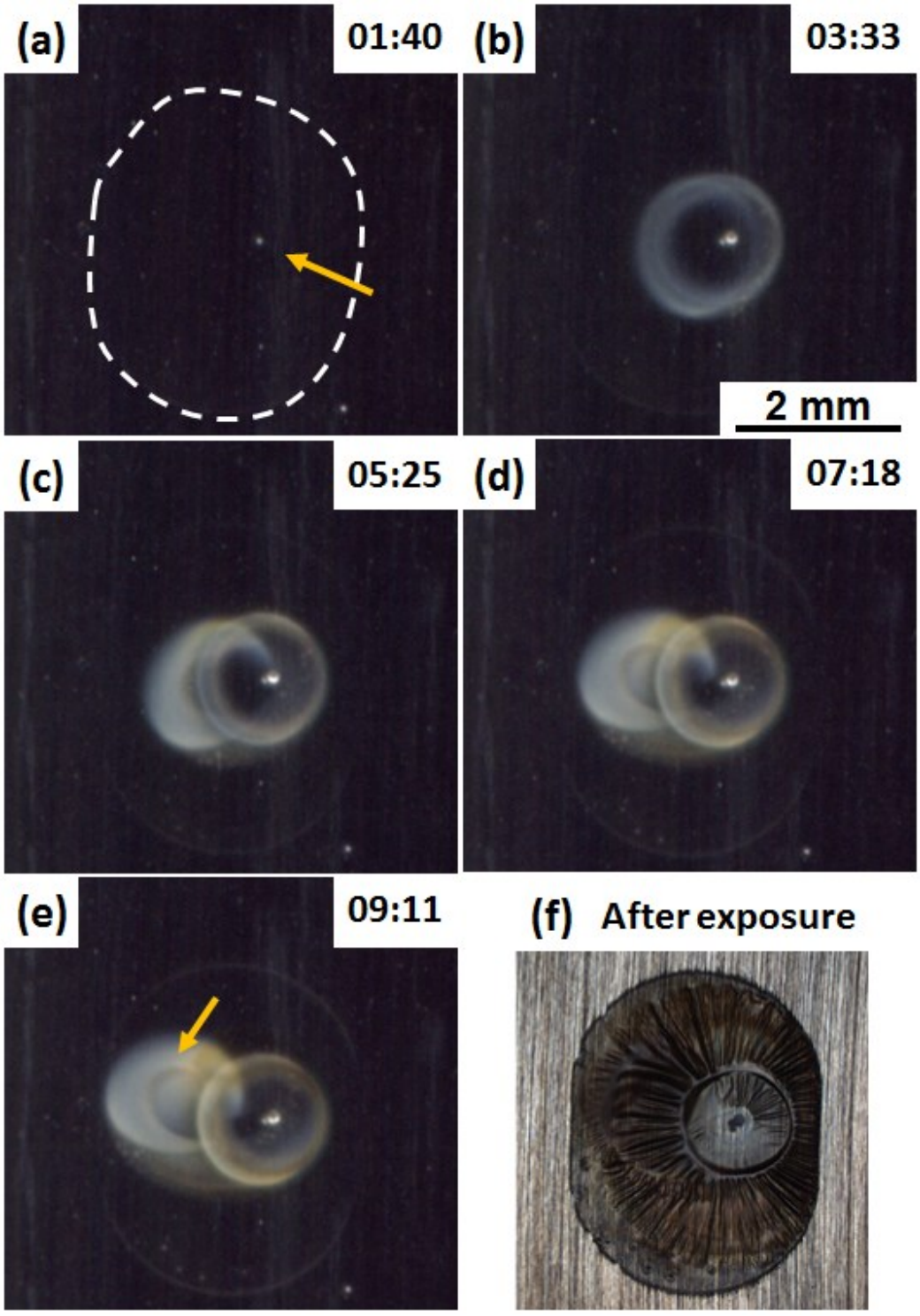

Figure 4-6 Timelapse of the development of corrosion under a 4 µL droplet of $CaCl_2$ on 304L stainless steel, exposed at a temperature of 30 °C and humidity of 43 %rh. CDD was ~1000 µg/cm^2. The time from deposition (hours:minutes) is shown in the top right of each image. The perimeter of the droplet is shown in (a) by the dashed white line, and the initiation point of the pit is indicated by a yellow arrow. The white growth from the pit is highlighted in (e) by the yellow arrow. (f) is an optical microscope image at the end of the exposure period (7 days).

Figure 4-7 shows the development of a corrosion site under a low CDD (~1 µg/cm^2) $MgCl_2$ droplet. Unlike at higher CDDs where corrosion sites generally developed into single pits, corrosion under lower CDD conditions developed in a track-like manner. Ex-situ analysis showed only the final state of the corrosion site (Figure 4-7(a)), but the in-situ monitoring allows the development of the corrosion site to be monitored with time (Figure 4-7(c)). This shows that the corrosion begins at a single site, before propagating in a track-like manner, with further corrosion sites branching off of existing sites. The in-situ monitoring of the development of this corrosion morphology gives a useful insight into the likely mechanism behind this form of corrosion.

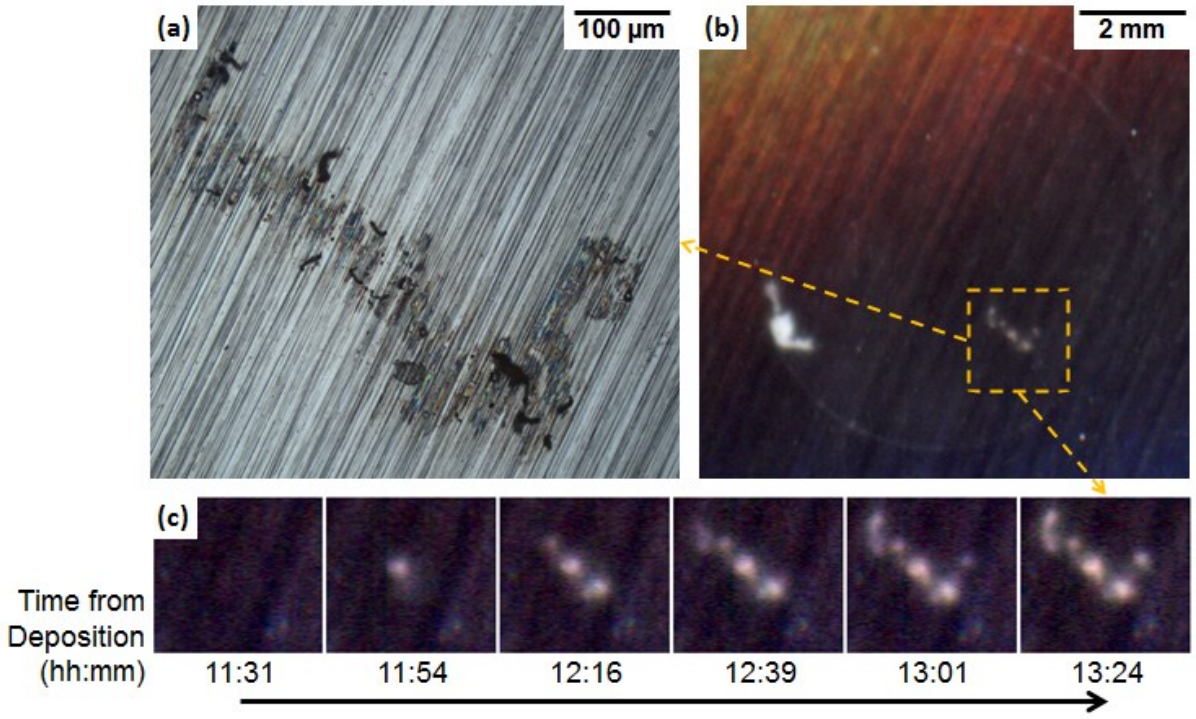

Figure 4-7 Development of corrosion under a 4 µL droplet of $MgCl_2$ on 304L stainless steel, exposed at a temperature of 30 °C and humidity of 43 %rh. CDD was ~1 µg/cm^2. (a) corrosion site at the end of exposure, after rinsing with DI. (b) In-situ image of droplet taken with the scanner. (c) site of corrosion before initiation (11:31 from deposition), and in subsequent scans.

4.6 Conclusions

A flatbed document scanner was assessed for its utility in providing in-situ optical monitoring of stainless steel samples undergoing atmospheric corrosion tests. The scanner was judged to be a beneficial and cost-effective tool to easily capture in-situ optical images of samples as they were exposed to environments of interest, allowing as many samples as can fit under the glass platen (an area of ~200 x 300 mm) to be imaged in parallel.

- The resolution of the scanner was sufficient to identify the initiation of corrosion sites under droplets of $MgCl_2$ and $CaCl_2$ salt solutions, even when the samples were separated from the glass platen by ~4-5 mm.
- The optical output of the scanner was assessed to be primarily blue and yellow light, the wavelengths of which are unlikely to affect the passive oxide layer, or the corrosion product of the stainless steel. Furthermore the thermal output of the scanner was seen to be negligible.
- The more frequent inspection interval provided by the in-situ monitoring of atmospheric corrosion samples allowed new information on corrosion processes to be obtained, such as monitoring the propagation and deposition of corrosion product, the identification of an unknown structure within the corrosion product, and the order of development of corrosion sites under low CDD droplets.

4.7 Acknowledgements

Angus Cook is funded by EPSRC grant EP/I036397/1, and Radioactive Waste Management Ltd. contract NPO004411A-EPS02.

4.8 References

1. Padovani C, Albores-Silva OE, Charles EA. Corrosion Control of Stainless Steels in Indoor Atmospheres—Laboratory Measurements Under MgCl2 Deposits at Constant Relative Humidity (Part 1). Corrosion. 2015;71(3):292-304.

2. Prosek T, Iversen A, Taxen C, Thierry D. Low-Temperature Stress Corrosion Cracking of Stainless Steels in the Atmosphere in the Presence of Chloride Deposits. Corrosion. 2009;65(2):105-17.

3. Stratmann M, Streckel H. On the atmospheric corrosion of metals which are covered with thin electrolyte layers—I. Verification of the experimental technique. Corrosion Science. 1990;30(6-7):681-96.

4. Cheng C-Q, Klinkenberg L-I, Ise Y, Zhao J, Tada E, Nishikata A. Pitting corrosion of sensitised type 304 stainless steel under wet–dry cycling condition. Corrosion Science. 2017;118:217-26.

5. Frankel GS, Stratmann M, Rohwerder M, Michalik A, Maier B, Dora J, et al. Potential control under thin aqueous layers using a Kelvin Probe. Corrosion Science. 2007;49(4):2021-36.

6. Kowal K, DeLuccia J, Josefowicz JY, Laird C, Farrington GC. In Situ Atomic Force Microscopy Observations of the Corrosion Behavior of Aluminum-Copper Alloys. Journal of The Electrochemical Society. 1996;143(8):2471-81.

7. Ghahari M, Krouse D, Laycock N, Rayment T, Padovani C, Stampanoni M, et al. Synchrotron X-ray radiography studies of pitting corrosion of stainless steel: Extraction of pit propagation parameters. Corrosion Science. 2015;100:23-35.

8. Maurice V, Peng H, Klein LH, Seyeux A, Zanna S, Marcus P. Effects of molybdenum on the composition and nanoscale morphology of passivated austenitic stainless steel surfaces. Faraday Discuss. 2015;180(0):151-70.

9. Cruz RPV, Nishikata A, Tsuru T. Pitting corrosion mechanism of stainless steels under wet-dry exposure in chloride-containing environments. Corrosion Science. 1998;40(1):125-39.

10. Cruz RPV, Nishikata A, Tsuru T. AC impedance monitoring of pitting corrosion of stainless steel under a wet-dry cyclic condition in chloride-containing environment. Corrosion Science. 1996;38(8):1397-406.

11. Street SR, Mi N, Cook AJMC, Mohammed-Ali HB, Guo L, Rayment T, et al. Atmospheric pitting corrosion of 304L stainless steel: the role of highly concentrated chloride solutions. Faraday Discuss. 2015;180(0):251-65.

12. Rafla V, King AD, Glanvill S, Parsons A, Davenport A, Scully JR. Operando Observation of Galvanic Corrosion Between Aluminum Alloy 7050-T7451 and 304 Stainless Steel in a Simulated Fastener Arrangement Using X-Ray Tomography. CORROSION. 2015;71(10):1171-6.

13. Cook AJMC, Padovani C, Davenport AJ. Effect of Nitrate and Sulfate on Atmospheric Corrosion of 304L and 316L Stainless Steels. Journal of The Electrochemical Society. 2017;164(4):C148-C63.

14. Azmat NS, Ralston KD, Muster TH, Muddle BC, Cole IS. A High-Throughput Test Methodology for Atmospheric Corrosion Studies. Electrochemical and Solid-State Letters. 2011;14(6):C9-C11.

15. Dannoura M, Kominami Y, Oguma H, Kanazawa Y. The development of an optical scanner method for observation of plant root dynamics. Plant Root. 2008;2:14-8.

16. Adu MO, Chatot A, Wiesel L, Bennett MJ, Broadley MR, White PJ, et al. A scanner system for high-resolution quantification of variation in root growth dynamics of Brassica rapa genotypes. Journal of Experimental Botany. 2014;65(8):2039-48.

17. Smith HC, Niewohner DJ, Dewey GD, Longo AM, Guy TL, Higgins BR, et al. Using Flatbed Scanners to Collect High-resolution Time-lapsed Images of the Arabidopsis Root Gravitropic Response. Journal of Visualized Experiments : JoVE. 2014(83):50878.

18. Gale AS, Young JR, Shackleton NJ, Crowhurst SJ, Wray DS. Orbital tuning of Cenomanian marly chalk successions: towards a Milankovitch time-scale for the Late Cretaceous. Philosophical Transactions of the Royal Society of London Series A:Mathematical, Physical and Engineering Sciences. 1999;357(1757):1815-29.

19. Kemp DB. Colorimetric characterisation of flatbed scanners for rock/sediment imaging. Computers & Geosciences. 2014;67:69-74.

20. De Kock T, Dumon M, Lanzón M, Verbrugge A, Ranst EV, Crombé P, et al. Mineralogical transformations in sandstone: a fingerprint for prehistorical heating of Palaeolithic hearth stones. European Journal of Mineralogy. 2015;27(5):651-7.

21. Korte L, Bastide S, Lévy-Clément C. Measurements of effective optical reflectivity using a conventional flatbed scanner—Fast assessment of optical layer properties. Solar Energy Materials and Solar Cells. 2008;92(8):844-50.

22. van't Spijker A, Kreulen CM, Bronkhorst EM, Creugers NHJ. Assessment of early attrition using an ordinary flatbed scanner. Journal of Dentistry. 2012;40(7):603-8.

23. Sullivan K, Kloess J, Qian C, Bell D, Hay A, Lin YP, et al. High throughput virus plaque quantitation using a flatbed scanner. Journal of Virological Methods. 2012;179(1):81-9.

24. Fujimoto S, Yamada T, Shibata T. Improvement of Pitting Corrosion Resistance of Type 304 Stainless Steel by Modification of Passive Film with Ultraviolet Light Irradiation. Journal of The Electrochemical Society. 1998;145(5):L79-L81.

25. Macdonald DD, Heaney DF. Effect of variable intensity ultraviolet radiation on passivity breakdown of AISI Type 304 stainless steel. Corrosion Science. 2000;42(10):1779-99.

26. Moussa SO, Hocking MG. The photo-inhibition of localized corrosion of 304 stainless steel in sodium chloride environment. Corrosion Science. 2001;43(11):2037-47.

27. Bessho M, Shimizu K. Latest trends in LED lighting. Electronics and Communications in Japan. 2012;95(1):1-7.

5 HI-THROUGHPUT IN-SITU OPTICAL MONITORING OF ATMOSPHERIC CORROSION USING A FLAT-BED SCANNER – PART 2: TIME DEPENDENT PIT GROWTH

Preface

The following chapter has been formatted in preparation for submission to an academic journal; the section contains its own list of references at the end, and the reference numbering for this section is self-contained. The section numbering, figure and table numbering, and pagination, however, has been continued from the main text of the thesis in order to aid readability and navigation in the context of the whole document.

Angus Cook is the lead author of the following paper, having conducted the entirety of the experimental work and write-up. Alison Davenport and Trevor Rayment provided editorial advice on the structure and clarity of the text and figures.

Hi-throughput in-situ optical monitoring of atmospheric corrosion using a flat-bed scanner – Part 2: Time dependent pit growth

Angus J. M. C. Cook[1], Trevor Rayment[2], Alison Davenport[1]

[1] School of Metallurgy and Materials, University of Birmingham, Edgbaston, Birmingham, UK, B15 2TT.

[2] School of Chemistry, University of Birmingham, Edgbaston, Birmingham, UK, B15 2TT

5.1 Abstract

Large arrays of chemically distinct droplets on stainless steel samples were optically monitored under atmospheric conditions in-situ using a novel flatbed scanner technique. $MgCl_2$ and $CaCl_2$ droplets were deposited onto 304L and 316L stainless steel samples using an automated pipetting machine, exposed to an environment of 30 °C, 43 %rh for 7 days, and imaged throughout the exposure period. The time to the initiation of corrosion was recorded for each droplet composition and alloy. Corrosion on 304L was seen to initiate earlier than on 316L. $CaCl_2$ initiated corrosion earlier than $MgCl_2$, and lower deposit densities of chloride (thinner droplets) tended to corrode later than higher deposit densities. When below a certain chloride deposit density the main corrosion process changed from a single pit per droplet to small 'track-like' attack, which occurred earlier than some of the single pitting events. Initiation times are rationalised in terms of the likelihood of a metastable pit transitioning to stability. Data relating the square of the depth and the age of corrosion sites was not sufficient to show that the depth of corrosion sites under atmospheric conditions was controlled solely by diffusion.

5.2 Introduction

The study of the atmospheric corrosion of stainless steels is of relevance to many industries, not least of which are those related to the long-term storage of radioactive waste.[1] The UK, in particular, stores intermediate level waste (ILW) in austenitic stainless steel containers (grades 304L and 316L), which may reside in above-ground storage conditions for several decades before being moved for permanent disposal in an underground facility.[2] During storage the deposition of atmospheric aerosols onto these stainless steel surfaces may allow the formation of corrosive electrolyte solutions, leading to localised corrosion and potential container failure.[3]

The chrome-rich passive layer, which gives stainless steels their general corrosion resistance, allows them to become susceptible to localised corrosion attack, such as pitting.[4, 5] Pitting may initiate at defects or inhomogeneities in the passive layer, such as inclusions; the oxidation of metal ions may locally lower the pH due to hydrolysis of the electrolyte, which may further destabilise the local passive layer or keep it from reforming, allowing further pitting propagation to continue.[6] 'Metastable' pitting, where small dissolution events occur but fail to propagate stably, have been observed in conditions less aggressive (in terms of applied potential, chloride concentration etc.) than those where the onset of stable pitting is seen.[7-9] The probability of observing a stable pit may be expressed as a function of the rate of metastable events, and the likelihood of a metastable event transitioning to stability.[10] The likelihood for a metastable event to transition to a stable pit is therefore dependent on the exposure environment.

Droplets of chloride containing salts have been used previously to form thin-films of electrolyte which may be used to simulate atmospheric corrosion conditions.[7, 11-

15] The ambient relative humidity dictates the equilibrium water activity of the electrolyte, and so affects the concentration of ionic species.[12] The onset of stable pitting under these conditions has been shown to depend on the chloride concentration of, and so the ambient relative humidity surrounding, the droplet.[7, 12, 16, 17]

The growth of pits on stainless steel is considered to depend on the diffusion of metal ions from the active interface out into the surrounding electrolyte.[6, 18] Experiments using idealised one dimensional (1D) pits, or ‘lead-in-pencil’ electrodes, have shown that the rate of growth (current density) is inversely proportional to the depth of the pit, if a salt film is present at the corroding interface.[19] This relation may be further developed to predict the propagation of the depth of the pit with time, such that the square of the depth is proportional to the age of the pit.[20] The diffusion limitation between the corroding interface and the pit opening has been also shown to apply to two dimensional (2D) pits.[20-22] For three dimensional (3D) systems the observed relationship between depth and time is less clear, with seemingly contradictory results in the reported literature.[23, 24]

Recently, the automated deposition of large arrays of droplets onto stainless steel samples has been used to gather statistically significant amounts of data using a high-throughput technique.[25, 26] In this paper a large-scale automated droplet deposition technique is coupled with a high-throughput in-situ monitoring technique, by imaging samples with a flatbed scanner over the period of exposure (see Part 1) in order to accurately monitor the initiation frequency of corrosion sites under different conditions.

5.3 Methodology

5.3.1 Materials and sample preparation

304L and 316L stainless steel plate was provided by Aperam France. The plate was cold-rolled, solution annealed between 1040-1100 °C and forced-air cooled before receipt. A chemical assay provided by the foundry is available in Table 5-1. Samples were cut to dimensions of 30 x 100 mm, 3 mm thickness unaltered, with the rolling direction parallel to the long axis. Samples were wet ground with P400 and P800 grit SiC discs, ultrasonically cleaned and rinsed with de-ionised water (DI) (Millipore >15 MΩ·cm) before being dried under an air-stream. Samples were then left in a covered ambient laboratory environment for 24 hours to allow the passive layer on the steel to re-grow.

Table 5-1 Chemical composition of alloys used in this paper, as reported by the foundry.

	Element (wt%)										
Alloy	C	Si	Mn	Ni	Cr	Mo	N	S	P	Co	Fe
304L	0.023	0.44	1.46	8.00	18.08	-	0.072	0.0033	0.032	0.171	Bal.
316L	0.024	0.38	1.25	10.04	16.55	2.000	0.044	0.0032	0.034	0.189	Bal.

5.3.2 Solutions

Stock solutions of $MgCl_2$ and $CaCl_2$ were made up with ACS grade reagents ($MgCl_2 \cdot 6H_2O$ and $CaCl_2 \cdot 2H_2O$, Sigma-Aldrich) and DI water. From these stock solutions, a MultiPROBE II Ex robotic liquid handler (Packard Biosciences) was used to dilute the stock solutions down to a chloride concentration of 0.615 M. This was chosen as it gives an approximate chloride deposition density (CDD) of 1000 µg/cm^2 for a 4 µL droplet, covering an area of ~8.7 mm^2. This volume – area relation was

observed in previous experiments. Using serial dilution, additional solutions with chloride concentrations of 61.5 mM, 6.15 mM, 615 µM and 61.5 µM were also mixed, giving equivalent CDDs of 100 µg/cm^2, 10 µg/cm^2, 1 µg/cm^2 and 0.1 µg/cm^2, respectively.

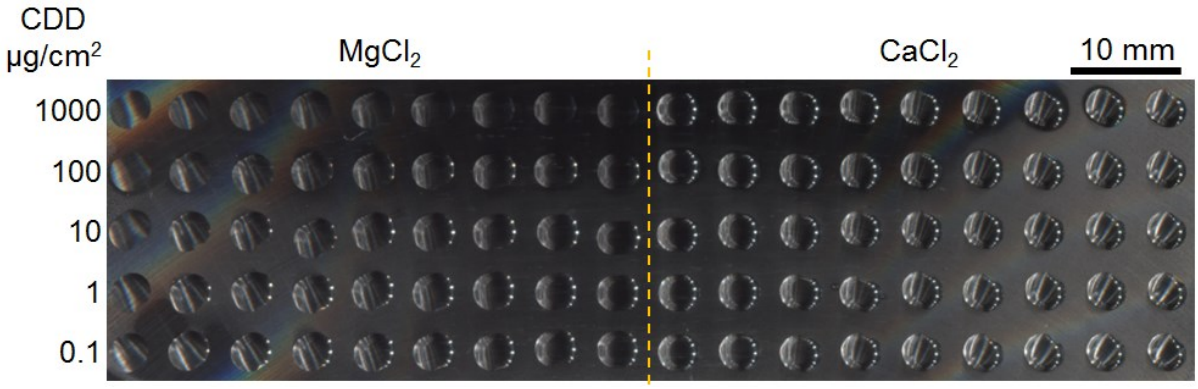

Figure 5-1 Photo of deposition layout for each plate. Each plate holds 10 different exposure conditions (2 salts x 5 CDDs) with 9 repeats for each condition.

5.3.3 Droplet deposition

Arrays of 4 µL droplets were deposited onto the stainless steel samples using the same MultiPROBE II Ex as was used for solution mixing. The deposition layout is indicated in Figure 5-1. $MgCl_2$ droplets were deposited on one half of each sample, and $CaCl_2$ droplets deposited on the other half. Droplets varied logarithmically in CDD, from 1000 µg/cm^2 to 0.1 µg/cm^2, with 9 repeats of each condition. In total 90 droplets were deposited on each sample, with the time of deposition recorded for each droplet. Deposition took ~25 minutes per sample. After deposition, the samples were photographed with a DSLR camera and placed inside an environmental chamber with controllable temperature and humidity (Temperature Applied Sciences Ltd.) alongside a temperature and humidity data logger (Lascar Electronics).

5.3.4 In-Situ monitoring

In order to monitor the samples in-situ the samples were placed underneath a flatbed scanner (Perfection V37, Epson) within the chamber, with ~2-3 mm separation between the droplets and the glass platen. A more detailed discussion of this technique is given in Part 1. High resolution images (4800 dpi, ~5 μm/pixel) were captured approximately every 25 minutes (15 minute delay, ~9 minute scan duration, ~1 minute file-writing) and saved as Tagged Image Files (TIFs). The time for a scan was proportional to both the quality of the scan, and the size of the area scanned (~60x100 mm); the area to be scanned was cropped around the two samples in order to minimise both the scan time and the individual scan file sizes. Files were saved in compressed TIF format in order to reduce the required storage space. File sizes were ~900 MB uncompressed, ~200 MB compressed.

It is worth highlighting that, due to the nature of a scanned image, that the data recorded at the start of the scan is ~9 minutes older than the data taken at the end of the scan. As such the image taken in a single scan is not taken at a specific point in time, but rather encompasses a 9 minute window, so events occurring at separate points in the image cannot be assumed to be occurring at the same time.

In the current work this limitation is not a problem, as it is the same points across different images which are being compared, rather than different points on the same image. Due to the regular time interval between scans, and the regular duration of the scan, the time interval between the same point on successive images will be constant. Over the area of a single droplet, the time window will be a few tens of seconds, which is sufficient temporal resolution for the system under observation.

5.3.5 Exposure

The environmental chamber was programmed to hold at a humidity of 80 %rh for one hour after sample insertion in order to allow the droplets to equilibrate with the environment. This was intended to ensure that all droplets reached the same concentration before being exposed to a lower humidity for the rest of the test, so that any time differences in terms of initiation came about only due to the composition of the droplets, rather than any differences between their relative drying times. In previous preliminary work a 4 µL droplet of DI water has been seen to fully evaporate in the laboratory environment in ~22 minutes from deposition, and so the authors are confident that an hour is a sufficient equilibration period.

Condensation was observed to form on the samples upon insertion because the ambient laboratory temperature was lower than the dew-point within the chamber. The condensation cleared within ~20 minutes, as the temperature of the stainless steel plates reached 30 °C. After an hour, the humidity was set to 47 %rh with a humidity of ~50 %rh recorded within ~5 minutes. After ~24 hours exposure the humidity unexpectedly shifted to a slightly lower value (~44 %rh), where it stayed for the remaining 6 days (Figure 5-3)

After 7 days of exposure the samples were removed from the sample chamber. Images of each sample and droplets were taken both before and after a DI rinse. Pit depths were recorded using an optical microscope and differential focusing technique, and select readings were verified with a confocal microscope. It should be noted that this technique is only able to measure pit depths based on what is observable from the pit mouth, and any propagation away from the pit mouth may not be fully recorded.

5.3.6 Data analysis

Data captured from the scanner was processed using the FIJI software package.[27] Over 7 days the scanner produced ~270 images (total size ~54 GB compressed, ~243 GB uncompressed). The area around each droplet was cropped from the original scan data and saved separately, thereby decreasing the computer memory required to hold the entire time-series of each droplet and assisting further analysis.

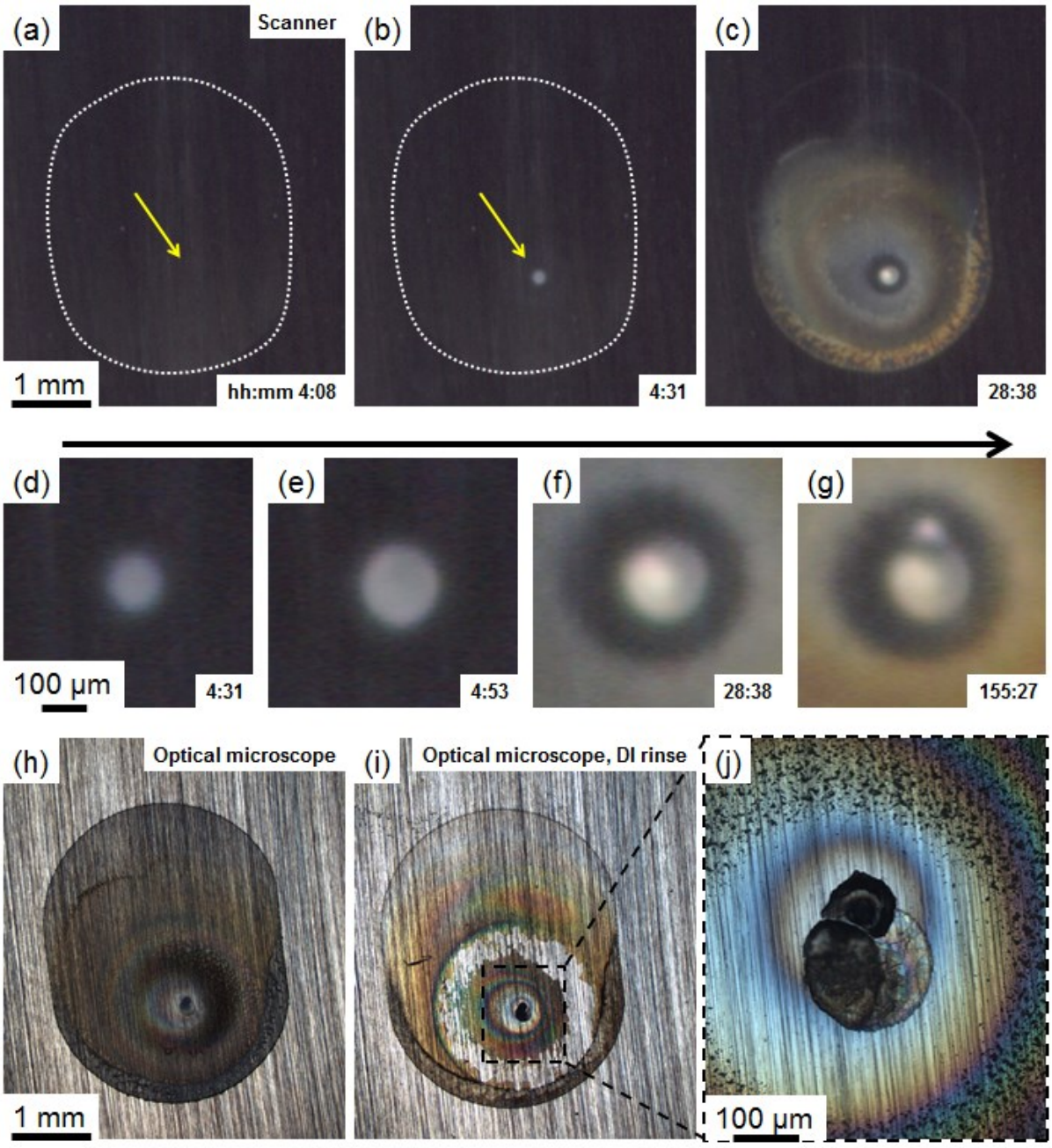

Figure 5-2 Example of in-situ scan data (a-g) and corresponding ex-situ micrographs (h-j) of a 4 µL 1000 µg/cm^2 CDD $MgCl_2$ droplet on 304L stainless steel. Scanner data shows exposure time (hh:mm) in bottom right corner. (a) image of droplet from scan immediately preceding corrosion initiation, (b) subsequent scan (~23 minutes later) where initiation was first observed (white dashed line indicates approximate droplet boundary, yellow arrow indicates corrosion initiation site). (c) scanner image of droplet 24 hours after initiation. (d-g) magnification of pitting site development as recorded by scanner. (h) image of droplet after 7 day exposure, after removal from environmental chamber, (i) after rinsing sample under DI water to remove salt droplet. (j) corrosion pit initiated in (b).

The time series of each individual droplet was studied in order to identify the first visible signs of a corrosion process, indicated by a yellow arrow in Figure 5-2. When the first sign of a corrosion process was observed the scan time was logged and compared to the deposition time for that droplet in order to establish a 'time to initiation' for each droplet under the given conditions.

5.4 Results

5.4.1 Verification of exposure conditions

Temperature and humidity data from the first 30 hours of exposure are shown in Figure 5-3. Temperature remained largely constant during the test, with the data logger recording an average of 30.8 ± 0.6 °C during the testing period. For the first ~22 hours of the test, after the programmed humidity decrease, the humidity within the chamber remained stable at 47.0 ± 0.1 %rh. Over a subsequent 2 hours period, however, the humidity was observed to decrease by ~3 %rh, to settle at 43.6 ± 0.3 %rh and the temperature rose to 31 °C for the remainder of the testing period. This shift can be observed at point 'B' in Figure 5-3.

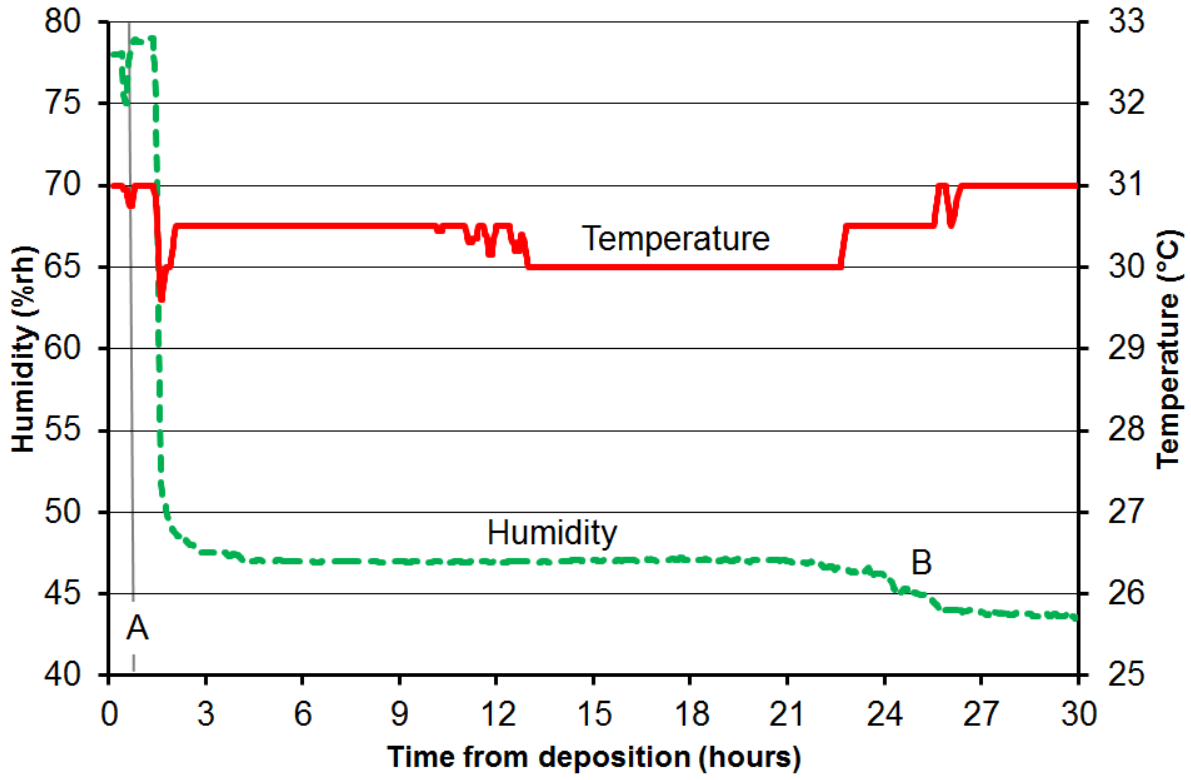

Figure 5-3 Data from temperature and humidity logger placed alongside samples during exposure. Data was recorded every 60 seconds, with plotted data averaged over 10 readings (10 minutes). Samples placed within chamber at A, with programmed humidity drop occurring 1 hour later. B indicates un-programmed humidity change.

The source of this small humidity shift 24 hours after sample insertion is unknown, though may have occurred due to an oversight during the chamber programming. Analysis of the initiation data does not show any significant regime change after 24 hours exposure, and so the authors conclude that the effect of this humidity shift has not impacted the results significantly.

5.4.2 Morphology of corrosion processes

Corrosion sites were examined *via* optical microscope after 7 days of exposure. A selection of typical morphologies is shown in Figure 5-4. Single pits were typically observed for CDDs in the range 10-1000 µg/cm^2 (Figure 5-4(a-c)), though some droplets in this CDD range formed multiple separate pits. Clusters of pits were also

observed, more commonly at a CDD of 10 µg/cm^2. At a CDDs of 1-10 µg/cm^2 a different 'track-like' morphology was also observed (Figure 5-4(d,h)). Small pits (~20 µm dia.) were also observed under 1 µg/cm^2 CDD $CaCl_2$ droplets on 316L, and were only common in these conditions. No corrosion was detected on either alloy at a CDD of 0.1 µg/cm^2. Small patches of some form of residue was observed in droplets with a CDD of 1 µg/cm^2 (arrow in Figure 5-4(d)).

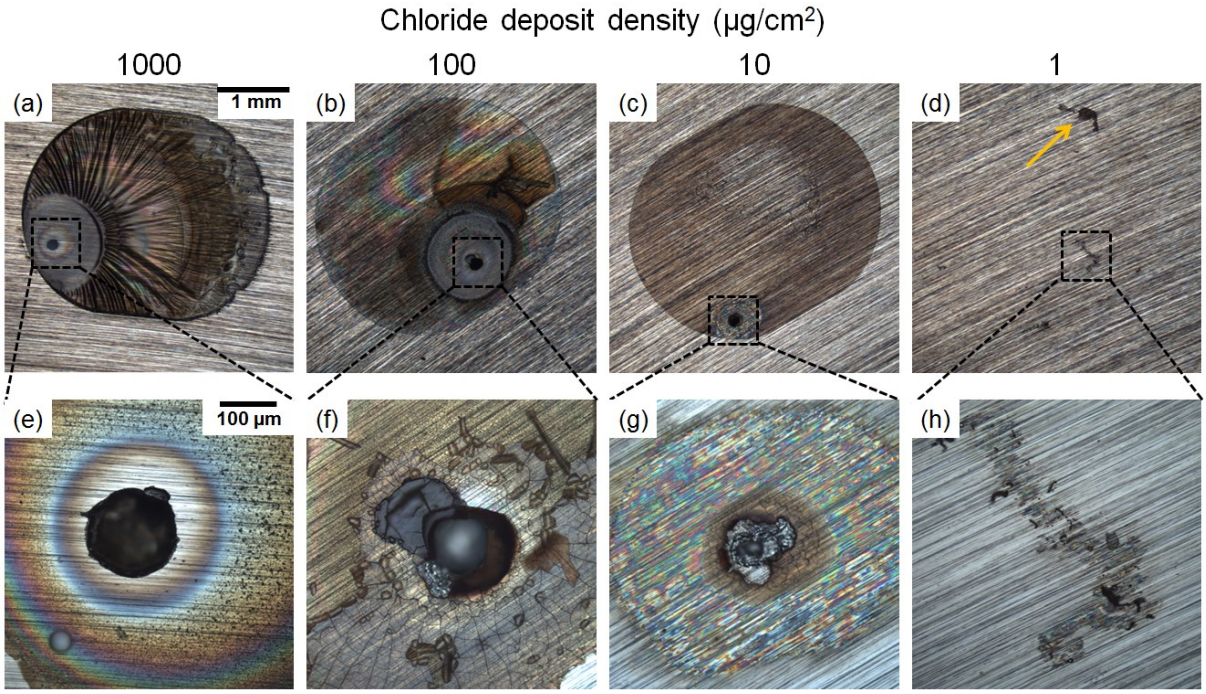

Figure 5-4 Typical examples of corrosion morphology on 304L under 4 µl droplets of different CDD. (a) $CaCl_2$ droplet, (b-d) $MgCl_2$ droplets. (a-d) droplets after 7 day exposure, without rinsing. (e-h) corrosion sites found in (a-d), after a DI rinse. Residue found in low CDD droplets (1 µg/cm^2) is highlighted in (d) with an orange arrow.

SEM images of 'track-like' corrosion morphologies showed that they consisted of a series of small pits, a few microns in diameter (Figure 5-5(c)). Increased levels of aluminium and titanium were detected in connection to some of these sites (arrows, Figure 5-5(b)), but not for all, and a firm association between the sites and alloy inclusions was not able to be established.

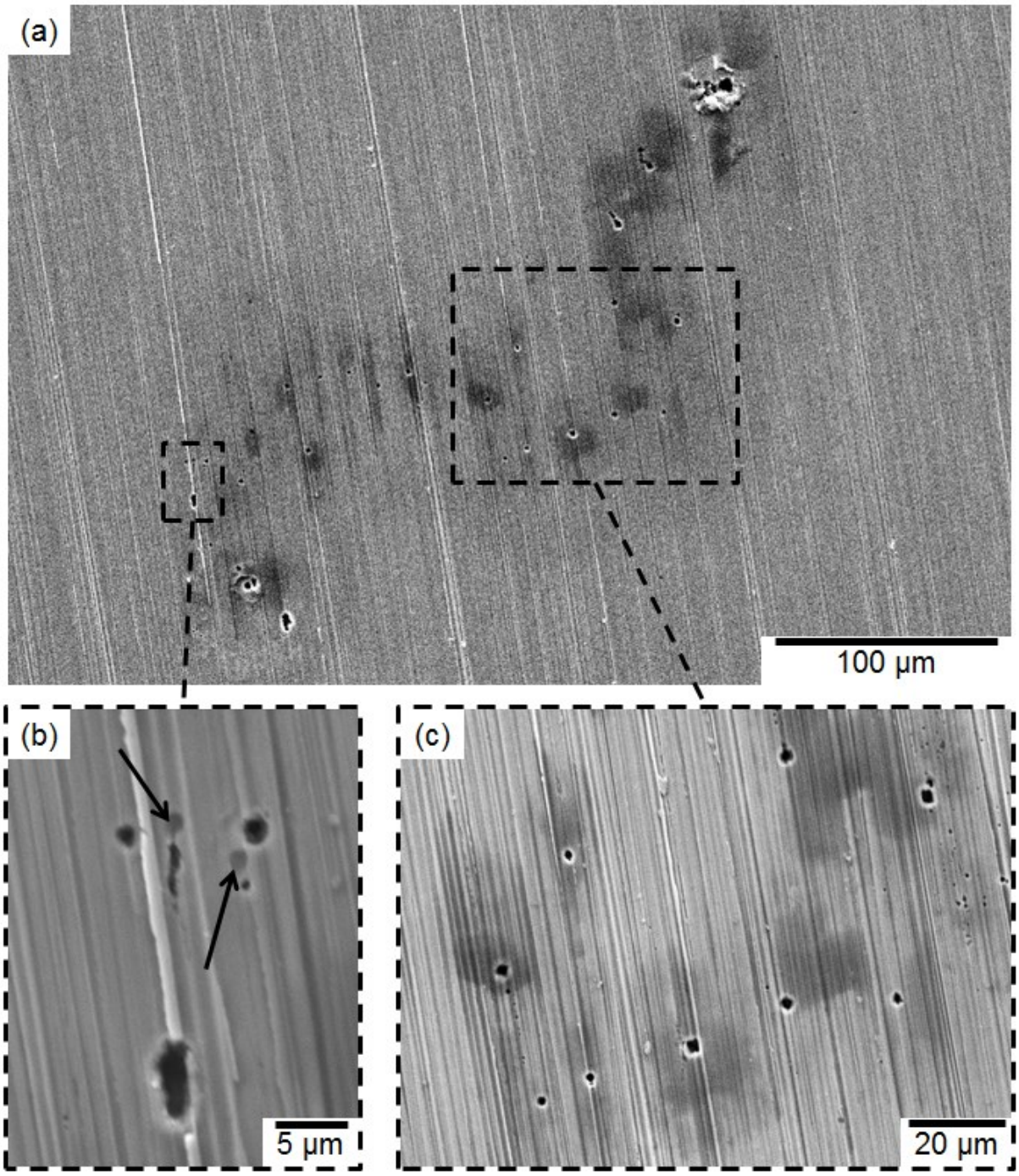

Figure 5-5 SEM images of corrosion 'tracks' occurring under a 1 µg/cm^2 CDD droplet on 304L stainless steel. (a) Image of an entire 'track', (b) arrows indicate potential inclusions, (c) magnified image of corrosion sites.

The purpose of this research was to more accurately characterise corrosion morphologies by their relative age, rather than assuming that the feature age was

equivalent to the exposure period. Further pit morphology results (specifically the depth of corrosion sites) will be presented later, in the context of their true 'age'.

5.4.3 Initiation times

Images of each droplet time-series were analysed to inspect for signs that corrosion had initiated. The results of this analysis are displayed in Figure 5-6 for the 304L sample and Figure 5-7 for the 316L sample. It should be noted that the timing data for each droplet are recorded from the deposition of that droplet, and include the 1 hour hold at 80 %rh.

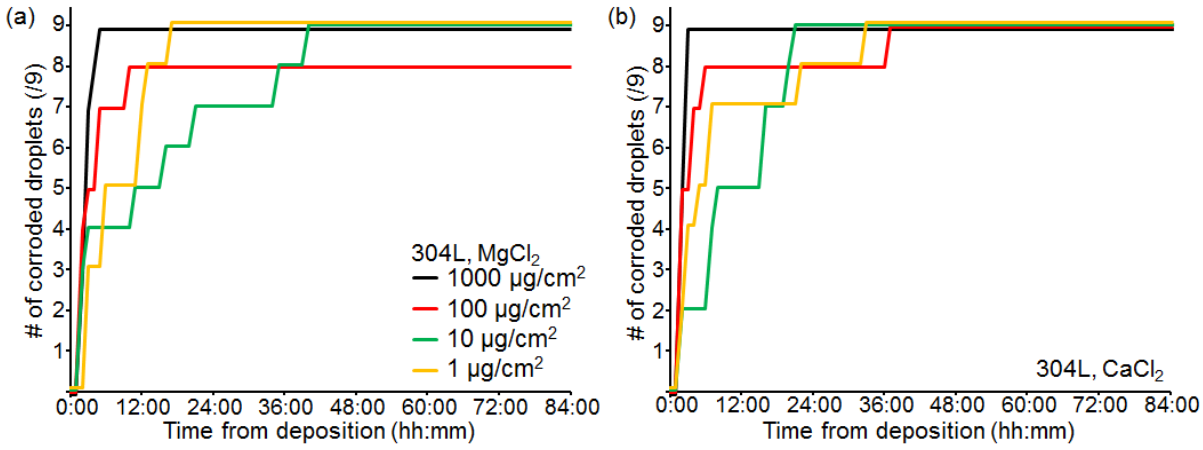

Figure 5-6 Time between the deposition of 4 µL salt droplets and the initiation of corrosion on 304L stainless steel. (a) $MgCl_2$, (b) $CaCl_2$. The graph is confined to the first 84 hours of experiment, as no new corrosion sites appeared after this in previously 'uncorroded' droplets.

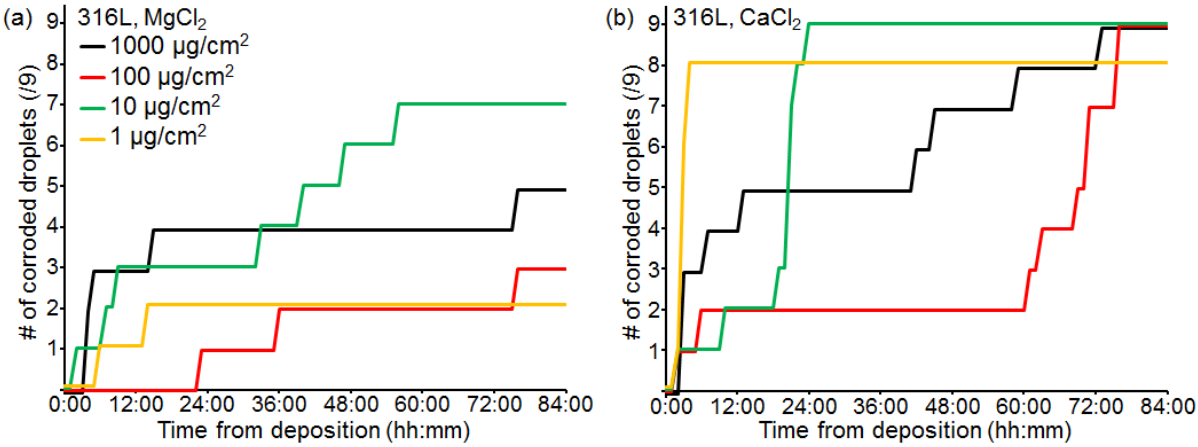

Figure 5-7 Time between the deposition of 4 µL salt droplets and the initiation of corrosion on 316L stainless steel. (a) $MgCl_2$, (b) $CaCl_2$. The graph is confined to the first 84 hours of experiment, as no new corrosion sites appeared after this in previously 'uncorroded' droplets.

5.4.3.1 Effect of alloy on initiation times

On 304L all corroded droplets initiated within ~42 hours of deposition (Figure 5-6). On 316L it took ~82 hours for all corroded droplets to initiate (Figure 5-7). In addition, fewer total droplets corroded on 316L than on 304L, though this was also dependent on salt type (see below).

5.4.3.2 Effect of salt type

$CaCl_2$ was generally more aggressive than $MgCl_2$, initiating corrosion at a slightly higher rate on 304L, though the total number of corroded droplets for each salt on this alloy were almost equal (45/45 corroded $CaCl_2$ droplets, 44/45 corroded $MgCl_2$ droplets). On 316L both the initiation rate and the total number of corroded droplets was higher for $CaCl_2$, compared to $MgCl_2$ (44/45 for $CaCl_2$ droplets, 17/45 for $MgCl_2$ droplets).

5.4.3.3 Effect of CDD

On 304L a decrease in the CDD between 1000 to 10 µg/cm^2 generally led to a decrease in the initiation rate of corrosion, with all 1000 µg/cm^2 droplets initiating

within ~6 hours of deposition, compared to the ~42 hours for all 10 µg/cm^2 $MgCl_2$ droplets to initiate (~24 hours for $CaCl_2$ droplets). The initiation rate of corrosion sites under 1 µg/cm^2 CDD droplets, however, did not follow this trend, showing an initiation rate between that of 100 and 10 µg/cm^2 droplets.

On 316L trends are more difficult to identify. This is not aided by the relatively low statistics given by the $MgCl_2$ droplets on 316L, due to the corrosion resistance of this alloy. In general, a decrease in CDD from 1000 to 100 µg/cm^2 lowers the initiation rate, but a further decrease to 10 µg/cm^2 puts the initiation rate above that of 1000 µg/cm^2 for both salts. Furthermore, $CaCl_2$ droplets with a CDD of 1 µg/cm^2 show a much higher initiation rate on 316L than they do on 304L. It should be noted that many of these corrosion sites formed under the residue common in 1 µg/cm^2 CDD droplets, and it was difficult to clearly identify an initiation time for these corrosion sites. The data presented in Figure 5-7(b) for the 1 µg/cm^2 CDD droplets indicate the formation of the surface residue, and may be an overestimate of the actual initiation time of the corrosion sites underneath.

5.4.4 Pit penetration rate

5.4.4.1 Nominal vs. true growth rates

The availability of in-situ data on the precise initiation times of corrosion sites allows a ‘true’ pit growth rate to be calculated using the actual lifetime of the corrosion site, for comparison to what would otherwise be a ‘nominal’ rate, whereby the duration of pitting is assumed to be equivalent to the total exposure time.

Figure 5-8 shows a comparison between the ‘nominal’ and ‘real’ linear growth rates of pits from the experiment. In general, there is little difference between the two sets of data, with significant differences only really observed in the case of 100 µg/cm^2

CDD $CaCl_2$ droplets on 316L, with less significant differences also observed for other tests on 316L.

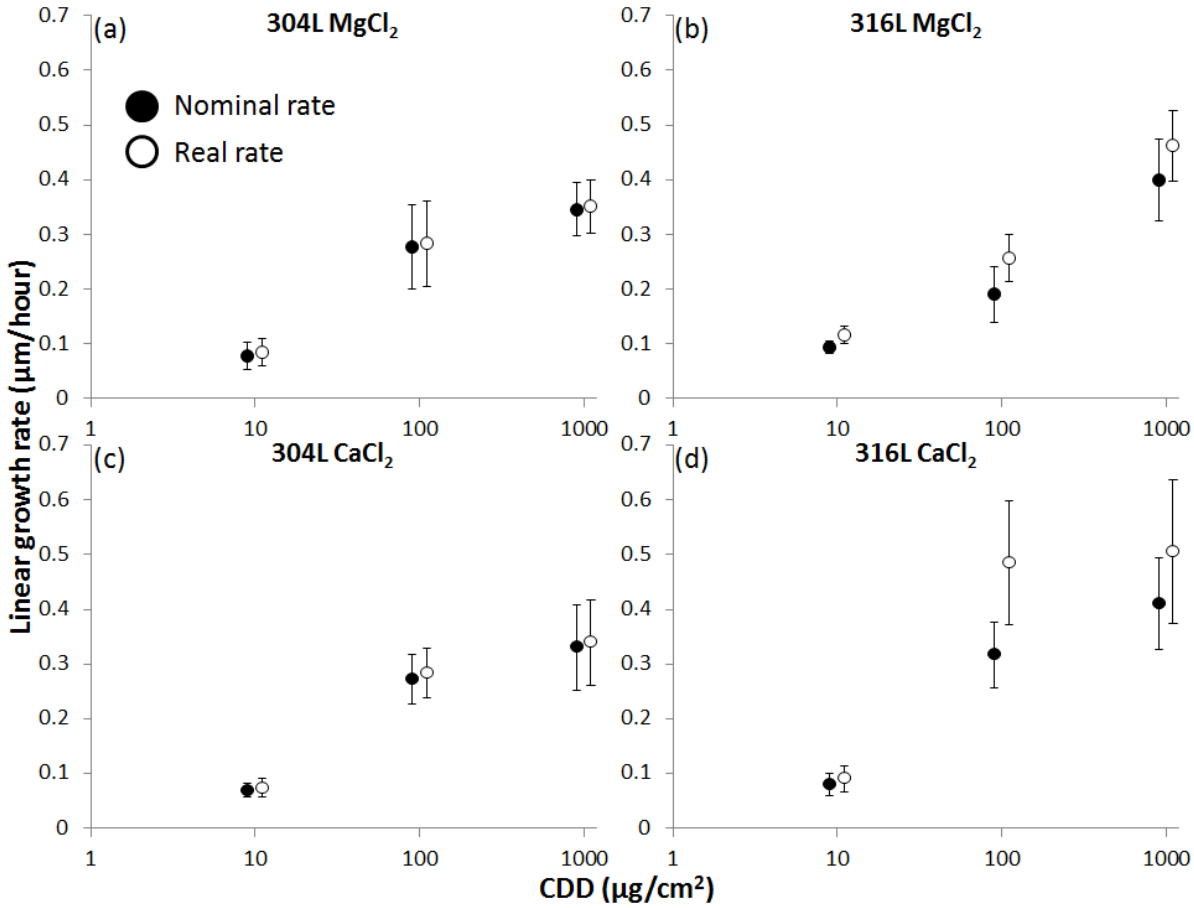

Figure 5-8 Data comparing 'nominal' growth rates (i.e. depth/total exposure time) and 'real' growth rates (depth/actual site lifetime) for corrosion pits under $MgCl_2$ and $CaCl_2$ droplets, on 304L and 316L stainless steels.

The depth of a 1D pit that is growing under diffusion limited conditions may be expressed as

$$h^2 = \frac{MD_{eff}C_{sat}}{\rho}\, t, \qquad \text{Equation 5-1}$$

where h is the depth of the pit, M is the molar mass of the metal, D_{eff} is the effective diffusion coefficient of the metal ions, C_{sat} is the saturation metal ion concentration, ρ

is the metal density, and t is the age of the pit.[20] If these properties are constant for a given system a plot of h^2 vs. t should be linear, meeting the y-axis at the origin.

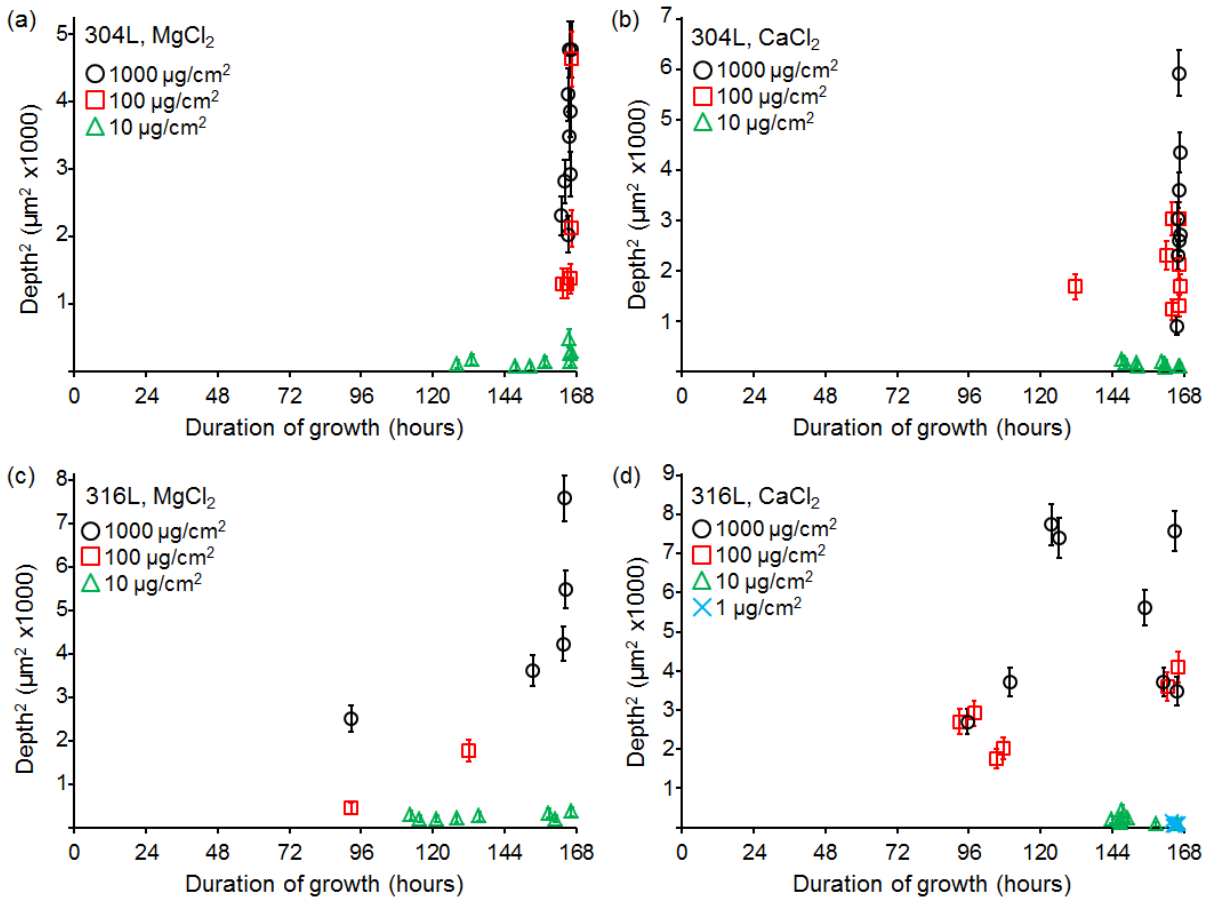

Figure 5-9 Depth^2 vs. duration of growth for corrosion sites on 304L (a,b), and 316L (c,d) under droplets of $MgCl_2$ (a,c), and $CaCl_2$ (b,d).

Figure 5-9 shows plots of the square of the depth (h^2) vs. duration of growth (t) for the four systems investigated. The data were excluded if the droplet contained more than one corrosion site, as the appearance of a second corrosion site might suggest that the first has ceased growing, and the assumption made is that the corrosion site continues to grow until the end of the exposure period. There is no clear linear trend in any of the data. For 304L samples (Figure 5-9(a),(b)) this is due to the very prompt initiation of corrosion, leading to the majority of sites having developed for >144

hours and giving a poor spread of data in the time axis. For 316L samples there is a somewhat better spread in terms of timing data but there is still significant scatter in the depth data, which was also seen for data from 304L samples.

5.5 Discussion

5.5.1 Corrosion morphology

The form of corrosion for the majority of higher CDD droplets (i.e. greater than or equal to 100 µg/cm^2) was a single pit per droplet, as has been observed previously.[26, 28] For CDDs of 10 - 1 µg/cm^2 another, different, form of attack was commonly observed, one which shared traits with filiform corrosion; surface attack which progressed in a track-like manner. There are two main differences between this form of attack and the single pits found under thicker droplets: (1) Multiple corrosion sites are active simultaneously. (2) Corrosion sites tended to promote new corrosion sites nearby. To understand this phenomenon both aspects should be explained.

Corrosion under thicker droplets tends to be in the form of a single pit. As there are multiple viable initiation sites for corrosion under a 4 µL droplet on this alloy the fact that all sites do not propagate simultaneously suggests that the ‘champion pit’ cathodically protects the rest of the metal surface under the droplet.[16, 29] Under thinner solution layers, however, multiple corrosion sites were observed, suggesting that the effect of the cathodic protection is reduced. This is likely due to the solution layer causing a larger IR drop between cathode and anode in this system compared to thicker droplets, reducing the area around the original pit which is acting as the coupled cathode.

This line of argument, however, would lead to the expectation that the entire droplet should be full of corrosion sites, which is not observed. What is seen is that corrosion sites initiate around the original corrosion site. This may be explained by the reduced pH in the area around the initial corrosion site, caused by hydrolysis of the dissolved metal ions. A lower pH in the region would be sufficient to promote the initiation of corrosion in new sites local to the original pit.

Importantly this effect of promoted corrosion local to the original pit was not observed for thicker droplets. This suggests that it is a combination of the decreased cathodic protection and the decreased pH which lead to the observed track-like morphology.

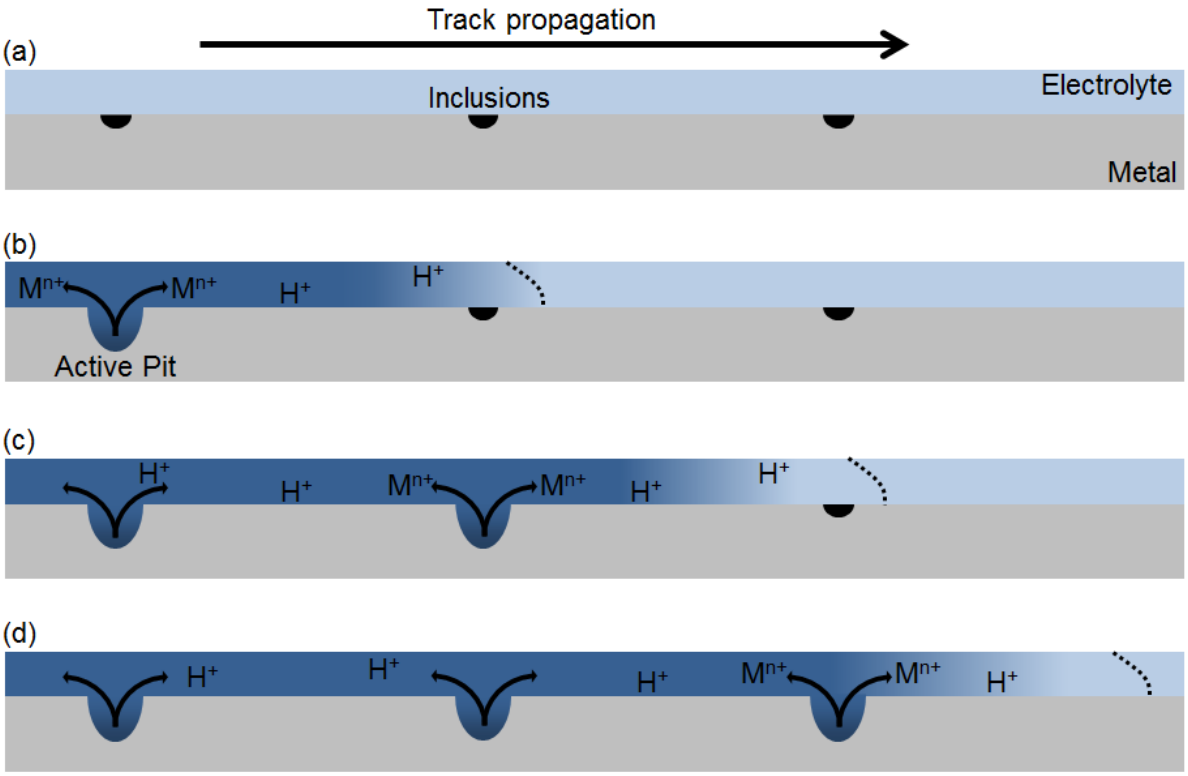

Figure 5-10 Schematic of the track-like progression of corrosion sites found under droplets with a CDD of 1 µg/cm^2 on 304L. The initial corrosion site initiates at the leftmost corrosion site in (a). During the propagation of the initial pit metal ions are released into the electrolyte, lowering the local pH in the area around the initial corrosion site which may also contain another site susceptible to corrosion (middle inclusion, (b)). The decreased pH around the middle site allows it to initiate into a corrosion site, further extending the area of decreased pH (d).

Analysis of the in-situ monitoring data suggested that low CDD droplets (1 µg/cm^2) formed some kind of residue within the droplet as they dried. For $MgCl_2$ droplets on 304L and 316L, and $CaCl_2$ droplets on 304L this residue did not affect the development of corrosion under these droplets. Small pits (~20 µm dia.) were observed under $CaCl_2$ 1 µg/cm^2 CDD droplets on 316L samples, which did not fit the track-like morphology observed for the other salt and alloy combinations at a CDD of 1 µg/cm^2. These small pits exclusively formed in the same location as the residue, and so were likely affected by its presence. The residue was not directly analysed, but was removed easily after a DI water rinse, suggesting that it was either soluble or

not strongly attached to the metal surface. The reason for the formation of corrosion sites under the residue for $CaCl_2$ droplets on 316L samples is likely that the residue acted as a diffusion barrier, making the stabilisation of any corrosion processes under the barrier more likely.

5.5.2 Initiation times

Pitting of stainless steel under atmospheric conditions is generally assumed to occur once the chloride concentration of the electrolyte has increased to a critical level.[7] In the current work all tests with a given salt are expected to give the same chloride concentration, as this is dictated by the exposure humidity which was identical for all tests (the chloride concentration in $MgCl_2$ and $CaCl_2$ solutions respectively was calculated to be ~8.4 M and ~8.9 M). After the initial equilibration period at 80 %rh and subsequent decrease in humidity to ~47 %rh almost all salt / CDD / alloy combinations showed at least one example of a corrosion site initiating, which suggests that all droplets reached the critical chloride concentration for corrosion to initiate within the same ~20 minute interval. There is, however, markedly different behaviours in terms of timing even though the chloride concentration of each droplet should be the same.

The results may be interpreted by considering metastable pitting, and the transition to stable pitting. For a metastable pit to successfully transition to a stable pit it must maintain an aggressive, low pH solution within itself to keep the local passive layer from re-forming and for dissolution to continue; this competes with the loss of the aggressive pit solution out into the bulk electrolyte.[8, 30]

Conditions which showed a comparatively higher rate of corrosion initiation matched conditions in which it would be easier for a metastable pit to transition to a stable pit.

Thicker droplets (higher CDD) tended to show corrosion sites earlier, likely due to the reduced IR drop within the electrolyte between cathode and anode. This allows a higher potential at the corrosion site, which can promote a higher rate of metal dissolution, and so encourage a more stable pit solution. Metastable pitting events have been reported to grow under diffusion control, suggesting that a saturated salt layer is present within these sites.[8] Such a salt layer will have a greater thickness in systems under a larger potential, such as those under thicker droplets.[31] An increase in the thickness of the salt layer may help to maintain the aggressive chemistry within the metastable pit during any transients in the environment of the pit. The increased dissolution rate will also allow the metastable pit to maintain the aggressive pit solution under more severe increases to the diffusion rate, such as through changing pit morphology, or pit cap rupture.[8]

Droplets on 316L took longer to develop corrosion than droplets on 304L, likely due to the addition of Mo acting to reduce dissolution and promote passivation within metastable sites; it is also important to note that the frequency of metastable pitting events has been found to be lower on 316 alloys compared to 304 alloys.[32, 33] The slightly higher chloride concentration in $CaCl_2$ solutions compared to $MgCl_2$ solution allows easier electro-migration of Cl^- ions into the developing pit, allowing charge-balancing to occur more easily and to promote pit stability.[34] Ca^{2+} ions will also more readily hydrolyse than Mg^{2+} ions, suggesting that the pH may be lower in a $CaCl_2$ droplet than a $MgCl_2$ droplet, making it more likely that the low pH within a developing pit solution can be maintained.[35]

Generally very low CDD droplets between 10-1 $\mu g/cm^2$, did not follow the pattern for initiation described above, often initiating quicker than some higher CDD droplets. Importantly these droplets were also often cases where corrosion did not propagate

as a single pit, but instead often with a track-like morphology. For these features it may be that the reduced solution layer thickness, which acted to reduce the cathodic range of the corrosion sites, also acted as a diffusion barrier to metal ion and H^+ transport directly above the site, allowing a metastable-pit to more easily transition to stability than would have possible under a thicker 'bulk' solution layer, which would have allowed metal ions to diffuse from the corrosion site more readily.

5.5.3 Pit penetration rate

The large amount of scatter in the square of the depth for pits of a similar age, and the narrow spread in terms of time points makes it difficult to justify drawing a linear relationship between the square of the depth and time. The scatter in the data alone suggests that a simple diffusion-limited model of pit growth does not fully reflect the growth of a pit in three dimensions.

There are three main assumptions in the measurement of the data and Equation 5-1 which bear further scrutiny. Firstly, the depth data was taken by finding the lowest point directly below the pit mouth, as this was the only part of the pit that could be observed with the microscope. If the pit instead propagated sideways away from the pit mouth then the actual pit depths could be larger than those recorded. Another assumption was that the pit continues to grow for the entire length of time from initiation. If the pit instead stopped growing, for whatever reason, then the duration data recorded would instead be an over-estimate.

The assumption we must inspect in Equation 5-1 is that $\frac{MD_{eff}C_{sat}}{\rho}$ is a constant. M and ρ, the average molar mass, and average density of the material, are material properties of the metal and it is difficult to argue that they may reasonably change. The effective diffusion constant D_{eff} and the difference in metal ion concentration

between the pit bottom and the pit mouth C_{sat}, however, are more likely candidates. More generally the term C_{sat} is ΔC, the difference between the metal ion concentration at the top and the bottom of the pit. If a salt layer is present at the bottom of the pit, and there is sufficient bulk electrolyte at the pit mouth, then $\Delta C = C_{bottom} - C_{mouth} = C_{sat} - 0 = C_{sat}$. This assumption is generally applied to studies in bulk electrolytes, where metal ions escaping from the pit mouth are quickly lost into the bulk solution. In atmospheric cases, however, the amount of electrolyte above the pit is much less, and it is reasonable to assume that the diffusion of metal ions from the pit is not as easy. Therefore ΔC may be less than C_{sat}, and indeed may change over time as more metal ions are released into the thin electrolyte layer.

It is interesting to note, however, that even if ΔC is changing with time, it is not unreasonable to assume that it will change in a predictable and repeatable way; the build-up of metal ions around a pit mouth for the same solution layer thickness is unlikely to vary significantly from site to site. As such this does not explain the variation observed with pit depth data for pits which grew for similar times.

Lastly, it is worth recognising that the relationship given in Equation 5-1 has been derived for idealised 1-dimensional pits. Although it has been observed to hold in electrochemical tests on 1-dimensional 'lead-in-pencil' electrodes, as well as 2-dimensional foils, it may be that 3-dimensional atmospheric tests do not satisfy some of the simplifications and assumptions used in its derivation.

5.6 Conclusions

The development of atmospheric corrosion of 304L and 316L stainless steels under droplets of $MgCl_2$ and $CaCl_2$ was monitored in-situ using a flat-bed scanner over a 7 day period. The time between the deposition of a chloride droplet and the initiation of

corrosion under that droplet was recorded, and an accurate relationship between the depth of corrosion sites and their age was drawn.

- Corrosion was observed for both 304L and 316L, under both $MgCl_2$ and $CaCl_2$ droplets, between chloride deposit densities (CDDs) of 1000 (the maximum tested) to 1 µg/cm^2. No corrosion was detectable at a CDD of 0.1 µg/cm^2.

- The morphology of the corrosion sites was either a single (or a few) pit ~100 to 20 µm dia., or the development of a series of small (<5 µm dia.) pits connected by a 'track' of corrosion product. This 'track-like' morphology was only observed under thinner droplets (CDD 10-1 µg/cm^2), though single pits were also observed under these conditions.

- In-situ observations showed that the 'track-like' morphology developed sequentially from a single point and developed in parallel. It is proposed that a local decrease in the pH around the initial corrosion site allowed further corrosion sites to activate in the vicinity of the first, and the increased IR drop caused by the thinner solution layer allowed multiple sites to develop at once.

- In studying variations in the initiation time of corrosion sites, it was seen that corrosion initiated more readily when conditions were 'more aggressive' (lower IR drop, higher chloride concentration (in $CaCl_2$ solutions compared to $MgCl_2$ solutions), more susceptible metal, lower pH). This was rationalised in terms of the likelihood of a metastable pit transitioning to stability, with more aggressive conditions increasing the likelihood that a given metastable pit could maintain an aggressive pit-

solution. Solution thickness may also have played a part in limiting diffusion of ions from metastable pits, when the solution thickness was very low

- Data relating the square of the depth of a corrosion site and its age did not suggest a linear relationship, and there was a high degree of scatter between the depths of sites with similar ages. The diffusion limited nature of 3D pits growing under conditions with a thin electrolyte film could not be supported.

5.7 Acknowledgements

Angus Cook is funded by EPSRC grant EP/I036397/1, and Radioactive Waste Management Ltd. contract NPO004411A-EPS02.

5.8 References

1. Nuclear Decomissioning Authority, *Geological Disposal: Package Evolution Status Report*, Nuclear Decomissioning Authority, 2010, NDA/RWMD/031

2. Nuclear Decomissioning Authority, *Geological Disposal: An overview of the generic Disposal System Safety Case*, Radioactive Waste Management Limited, 2010.

3. Padovani, C., R.J. Winsley, N.R. Smart, P.A.H. Fennell, C. Harris, and K. Christie, *Corrosion Control of Stainless Steels in Indoor Atmospheres—Practical Experience (Part 2).* Corrosion, 2015. **71**(5): p. 646-666.

4. Frankel, G.S., *Pitting Corrosion of Metals: A Review of the Critical Factors.* Journal of The Electrochemical Society, 1998. **145**(6): p. 2186-2198.

5. Hans-Henning, S., *Mechanisms of Pitting Corrosion*, in *Corrosion Mechanisms in Theory and Practice*. 2002, CRC Press. p. 243-285.

6. Galvele, J.R., *Transport processes and the mechanism of pitting of metals.* J. Electrochem. Soc: Electrochemial science and technology, 1976. **123**(4): p. 464-474.

7. Tsutsumi, Y., A. Nishikata, and T. Tsuru, *Initial Stage of Pitting Corrosion of Type 304 Stainless Steel under Thin Electrolyte Layers Containing Chloride Ions.* Journal of The Electrochemical Society, 2005. **152**(9): p. B358-B363.

8. Pistorius, P.C. and G.T. Burstein, *METASTABLE PITTING CORROSION OF STAINLESS-STEEL AND THE TRANSITION TO STABILITY.* Philosophical Transactions of the Royal Society of London Series a-Mathematical Physical and Engineering Sciences, 1992. **341**(1662): p. 531-559.

9. Frankel, G.S., L. Stockert, F. Hunkeler, and H. Bohni, *Metastable pitting of stainless steel.* Corrosion 1987. **43**: p. 429-436.

10. Williams, D.E., J. Stewart, and P.H. Balkwill, *The nucleation, growth and stability of micropits in stainless steel.* Corrosion Science, 1994. **36**(7): p. 1213-1235.

11. Tsuru, T., K.I. Tamiya, and A. Nishikata, *Formation and growth of micro-droplets during the initial stage of atmospheric corrosion.* Electrochimica Acta, 2004. **49**(17-18): p. 2709-2715.

12. Tsutsumi, Y., A. Nishikata, and T. Tsuru, *Pitting corrosion mechanism of Type 304 stainless steel under a droplet of chloride solutions.* Corrosion Science, 2007. **49**(3): p. 1394-1407.

13. Örnek, C., X. Zhong, and D.L. Engelberg, *Low-Temperature Environmentally Assisted Cracking of Grade 2205 Duplex Stainless Steel Beneath a MgCl2:FeCl3 Salt Droplet.* CORROSION, 2016. **72**(3): p. 384-399.

14. Cook, A.B., S.B. Lyon, N.P.C. Stevens, R.C. Newman, M. Gunther, G. McFiggans, and D.L. Engelberg, *Under-Deposit Chloride-Induced Stress Corrosion Cracking in Austenitic Stainless Steels: Aspects Associated with Deposit Type, Size and Composition.* ECS Transactions, 2014. **58**(29): p. 25-39.

15. Maier, B. and G.S. Frankel, *Pitting Corrosion of Bare Stainless Steel 304 under Chloride Solution Droplets.* Journal of the Electrochemical Society, 2010. **157**(10): p. C302-C312.

16. Cheng, C., L. Klinkenberg, Y. Ise, J. Zhao, E. Tada, and A. Nishikata, *Pitting corrosion of sensitised type 304 stainless steel under wet–dry cycling condition.* Corrosion Science, 2017. **118**: p. 217-226.

17. Hastuty, S., Y. Tsutsumi, A. Nishikata, and T. Tsuru, *Pitting Corrosion of Type 430 Stainless Steel in the Process of Drying of Chloride Solution Layer.* Isij International, 2012. **52**(5): p. 863-867.

18. Tester, J.W. and H.S. Isaacs, *Diffusional Effects in Simulated Localized Corrosion.* Journal of The Electrochemical Society, 1975. **122**(11): p. 1438-1445.

19. Gaudet, G.T., W.T. Mo, T.A. Hatton, J.W. Tester, J. Tilly, H.S. Isaacs, and R.C. Newman, *Mass transfer and electrochemical kinetic interactions in localized pitting corrosion.* AIChE Journal, 1986. **32**(6): p. 949-958.

20. Ghahari, M., D. Krouse, N. Laycock, T. Rayment, C. Padovani, M. Stampanoni, F. Marone, R. Mokso, and A.J. Davenport, *Synchrotron X-ray radiography studies of pitting corrosion of stainless steel: Extraction of pit propagation parameters.* Corrosion Science, 2015. **100**: p. 23-35.

21. Ryan, M.P., N.J. Laycock, H.S. Isaacs, and R.C. Newman, *Corrosion pits in thin films of stainless steel.* Journal of the Electrochemical Society, 1999. **146**(1): p. 91-97.

22. Ernst, P. and R.C. Newman, *Pit growth studies in stainless steel foils. I. Introduction and pit growth kinetics.* Corrosion Science, 2002. **44**(5): p. 927-941.

23. Mankowski, J. and Z. Szklarskasmialowska, *Studies on accumulation of chloride-ions in pits growing during anodic polarization.* Corrosion Science, 1975. **15**(8): p. 493-501.

24. Alkire, R.C. and K.P. Wong, *The Corrosion Of Single Pits On Stainless-Steel In Acidic Chloride Solution.* Corrosion Science, 1988. **28**(4): p. 411-&.

25. Cook, A.J.M.C., C. Padovani, and A.J. Davenport, *Effect of Nitrate and Sulfate on Atmospheric Corrosion of 304L and 316L Stainless Steels.* Journal of The Electrochemical Society, 2017. **164**(4): p. C148-C163.

26. Street, S.R., N. Mi, A.J.M.C. Cook, H.B. Mohammed-Ali, L. Guo, T. Rayment, and A.J. Davenport, *Atmospheric pitting corrosion of 304L stainless steel: the role of highly concentrated chloride solutions.* Faraday Discussions, 2015. **180**(0): p. 251-265.

27. J. Schindelin, I.A.-C., E. Frise, V. Kaynig, M. Longair, T. Pietzsch, S. Preibisch, C. Rueden, S. Saalfeld, B. Schmid, J. Tinevez, D.J. White, V. Hartenstein, K. Eliceiri, P. Tomancak, A. Cardona, *Fiji: an open-source platform for biological-image analysis.* Nature Methods, 2012. **9**(7): p. 7.

28. Mohammed Ali, H.B., *Atmospheric pitting corrosion of stainless steel* [Ph.D. thesis]. University of Birmingham; 2016

29. Suleiman, M.I. and R.C. Newman, *The use of very weak galvanostatic polarization to study localized corrosion stability in stainless steel.* Corrosion Science, 1994. **36**(9): p. 1657-1665.

30. Pistorius, P.C. and G.T. Burstein, *Growth of corrosion pits on stainless steel in chloride solution containing dilute sulphate.* Corrosion Science, 1992. **33**(12): p. 1885-1897.

31. Isaacs, H.S., *Behavior Of Resistive Layers In Localized Corrosion Of Stainless-Steel.* Journal of the Electrochemical Society, 1973. **120**(11): p. 1456-1462.

32. Ilevbare, G.O. and G.T. Burstein, *The role of alloyed molybdenum in the inhibition of pitting corrosion in stainless steels.* Corrosion Science, 2001. **43**(3): p. 485-513.

33. Ilevbare, G.O. and G.T. Burstein, *The inhibition of pitting corrosion of stainless steels by chromate and molybdate ions.* Corrosion Science, 2003. **45**(7): p. 1545-1569.

34. Ryan, M.P., D.E. Williams, R.J. Chater, B.M. Hutton, and D.S. McPhail, *Why stainless steel corrodes.* Nature, 2002. **415**(6873): p. 770-774.

35. Perrin D. D., *Ionisation Constants of Inorganic Acids and Bases in Aqueous Solutions, Second Edition*. 1982, Oxford: Pergamon.

6 THE EFFECT OF NaCl PRECIPITATES ON THE ATMOSPHERIC CORROSION OF STAINLESS STEELS UNDER DROPLETS CONTAINING $MgCl_2$ AND $CaCl_2$

Preface

The following chapter has been formatted in preparation for submission to an academic journal; the section contains its own list of references at the end, and the reference numbering for this section is self-contained. The section numbering, figure and table numbering, and pagination, however, has been continued from the main text of the thesis in order to aid readability and navigation in the context of the whole document.

Angus Cook is the lead author of the following paper, having conducted the entirety of the experimental and write-up work. Alison Davenport, Trevor Rayment and Cristiano Padovani provided editorial advice on the structure and clarity of the text and figures, and Cristiano Padovani contributed to sections of the introduction.

The effect of NaCl precipitates on the atmospheric corrosion of stainless steels under droplets containing $MgCl_2$ and $CaCl_2$

Angus J. M. C. Cook[1], Trevor Rayment[2], Cristiano Padovani[3], Alison Davenport[1]

[1] School of Metallurgy and Materials, University of Birmingham, Edgbaston, Birmingham, UK, B15 2TT

[2] School of Chemistry, University of Birmingham, Edgbaston, Birmingham, UK, B15 2TT

[3] Wood, Harwell Science Park, Oxford, UK, OX11 0QB

6.1 Abstract

Droplets of binary chloride salts (NaCl + $MgCl_2$ or NaCl + $CaCl_2$) were deposited onto 304L stainless steel and then exposed at a relative humidity (~44 %rh) that was low enough for the precipitation of NaCl, in order to study the effect of NaCl precipitates on atmospheric corrosion. It was found that NaCl crystals could act as crevice formers, with shallow corrosion and etching observed when the corrosion site and crystal were coincident. As a result shallower corrosion was observed in mixed solution droplets in which NaCl were present (particularly when large crystals formed) compared with control droplets which contained only a single, fully aqueous salt. Pits that developed in droplets containing precipitates, but were not located underneath them, grew with narrower pit mouths than pits in control droplets, indicating that the presence of precipitates decreased the driving force for corrosion within the droplet. Similar effects were seen using chemically inert glass shards in place of the NaCl crystals, suggesting the physical barrier provided by the NaCl crystal was of more importance than its chemical properties.

6.2 Introduction

The UK policy to deal with radioactive waste is that of geological disposal, that is permanent deposition within a stable, sealed underground geological disposal facility (GDF).[1] The siting, construction and operation of this facility, however, are likely to occur over several decades. In line with international standards, the UK classifies its radioactive waste into several categories based on its activity and resulting radiological and thermal properties; intermediate level nuclear waste (ILW) – typically comprising materials displaying significant contamination with radioactive substances or substantial activation due to previous irradiation in nuclear reactors – represents a large volume of the UK inventory, thus requiring due consideration. In the UK, ILW is currently stored in stainless steel containers (grades 304L and 316L) in interim storage facilities where it will remain until it can be disposed of within a GDF. After transport to the GDF, ILW will be subjected to further long periods of exposure to atmospheric conditions associated with the operational period of the facility, before its final backfilling and closure.

During the interim storage and the GDF operational period, these stainless steel containers will be subjected to deposition of atmospheric aerosols, which are known to include corrosion promoters such as chlorides.[2] The availability of water in the atmosphere (relative humidity, RH) and daily and seasonal temperature cycling will lead to some chemical species deliquescing (i.e. taking in water and becoming a liquid electrolyte), and others effloresing (losing water and precipitating into a solid phase) at different times. Although stainless steel has excellent general corrosion resistance, in the presence of chloride it is known to be susceptible to localised corrosion such as pitting, which may then lead to stress corrosion cracking (SCC), resulting in structural failure of the container. As such, the performance of stainless

steels under ILW storage conditions (0-30 °C, 30-100 %rh)[2] over several decades is of interest to the nuclear industry and, more broadly, for applications envisaging the use of stainless steel in indoor conditions over long periods of time.

While there is a considerable body of literature focusing on the electrochemical testing of 304L and 316L stainless steels (of great relevance to aqueous exposure conditions), there is rather less that focuses on corrosion under atmospheric conditions, which are characterised by higher solution concentrations than typically present in aqueous conditions, and thin electrolyte films. Work undertaken by Shoji and Ohnaka showed that low temperature (~23 °C) stress corrosion cracking occurring on 304L and 316L stainless steels under artificial seawater droplets could be attributed to the $MgCl_2$ content of these solutions.[3] Subsequently many researchers have used pure $MgCl_2$ as a proxy for more complicated seawater solutions, studying both pitting and cracking development. Other common chloride salts employed have included NaCl (very common in the natural environment), $CaCl_2$ (a component of seawater with similar properties to $MgCl_2$), and $FeCl_3$ (present as a corrosion product of steels in aggressive conditions). [4-13] Most of these studies have employed only a single salt type per solution, and all have looked at solutions with only a single phase (i.e. either solid *or* aqueous).

Cook *et al.* have highlighted the mixed phase nature of ocean-water droplets subjected to a decreasing relative humidity, with different chemical components precipitating as the humidity decreases, leading to mixed-phase deposits.[14] Salt deposits within indoor facilities, however, comprise a variety of chemicals not just from marine sources but also, among others, from industrial, urban and agricultural sources. This leads to different combinations and amounts of several chemical species typically found on surfaces subjected to natural aerosols deposition, with no

single representative combination. [2] In addition to this, natural aerosols, particularly marine aerosols containing organic matter, may also have an effect on the chemistry of the surfaces affected.[15]

Whilst, in the context of radioactive waste management, the atmospheric corrosion behaviour of stainless steel surfaces subjected to NaCl, $MgCl_2$ and, to an extent, nitrates and sulphates in different ranges of temperature, humidity and deposit density has been extensively studied, there remain important outstanding questions associated with the behaviour of the system, including a good mechanistic understanding of the behaviour of mixed chloride solutions (likely to be the main sources of free chloride in the natural environment), of the effect of solid phases (invariably present in the system), and the effect of organic material (also likely to be present).[2, 12, 16, 17] This paper focuses on the second and, to an extent, the first of these aspects. In particular, it aims at establishing whether insoluble or limited-solubility solid phases that may deposit or form on the surfaces during dry cycles have a significant effect on the corrosion behaviour of chloride-containing systems and whether the behaviour of mixed NaCl + $MgCl_2$ and NaCl + $CaCl_2$ systems in the presence of NaCl precipitates (relatively low RH) can be rationalised on the basis of key parameters (e.g. their respective amounts).

In this context, Guo *et al.* have studied the development of corrosion under a binary solution of NaCl + $MgCl_2$, seeing evidence of altered corrosion site morphology under precipitates.[18] Modelling of this system has been undertaken which predicts both an increased electrolyte resistance and cathodic blockage due to the presence of precipitates within the electrolyte.[19] Studies have also used thin silica particulate layers to mimic precipitates in corrosion tests.[20-22] In addition, work has also been carried out with ‘organically-enriched artificial sea salt’, which resulting in an instance

of stress corrosion cracking originating from underneath a NaCl precipitate on a 304L U-bend specimen, and crystalline precipitates have also been seen to cause crevice-like attack in atmospheric tests using a mixed chloride and nitrate or sulphate salts.[16, 23]

In this work a high-throughput droplet deposition methodology has been used to investigate the effect of mixed-phase salts on the atmospheric corrosion of stainless steel. The aim was to gain statistically-significant data on pit damage and morphology under a wide range of binary solution compositions, under environmental conditions of relevance to an indoor facility. Binary salt solutions containing NaCl and either $MgCl_2$ or $CaCl_2$ were tested at a humidity of ~44 %rh. This humidity was chosen because it was expected to result in a solution containing fully dissolved $MgCl_2$ or $CaCl_2$ (their deliquescence humidity is ~33 %rh and ~12 %rh, respectively) but full precipitation of NaCl crystals (deliquescence humidity is around 75 %rh), thus allowing the testing of solutions containing solid phases.[24, 25]

These tests have been compared with control tests, comprising single salt solutions matching the different concentrations of $MgCl_2$ or $CaCl_2$ used in the binary salt solutions, but without the addition of NaCl. These control tests have been used to observe and isolate any effects that different quantities of aqueous electrolyte have on corrosion, without any interference of NaCl precipitates, and also simulate the ‘removal’ of aqueous chloride from a droplet due to the precipitation of NaCl. The chloride content of all *binary* solutions has been kept the same, only the ratio of cations has been altered. Further details on solution compositions are given in the Methodology.

6.3 Methodology

6.3.1 Sample Preparation

304L stainless steel plate of 3 mm thickness was provided by Aperam France. The plate was cold rolled and solution annealed (1040 – 1100 °C, forced air cooling). A chemical analysis of the steel provided by the foundry is shown in Table 6-1. Samples were cut with alumina discs to either 25x25 mm or 75x25 mm and cold mounted, then wet ground from P400 to P800 grit using SiC papers. Samples were then ultrasonically cleaned in de-ionised water (DI) (>15 MΩ·cm, Millipore) for ~5 minutes, rinsed with DI water, and dried under an ambient airstream. The samples were left in covered ambient conditions for 24 hours before deposition of selected salts or salt mixtures, to allow the passive layer to re-form after grinding. Ambient conditions were between 21 – 24 °C, 41 – 51 %rh over the testing period.

Table 6-1 Chemical analysis of 304L stainless steel, provided by manufacturer.

	Chemical Analysis (wt-%)											
Alloy	C	Si	Mn	Ni	Cr	Mo	Ti	N	S	P	Co	Fe
304L	0.023	0.44	1.46	8.00	18.08	-	-	0.072	0.0033	0.032	0.171	Bal.

6.3.2 Binary chloride salts

All solutions were made from ACS grade chemicals. Stock solutions were made up with NaCl, $MgCl_2 \cdot 6H_2O$, $CaCl_2 \cdot 2H_2O$ (Sigma-Aldrich), and DI water to 0.7 M by chloride. This concentration was chosen so that a 2 µL droplet of each solution, covering ~5 mm^2, would result in a chloride deposit density (CDD) of ~1000 $\mu g/cm^2$. A deposit density of 1000 $\mu g/cm^2$ is one order of magnitude greater than those currently assumed to be present indoors, based on a limited amount of information,

over periods of many decades and used in other recent work.[2, 16, 17] This was done to enhance the extent of corrosion observed in different conditions, helping to elicit effects described in this paper, whilst providing a bounding case for more realistic situations.

Tests which used glass shards to mimic precipitates (discussed in detail below) used a chloride solution concentration of 0.07 M (i.e. 0.035 M $MgCl_2$), making the chloride deposit density ~100 µg/cm^2. This was to mimic a mixed salt solution containing a low amount of $MgCl_2$ and a high level of NaCl.

For mixed salt experiments, the stock solutions were mixed to obtain four sets of solutions, comprising mixtures of NaCl + $MgCl_2$, NaCl + $CaCl_2$, DI water + $MgCl_2$ and DI water + $CaCl_2$, with the latter two solutions equivalent to simply diluting samples of the stock solution of $MgCl_2$ or $CaCl_2$ by varying amounts. The mixing regime is detailed in Table 6-2 and was carried out by a MultiPROBE II Ex automated liquid handling system (MPII) (Packard Biosciences).

In this work the solution compositions will generally be referred to by the volume ratio of the two component solutions (the ratio of NaCl or DI water : $MgCl_2$ or $CaCl_2$).

Table 6-2 Mixing details for both binary salt and single salt solutions. Concentration of all stock salt solutions is equivalent to 0.7 M [Cl^-] (i.e. 0.7 M [NaCl], 0.35 M [$MgCl_2$], 0.35 M [$CaCl_2$]).

		Solution mixing ratio (volume NaCl or DI water : volume $MgCl_2$ or $CaCl_2$)										
		10:0	**9:1**	**8:2**	**7:3**	**6:4**	**5:5**	**4:6**	**3:7**	**2:8**	**1:9**	**0:10**
NaCl + $MgCl_2$ or $CaCl_2$	**[NaCl] (mol/L)**	0.7	0.63	0.56	0.49	0.42	0.35	0.28	0.21	0.14	0.07	0
	[$MgCl_2$] or [$CaCl_2$] (mol/L)	0	0.035	0.07	0.105	0.14	0.175	0.21	0.245	0.28	0.315	0.35
	Total [Cl] (mol/L)	0.7	0.7	0.7	0.7	0.7	0.7	0.7	0.7	0.7	0.7	0.7
DI water + $MgCl_2$ or $CaCl_2$	**[NaCl] (mol/L)**	0	0	0	0	0	0	0	0	0	0	0
	[$MgCl_2$] or [$CaCl_2$] (mol/L)	0	0.035	0.07	0.105	0.14	0.175	0.21	0.245	0.28	0.315	0.35
	Total [Cl] (mol/L)	0	0.07	0.14	0.21	0.28	0.35	0.42	0.49	0.56	0.63	0.7

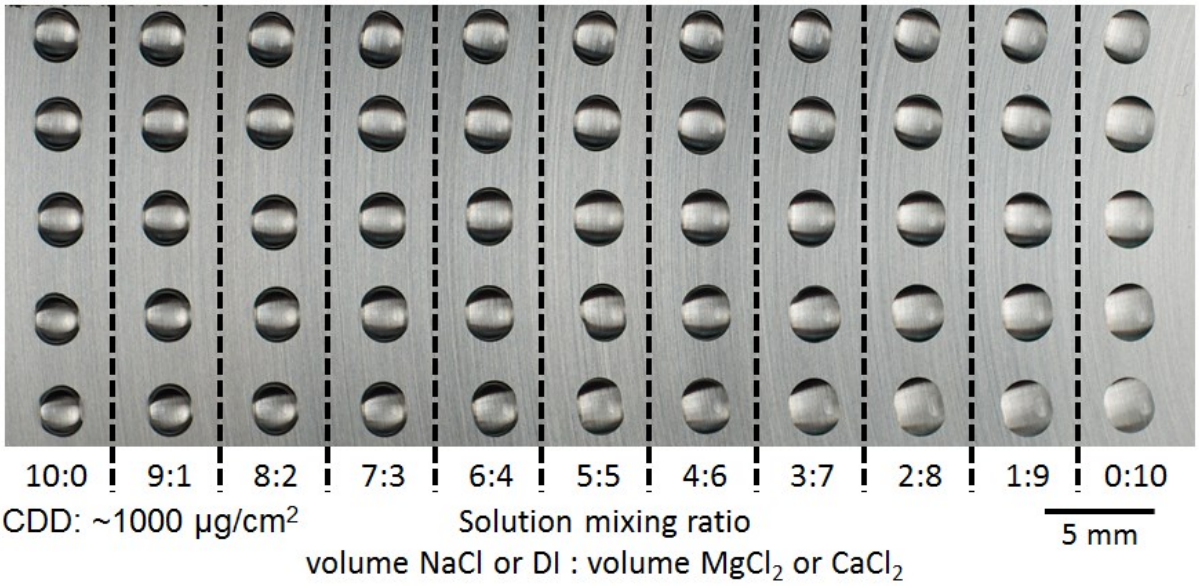

Figure 6-1 Deposition layout of 5x11 array of 2 µL droplets of binary chloride solution.

A typical array of freshly deposited droplets is shown in Figure 6-1. Droplets were deposited automatically using the MPII (Packard Biosciences). 2 µL droplets were deposited, resulting in an average area of 5.9 ± 0.3 mm^2 for $MgCl_2$ containing droplets, and 4.8 ± 0.2 mm^2 for $CaCl_2$ containing droplets. This resulted in droplets with the highest chloride concentration (0.7 M) having CDDs of 850 ± 40 µg/cm^2 for $MgCl_2$ containing droplets, and 1040 ± 60 µg/cm^2 for $CaCl_2$ containing droplets. The samples were then placed into desiccators containing a saturated solution of K_2CO_3 to maintain a fixed relative humidity at ~43 %rh, along with a temperature and humidity data logger (Lascar Electronics)[24]. The desiccators were then placed into a temperature controlled oven at 31 °C (Temperature Applied Sciences Ltd.).

Figure 6-2 shows the recorded temperature and humidity within a desiccator during sample placement. The temperature transient occurred when the desiccator was removed from the temperature chamber while the samples were inserted. The humidity transient occurs as the deposited droplets have both an initial water activity and surface:volume ratio higher than that of the saturated K_2CO_3, and so the

humidity within the desiccator rises faster than can be buffered by the mediating K_2CO_3 solution. The substantially larger volume of the K_2CO_3 solution relative to the deposited droplets, however, means that the humidity drops back to ~43 %rh within a few hours of sample insertion. This has been noted in previous experiments.[16]

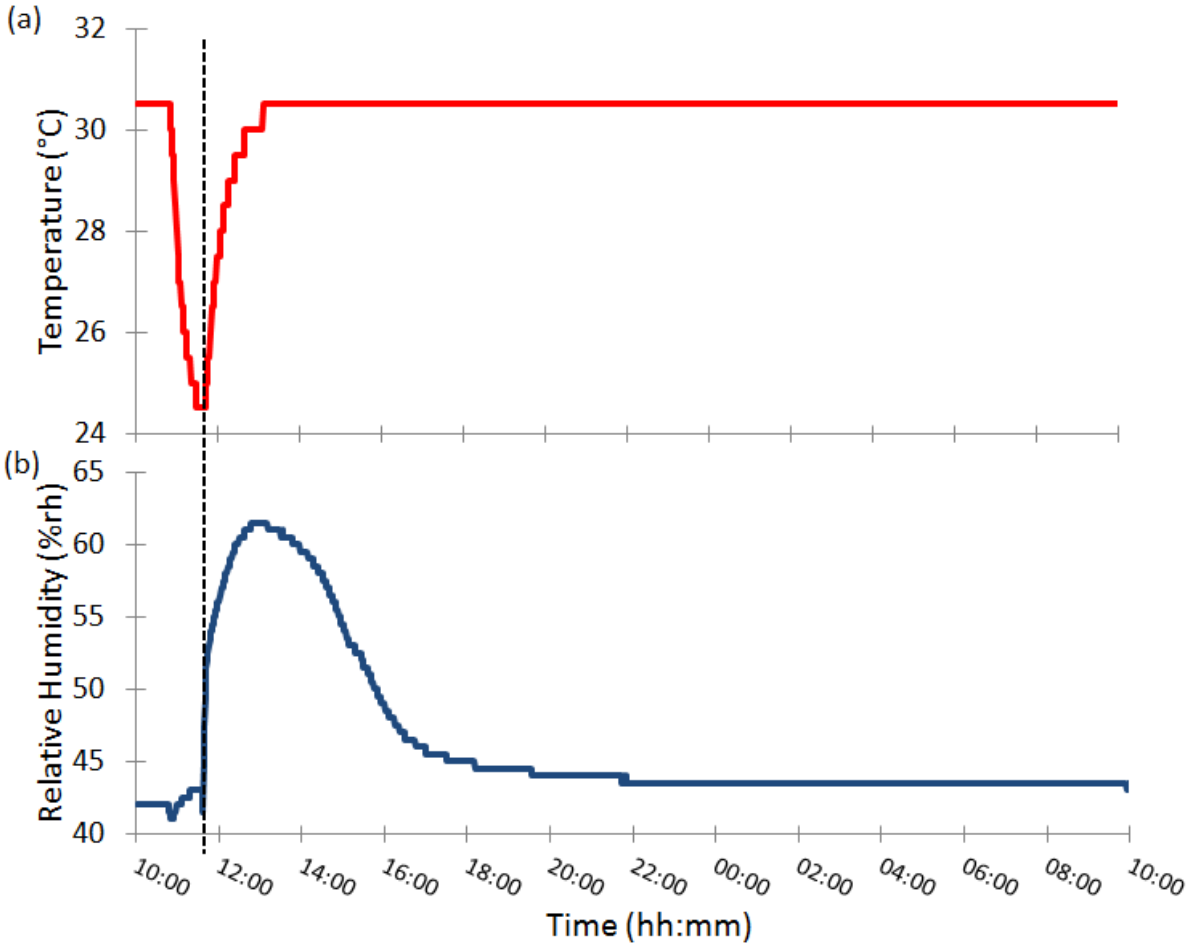

Figure 6-2 Temperature (a) and humidity (b) readings within desiccator during sample emplacement.

6.3.3 Inert crystals

The effect of chemically inert glass shards on the development of corrosion was also investigated for comparison with the presence of NaCl precipitates. A glass microscopy coverslip was cleaned in methanol and then DI water, before being broken into shards of comparable size to the NaCl precipitates observed in the binary solution tests, described above. These shards were scattered on a 25x25 mm

304L stainless steel sample, and a series of $MgCl_2$ 2 µL droplets were deposited over the top, shown in Figure 6-3(a). A second sample held an array of 2 µL binary solution only (no glass shards), with a solution ratio (volume NaCl : volume $MgCl_2$ at 0.7 M chloride) of 9:1, rich in NaCl and thus likely to yield to the formation of large crystals (Figure 6-3(b)). A third sample held an array of pure $MgCl_2$ 2 µL droplets (no glass shards and no salt crystals) (Figure 6-3(c)). The $MgCl_2$ composition of each solution was 0.035 M, in order that each droplet gave an effective aqueous CDD (i.e. due only to $MgCl_2$) of ~100 µg/cm^2. In this case, differently from the case of mixed solutions, droplet deposition of all three samples was undertaken manually *via* micropipette (Eppendorf). Exposure conditions were identical to the test above on binary chloride salts.

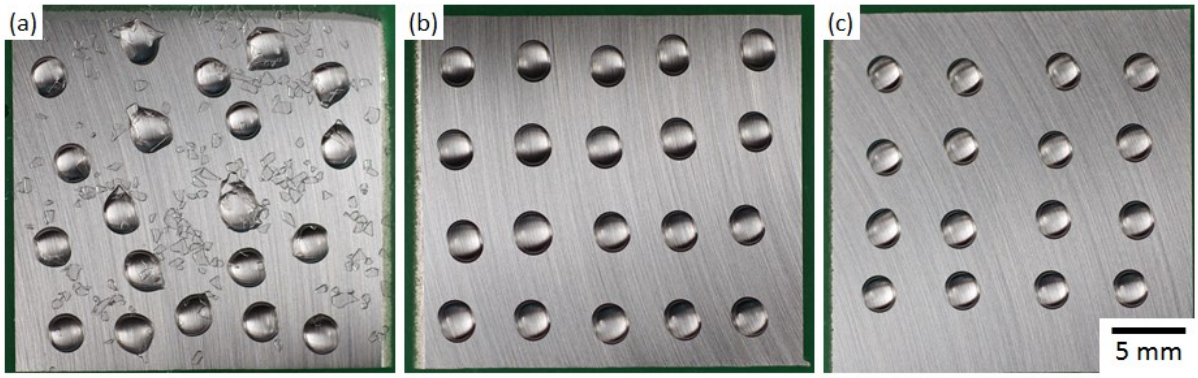

Figure 6-3 304L stainless steel samples with 2 µL droplets of salt solution, directly after droplet deposition. (a) 0.035 M [$MgCl_2$] solution deposited over glass shards, (b) 0.035 M [$MgCl_2$] + 0.63 M [NaCl] solution, (c) 0.035M [$MgCl_2$] solution.

A further test to investigate the role of inert crystals was performed on 25x25 mm 304L stainless steel sample, which was optically monitored during the exposure period. The sample was prepared as above, although the concentration of the $MgCl_2$ solution deposited over the shards was increased to 0.35 M [$MgCl_2$], and the droplet deposition method was automatic, using the MPII (Packard Biosciences). The

sample was placed into an environmental chamber, rather than a desiccator as had been used for previous experiments, which controlled both the temperature and humidity (TAS Ltd.). The exposure conditions were 31 °C at a humidity of 46 %rh, for 4 days. No significant temperature or humidity transients, as observed immediately after placing samples into desiccators (Figure 6-2), were observed for the sample within the environmental chamber.

This sample was optically monitored during exposure using an USB microscope (Celestron) and automated XY stage. Images of each droplet were captured in series, with the time taken to capture the entire series of 24 droplets being ~11 minutes. The time between successive images of the same droplet was ~12 minutes.

6.3.4 Post-mortem characterisation of corrosion damage

After exposure, samples were imaged using a digital camera and optical microscope. The samples were imaged directly after exposure (i.e. with the salt film still present), and after a rinse with DI water (to remove the salt). Selected samples were further processed by ultrasonic cleaning in DI water for 5 minutes, and further analysed optically (as above), *via* confocal microscopy (OLS 3100, LEXT), and with a SEM.

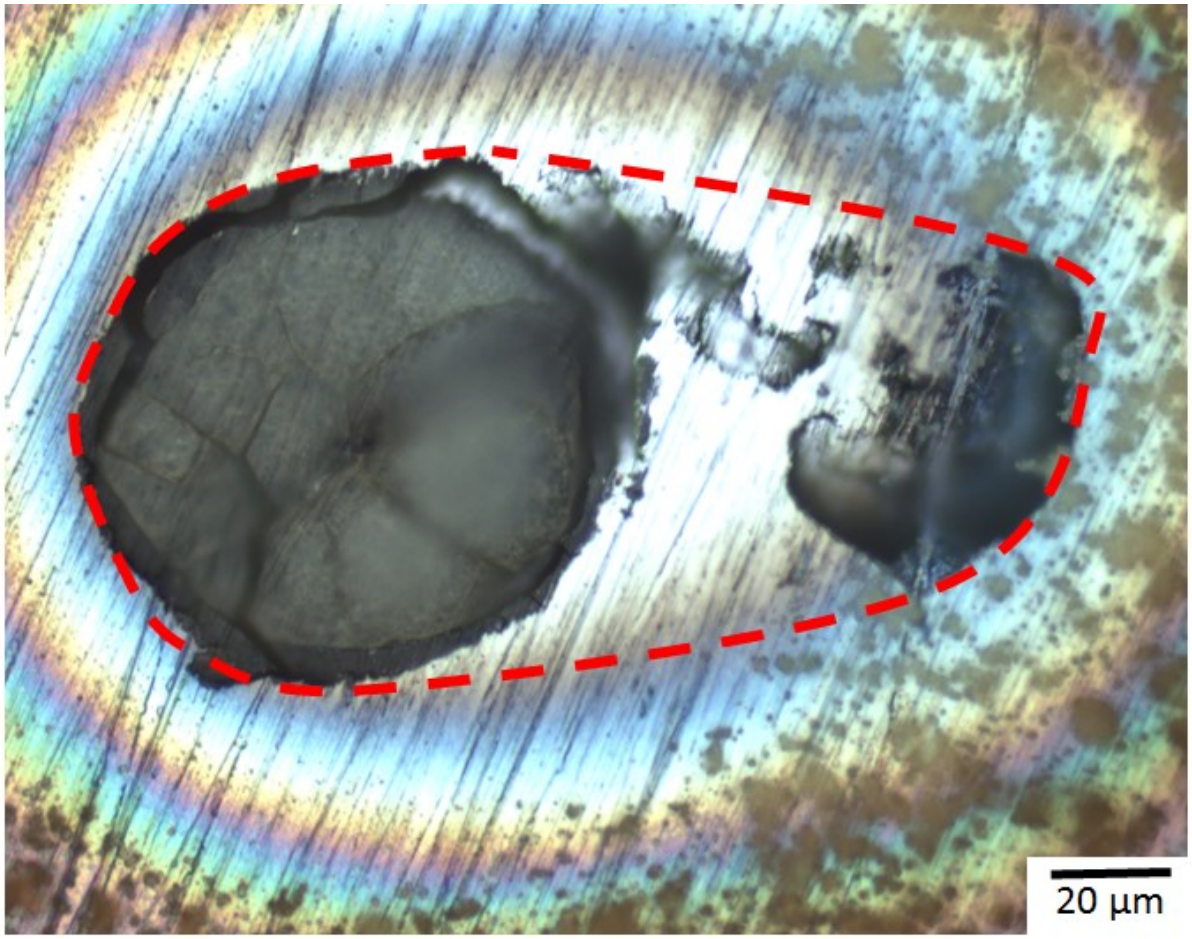

Figure 6-4 Example of a corrosion area measurement where adjacent corrosion sites are judged to be connected, and the pit area is approximated. The area bounded by the red dashed line would be taken as the area measurement for this site.

Corrosion areas were manually measured using the FIJI image processing software package.[26] If adjacent corrosion sites were judged to be connected under the surface their joint area was recorded by approximating the connection geometry (Figure 6-4). Maximum corrosion site depths were calculated under each droplet by comparing the focussing positions between the metal surface and the deepest point of the corrosion site using the optical microscope. If a droplet contained multiple corrosion sites, the largest value for each measurement (area and depth) was chosen, which were not necessarily from the same site.

6.3.5 Thermodynamic calculations for mixed salts

Thermodynamic calculations to predict the precipitation behaviour of the NaCl + $MgCl_2$ and NaCl + $CaCl_2$ mixed salt systems was conducted using OLI Stream Analyser Version 9.3, using the mixed solvent electrolyte model (MSE), main databank (H_3O^+ ion). The calculation conditions were set to 30 °C, 1 atm, with no vapour phase.

6.4 Results

Figure 6-5 shows both 304L stainless steel plates with mixed salt (NaCl + $CaCl_2$ (a), and NaCl + $MgCl_2$ (b)) immediately after being removed from the exposure environment. The morphology of corrosion sites under both $MgCl_2$ and $CaCl_2$ containing droplets was observed to be largely similar, so examples of key observations (Figure 6-6 to 6-9) have been taken only from the NaCl + $MgCl_2$ plate.

6.4.1 Precipitates

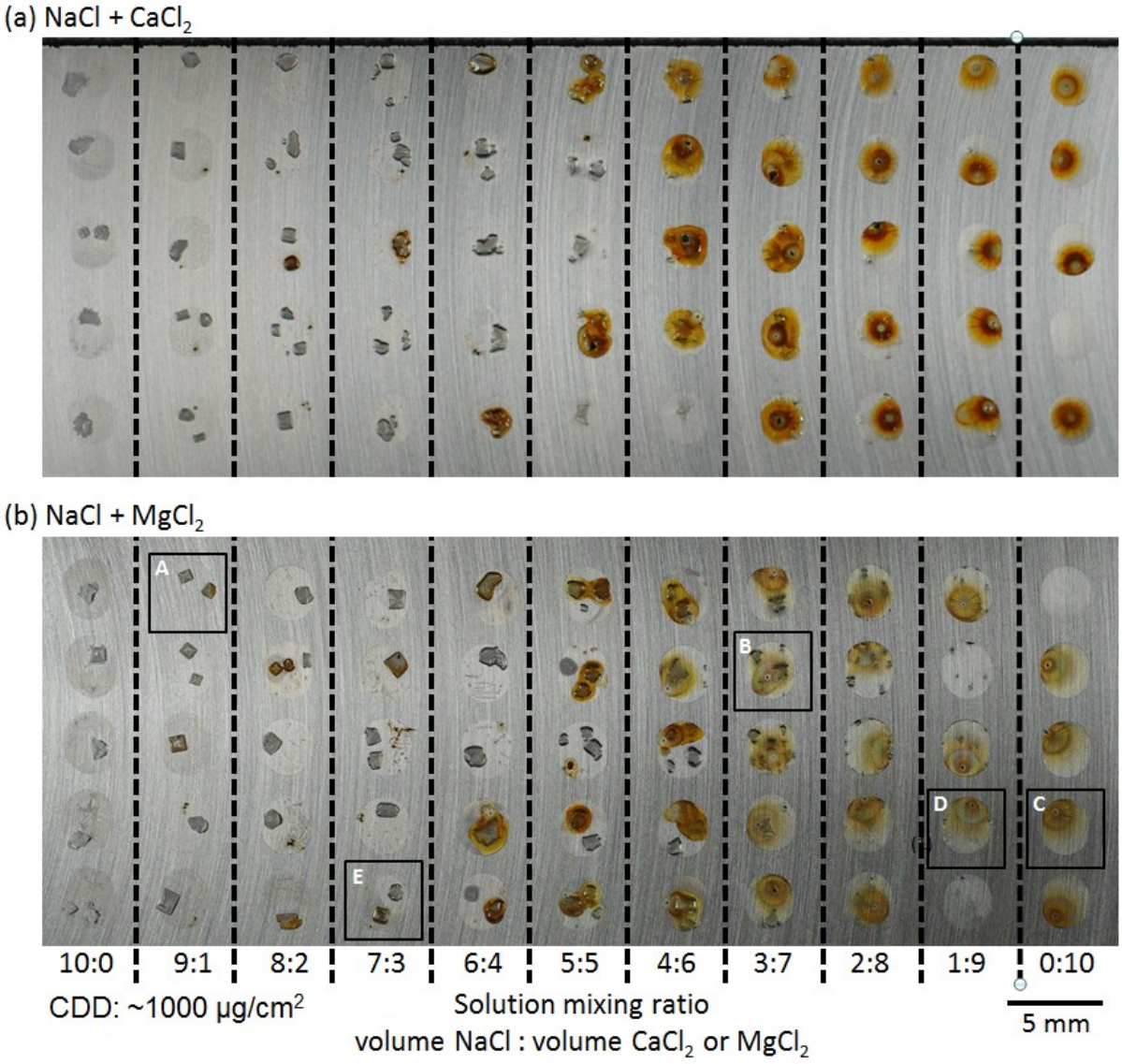

Figure 6-5 304L stainless steel with (a) 2 µL droplets of binary NaCl + $CaCl_2$ solutions and (b) 2 µL droplets of binary NaCl + $MgCl_2$ solutions. Exposed at 31 °C, 44 %rh for 7 days. Images taken directly after exposure. Selected droplets are shown in more detail below: A - Figure 6-6(A), B - Figure 6-6(B-1 – B-3), C - Figure 6-7, D - Figure 6-8, E - Figure 6-9.

Cubic crystals were observed to precipitate in every droplet that contained NaCl; examples of this are shown in Figure 6-6(A, B-1). The size of these crystals increased as the fraction of NaCl increased, although in contrast the number of individual crystals decreased (Figure 6-5). While the chemical composition of the

crystals was not directly measured, their cubic shape and the conditions under which they were observed make it highly probable that these were NaCl precipitates.

In preliminary tests under ambient lab conditions (23 °C, 30 %rh) using a binary solution of NaCl + $CaCl_2$ at a solution mixing ratio of 5:5, precipitation of NaCl crystals was always observed before the initiation of corrosion, within ~15 minutes of deposition. In some of these samples the initiation of corrosion was also seen to occur at or just after the precipitation of NaCl.

Where both precipitation and corrosion had occurred in the same droplet, ‘footprints’ left in the corrosion product by the precipitates could be observed, as shown in Figure 6-6(B-3).

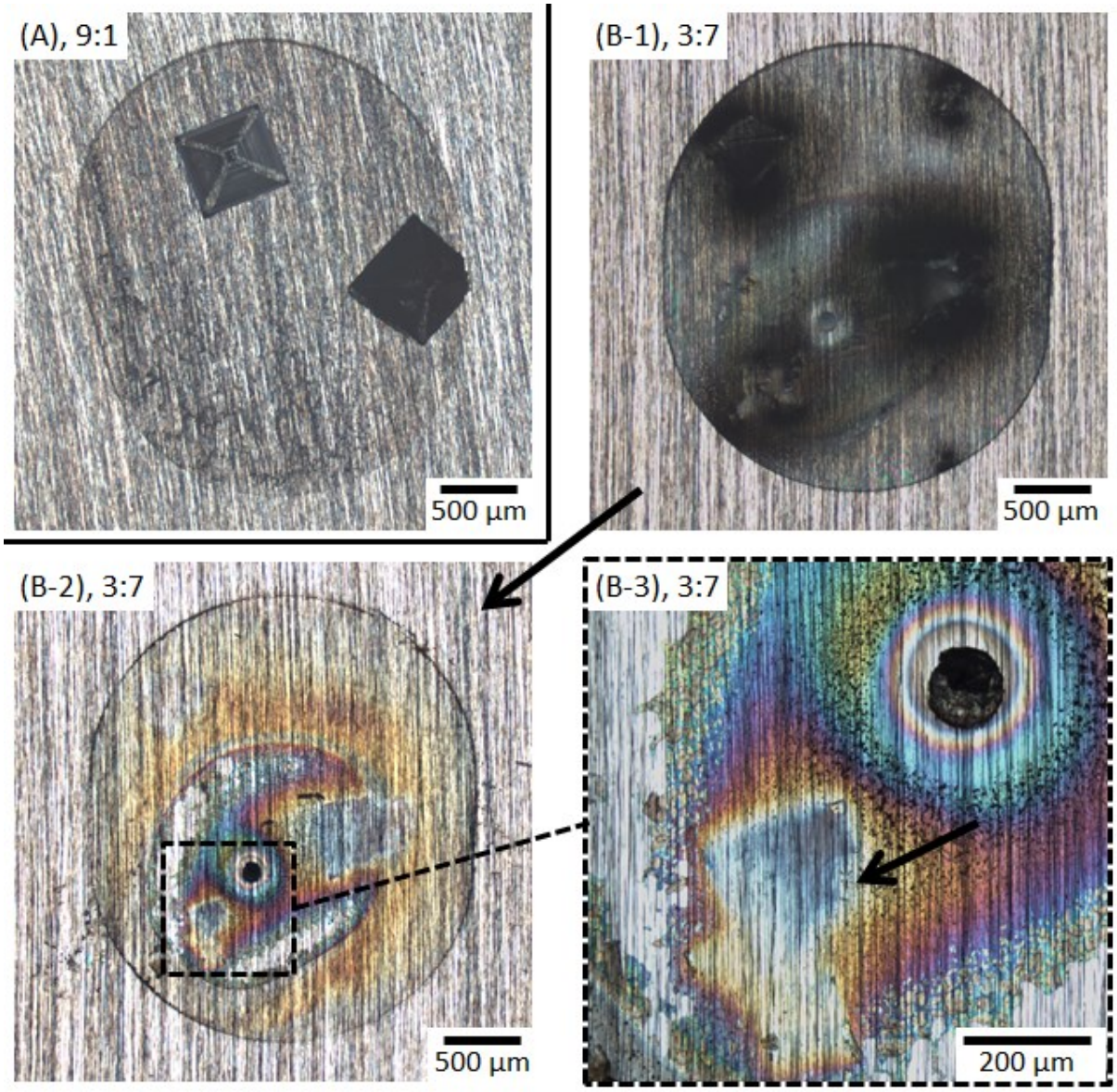

Figure 6-6 Binary NaCl + $MgCl_2$ droplets (2 µL) after 7 day exposure at 31 °C, 44 %rh on 304L stainless steel. (A) 9:1 binary solution ratio (volume NaCl : volume $MgCl_2$ at 0.7 M by chloride) as removed from desiccator. (B-1 – B-3) 3:7 binary solution ratio, (B-1) as removed from desiccator, (B-2,B-3) after solution has been washed off with DI water, with NaCl footprint in corrosion product visible (indicated by arrow in B-3)).

6.4.2 Pit morphology

Corrosion was observed under many of the droplets tested. The form of corrosion varied between: pits, 'crevice-like' surface attack, or a combination of the two. The type of attack was dependent on the presence of precipitates within the droplet. It was common to find a single corrosion site per droplet, though multiple sites under a

droplet were also seen. Multiple sites per droplet were more common under droplets containing NaCl precipitates.

Pitting corrosion was usually seen to lead to circular-mouthed pits; an example of this is given in Figure 6-7. This morphology was most commonly seen when the corrosion site developed under an ‘open geometry’, i.e. not underneath a precipitate.

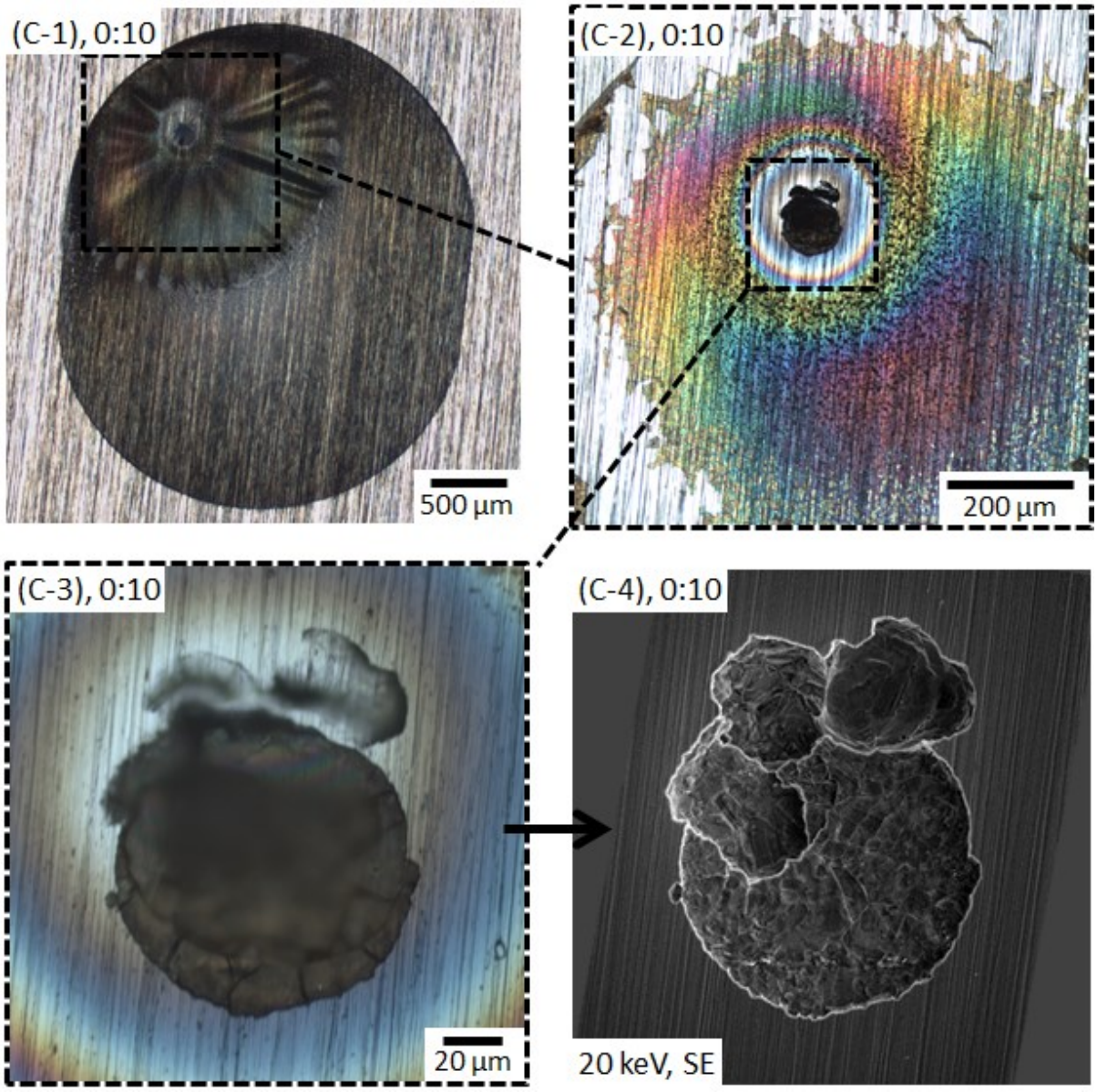

Figure 6-7 Example of a corrosion pit having developed under an 'open-geometry'. Pure $MgCl_2$ 2 µL droplet (binary solution ratio 0:10) on 304L stainless steel, after 7 days exposure at 31 °C, 44 %rh. (C-1) immediately after exposure, (C-2, C-3) show (C-1) after sample has been washed in DI water, (C-4) SEM image of (C-3) after ultrasonic cleaning, secondary electron image, 20 keV.

Pits were also observed which showed a more angular morphology (Figure 6-8). These were commonly observed in droplets containing NaCl that developed 'small' precipitates, that is precipitates which were approximately the size of an 'open-geometry' pit (~100 µm across).

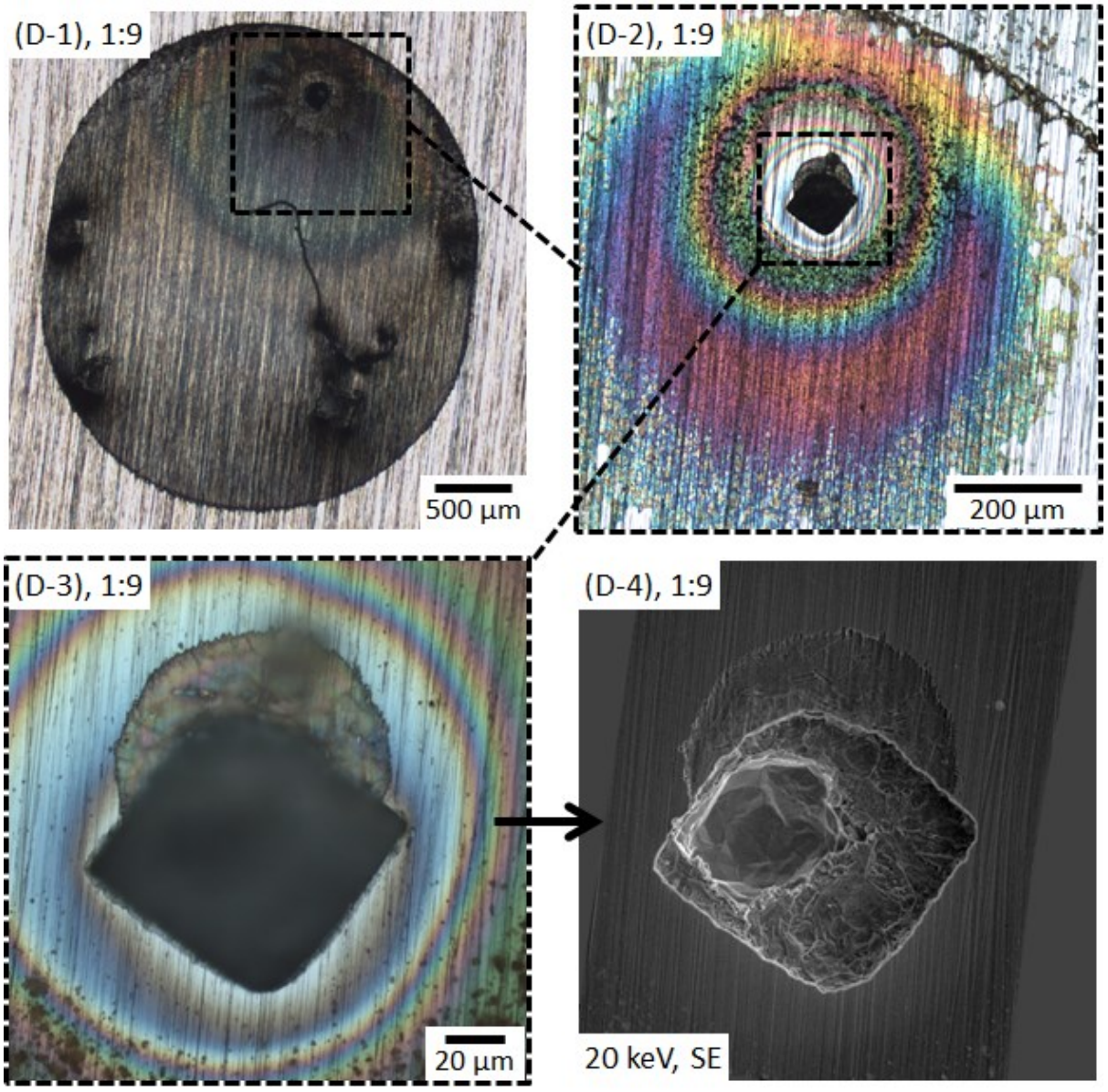

Figure 6-8 Example of a corrosion pit having developed under a 'small' precipitate. Binary NaCl + $MgCl_2$ 2 µL droplet (solution ratio 1:9) on 304L stainless steel, after 7 days exposure at 31 °C, 44 %rh. (D-1) immediately after exposure, (D-2, D-3) show (D-1) after sample has been washed in DI water, (D-4) shows SEM image of (D-3) after ultrasonic cleaning, 20 keV, secondary electron image.

Crevice-like attack was observed under mixed phase solutions where corrosion had occurred under 'larger' precipitates, typically >300 µm across. These corrosion sites were generally much wider than pits, but also shallower. The edges were often conformal to precipitate 'footprints', with the preference for continued attack remaining under the precipitate, rather than on metal more exposed to the bulk

solution. Microstructural etching was often observed in such sites. An example of such a site is given in Figure 6-9. It is important to note that not all corrosion sites occurring under a ‘larger’ precipitate continued to propagate in a crevice-like manner, with many having a small region of deeper, more localised attack within the area of shallow attack.

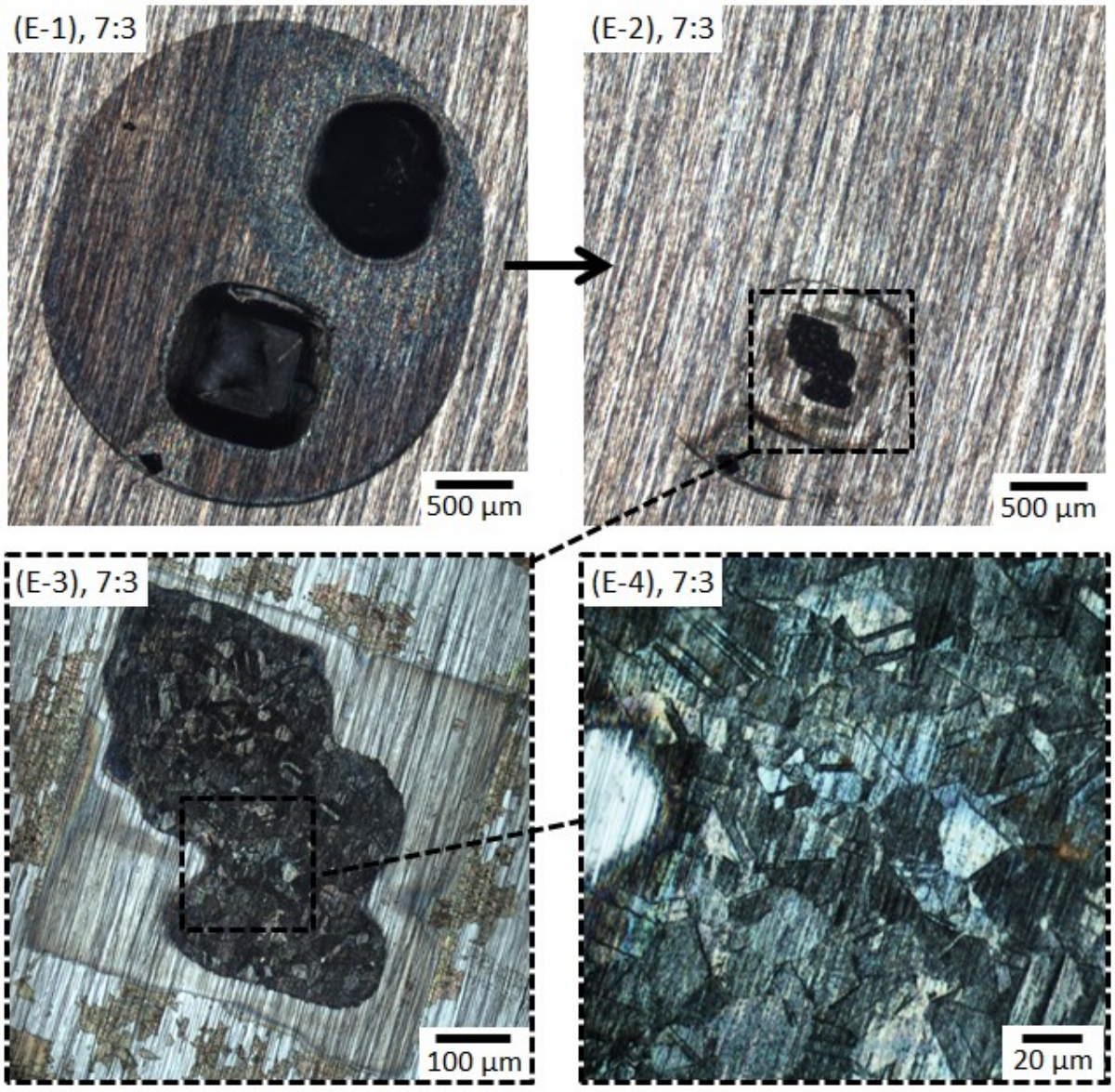

Figure 6-9 Example of a corrosion site having developed under a ‘large’ precipitate. Binary NaCl + $MgCl_2$ 2 µL droplet (solution ratio 7:3) on 304L stainless steel, after 7 days exposure at 31 °C, 44 %rh. (E-1) immediately after exposure, (E-2 – E-4) show (E-1) after sample has been washed in DI water.

The ‘crevice-like’ attack was also observed in tests which used chemically inert glass shards to mimic NaCl precipitates. An example is shown in Figure 6-10. Analysis of data from the in-situ monitoring of droplets containing glass shards (acting as precipitate analogues) showed that the region of shallow attack was the one formed initially, followed by the formation of deeper penetrations in a smaller region. Corrosion sites with morphology typical of that formed under ‘open conditions’ (i.e. no overlaying solids) were also observed within this set of droplets.

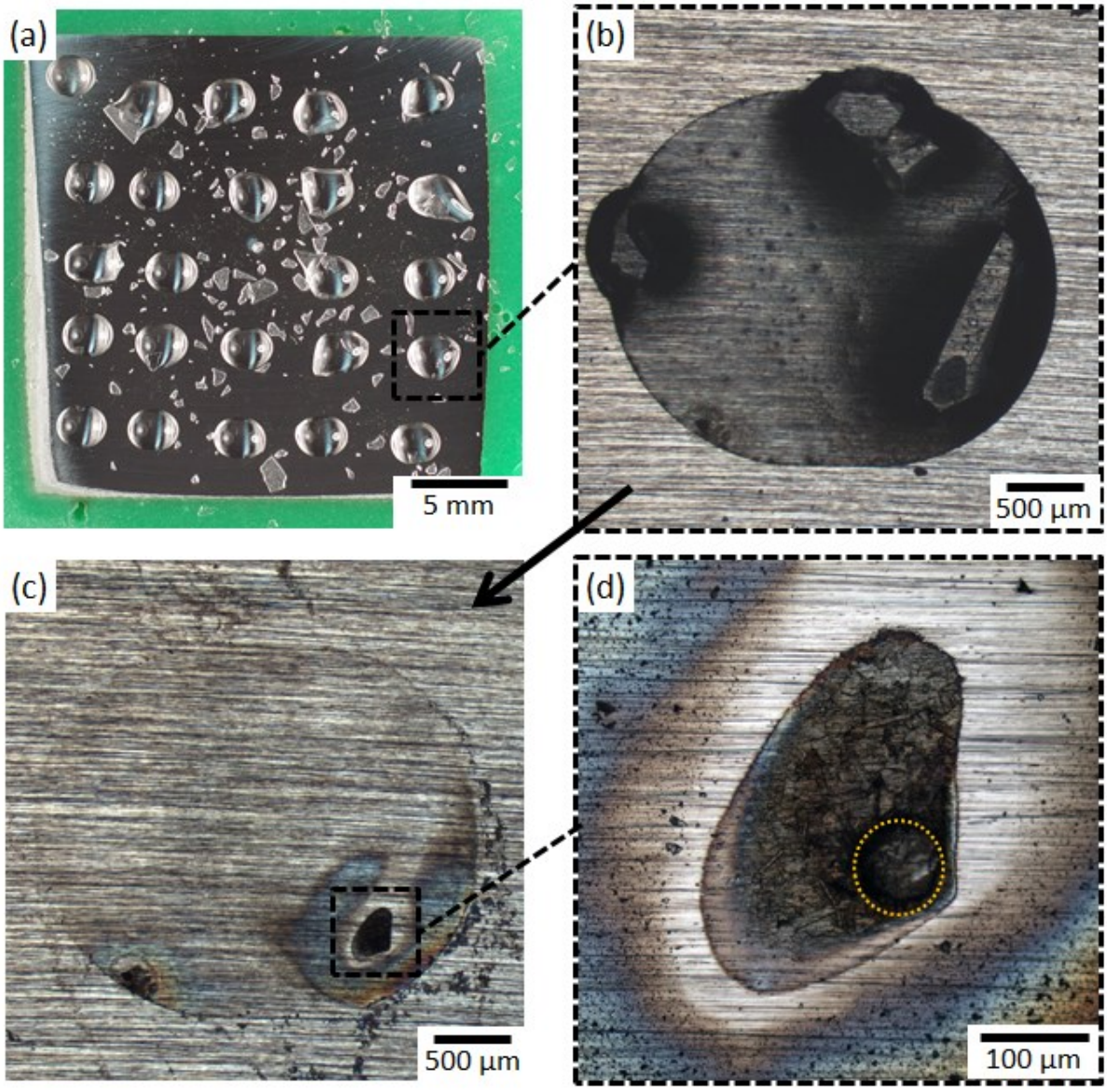

Figure 6-10 Example of 'crevice-like' attack occurring under a chemically inert glass shard, within a 2 µL droplet of $MgCl_2$ (0.35 mol/L, ~1000 µg/cm^2). 304L stainless steel exposed to 31 °C, 46 %rh for 4 days. (a) sample after deposition, before exposure. (b) after exposure. (c,d) show (b) after DI water wash. The approximate region of more localised, deeper attack has been highlighted in image (d) with a dotted circle.

6.4.3 Effect of precipitates on corrosion depth

Corrosion was observed in the majority of droplets, though the severity of the corrosion depended on the chemical composition of the droplet. No corrosion was observed under pure NaCl droplets, nor under pure DI water droplets, the latter having evaporated by the end of the exposure period. Qualitatively, the amount of

visible corrosion product (rust) was seen to decrease in binary solution droplets as the amount of NaCl increased, as can be seen in Figure 6-5.

The maximum depth of corrosion sites was observed to vary as a function of the droplet composition (Figure 6-11). The average maximum depth of corrosion sites that grew under pure $MgCl_2$ or $CaCl_2$ droplets (blue, filled, circular datapoints) was 58 ± 14 µm, with no significant difference between $MgCl_2$ and $CaCl_2$ droplets. Binary solutions (red, empty, square datapoints) with a low or moderate NaCl content (i.e. a ratio of 4:6 or lower) showed a similar maximum corrosion site depth as those found under pure droplets. However, at solution composition ratios of 5:5 and above for $CaCl_2$ containing droplets, and 7:3 and above for $MgCl_2$ containing droplets, the average maximum corrosion site depth decreased significantly from those found under control droplets. Given the relatively low statistical sampling for each solution ratio ($n \leq 5$) the authors do not rule out statistical variation in explaining this difference in critical composition ratios between $MgCl_2$ and $CaCl_2$ containing solutions.

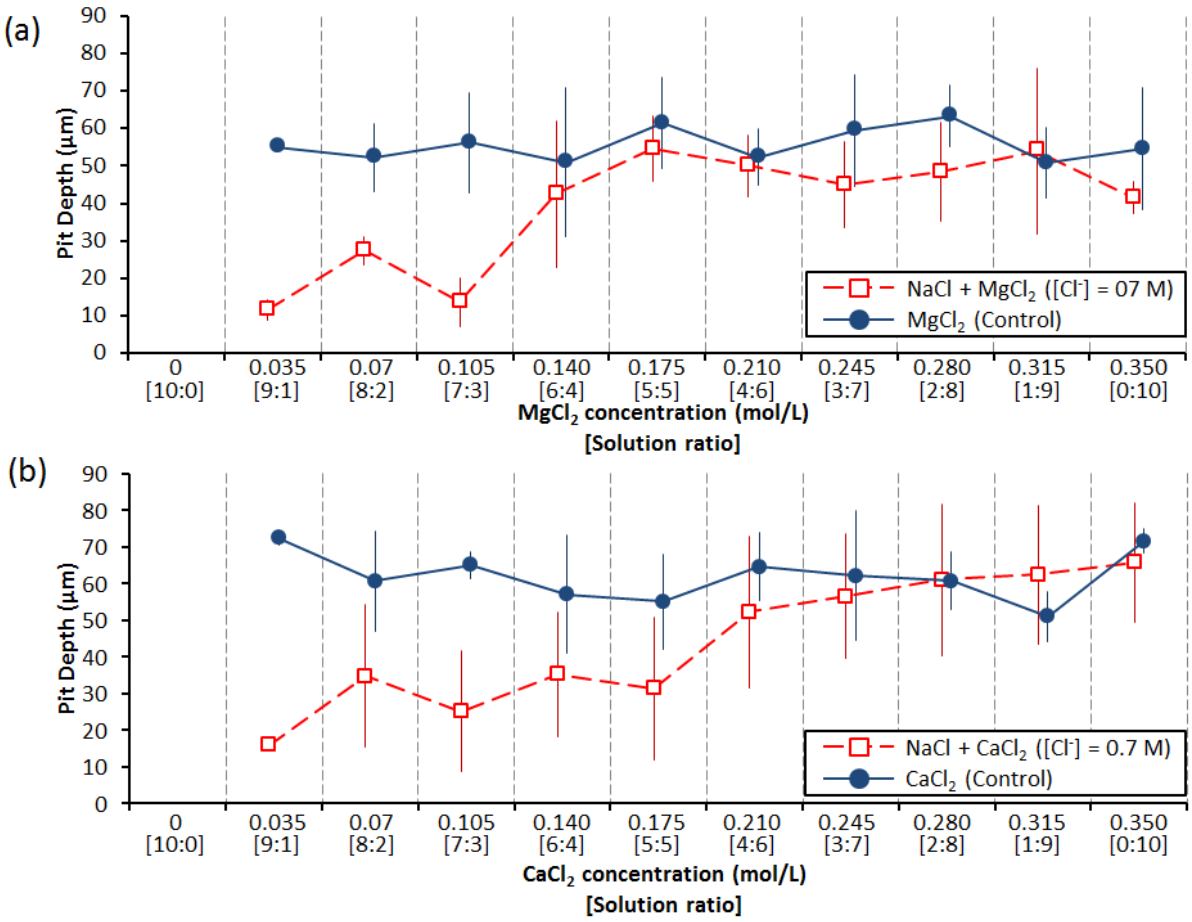

Figure 6-11 Average corrosion site depth for binary (NaCl + $MgCl_2$, NaCl + $CaCl_2$) and single salt ($MgCl_2$ or $CaCl_2$) solution mixtures. (a) shows data for $MgCl_2$ based solutions, and (b) shows data for $CaCl_2$ based solutions. For details on solution composition, see Table 2-1. Error bars indicate the standard deviation of the depth data.

Data on the 'pit mouth area' were also taken from this series of tests. In this case a viable 'pit' was defined as one which could be said to have grown under 'open geometry' i.e. not under crystals or other physical barriers (glass shards). Pits were excluded from the measurement when the propagation was judged to have been affected by NaCl precipitates, by precipitated corrosion product or by having grown at the edge of the droplet, where the constrained solution geometry may have affected growth. Furthermore pits were only selected if they were the only corrosion site within a droplet. It is worth noting that, due to the selection criteria, some solution

compositions were not represented in the measurement. The data from viable sites is shown in Figure 6-12.

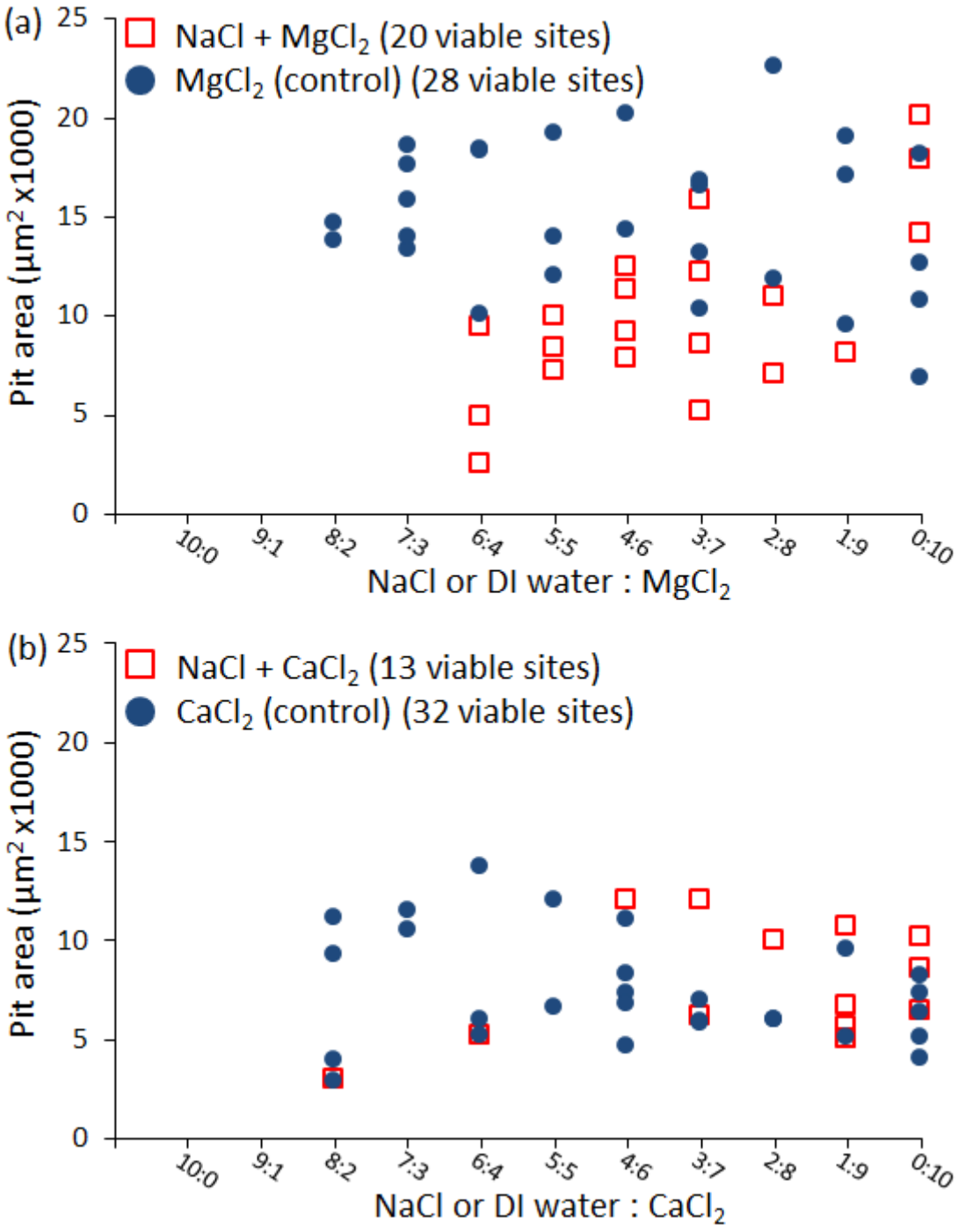

Figure 6-12 Area measurements of single corrosion pits which had developed under an 'open geometry', i.e. sites not obstructed by NaCl precipitates, corrosion product or droplet geometry. (a) $MgCl_2$ based solutions, (b) $CaCl_2$ based solutions.

For magnesium-based binary solutions (Figure 6-12(a)), although there is a fair amount of scatter in the data, it can be seen that an increasing level of sodium in the solution leads to a decrease in the pit mouth area, compared to pure $MgCl_2$ solutions. There is a lack of comparable ‘open-geometry’ pits for calcium based binary solutions with an increasing level of sodium (Figure 6-12(b)), though the available data do fit the same trend observed for magnesium based solutions. In general pits under magnesium solutions had a larger pit mouth area than those found under calcium based solutions.

The outcome of tests comparing the morphology of corrosion sites under NaCl precipitates and chemically inert glass shards are summarised in Figure 6-13. The fraction of droplets which led to significant (optically detectable) corrosion was highest for pure $MgCl_2$ solutions (about 80%), than for $MgCl_2$ + glass shards and $MgCl_2$ + NaCl precipitates (about 50% in both cases). In addition, lower values of the corrosion depth were observed in the case of solutions containing glass shards or NaCl compared with pure $MgCl_2$ solutions. There was some indication that pit mouth areas in droplets containing glass shards or precipitates were smaller than for pits under pure $MgCl_2$ solutions. Although the large scatter in the available data does not make this a significant observation on its own, when considered with the data already presented (Figure 6-12), it is reasonable to assume that the presence of precipitates or glass shards had an effect on the pit mouths of pits within droplets.

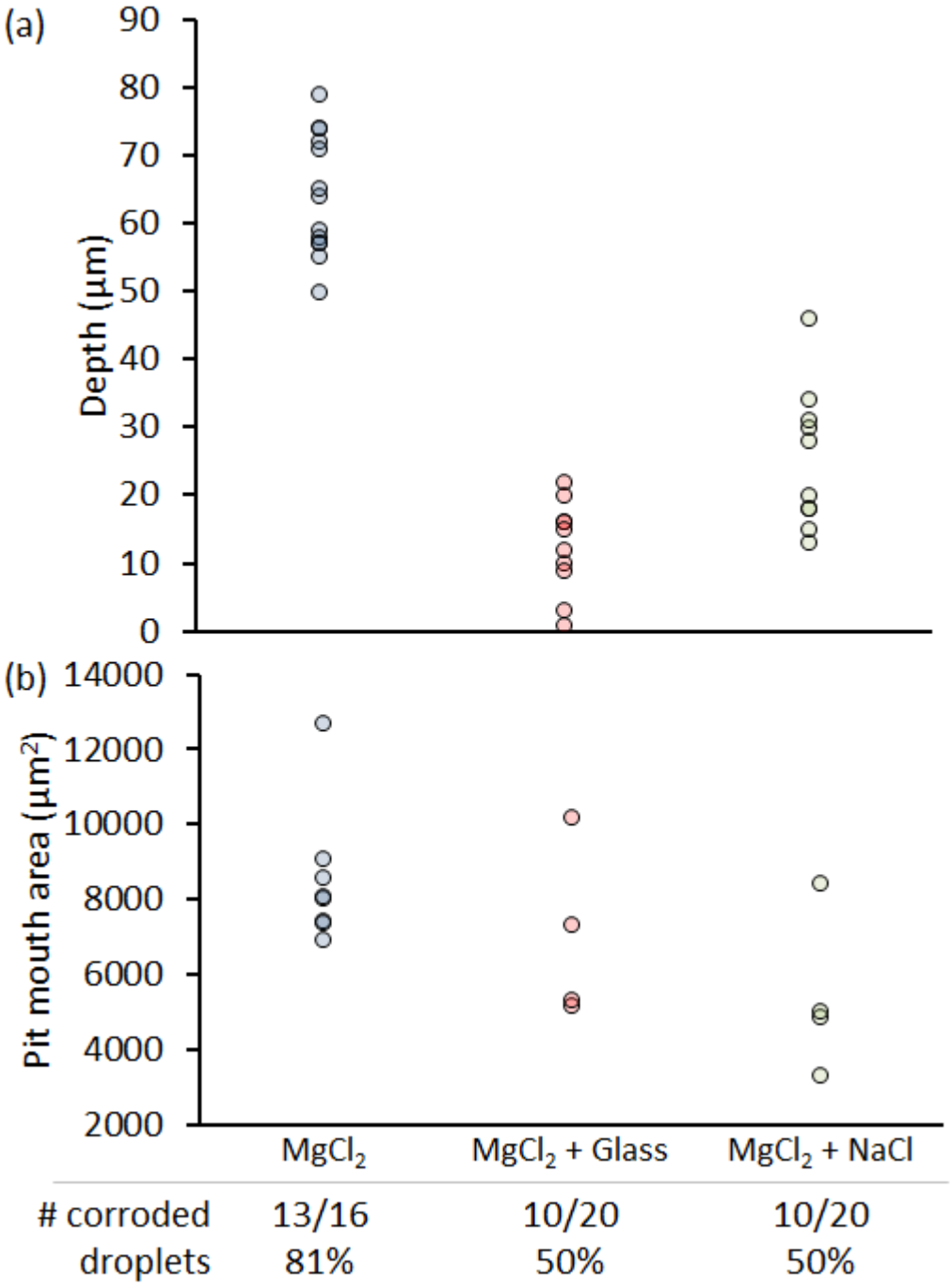

Figure 6-13 Comparison of (a) pit depths and (b) pit mouth areas of unobstructed pits, between pure $MgCl_2$ droplets, $MgCl_2$ droplets with glass shards, and droplets of binary NaCl + $MgCl_2$ solution. $MgCl_2$ concentration was the same for all deposited solutions. Droplet volume was 2 µL on 304L stainless steel, exposure environment was 31 °C, 43 %rh for 7 days. The overall percentage of droplets showing visible signs of corrosion in the tests is also reported under the x-axis.

6.5 Discussion

6.5.1 Precipitation

The precipitation behaviour of solutions containing a mixture of salts is more complex than the behaviour of each salt solution in isolation; the salt mixture may remain fully aqueous below the precipitation point of each salt.[16, 27] The exact behaviour depends on both the relative amounts of each salt, and the salts in question.

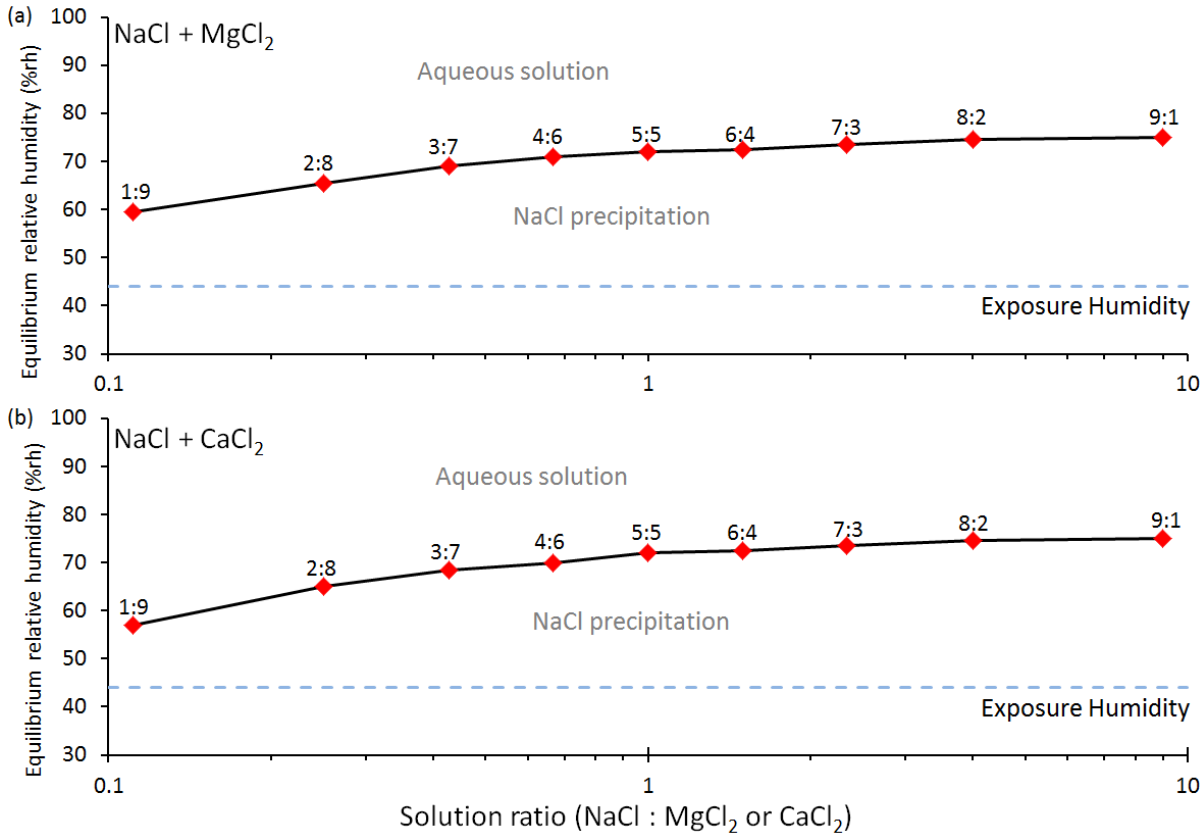

Figure 6-14 Thermodynamic calculations for (a) NaCl + $MgCl_2$ and (b) NaCl + $CaCl_2$ solutions, indicating expected precipitation conditions. Diamond markers correspond to the ratios investigated in this experiment. The approximate exposure humidity (44 %rh) is marked with the dashed line.

Figure 6-14 shows the calculated precipitation conditions for both salt mixtures (NaCl + $MgCl_2$ and $NaCl_2$ + $CaCl_2$). As the relative composition of NaCl decreases and the composition of either $MgCl_2$ or $CaCl_2$ increases (solution ratio decreases) the

humidity at which NaCl precipitation is expected decreases. For all tested solution ratios, however, NaCl precipitation is still expected to occur before reaching the exposure relative humidity of ~44 %rh. This agrees with observations of precipitates in all droplets which contained any amount of NaCl.

Further calculations suggest that in order for a mixed solution to remain fully aqueous at 44 %rh (i.e. for no precipitation to occur) the solution ratio would have to be ~1:50 and ~1:30 for NaCl + $MgCl_2$ and NaCl + $CaCl_2$, respectively. The relative levels of sodium found in current stores is generally much higher than these ratios, and so the presence of NaCl precipitates is not likely to be reduced significantly due to the presence of $MgCl_2$ and $CaCl_2$, though the presence of other salts which may have a significant effect must be highlighted.[2]

6.5.2 Morphology

Pits occurring under an ‘open geometry’, such as that shown in Figure 6-7, tended to grow into approximately circular shapes, e.g.[10, 11, 13]. The initial growth of corrosion sites is radial, due to the spread of metal ions and H^+ ions from hydrolysis.

Sites growing under a precipitate or other physical barrier, however, will have the movement of metal and H^+ ions altered; in these cases it is easier for the ions to accumulate under the barrier, as the physical barrier hinders ion diffusion and transport between the more dilute solution elsewhere and the metal and H^+ ions.[28] This explains why the corrosion sites found under precipitates often had angular edges which followed the edge of the overlaying barrier (e.g. Figure 6-9(E-3)), rather than more circular edges found in ‘open geometry’ pits (e.g. Figure 6-7(C-3)). Similar morphologies have been observed under tests using NaCl precipitates.[18] Experiments to mimic precipitates using silica-particulate layers did not show

corrosion sites to develop in quite the same manner, though pits growing to ‘uniform depth and uneven shape’ were reported.[20, 22] This is likely to be a result of the difference in particulate size and permeability between NaCl precipitates and silica-particulate layers, i.e. that the silica layer allows some diffusion between particulates.

As this angular morphology was observed under both NaCl precipitates and chemically inert glass shards it is concluded that the effect is primarily a physical one, and that no chemical effect of the NaCl precipitates was significant. As such these findings are likely to apply to a range of precipitates, not just NaCl. It was observed, however, that angular/crevice-like attack was more common under NaCl precipitates than under glass shards. Also when corrosion occurred close to the edge of a glass shard, the propagation of the corrosion site was less tightly conformal to the edge of the shard. It is proposed that the precipitating NaCl crystals develop in a much closer and conformal manner to the surface of the metal, leading to a tighter crevice than that provided by the glass shards, and so is more likely to lead to an accumulation of metal and H^+ ions, and also more likely to prevent O_2 access to the metal surface underneath. As such, while the use of glass shards as surrogates for NaCl precipitates has been useful in the current work, they are perhaps not a fully comparable analogue to artificially mimic precipitation within solutions in general.

6.5.3 Corrosion site propagation

6.5.3.1 Difference in depth

The depth of corrosion sites was seen to decrease as the amount of NaCl was increased in binary solutions (Figure 6-11). Control solutions which replaced the NaCl in solution with DI water, in order to maintain the different $MgCl_2$ or $CaCl_2$ deposition concentrations, showed no such trend, pointing to the presence of larger NaCl precipitates and the barrier to ionic transport they present, rather than the

simple loss in electrolyte volume and chloride content due to the reduction in $MgCl_2$ or $CaCl_2$ from these solutions, as the key factor affecting the development of corrosion.

Experiments with idealised 1D pits, or ‘lead-in-pencil’ pits, have shown that the growth rate of pits is limited by the diffusion of metal ions from the pit bottom to the pit mouth (from a point saturated with metal ions, to a point with a negligible metal ion concentration).[29] In more realistic 3D pits, this equates to the depth of the pit being limited by the diffusion of metal ions from the pit bottom.[30] In 1D pits the rate of growth is proportional to 1/x, where x is the depth of the pit, or the diffusion length.[31] The barrier over the corrosion site acts to increase the diffusion length, as the region where the amount of metal ions is negligible is now around the edge of the barrier rather than at the ‘mouth’ of the corrosion site. As such one would expect the diffusion of metal ions from a site under such a barrier to be slower than for a site not under a barrier, and so for the site under the barrier to grow in depth more slowly.

6.5.3.2 Pit mouth area

Pits which grew under open geometry but shared a droplet with precipitates were seen to have a decreased pit mouth area compared to pits which did not share droplet with precipitates. This observation has also been reported by Guo *et al.*.[18] Ghahari *et al.* showed that the area of the pit mouth was controlled by the interfacial potential at the pitting site.[30] Generally the two main factors influencing the interfacial potential are the reactions at the cathode and anode, and the IR drop in solution between the cathode and anode. The presence of precipitates may affect both of these factors:

1. IR drop in solution: The presence of physical barriers within the electrolyte will mean that the migration of charged species is more difficult than through unobstructed solution, thus raising the electrical resistance of the electrolyte. Furthermore, capillary action of the electrolyte on the precipitates is likely to cause an inhomogeneous distribution of the electrolyte, compared to droplets without either glass shards or NaCl crystals. This has been observed by Guo *et al.*, and is shown schematically in Figure 6-15.[18] This will lead to areas where the electrolyte layer is thinner, and so more resistive to ion movement. Areas around precipitates may have a thicker electrolyte layer than elsewhere, meaning that locally ion migration is easier, but these areas are small compared to the total area of the droplet.

2. Reaction rate of cathode: The reaction rate at the cathode depends on the availability of O_2 at the metal surface. The physical barrier created by the precipitates blocks O_2 access to the metal below them, thus reducing the area able to be involved in the cathodic reaction.[21] This will decrease the available potential in the system, leading to a lower interfacial potential at the pit mouth. On the other hand, the thinning of the electrolyte layer due to capillary action (Figure 6-15) means that it may be easier for dissolved O_2 to reach the metal surface as the diffusion pathway decreases. The importance of this effect, however, may be limited at low RH (very thin moisture layers), since below solution thicknesses of ~20 µm O_2 availability becomes limited by the sorption rate from the atmosphere rather than by the diffusion rate in the electrolyte.[10]

These two factors have been previously predicted through modelling work conducted by Agarwal *et al.* in systems where particulates were present in the electrolyte solution and on the cathode.[19]

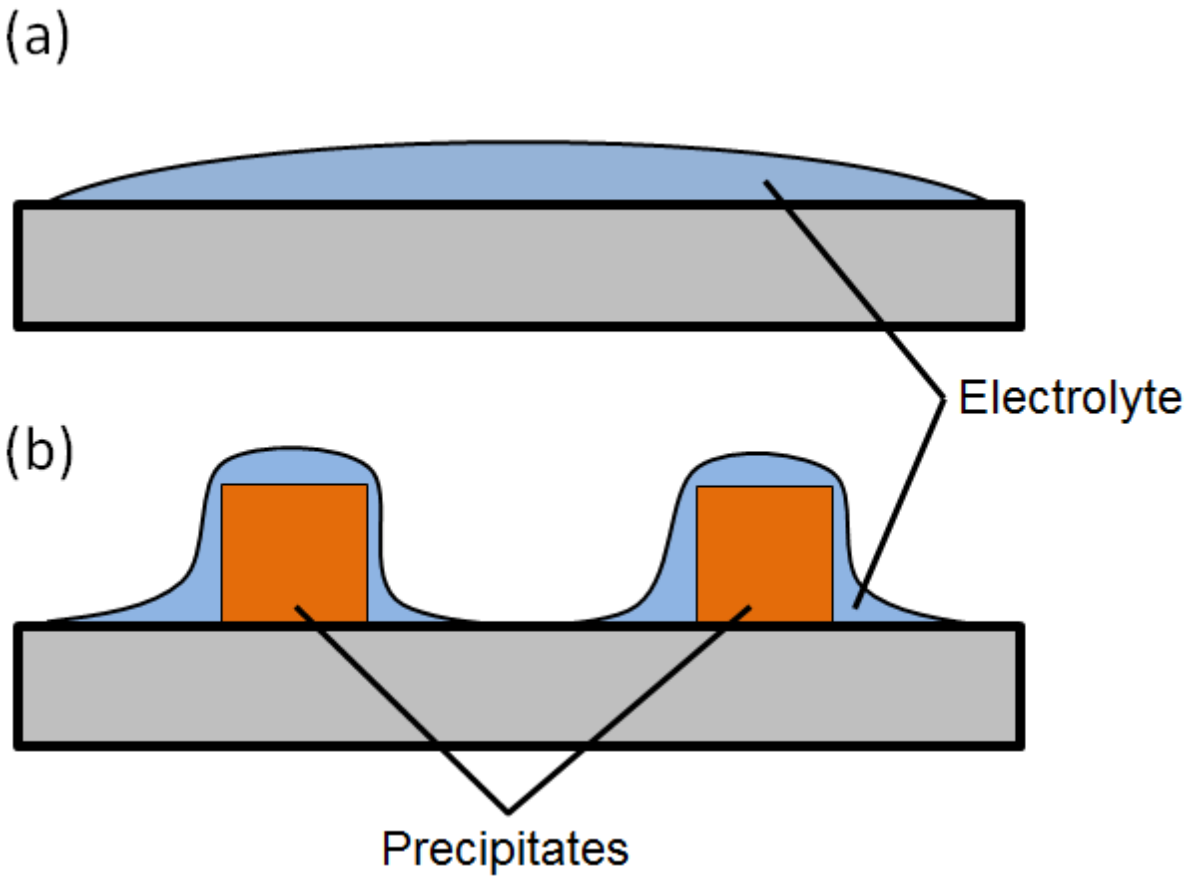

Figure 6-15 Illustration of the distribution of electrolyte (a) without and (b) with precipitates/glass shards. Note that the volume of liquid electrolyte in (a) and (b) are the same.

6.6 Conclusions

The behaviour of mixed chloride solutions (NaCl + $MgCl_2$ and NaCl + $CaCl_2$) on the atmospheric corrosion of 304L stainless steel under relatively low RH (~44 %rh) was investigated. Their behaviour was compared with that of both solutions containing glass shards, to simulate insoluble phases, and single salt solutions containing no precipitates, but decreasing amounts of either $MgCl_2$ or $CaCl_2$ to mimic the loss of chloride from solution during precipitation. The presence of phases which had limited

solubility (NaCl precipitates) or were insoluble (glass shards) at the humidity tested within a liquid electrolyte led to less penetrating corrosion (shallower corrosion sites, narrower unobstructed pit mouths, wider areas of superficial attack) than that found with bare $MgCl_2$ and $CaCl_2$ solutions. Under realistic conditions within ILW stores or an operational GDF, where NaCl is expected provide the main source of chloride and where the presence of insoluble phases (e.g. sulphates and carbonates) is expected, the results of this study indicate that corrosion is likely to be less penetrating than that observed in laboratory tests using only aqueous electrolytes.

In general, mixed phase electrolytes have been shown to result in different corrosion behaviour compared with single phase electrolytes, so the simultaneous presence of different types of chlorides, and indeed other salts, should not be overlooked when considering atmospheric corrosion systems. More work, however, is required to explore and contextualise the likely behaviour of stainless steel in the presence of mixed chlorides in a range of relative humidities, deposit densities, and other environmental variables (e.g. temperature and presence of more complex surface chemistries). More specifically conclusions of this work are as follows:

- Corrosion sites unobstructed by NaCl precipitates or glass shards were in the form of pits with round mouths, as reported elsewhere for both $MgCl_2$ and $CaCl_2$ containing droplets.
- Corrosion sites under NaCl precipitates tended to progress in one of two ways. For smaller crystals (~100 µm) pit mouths were observed to grow with angular edges, suggesting conformal growth with the edge of the crystal. Under larger crystals, shallow yet wide-spread etching attack was observed, often associated with a smaller region of deeper attack.

- NaCl precipitates were shown to reduce the depth of corrosion sites above given solution ratio. This was ~7:3 for NaCl + $MgCl_2$ solutions, and ~5:5 for NaCl + $CaCl_2$ solutions.
- The presence of precipitates within droplets caused pits growing in the droplet (but not under the precipitate) to have narrower pit mouths than pits in precipitate-free control droplets.
- The observed phenomena attributed to NaCl precipitates (conformal growth, shallower sites, narrower pit mouths) were to a large extent replicated with chemically inert glass shards, indicating that physical effects play a major role in the behaviour observed.
- The observations above may be explained by the fact that the physical barrier provided by precipitates and insoluble phases created a diffusion barrier to both dissolved oxygen, and to metal ion migration, which likely led to a decrease in the cathodic reaction, an increased IR-drop between cathode and anode, and a longer diffusion length for metal ions leaving the anode.

6.7 Acknowledgements

The authors would like to thank Liya Guo (Imperial College, London) for helpful discussions, as well as the University of Birmingham Centre for Electron Microscopy for the use of their equipment. Angus Cook is funded by EPSRC grant EP/I036397/1, and Radioactive Waste Management Ltd. contract NPO004411A-EPS02.

6.8 References

1. Nuclear Decomissioning Authority, *Geological Disposal: An overview of the generic Disposal System Safety Case*, Radioactive Waste Management Limited, 2010.

2. Padovani, C., R.J. Winsley, N.R. Smart, P.A.H. Fennell, C. Harris, and K. Christie, *Corrosion Control of Stainless Steels in Indoor Atmospheres—Practical Experience (Part 2).* Corrosion, 2015. **71**(5): p. 646-666.

3. Shoji, S. and N. Ohnaka, *Effects of Relative Humidity and Kinds of Chlorides on Atmospheric Stress Corrosion Cracking of Stainless Steels at Room Temperature.* CORROSION ENGINEERING, 1989. **38**(2): p. 92-97.

4. Prosek, T., A. Iversen, C. Taxen, and D. Thierry, *Low-Temperature Stress Corrosion Cracking of Stainless Steels in the Atmosphere in the Presence of Chloride Deposits.* Corrosion, 2009. **65**(2): p. 105-117.

5. Prosek, T., A. Le Gac, D. Thierry, S. Le Manchet, C. Lojewski, A. Fanica, E. Johansson, C. Canderyd, F. Dupoiron, T. Snauwaert, F. Maas, and B. Droesbeke, *Low-Temperature Stress Corrosion Cracking of Austenitic and Duplex Stainless Steels Under Chloride Deposits.* Corrosion, 2014. **70**(10): p. 1052-1063.

6. Örnek, C., X. Zhong, and D.L. Engelberg, *Low-Temperature Environmentally Assisted Cracking of Grade 2205 Duplex Stainless Steel Beneath a MgCl2:FeCl3 Salt Droplet.* CORROSION, 2016. **72**(3): p. 384-399.

7. Cruz, R.P.V., A. Nishikata, and T. Tsuru, *Pitting corrosion mechanism of stainless steels under wet-dry exposure in chloride-containing environments.* Corrosion Science, 1998. **40**(1): p. 125-139.

8. Hastuty, S., A. Nishikata, and T. Tsuru, *Pitting corrosion of Type 430 stainless steel under chloride solution droplet.* Corrosion Science, 2010. **52**(6): p. 2035-2043.

9. Tsutsumi, Y., A. Nishikata, and T. Tsuru, *Initial Stage of Pitting Corrosion of Type 304 Stainless Steel under Thin Electrolyte Layers Containing Chloride Ions.* Journal of The Electrochemical Society, 2005. **152**(9): p. B358-B363.

10. Tsutsumi, Y., A. Nishikata, and T. Tsuru, *Pitting corrosion mechanism of Type 304 stainless steel under a droplet of chloride solutions.* Corrosion Science, 2007. **49**(3): p. 1394-1407.

11. Street, S.R., N. Mi, A.J.M.C. Cook, H.B. Mohammed-Ali, L. Guo, T. Rayment, and A.J. Davenport, *Atmospheric pitting corrosion of 304L stainless steel: the role of highly concentrated chloride solutions.* Faraday Discussions, 2015. **180**(0): p. 251-265.

12. Padovani, C., O.E. Albores-Silva, and E.A. Charles, *Corrosion Control of Stainless Steels in Indoor Atmospheres—Laboratory Measurements Under MgCl2 Deposits at Constant Relative Humidity (Part 1).* Corrosion, 2015. **71**(3): p. 292-304.

13. Maier, B. and G.S. Frankel, *Pitting Corrosion of Bare Stainless Steel 304 under Chloride Solution Droplets.* Journal of the Electrochemical Society, 2010. **157**(10): p. C302-C312.

14. Cook, A.B., B. Gu, S.B. Lyon, R.C. Newman, and D.L. Engelberg, *Towards a more Realistic Experimental Protocol for the Study of Atmospheric Chloride-Induced Stress Corrosion Cracking in Intermediate Level Radioactive Waste Container Materials.* MRS Proceedings, 2014. **1665**: p. 225-230.

15. Gunther, M., N.P.C. Stevens, G. McFiggans, and A.B. Cook, *Investigation into composition and deposition of artificially produced marine aerosols on austenitic stainless steels.* Corrosion Engineering Science and Technology, 2014. **49**(6): p. 509-513.

16. Cook, A.J.M.C., C. Padovani, and A.J. Davenport, *Effect of Nitrate and Sulfate on Atmospheric Corrosion of 304L and 316L Stainless Steels.* Journal of The Electrochemical Society, 2017. **164**(4): p. C148-C163.

17. Harris, C., *Investigation Into the Atmospheric Corrosion of Stainless Steel ILW containers – Tests With Salt Mixtures and in Conditions of Cyclic Relative Humidity*, AMEC, 2016, 17391/TR/0009-4

18. Guo, L., *Atmospheric localised corrosion of type 304 austenitic stainless steels* [PhD thesis]. Birmingham (UK): University of Birmingham; 2016

19. Agarwal, A.S., U. Landau, and J.H. Payer, *Modeling Particulates Effects on the Cathode Current Capacity in Crevice Corrosion.* Journal of The Electrochemical Society, 2008. **155**(5): p. C269-C278.

20. Tada, E. and G.S. Frankel, *Effects of particulate silica coatings on localized corrosion behavior of AISI 304SS under atmospheric corrosion conditions.* Journal of the Electrochemical Society, 2007. **154**(6): p. C318-C325.

21. Tada, E. and G.S. Frankel, *Electrochemical Behavior of AISI 304SS with Particulate Silica Coating in 0.1 M NaCl.* Journal of The Electrochemical Society, 2007. **154**(6): p. C312-C317.

22. Maier, B. and G.S. Frankel, *Pitting Corrosion of Silica-Coated Type 304 Stainless Steel Under Thin Electrolyte Layers.* CORROSION, 2011. **67**(3): p. 035004-1-035004-10.

23. Cook, A.B., S.B. Lyon, N.P.C. Stevens, R.C. Newman, M. Gunther, G. McFiggans, and D.L. Engelberg, *Under-Deposit Chloride-Induced Stress Corrosion Cracking in Austenitic Stainless Steels: Aspects Associated with Deposit Type, Size and Composition.* ECS Transactions, 2014. **58**(29): p. 25-39.

24. ASTM. E104-02(2007) "Standard Practice for Maintaining Constant Relative Humidity by Means of Aqueous Solutions" [cited 08/06/2011]. Available from: www.astm.org

25. Gough, R.V., V.F. Chevrier, and M.A. Tolbert, *Formation of liquid water at low temperatures via the deliquescence of calcium chloride: Implications for Antarctica and Mars.* Planetary and Space Science, 2016. **131**: p. 79-87.

26. J. Schindelin, I.A.-C., E. Frise, V. Kaynig, M. Longair, T. Pietzsch, S. Preibisch, C. Rueden, S. Saalfeld, B. Schmid, J. Tinevez, D.J. White, V. Hartenstein, K. Eliceiri, P. Tomancak, A. Cardona, *Fiji: an open-source platform for biological-image analysis.* Nature Methods, 2012. **9**(7): p. 7.

27. Fraser King, P.R., Claire Watson, Sarah Watson, Richard Metcalfe, Jenny Burrow, *The Atmospheric Corrosion of Stainless Steel in Stores (ACSIS) Model*, Radioactive Waste Management Limited, 2016, 17391-TR-010

28. Nishimoto, M., J. Ogawa, I. Muto, Y. Sugawara, and N. Hara, *Simultaneous visualization of pH and Cl− distributions inside the crevice of stainless steel.* Corrosion Science, 2016. **106**: p. 298-302.

29. Tester, J.W. and H.S. Isaacs, *Diffusional Effects In Simulated Localized Corrosion.* Journal of the Electrochemical Society, 1975. **122**(11): p. 1438-1445.

30. Ghahari, M., D. Krouse, N. Laycock, T. Rayment, C. Padovani, M. Stampanoni, F. Marone, R. Mokso, and A.J. Davenport, *Synchrotron X-ray radiography studies of pitting corrosion of stainless steel: Extraction of pit propagation parameters.* Corrosion Science, 2015. **100**: p. 23-35.

31. Isaacs, H.S., *Behavior Of Resistive Layers In Localized Corrosion Of Stainless-Steel.* Journal of the Electrochemical Society, 1973. **120**(11): p. 1456-1462.

7 EFFECT OF NITRATE AND SULFATE ON ATMOSPHERIC CORROSION OF 304L AND 316L STAINLESS STEELS

Preface

The following chapter consists of a paper published in the Journal of the Electrochemical Society. The formatting, figure and table numbering and pagination are as they appeared in the published work. The full reference is given below:

Cook, A.J.M.C., C. Padovani, and A.J. Davenport, Effect of Nitrate and Sulfate on Atmospheric Corrosion of 304L and 316L Stainless Steels. Journal of The Electrochemical Society, 2017. 164(4): p. C148-C163.

Angus Cook is the lead author of the following paper, having conducted the entirety of the experimental and write-up work. Alison Davenport and Cristiano Padovani provided editorial advice on the structure and clarity of the text and figures.

Effect of Nitrate and Sulfate on Atmospheric Corrosion of 304L and 316L Stainless Steels

Angus J. M. C. Cook,[a] Cristiano Padovani,[b] and Alison J. Davenport[a,*,z]

[a]*School of Metallurgy and Materials, University of Birmingham, Edgbaston, Birmingham, West Midlands B15 2TT, United Kingdom*
[b]*Radioactive Waste Management Ltd., Curie Avenue, Harwell, Oxfordshire OX11 0RH, United Kingdom*

The effects of nitrate and sulfate salts on the chloride-induced atmospheric pitting corrosion of 304L and 316L stainless steel was investigated through automated deposition of droplets of magnesium and calcium salts. Nitrate was found to inhibit pitting under magnesium salt droplets when the ratio between the deposition density of nitrate anions and chloride anions was above a critical value, which was the same for both 304L and 316L. This critical ratio was found to decrease with increasing humidity. Sulfate was also observed to inhibit pitting for $MgCl_2 + MgSO_4$ mixtures, but only at higher humidities. Sulfate did not show any inhibition for $CaCl_2 + CaSO_4$ mixtures, an effect attributed to the low solubility of $CaSO_4$. At low relative humidities, precipitation of the inhibiting salt was observed, leading in some cases to crevice-like corrosion under salt crystals. The pitting behavior was explained in terms of the thermodynamic behavior of concentrated solutions.
 [DOI: 10.1149/2.0921704jes]

Manuscript submitted August 5, 2016; revised manuscript received February 1, 2017. Published February 9, 2017.

In the UK, stainless steel is used to package intermediate level radioactive waste, ILW, which is characterized by relatively large volumes and variable levels of radioactivity.[1] Whatever the strategic approach to its management[c], most ILW has been packaged in thin-walled containers (2.3–6 mm thick, typically grades 304L or 316L, UNS S304003 and UNS S316003, respectively) and will undergo long periods of exposure to atmospheric conditions, either in surface or underground facilities prior to permanent disposal.

During these periods, waste containers will be exposed to regimes of varying temperature and relative humidity (RH), as well as to chloride-containing salts arising from aerosol deposition. As a result, it is important to identify suitable storage conditions to ensure durability of waste containers, in particular to avoid conditions associated with the development of pitting and, even more importantly, atmospherically-induced stress corrosion cracking (AISCC).[2,3]

Monitoring of ILW storage facilities and other indoor locations considered broadly representative of ILW stores suggests that temperature and relative humidity, which are key parameters in the development of atmospheric corrosion, are expected to vary between ∼0–30°C and ∼30–100% RH, respectively.[3] Ionic chemical species deposited on surfaces after relatively long periods of indoor storage found in swab tests in a variety of real storage facilities include calcium, magnesium, sodium, potassium, chloride, nitrate and sulfate ions. Inside the storage buildings surveyed, chloride deposition densities were found to be below ∼20 $\mu g/cm^2$, with deposition rates of the order of 1 $\mu g/cm^2$ per year estimated.[3] With such a deposition rate, the chloride deposition density could increase to ∼100 $\mu g/cm^2$ over the next century.

In atmospheric conditions relevant to this work, a number of tests have been carried out to evaluate the atmospheric pitting corrosion of stainless steel in the presence of chloride deposits (e.g., Refs. 2, 4–6) but none of these have been carried out in the presence of ionic species other than chloride. In particular, anions such as nitrate and sulfate, which are likely to be present in amounts comparable to chlorides in waste stores,[3] have been shown to inhibit corrosion processes in bulk solutions above specific critical ratios to the chloride ion.[7–17]

The concentration of $MgCl_2$ in equilibrium with an ambient RH of 90% is ∼1.5 M, and increases with decreasing humidity.[18] Inhibition ratios found in bulk experiments (typically at concentrations below 1 M) may not be representative of atmospheric conditions.[19] For example, the relative humidity in typical stores is expected to vary between ∼30% and ∼100% RH (equivalent to $MgCl_2$ at saturation (∼5 M) and 'infinite dilution', respectively).[20] Furthermore, atmospheric corrosion differs from full immersion corrosion in a number of other ways. The thin electrolyte layer both allows easier oxygen access to the metal surface, and may limit ion migration and current flow through the electrolyte. Conversely, the increasing solution concentration decreases the solubility of O_2, which will decrease the access of oxygen to the metal surface. Furthermore, the area available for the cathodic reaction is limited by the coverage of the electrolyte (i.e. the footprint of the droplet).[20,21]

Methods employed to simulate atmospheric corrosion conditions used in previous studies include the formation of extended thin-films of electrolyte,[22–24] ink-jet printing of salt layers that deliquesced to form droplets,[21,25,26] and direct droplet deposition.[2,20,27–29] The current work uses automated deposition of combinatorial arrays of droplets to identify inhibiting nitrate:chloride deposition density ratios (NDD:CDD) and sulfate:chloride deposition density ratios (SDD:CDD) for both 304L and 316L stainless steels, at ∼31°C and several fixed exposure humidities.

The corrosion that develops in stores is likely to be a result of deliquescence of a salt layer that accumulates over time via aerosol deposition. However, in the current work, deposition of salt droplets was selected as a simple reproducible method for generating a wide range of different solution chemistries on a single metal plate. The findings from the current work are likely to be conservative, since initiation takes place under a relatively large droplet with a correspondingly large cathodic area compared with the smaller, patchy and disconnected areas of electrolyte that are likely to form in the early stages of aerosol deposition.

The aim of this study is to evaluate the inhibiting effects under low temperature atmospheric conditions, representative of storage environments for radioactive wastes as well as many other indoor facilities.[3] Beyond helping to build a comprehensive picture of the key factors controlling long-term atmospheric corrosion processes, this information is being used in the development of a corrosion prediction model.[30]

Experimental

Materials and surface preparation.—Type 304L and Type 316L stainless steel plate (UNS S30403 and UNS S316003, respectively) with 3 mm thickness was provided by Aperam France in a cold rolled and solution annealed (1040–1100°C, forced air cooling) condition.

*Electrochemical Society Member.
[z]E-mail: a.davenport@bham.ac.uk
[c]The strategy for the management of higher activity radioactive waste in England, Wales and Northern Ireland is currently permanent disposal in a geological disposal facility (GDF). After interim storage in surface facilities, radioactive wastes will be emplaced in a GDF which will then be backfilled and sealed. In Scotland, the current strategy for the management of higher activity radioactive wastes is long-term storage and near-surface disposal.[2]

Table I. Cast analysis provided by foundry for 304L and 316L stainless steel plate.

	Chemical Analysis (wt-%)											
Alloy	*C*	*Si*	*Mn*	*Ni*	*Cr*	*Mo*	*Ti*	*N*	*S*	*P*	*Co*	*Fe*
304L	0.023	0.44	1.46	8.00	18.08	–	–	0.072	0.0033	0.032	0.171	Bal.
316L	0.024	0.38	1.25	10.04	16.55	2.000	–	0.044	0.0032	0.034	0.189	Bal.

A cast analysis is provided in Table I. Plate was cut to appropriate size (either 30 × 50 or 25 × 75 mm) and mounted to aid handling. The samples were wet-ground to P800 grit using SiC discs such that the rolling direction of the alloy was perpendicular to the final grinding direction.

Samples were then ultrasonically cleaned in and then rinsed with >15 MΩ · cm de-ionized (DI) water (Millipore), dried under an air-stream, and left in a sheltered, ambient lab environment for 24 hours before deposition (20–26°C, 18–54% RH). It should be noted that the surface finish used in the current work is highly reproducible, but not identical to the surface finish of ILW containers, which are typically wet bead blasted.[31]

Solution arrays.—Stock solutions of $MgCl_2$, $CaCl_2$, $Mg(NO_3)_2$, $CaSO_4$ and $MgSO_4$ were made using ACS grade reagents: $MgCl_2 \cdot 6H_2O$, $CaCl_2 \cdot 2H_2O$, $Mg(NO_3)_2 \cdot 6H_2O$, $CaSO_4 \cdot 2H_2O$ (Sigma-Aldrich) and $MgSO_4 \cdot 7H_2O$ (Arcos Organics) and >15 MΩ · cm DI water (Millipore). Due to the low solubility of $CaSO_4$, a suspension was maintained using a magnetic stirrer during solution handling. Stock solutions were described in terms of anion concentration, and were approximately 1.0, 0.6 and 0.4 mol/L for chloride, nitrate and sulfate (apart from $CaSO_4$) solutions, respectively. The $CaSO_4$ stock solution was made to 0.26 mol/L.

Arrays of solutions with combinatorial ratios of anions were prepared from the stock solutions by a MultiPROBE II Ex automated liquid handler (Packard Biosciences) via serial dilution. Solutions were stored in well plates before deposition.

Two types of arrays were used:

- The first approach ('logarithmic' tests) varied both the chloride deposition density (CDD, mass per unit area of Cl^-, between 8.5–850 μg/cm^2) and either the nitrate or sulfate deposition densities (NDD, mass per unit area of NO_3^- or SDD, mass per unit area of SO_4^{2-}, between 0–850 μg/cm^2) 'logarithmically' across the same plate, with multiple plates used to replicate experiments (Figure 1a).
- The second ('linear' tests) consisted of a fixed CDD (~1200 μg/cm^2) across an entire plate, with linearly increasing NDD or SDD across the width of the plate. In these arrays, the NDD or SDD was varied linearly between 0 μg/cm^2 and an upper value chosen for each experiment (Figure 1b). It should be noted that the CDD chosen for these linear tests (~1200 μg/cm^2) is significantly higher than the range of CDDs expected in a store environment (up to ~100 μg/cm^2).[3] This was done in order to provide an aggressive environment, so that any inhibiting effects could be clearly identified.

For logarithmic arrays both 304L and 316L plates were investigated. For linear arrays only a single alloy was used for each exposure condition (salt type, humidity).

When evaluating inhibitor/chloride deposition densities (IDD:CDD) from the logarithmic and linear variation tests, it should be noted that the logarithmic variation tests provide better statistics (≥12 trials for IDD:CDD between 10–0.1) but larger increments (logarithmic IDD:CDD increments of 0.3, 1, 3 etc.), while the linear variation tests provide poorer statistics (4 trials per condition) but finer increments (linear NDD:CDD increments of ~0.17).

Additionally, pure $MgCl_2$ droplets (i.e. droplets with no inhibiting salt additions) were used as control tests to assess the aggressiveness of the exposure conditions and provide a baseline for comparison with the tests containing salt mixtures. These control droplets covered the same range of CDDs as tested in the mixed salt systems (i.e. 0.85–1200 μg/cm^2)

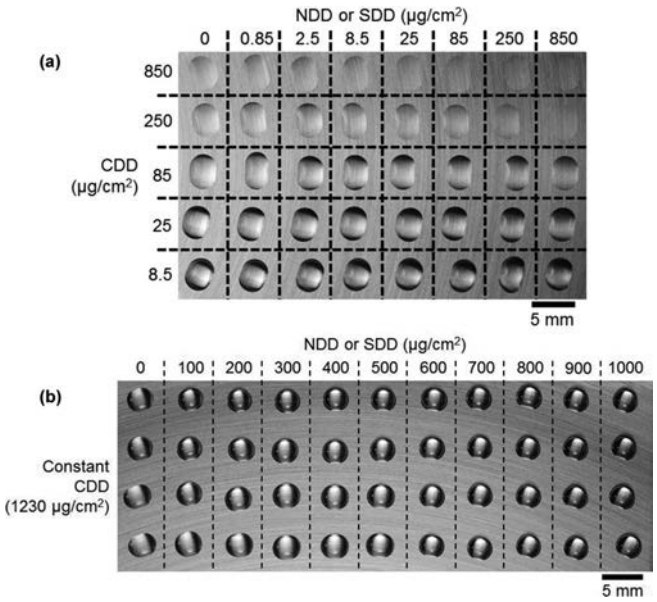

Figure 1. Array design for (a) logarithmic variation (3.3 mm diameter droplets) of both nitrate or sulfate deposition density (NDD or SDD) and chloride deposition density (CDD), (b) Linear variation (3.0 mm diameter droplets) of nitrate or sulfate deposition density (NDD or SDD) with chloride deposition density (CDD) kept constant. Images acquired after deposition, before exposure period. Note that values in linear variation in NDD or SDD on (b) are given as examples. Actual values are indicated with relevant experiments.

Droplet deposition and exposure.—Deposition of droplet arrays was automated using the MultiPROBE II Ex. Droplet volume at deposition was 4 μL unless otherwise stated, and droplets are referred to by their deposition volume in the text. On logarithmically-varying tests, freshly-deposited droplets had an area of 8.4 ± 0.3 mm^2. On linearly varying tests freshly-deposited droplets were measured to give an area of 7.1 ± 0.4 mm^2. It is thought that differences in deposited solution concentration are the result of different spreading behavior immediately after deposition, with the higher concentration solutions (used in the linear variation tests) showing lower spreading. Comparisons between photos taken after deposition, and photos taken after exposure showed no evidence of spreading during exposure. Droplets were typically elliptical, extending preferentially along the grinding lines with an average aspect ratio of ~1.2. The droplet diameters quoted below are the diameter of a circular droplet with the same mean droplet area. For 4 μL droplets with a mean area of 8.4 ± 0.3 mm^2, the equivalent diameter is ~3.3 mm. 4 μL droplets with an area of 7.1 ± 0.4 mm^2 give an equivalent diameter of ~3.0 mm.

Plates with linear NDD or SDD variation took ~10 minutes for deposition to finish, with no observed drying of the droplets in the ambient lab conditions. Plates with logarithmic CDD and NDD or SDD variation took ~40 minutes for deposition to finish. When ambient humidity was lower than the exposure humidity, these plates were suspended over a water bath during deposition to increase the local

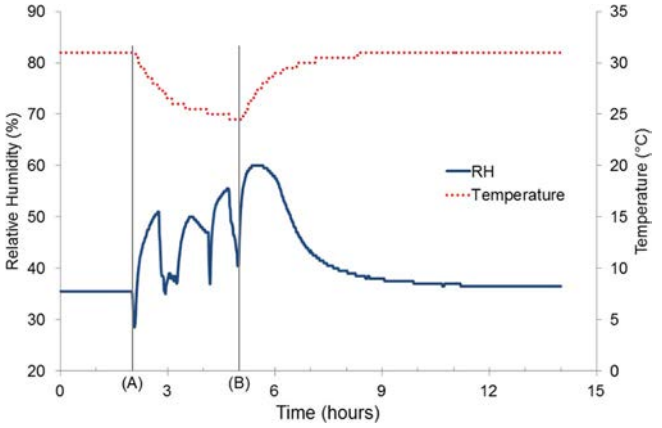

Figure 2. Data from temperature and humidity logger inside desiccator containing saturated $MgCl_2$ during sample placement plotted as a function of time from the beginning of droplet deposition onto the first batch of samples. The desiccator was taken out of the temperature chamber at (A). Between (A) and (B) 2nd–4th batch of samples underwent deposition and placement within the desiccator, with the deposition of the last (4th) batch of samples beginning ∼40 minutes preceding (B). The desiccator put back in oven at (B). Similar transient humidity increases were observed in all experiments just after sample insertion.

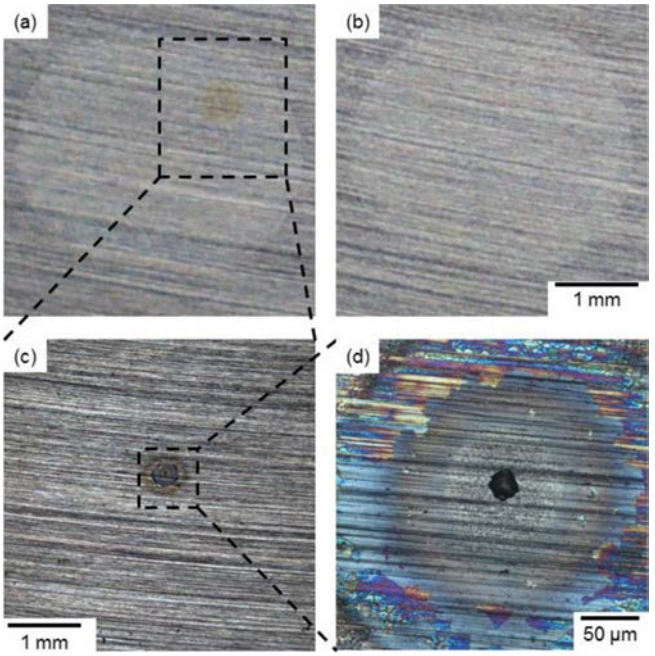

Figure 3. Example of the criterion for visual detection limit of pitting corrosion employed in the tests. (a) "pitted" droplet based on the observation of a rust stain (304L, 4 µL droplet, NDD:CDD of 2.5:8.5, 1 week exposure at 31°C, 46% RH), (b), "uncorroded droplet", no rust observed (304L, 4 µL droplet, NDD:CDD of 2.5:2.5, 1 week exposure at 31°C, 46% RH). (c) and (d), details of the pit from the droplet shown in (a), indicating that pits as small as 10s of µm in diameter were successfully detected by observation of the corrosion product from low magnification images.

humidity. Local humidity was typically increased by ∼5–10% RH by this method.

Where a test used a $CaSO_4$ suspension, an automated pipette was used to mix the suspension thoroughly, before aspirating sufficient solution for a single deposit. Each solution droplet was deposited individually, with the pipette tip returning to the stock solution well-plate each time to re-mix the solution. Due to the much longer deposition time required for this method (∼7 hours), $CaSO_4$ solutions were deposited first and allowed to dry before being over-deposited with a 2 µL droplet of the relevant chloride solution. Where the test with $CaSO_4$ employed a sulfate deposition density of 0 µg/cm^2, the area was pre-deposited with DI water. $CaSO_4$ coverage was generally fairly uniform, though in droplets with higher amounts of $CaSO_4$ the particles appeared to accumulate slightly toward the center of the droplet after being over deposited with $CaCl_2$, with deposits shrinking slightly back from the edge of the droplet.

Sample exposure.—After deposition, samples were photographed and placed within a selected exposure environment. Temperature was always set to 30°C. Humidity was controlled via saturated salt solutions within a desiccator ($MgCl_2$, K_2CO_3, NaBr or NaCl). The expected humidity fixed points (HFP) for the above salts at 30°C are 32.4 ± 0.2% RH, 43.2 ± 0.5% RH, 56.0 ± 0.4% RH and 75.1 ± 0.2% RH, respectively.[32] Samples were exposed alongside a temperature and humidity data logger (Lascar Electronics) to verify their exposure conditions. Samples were exposed for a period of 7 days, with previous preliminary work having shown that for CDDs between 10–1000 µg/cm^2 the majority of corrosion processes on 304L initiated within ∼48 hours of sample exposure.

Humidity verification.—The humidity within the desiccators was largely constant during the 7 day exposure. A significant divergence, common across all experiments, was observed just after samples were placed into the desiccator. At this time, the humidity was seen to increase sharply before slowly decreasing back to equilibrium (Figure 2). This was attributed to the evaporation of the dilute droplets as they equilibrated with the desiccator environment.

In previous work under pure magnesium chloride droplets on 304L, pits were observed to initiate within ∼1 hour of deposition, and so initiation under some droplets is expected to occur during this period of high humidity.[33] This was not expected to influence the results of the experiment, however, as the exposure conditions within the desiccator are thought become more aggressive over time as the system equilibrates (i.e. increase in temperature, increase in solution concentration), and it is assumed that any corrosion sites which initiated under higher humidity, lower temperature conditions would also have initiated under a constant higher temperature and lower humidity. In the general case, however, this humidity transient may affect systems where some of the samples contain dry salts at deposition, which may then deliquesce during the humidity transient, allowing corrosion to occur in this period. It may also affect the results of mixed binary chloride – inhibitor systems where the inhibitor becomes less effective at higher humidities (not expected in the current systems).

Average steady state temperature and humidity readings are given in Table II. In general, all samples to be exposed to a particular environmental condition were exposed together within the same desiccator. The exception to this was $MgCl_2$ + $Mg(NO_3)_2$ droplets on 304L samples at 46% RH, which were exposed separately to the rest. These data are highlighted in Table II.

Sample analysis.—Samples were photographed after exposure, washed in DI water, and photographed again. These photographs were used to assess whether or not corrosion had taken place under a given droplet. Corrosion sites were examined under an optical microscope.

Criteria used to interpret the tests.—A given droplet composition was deemed to allow/inhibit corrosion (pitting) based on the appearance of a rust stain. As examples, Figure 3a is considered a "corroded" droplet, while Figure 3b is considered a droplet where corrosion did not occur. The smallest pits detected from the observation of rust patches were ∼10–20 µm in diameter.

In some conditions (usually lower humidities), solid salt deposits precipitated out of solutions, and some droplets showed evidence of both precipitation and corrosion. Corrosion may be able to occur within a droplet with a nominally high inhibitor:chloride ratio if preceded by precipitation of the inhibitor, as precipitation within a

Table II. Nominal exposure conditions compared with measured exposure conditions. Recorded data given as average ± s.d., instrument error shown in header. Averages do not include humidity peak after sample insertion, common to every experiment (Figure 2).

	Temperature (°C)		Relative humidity (% RH)	
Experiment	Nominal	Recorded ± 0.5	HFP (Salt)	Recorded ± 3.0
$MgCl_2 + Mg(NO_3)_2/MgSO_4$ (Logarithmic)	30	31.2 ± 0.2	33 ($MgCl_2$)	35.5 ± 0.1
	30	31.5 ± 0.0*	43 (K_2CO_3)	46.0 ± 0.1*
	30	31.0 ± 0.2	43 (K_2CO_3)	46.8 ± 0.2
	30	31.4 ± 0.2	59 (NaBr)	58.3 ± 0.4
$MgCl_2 + Mg(NO_3)_2/MgSO_4$ (Linear)	30	31.0 ± 0.0	33 ($MgCl_2$)	34.7 ± 0.2
	30	31.0 ± 0.0	43 (K_2CO_3)	47.0 ± 0.1
	30	31.0 ± 0.1	59 (NaBr)	58.0 ± 0.2
$CaSO_4 + MgCl_2/CaCl_2$	30	31.0 ± 0.1	43 (K_2CO_3)	45.5 ± 0.1
	30	30.7 ± 0.2	59 (NaBr)	57.9 ± 0.2
	30	30.5 ± 0.1	75 (NaCl)	76.4 ± 0.6

*= 304L samples with $MgCl_2 + Mg(NO_3)_2$ droplets, which were exposed in a separate test.

droplet may remove the inhibiting anion from solution. As such, all judgements of inhibition ratios were taken from droplets without any precipitates.

In order to highlight scenarios where an inhibiting salt might precipitate from solution, and to more fully investigate the thermodynamic modelling of the binary salt system, it was of interest to record cases where precipitation had occurred due to environmental factors, i.e. when the exposure environment had led to precipitation within a droplet. It was important, however, to differentiate these cases from cases where precipitation may not have been caused purely by environmental factors, but by the presence of a corrosion site (though changing solution chemistry, or changes in surface morphology).[34]

When both corrosion and precipitation were observed under a droplet, the sequence of corrosion and/or precipitation was judged on the relationship between the corrosion products and the precipitate morphology. Figure 4 shows an example of the morphology of corrosion products and precipitates in these two cases. Figure 4a shows orange/brown corrosion products that are confined by precipitates, suggesting that in this case the corrosion product appeared after the precipitate (precipitation followed by corrosion). Conversely, in Figure 4b the corrosion product is found throughout the droplet and is independent of precipitate morphology, suggesting that it developed first, before the precipitation occurred. It should be noted that both types of behavior were observed for both nitrate- and sulfate-containing droplets.

In the following sections, cases of precipitation preceding corrosion are included in the text/graphs, indicating that the exposure environment was judged responsible. Cases where precipitation was thought to have followed corrosion have not been indicated, as in such cases it cannot be determined whether or not the precipitation was influenced by the changing solution chemistry or surface morphology brought about by corrosion.

Precipitates were identified visually from macrographs of the samples, so instances where only small levels of precipitation occurred may not have been recorded. Precipitates were not directly analyzed for composition, but in all cases were expected to be the inhibitor salt ($MgNO_3$ or $MgSO_4$), based on thermodynamic analysis.

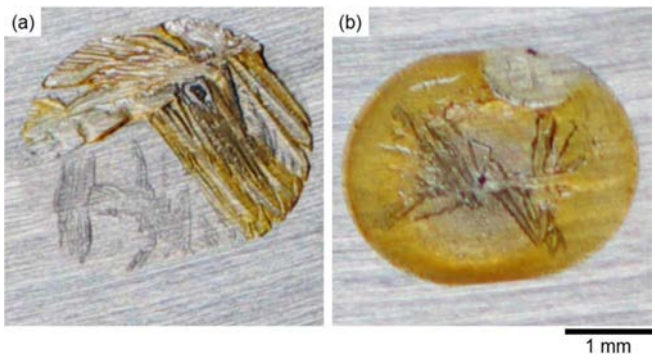

Figure 4. Examples of crystal growth (a) before and (b) after corrosion propagation under 3.3 mm diameter droplets on 304L at 31°C and 36% RH. (a) CDD 250 μg/cm^2, SDD 850 μg/cm^2. (b) CDD 850 μg/cm^2, NDD 250 μg/cm^2.

Thermodynamic analysis.—Thermodynamic analysis of the precipitation behavior of mixed salt solutions was carried out in order to complement the experimental work. Thermodynamic calculations were performed using OLI Stream Analyser Version 9.2, using the mixed solvent electrolyte model (MSE) main databank (H_3O^+ ion). All calculations were run at 30°C, 1 atm with vapor phases supressed.

Results

Control tests (no inhibitor present).—Table III shows the results of control tests carried out at different relative humidity values under pure $MgCl_2$ solutions on 304L and 316L. 316L samples had fewer occurrences of corrosion (rust patches) when compared with 304L. All corrosion was in the form of pitting. There appears to be a lower fraction of corroded droplets at intermediate RH (~45%), than at lower (~35%) or higher (~60%) RH.

In the case of 304L, the majority of control droplets (80–100% of tests) showed corrosion under the conditions tested, so any inhibition effect afforded by nitrate and sulfate salts should be very clear. However, in the case of tests on 316L, particularly at ~46% RH, far fewer droplets corroded than in the case of 304L (20–70% of tests). This indicates that the results on the potential inhibition effects of nitrate and sulfate need to be interpreted with care on 316L.

Table IV shows the results for a limited number of tests on smaller 2 μL (2.3 mm dia.) $CaCl_2$ and $MgCl_2$ droplets on 316L. These control tests were carried out to aid the interpretation of tests aimed at evaluating the inhibition properties of sulfate as $CaSO_4$ on 316L only, to complement the work with $MgSO_4$. Smaller droplets were used in order to fit a sufficiently large array onto each sample. In this limited set of tests no corrosion was seen under $MgCl_2$ droplets under the conditions tested. However, for $CaCl_2$, 2/5 droplets showed signs of corrosion, indicating that $CaCl_2$ is more corrosive than $MgCl_2$. While indicating a potentially higher corrosivity than $MgCl_2$, the limited incidence of corrosion in the control $CaCl_2$ tests (40% of tests) reinforces the idea that, particularly on 316L, the inhibition effects of sulfate need to be interpreted with care. Care should also be taken when comparing the $CaSO_4$ and $MgSO_4$ tests presented, as the different droplet volumes used are likely to have affected the likelihood of corrosion.[20]

Table III. Comparison between number of corroded 3.3 mm diameter $MgCl_2$ control droplets (as number and percentage) for 304L and 316L samples, exposed to humidities of 36% RH, 46/47% RH and 58% RH at 31°C. Results for all CDDs tested (8.5–850 μg/cm^2) are included.

	Number of corroded droplets (/40) and % corroded			
Relative Humidity (% RH)	304L		316L	
36	40	100%	27	68%
46,47	33	83%	9	23%
58	40	100%	19	48%

Table IV. Comparison between number of corroded 2 μL (2.3 mm diameter) $MgCl_2$ and $CaCl_2$ control droplets (as number and percentage) for 316L samples, exposed to humidities of 46% RH, 58% RH and 76% RH at 31°C. A 2 μL droplet of DI water was pre-deposited in the same location and allowed to dry before deposition of the salt solution. All tests had the same CDD of 1200 μg/cm^2.

	Corroded droplets (/5)			
Relative Humidity (% RH)	$CaCl_2$		$MgCl_2$	
46	2	40%	0	0%
58	0	0%	0	0%
76	0	0%	0	0%

Effect of magnesium nitrate on corrosion under magnesium chloride droplets.—Figure 5a shows an example of a test on 304L at 36% RH in which both chloride deposition density (CDD) and nitrate deposition density (NDD) are varied between 8.5 and 850 μg/cm^2 and 0 and 850 μg/cm^2, respectively. The micrographs show that at high CDD and low NDD, corrosion is observed in the form of pits surrounded by rust-like corrosion product. At high enough NDD, however, no rust is observed and corrosion is inhibited. Corrosion product coverage, which reflects the extent of pitting, varied with CDD, with higher CDDs leading to more extensive rust coverage and sufficiently low CCD (≤25 μg/cm^2) resulting in substantially less rust. Increasing the NDD for fixed CDD did not appear to affect the corrosion product coverage, until a cutoff where corrosion was inhibited, hence no rust was observed.

In all cases, corrosion was observed in the form of pits (Figures 5b and 5e). There was usually a single pit beneath each corroded droplet, although multiple pits were also observed under some conditions. Multiple pits were more common under lower CDD droplets (≤25 μg/cm^2) at 36% RH and 58% RH on 304L samples, but were also observed in other conditions. In some cases precipitation of salt crystals was observed. Under some precipitates (e.g. Figures 5d and 5g), pitting was observed.

Figure 6 shows the full set of results for both 304 and 316L under a range of humidities (36–58% RH). For 304L, at higher CDD and lower NDD values, all four tests for each condition showed corrosion (complete black circle) for most conditions. Above a critical NDD value, no corrosion was observed (open circle). However, for 304L at 36% RH (Figure 6a), as the NDD value increased further, some salt precipitation was observed in the droplets (superimposed light gray square). The precipitate was expected to be $MgNO_3$, as all tested humidities were above the deliquescence point for $MgCl_2$. At the highest NDD value (850 μg/cm^2), one or two examples of pits that were assumed to have initiated under salt crystals were observed (partially filled circle on a light gray square). This interpretation was based on the distribution of corrosion products (see Experimental Method).

In all conditions, 316L and 304L showed similar overall trends in corrosion susceptibility as a function of CDD and NDD, but 316L generally showed a lower probability of corrosion than 304L, particularly at 47% RH. In this paper, given the overall low corrosion probability for 316L (giving poorer statistics) and given that the effect of inhibition is more difficult to distinguish from the inherent corrosion resistance of the alloy (as shown by the control tests), inhibition ratios are generally evaluated on the basis of results on 304L and consistency with 316L is noted.

All tests indicated that corrosion inhibition is achieved on both alloys above specific NDD:CDD ratios. The effectiveness of nitrate as an inhibitor appears to be greater at higher humidity (i.e. less nitrate relative to chloride is required for inhibition at 58% RH than at 36% RH). No difference was observed between the critical ratio for corrosion inhibition for 304L and 316L. At low humidity (~36% RH), an inhibition ratio (NDD:CDD) between 1 and 3 on a mass basis can be inferred from these measurements (as shown in Figure 6 for 304L), decreasing to values below 1 at higher humidities (58% RH).

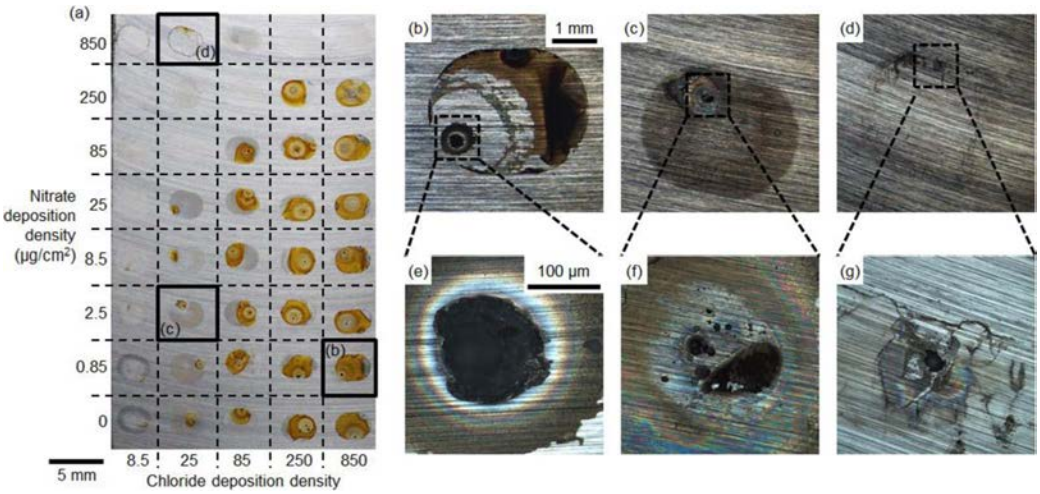

Figure 5. 304L plate with 3.3 mm diameter droplets of $MgCl_2 + Mg(NO_3)_2$ after 7 day exposure at 31°C, humidity of 36% RH, before DI rinse. (a) macrograph of the whole sample. (b-g) optical micrographs of droplets shown in (a) after DI rinse; (d,g) after further ultrasonic wash.

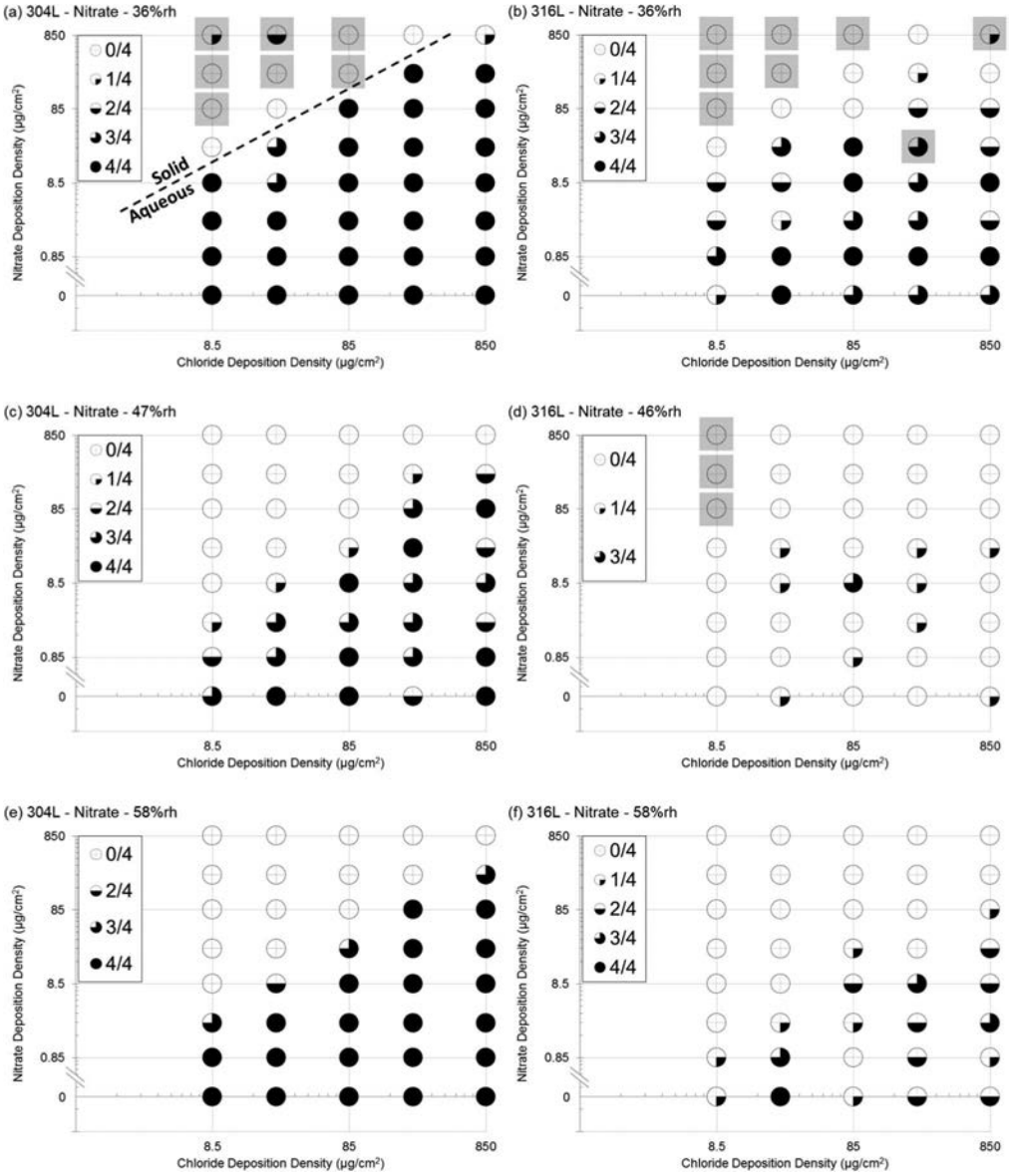

Figure 6. Data from 304L ([a], [c] and [e]) and 316L ([b], [d] and [f]) plates with 3.3 mm diameter droplets of $MgCl_2 + Mg(NO_3)_2$ solutions, exposed to humidity of 36% RH (a, b), 47% RH (c), 46% RH (d) and 58% RH (e, f). The fraction of each circle that is filled corresponds to fraction of droplets which showed corrosion (out of four tests). The data below the break in the y-axis indicates solutions with NDD of 0 $\mu g/cm^2$. Solution compositions where any salt crystals were observed that are assumed to have formed before any pitting (see Experimental Method) are indicated with gray squares. Salt crystal formation was highlighted if only a single instance within the four tests was observed. The thermodynamically predicted boundary for precipitation has been indicated in (a) calculated using OLI Analyser 9.2.,[18] NB: this boundary has not been indicated nor calculated on any other plot.

As noted above, at low humidities instances of corrosion sites developed after crystallization were observed (e.g. Figure 5a). These results indicate that, at low RH, inhibition may be lost or reduced due to the removal of nitrate from solution owing to formation of nitrate crystals and/or owing the formation of micro-crevices under these precipitates.

Further linear tests were conducted on 304L plate to explore conditions around the NDD:CDD threshold. In these tests the NDD was varied linearly, while the CDD was kept constant (at a value of ~1230 $\mu g/cm^2$). A typical example (plate exposed at 47% RH) is shown in Figure 7, while data from the full set of tests is shown in Figure 8.

As in the logarithmic tests, increasing the NDD showed clear evidence of corrosion inhibition. Similarly, increasing exposure RH reduced the NDD:CDD ratio required at which corrosion inhibition was observed (Figure 8). From these tests, with finer increments than the logarithmic tests, inhibition effects can be seen to commence for

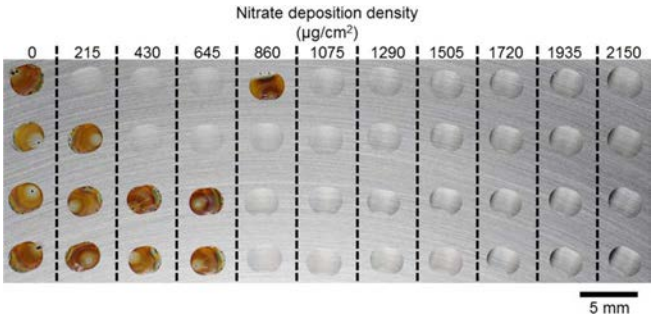

Figure 7. 304L plate with 3.0 mm diameter droplets of $MgCl_2 + Mg(NO_3)_2$, exposed at 31°C and at 47% RH for 7 days. Image taken after exposure, before DI rinse. Constant chloride deposition density of 1230 $\mu g/cm^2$ for each droplet, nitrate deposition density varied as shown.

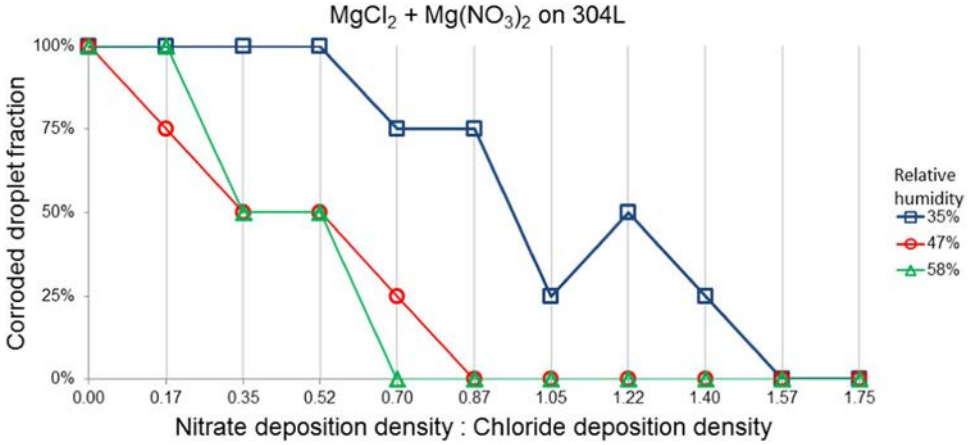

Figure 8. 304L samples with fixed CDD of at 1230 μg/cm^2 and linearly increasing nitrate deposition density (NDD) in steps of 215 μg/cm^2. 3.0 mm diameter droplets, exposed for 7 days at 31°C and humidity as shown. Plot shows number of corroded droplets (out of four repeats) for each NDD:CDD ratio and humidity.

NDD:CDD ratios above 0.1–0.5 on a mass basis, with full inhibition achieved at values of the order of 0.7–1.6, depending on exposure humidity.

Figure 9 shows the relationship between the critical inhibition nitrate:chloride ratio on both a deposited mass density basis (NDD:CDD) and a molar basis (NO_3^-:Cl^-), as a function of RH from both logarithmic variation and linear tests. For the logarithmic tests the "corrosion" point is the highest NDD:CDD ratio at which any corrosion was observed across all CDDs (0.85–850 μg/cm^2), excluding droplets with salt precipitates. The "no corrosion" point is the lowest value of the NDD:CDD ratio above the "corrosion" point (across all CDDs) at which no corrosion is observed. The linear variation data is plotted in the same way, but is relevant only for a single CDD (1230 μg/cm^2).

Figure 10 shows the inhibition ratios presented in Figure 6 as a function of chloride deposition density (for constant RH). In general, although there was variation in inhibition ratios with CDD, there was no clear trend in the variation, indicating no obvious dependence of the inhibition ratios on the deposition density.

Effect of magnesium sulfate on corrosion under magnesium chloride droplets.—Figure 11a shows an example (at a humidity of 46% RH) of a test varying both chloride deposition density (CDD) and sulfate deposition density (SDD) between 8.5–850 μg/cm^2 and 0–850 μg/cm^2 respectively on 304L. The micrographs show that corrosion is observed in most conditions, in the form of pits surrounded by rust-like corrosion product. In this example, corrosion was not prevented by the addition of sulfate for all tested values of SDD:CDD. As in the case of nitrate tests, corrosion (amount of rust observed) decreased significantly at low CDD, particularly below 25 μg/cm^2.

Corrosion was generally observed in the form of pits (Figures 11b and 11e), with multiple pits more common under low CDD droplets (≤25 μg/cm^2) at 36% RH and 58% RH humidity. Crevice-like attack was also observed under some droplets where $MgSO_4$ salt precipitates had acted as crevice formers (Figures 12c, 12d). Droplets with a high SDD:CDD ratio showed evidence of salt precipitation (Figures 11d and 11g). In general, the extent of precipitation was much greater than that observed in $MgCl_2$ + $Mg(NO_3)_2$ experiments, with precipitates observed at higher relative humidity and lower IDD:CDD ratios than those seen with $Mg(NO_3)_2$.

Figure 13 shows the full set of results for the effect of sulfate on both 304L and 316L at a range of relative humidities (36–58%). Salt precipitation was observed on both alloys across all humidities tested, particularly at higher SDD:CDD ratios. This was expected to be a $MgSO_4$ precipitate as all tested humidities are above the deliquescence point for $MgCl_2$. On 304L, no significant inhibition was observed at any relative humidity values across the full CDD range, though no corrosion was observed in high CDD (250 and 850 μg/cm^2) droplets with SDD:CDD ratios of 1 at 58% RH.

As noted above, from control tests (Table III) the probability of corrosion under magnesium chloride solutions on 316L (20–70%) is generally lower than 304L (80–100%), making it more difficult to

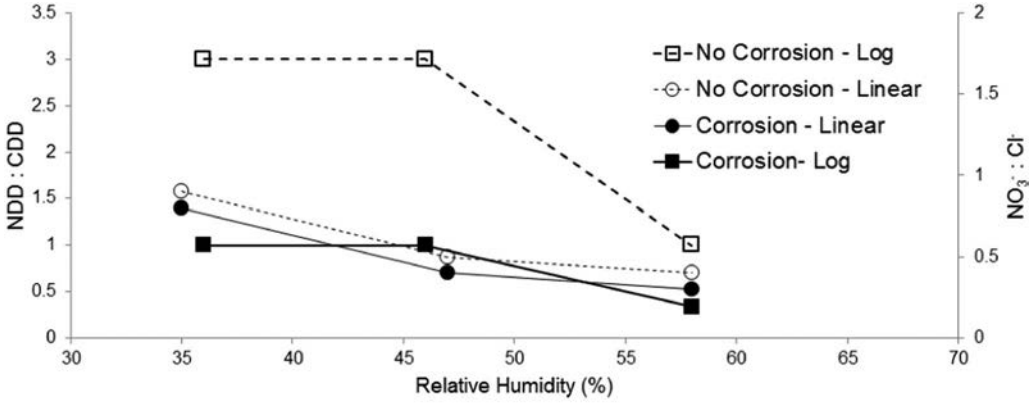

Figure 9. Nitrate:chloride inhibition ratio based on deposited mass (NDD:CDD) and molar basis (NO_3^-:Cl^-) as a function of RH. Data are taken from both logarithmic variation tests on 304L and 316L (Figure 6), and linear variation tests on 304L (Figure 8). Filled data points ("Corrosion") show the highest nitrate:chloride ratio at which pitting was observed across the range of CDDs examined. The open data points are the lowest value of the NDD:CDD ratio above the Corrosion point which showed no corrosion.

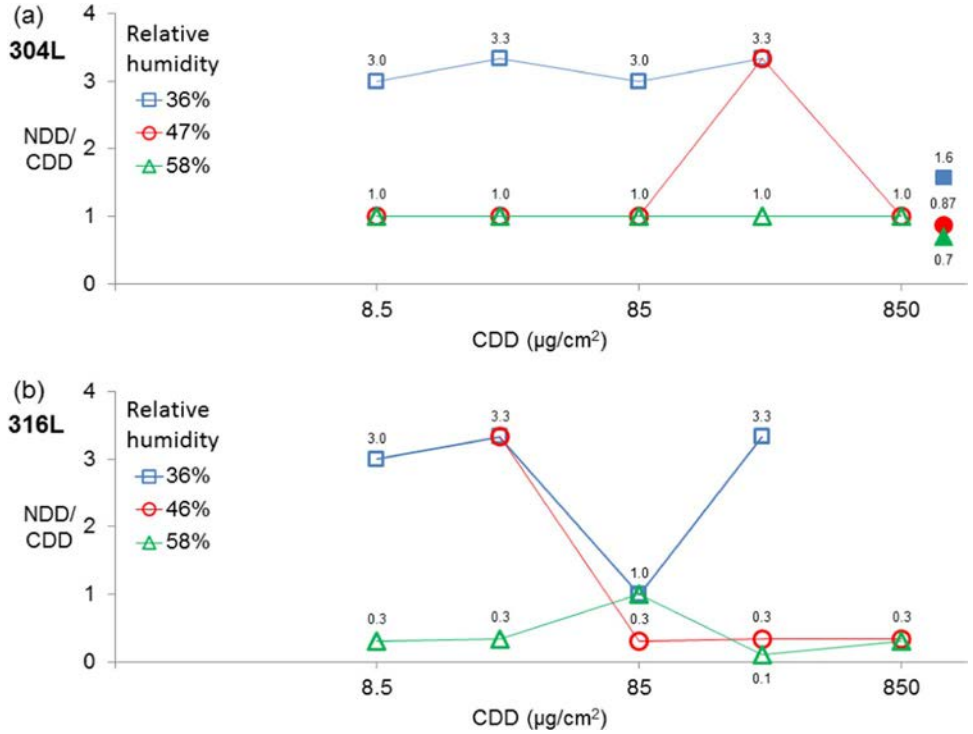

Figure 10. Nitrate:chloride inhibition ratios (NDD:CDD) on (a) 304L and (b) 316L alloys, at 36% RH, 46/47% RH and 58% RH, based on 'logarithmic tests' (Figure 6). Data points correspond to lowest NDD:CDD ratio where corrosion was not observed, data labels indicate NDD/CDD value. Droplets showing salt crystallization have been omitted. Filled data points in (a) at 1230 $\mu g/cm^2$ indicate ratios from linear tests (Figure 8). CDDs with no data point indicate conditions where inhibition was not observed.

assess inhibition effects on this alloy. However, comparing the probability of corrosion in Figure 13 with the results of Table III suggests that, whilst limited inhibition was observed at 36% RH, some inhibition was observed at a relative humidity of 58%, although the fraction of droplets showing corrosion was variable even at low SDD:CDD ratios. At 46% RH, the limited incidence and high variability of occurrence of corrosion in both the control and main tests was too great to determine any inhibiting effects. Corrosion variability was lower at 36% RH, but no clear trends in inhibitive effects of sulfate could be seen in this condition.

Further tests were conducted on 304L plate investigating linear variation in SDD while keeping CDD constant. The sample exposed to 58% RH humidity is shown in in Figure 14, while a summary of the whole set of tests at different humidity values is shown in Figure 15. Plates exposed at 35% RH and 47% RH showed no clear signs of inhibition with increasing SDD:CDD ratios. At 58% RH, however,

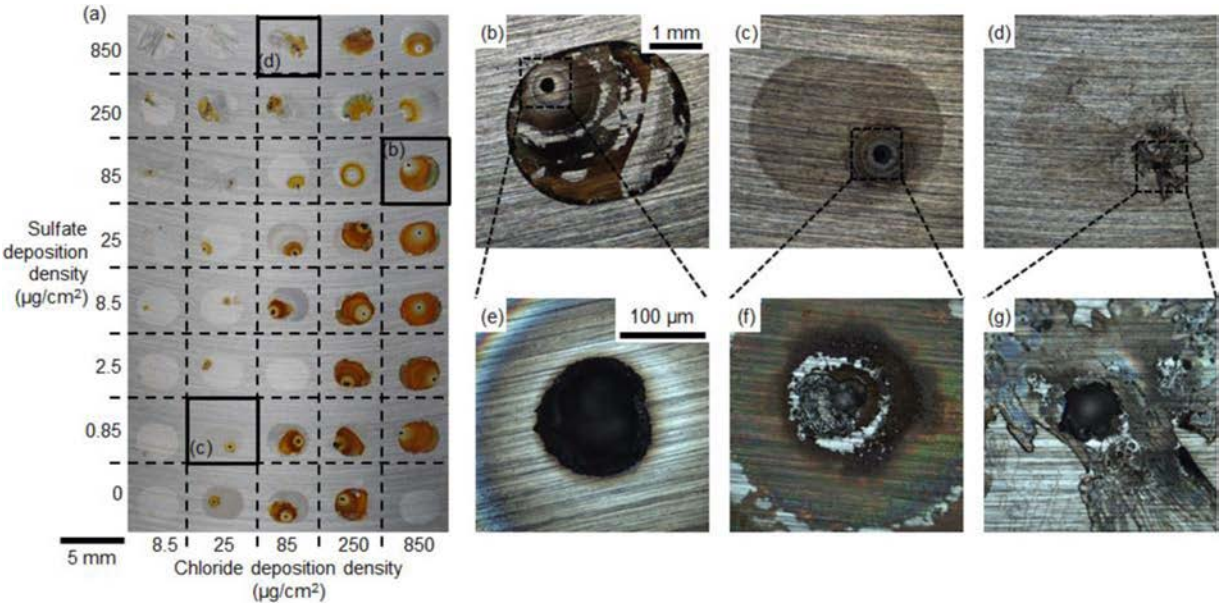

Figure 11. 304L plate with 3.3 mm diameter droplets of $MgCl_2 + MgSO_4$ after 7 day exposure at 31°C, humidity of 46% RH, before DI rinse. (a) micrograph of the whole sample. (b-g) optical micrograph of droplets shown in (a) after DI rinse; (d,g) after further ultrasonic cleaning.

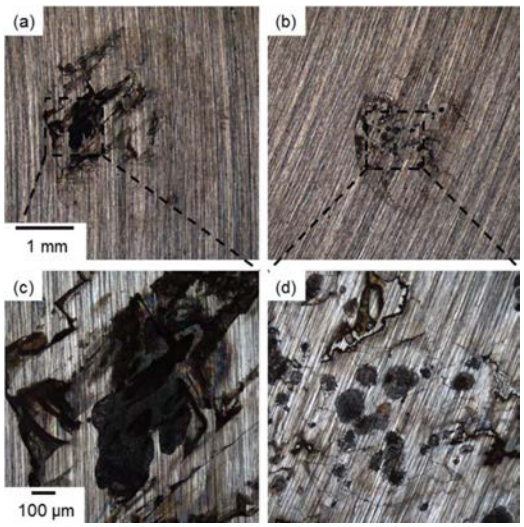

Figure 12. Examples of corrosion morphologies observed in 3.3 mm droplets of $MgCl_2 + MgSO_4$, where $MgSO_4$ precipitates affected corrosion site development. Both samples were 304L, exposed at 31°C. (a,c) 36% RH, 85 µg/cm^2 CDD, 850 µg/cm^2 SDD. (b,d) 58% RH, 8.5 µg/cm^2 CDD, 850 µg/cm^2 SDD.

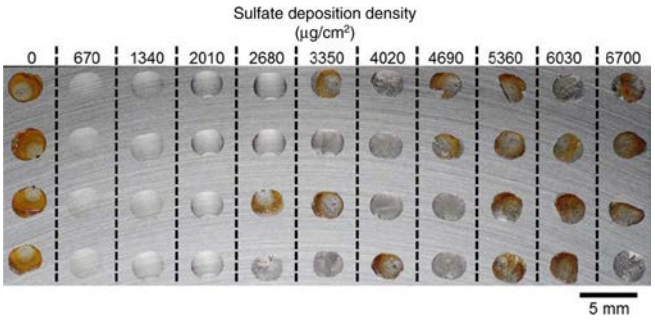

Figure 14. 304L plate with 3.3 mm diameter droplets of $MgCl_2 + MgSO_4$, exposed at 31°C and at 58% RH for 7 days. Image taken after exposure, before DI rinse. Constant chloride deposition density of 1230 µg/cm^2 for each droplet, sulfate deposition density varied as shown.

inhibition was observed between SDD:CDD ratios of 0.54 and 1.63. In droplets at higher SDD:CDD ratios, both salt precipitation and corrosion were observed, with all cases of corrosion occurring under precipitated droplets.

Effect of calcium sulfate on corrosion under magnesium chloride or calcium chloride droplets.—A preliminary investigation into the

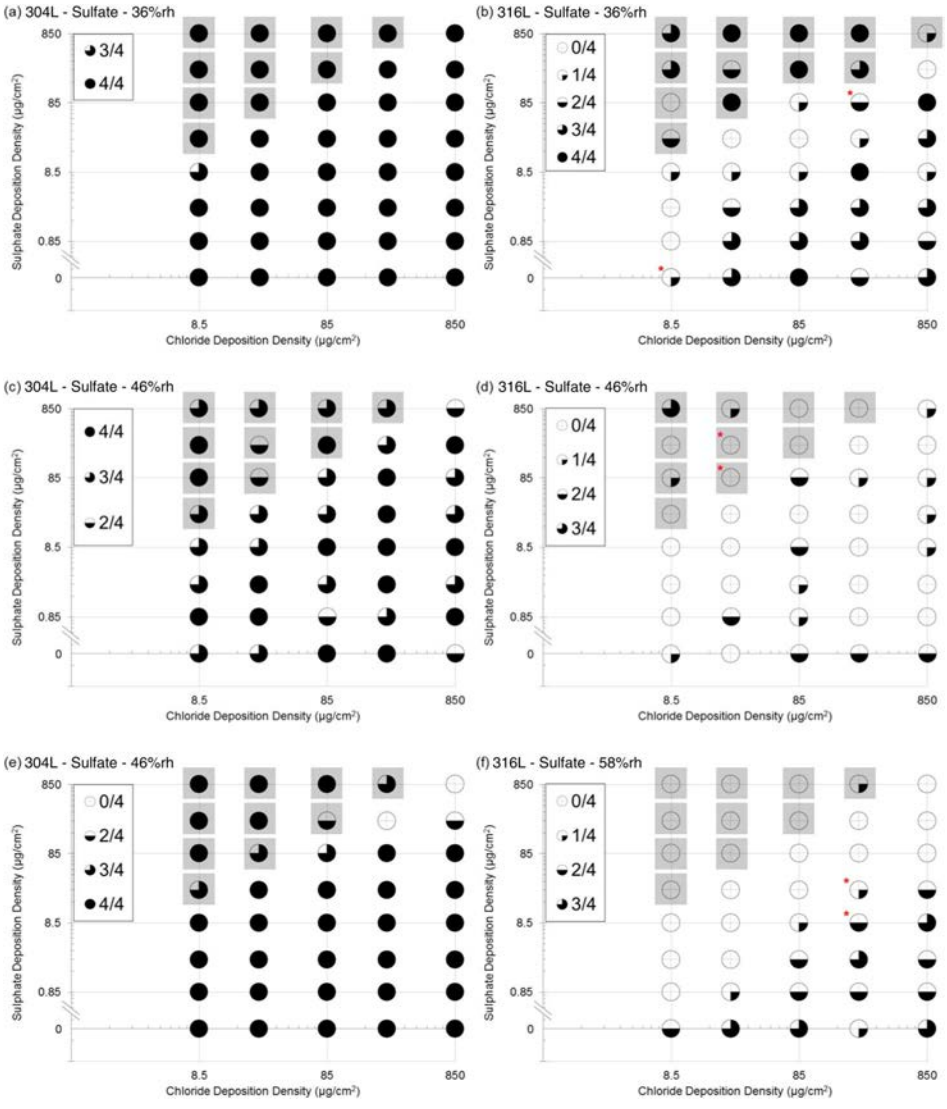

Figure 13. Data from 304L ([a], [c] and [e]) and 316L ([b], [d] and [f]) plates with 3.3 mm diameter droplets of $MgCl_2 + MgSO_4$ solutions, exposed to humidity of 36% RH (a, b), 46% RH (c, d) and 58% RH (e, f). The fraction of each circle that is filled corresponds to fraction of droplets which showed corrosion (out of four tests). The data below the break in the y-axis indicates solutions with NDD of 0 µg/cm^2. Solution compositions where any salt crystals were observed that are assumed to have formed before any pitting (see Experimental Method) are indicated with gray squares. Salt crystal formation was highlighted if only a single instance within the four tests was observed. Data points consisting of only 3 repeats have been indicated with an asterisk (*).

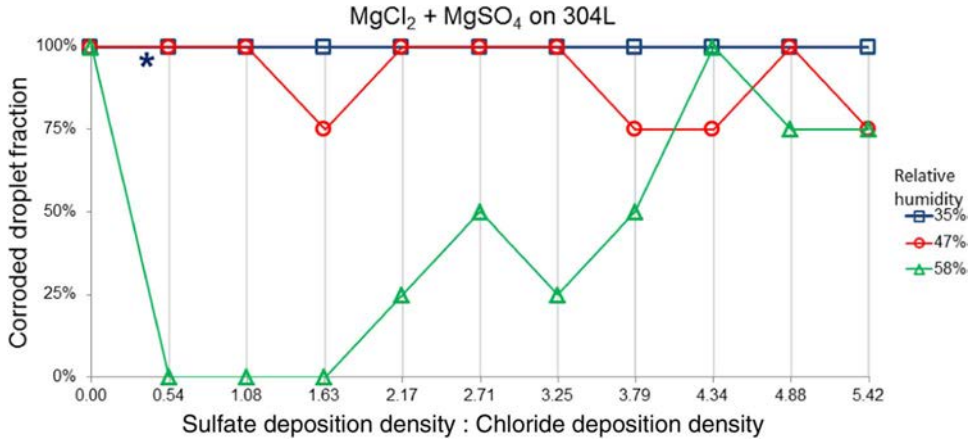

Figure 15. 304L samples with fixed CDD of at 1230 $\mu g/cm^2$ and linearly increasing sulfate deposition density (SDD) in steps of 670 $\mu g/cm^2$. 3.0 mm diameter droplets, exposed for 7 days at 31°C and humidity as shown. Plot shows number of corroded droplets (out of four repeats) for each SDD:CDD ratio and humidity. At an SDD:CDD ratio of 0.54 on the 35% RH test, two droplets were discounted due to a deposition error, and the pitting fraction is thus out of two (indicated by an asterisk *).

effects of calcium sulfate on corrosion was conducted under both magnesium and calcium chloride solutions. In contrast to the work presented so far, these tests were only carried out on 316L and across an elevated range of humidities (46–76% RH, compared to 36–58% RH used previously).

Figure 16 shows a typical sample used to investigate the effect of $CaSO_4$ on pitting under $CaCl_2$ solution on 316L stainless steel. 2 μL droplets were used (2.3 mm diameter). The CDD was kept constant at 1200 $\mu g/cm^2$, while the SDD was varied linearly between 0 and 1200 $\mu g/cm^2$. The $CaSO_4$ was pre-deposited onto the samples as a 2 μL suspended solution over a period of ~7 hours, and allowed to dry. The $CaSO_4$ was then over-deposited with chloride salt. Where an SDD of 0 $\mu g/cm^2$ was intended, the plate was pre-deposited with DI water.

No inhibition due to the presence of $CaSO_4$ was seen in these tests. In general the extent of corrosion was very low, with only 23/330 droplets showing signs of corrosion (16 of these corroded droplets can be seen in Figure 16). Similar to what observed in control experiments, corrosion occurred more frequently under $CaCl_2$ droplets than under $MgCl_2$ droplets (16/165 vs. 7/165 cases, respectively). The incidence of corrosion (about 10%), however, was similar to or even lower than that of the control experiments (20%), indicating limited (if any) inhibition effects. In all cases, corrosion was observed in the form of pits. $CaSO_4$ was highly insoluble, with a solid phase observed in all droplets with any $CaSO_4$ addition.

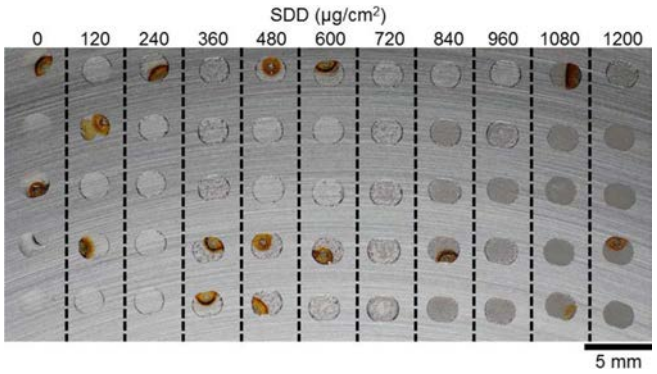

Figure 16. 316L with 2 μL droplets (2.3 mm diameter) with mixtures of $CaCl_2$ and $CaSO_4$. The CDD was 1200 $\mu g/cm^2$ for each droplet, while the sulfate deposition density (SDD) was as shown (pre-deposited as $CaSO_4$). 7 day exposure at 31°C, 46% RH. Image taken after exposure, before DI wash.

Discussion

The tests presented in this study were designed to evaluate the corrosion behavior of stainless steel in conditions of defined salt deposition densities. It was generally observed that, in both nitrate and sulfate tests, the corrosion product (rust) coverage under droplets (a good indicator of the amount of corrosion damage) was dependent on the CDD, with higher CDDs resulting in more extensive rust deposits (Figure 3a). Rust coverage tended to be relatively small at CCDs below 25 $\mu g/cm^2$ and greater at higher values. These observations are consistent with findings in pure $MgCl_2$ reported in previous studies.[2]

The expected range of CDDs within stores over the storage period is likely to be on the order of between 1–100 $\mu g/cm^2$, with the higher levels of CDD expected to accumulate toward the end of the storage period.[3] This range is lower than that in many of the results shown here. However, as shown in Figure 10 there is relatively little change in inhibition ratio with CDD, and there is generally good agreement between logarithmic and linear variation tests, which support the idea that inhibition ratios obtained at higher CDD ranges (as in this work) are likely to be applicable also to the lower CDD conditions found in stores.

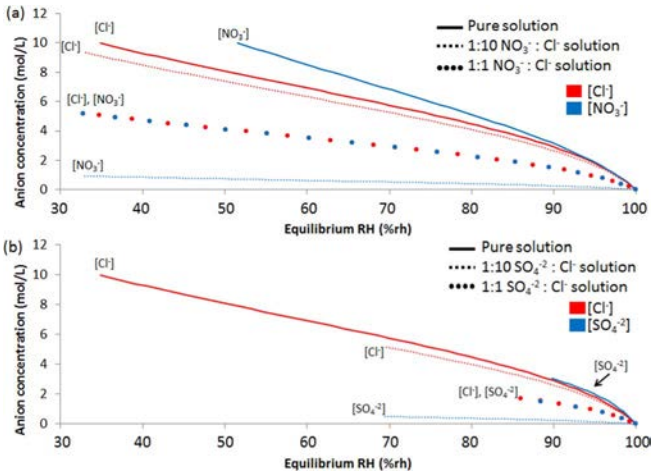

Figure 17. Calculated anion concentrations with respect to equilibrium RH, for solutions containing (a) $MgCl_2$ and $Mg(NO_3)_2$, including pure solutions; and (b) $MgCl_2$ and $MgSO_4$, including pure solutions.[18] Solution compositions are indicated on the relevant graphs. Note that the plots for solutions with a 1:1 anion composition overlay each other.

Exposure humidity.—The effect of the exposure humidity on the overall corrosion behavior in these tests can be evaluated by examining the control droplets (i.e. droplets with no nitrate or sulfate additions) on each sample. Across all logarithmic, tests the likelihood of corrosion occurring on both 304L and 316L was highest at a humidity of 36% RH (67 corroded droplets out of a total of 80), next at 58% RH (59/80), and lowest at 46% RH (42/80) (Table III). At lower humidity, the concentration of chloride in the droplet will be highest, providing a more aggressive chemistry for pit initiation (see Figure 17 for trends on anion concentration with respect to exposure RH).[4] According to this view, the most aggressive condition is expected to be at humidity just above the deliquescence point of $MgCl_2$, ~32% RH, with the solution decreasing in aggressiveness with increasing humidity.[32] A higher RH, however, will also increase the volume of the droplet, which, given that the droplets generally have the same diameter, leads to an increase in droplet height. In addition, in concentrated solutions, there is an increase in electrical conductivity as $MgCl_2$ solutions become more dilute.[33] Thus the IR-drop between any initiating anodic site and the cathode area is likely to be decreased as the RH increases, leading to a larger interfacial potential to drive the corrosion reaction.[21,33] It is speculated that the lowest level of observed pitting at 46% RH (particularly in control tests) may perhaps be explained as a cross-over point between these two factors, where the increase in concentration compared with 58% RH has increased the IR-drop within the droplet, but the chloride concentration is still not at its most aggressive to allow a critical corrosion chemistry to fully stabilize within a corrosion site.

Chloride dilution.—Although the inhibition mechanism of either nitrate or sulfate salts on pitting corrosion is not the focus of this work, it is worth highlighting an additional factor which may play a role under atmospheric conditions not found in full immersion tests. The concentration of a pure $MgCl_2$ droplet in equilibrium with an RH of 60% is ~7 M [Cl^-]. However, the chloride concentration in a mixed $MgCl_2$, $Mg(NO_3)_2$ droplet (Cl^-:NO_3^- = 1:1) in equilibrium with the same humidity is ~3.5 M (Figure 17a). Chloride concentration is known to be a key factor in pitting corrosion.[20,35] The 'dilution effect' of adding another salt into solution with a chloride salt, even if the added salt is not itself an inhibitor may change the chloride concentration of the solution for a given equilibrium RH such that corrosion does not take place. The effects of the inhibitors below cannot be fully explained by this phenomenon alone, but it is highlighted here as an additional factor to keep in mind when interpreting mixed salt systems under atmospheric conditions.

Droplet size.—Tests using both 4 μL and 2 μL droplets on 316L stainless steel were used in this study, with diameters of ~3.3 mm and ~2.3 mm, respectively. Larger droplets were more likely to cause corrosion; small droplets failed to cause corrosion at a humidity of 58%RH, while 48% of equivalent larger droplets caused corrosion under the same conditions. While this was not the main focus of the experiment, it may support the idea that corrosion is cathodically limited since increasing the droplet size increases the coverage of the electrolyte over the metal surface, thus increasing the available area for a cathodic reaction to take place.[21,29,36] As such, the propagation of initiation sites to stable and visible pits may be limited or even impeded under small droplets. Another factor may be that smaller areas of electrolyte are less likely to cover a suitable initiation site from which stable pitting can propagate.

It is also worth considering that the deposition method for the 2 μL droplets was different to that for the rest of the 4 μL droplets, in that the droplet area was pre-deposited with a $CaSO_4$ solution prior to the deposition of the chloride solution, which was then allowed to dry. It has been shown that the composition of the passive layer on 304 and 316 stainless steels can be affected by the exposure environment, specifically by the presence of a water layer. Cr enrichment has been found in the passive layer during the first stages of exposure to a wet-dry cycling process, which the deposition and then drying of a $CaSO_4$ solution may mimic.[37] As such, the passive layer present for the 2 μL droplets may well be of a composition more resistant to corrosion than that present for the 4 μL tests, where there was no pre-deposition of an aqueous solution before the deposition of chloride.

Alloy comparison.—Critical inhibition ratios for nitrate were found to be the same on both 304L and 316L alloys, within the experimental resolution (0.3, 1, 3 NDD:CDD ratios), though the fact that in control experiments 316L showed fewer instances of corrosion than 304L made it more difficult to evaluate any inhibition effects on this alloy.

In the case of sulfate, no inhibition was observed at 36% RH or 46% RH, but some evidence of inhibition was seen at 58% RH on both 304L (linear tests and logarithmic tests at CDD ≥250 μg/cm^2) and 316L (logarithmic tests). The ratio for inhibition from $MgSO_4$ on 316L was lower than that seen on 304L (0.1–0.3 compared with 0.3–0.5, SDD:CDD, respectively) and was independent of CDD. Corrosion under $MgSO_4$ precipitates was observed on 304L at 58% RH, and not observed (for the most part) in the same experiments on 316L. The total number of corroded droplets was less on 316L than on 304L. These differences in corrosion behavior are likely to be attributed to the addition of molybdenum in 316L, which acts to decrease susceptibility to pitting.[38,39]

Nitrate inhibition.—The inhibiting effects of nitrate on corrosion under chloride containing droplets are clear from both logarithmic and linear variation tests on 304L and 316L (Figure 9). The effective NDD:CDD inhibition ratio was seen to be dependent on the exposure humidity, with increasing humidity lowering the required ratio. While tests on 304L carried out in these studies can be considered easier to interpret than those obtained on 316L (due to the lower baseline incidence of pitting in the latter in control experiments in the absence of nitrate), similar values of the inhibition threshold were found on 304L and 316L.

The results based both on logarithmic tests at CDDs between 0.85 and 850 μg/cm^2, and on linear tests at a CDD of 1230 μg/cm^2, are summarized in Table V, which presents anion deposition density ratios required to obtained corrosion inhibition of all samples in a given condition (inhibition of corrosion in some but not all droplets was observed at lower values). Ratios are presented in terms of deposition density (a commonly measured parameter in atmospheric corrosion studies), deposited molar ratio, and calculated activity ratio.[18] The values from the linear and logarithmic variation tests are consistent, with the inhibition ratios found in the linear tests falling generally within the range observed by the logarithmic tests. The NDD:CDD inhibition ratio determined from the logarithmic tests is more reliable since there were 20 droplets for each condition rather than 4 for the linear tests. However, the finer composition increments of the linear tests suggest that the inhibition ratio is likely to be closer to the lower limit than the upper limit set by the logarithmic tests.

Examples of inhibition ratios for nitrate on 304 reported in other studies based on experiments in bulk solution are presented in Table VI. On a concentration (molar) basis, typical inhibition ratios (nitrate:chloride) are of the order of 0.2–0.4, which are somewhat lower than those observed at relative humidities of 35% and 46% in this study. At a higher humidity of 58% RH, however, the inhibition ratio approaches the upper end of those found in the literature. It is noteworthy that increasing the humidity (and hence the dilution of the droplet system) leads to conditions more similar to those typically present in tests in bulk solution, and results in lower values of the inhibition ratios, leading to values more similar to those found in the literature.

On an activity basis, results in bulk solutions found in the literature are more similar to those estimated in atmospheric conditions in this study across the RH range tested. In dilute conditions (high RH), again the predicted convergence with data from bulk solutions is somewhat unsurprising. The reasonable agreement in more concentrated solutions (lower RH), however, is an important result, and provides confidence in the inhibition ratios found in this study.

Few studies describe variation in critical inhibition ratio in different conditions, in particular in respect to solution concentration. An exception is the work of Leckie and Uhlig and Uhlig and Gilman, who

Table V. Summary of nitrate:chloride inhibition ratios for both logarithmic (304L and 316L together) and linear (304L) variation tests (Figure 9) on a mass, mole, and activity basis. Logarithmic tests summarize results obtained with CDDs between 0.85–850 μg/cm^2, showing the most conservative results (highest ratios), and give the range in which the inhibition ratio lies. Linear tests, at a CDD of 1230 μg/cm^2, give the inhibition ratio as the lowest nitrate:chloride ratio at which pitting was no longer observed. In all cases the inhibition ratios presented were those required to achieve inhibition for all samples tested, though some inhibition effects were observed at lower ratios. NO_3^-:Cl^- ratios are calculated from deposited solution composition. Activity ratios are calculated using OLI Analyser 9.2.[18]

	NDD:CDD			NO_3^-:Cl^-			$\{NO_3^-\}$:$\{Cl^-\}$		
Relative humidity	35%	46%	58%	35%	46%	58%	35%	46%	58%
Logarithmic variation (304L and 316L)	1–3	1–3	0.3–1	0.6–1.7	0.6–1.7	0.2- 0.6	>0.28*	0.33–1.1	0.12–0.39
Linear variation (304L)	1.6	0.9	0.7	0.9	0.5	0.4	0.47	0.29	0.26

*Activity ratio for the upper limit could not be calculated as solution is thermodynamically unstable.

developed a relationship between the inhibition ratio and the chloride activity.[7,11] However, they predicted that the critical $\{NO_3^-\}$:$\{Cl^-\}$ inhibition ratio would decrease as $\{Cl^-\}$ increases.[11] The opposite trend is seen in the present work, where a lower humidity, and thus a higher $\{Cl^-\}$, required a higher $\{NO_3^-\}$:$\{Cl^-\}$ ratio for inhibition. It is important to point out that this relation was calculated by Uhlig et al. via full immersion electrochemistry for anion activities below 1 (i.e. dilute conditions compared to atmospheric systems), and this may explain the discrepancy between it and the data derived from high concentration atmospheric testing produced in this work. It is worth noting that even the work undertaken at a chloride concentration of 3.12 M by Uhlig and Gilman is still not sufficient a concentration to cause pitting corrosion of 304L under atmospheric conditions using magnesium chloride.[20,29]

For droplets below the inhibition threshold, the amount of rust observed appeared to be independent of the amount of nitrate within the droplet (e.g. Figure 5). The extent of rust coverage is a reasonable proxy for pit volume, which was not measured in the current work. This suggests that nitrate addition does not have a significant effect on pit growth propagation kinetics but instead affects whether or not pits are stable at all. The addition of sufficient nitrate to an active pit solution has been shown to stifle pit growth and promote passivation in systems which have formed a salt layer, though active dissolution (i.e. no salt layer present) was not affected.[10,16] Nitrate has also been shown to eliminate slow rise electrochemical transients, associated with metastable pitting events which may form a salt layer.[9,40] Furthermore, nitrate has been shown to affect re-passivation kinetics on freshly scratched surfaces, with higher nitrate content leading to faster re-passivation.[40] In the current work, there was no gradual change in the amount of rust (and, by implication, pit volume) with increasing nitrate levels up to the point where complete inhibition occurred. This suggests that nitrate inhibits the early stage of pitting, possibly the metastable state, rather than pit propagation. This hypothesis is consistent with the idea that metastable pits contain a salt layer, and the observation that nitrate inhibits pitting in the presence of a salt layer rather than in the active state.[10,41]

Sulfate inhibition.—The inhibition effects produced by sulfate were more variable than those produced by nitrate. The data for 316L at 58% RH represent the only case where the exposure humidity affected the SDD:CDD critical inhibition ratio in a manner similar to that for nitrate. Moreover, inhibition was only observed with $MgSO_4$, not with $CaSO_4$. In environments containing calcium (such as concrete buildings), sulfate is expected to be present in the form of $CaSO_4$, originating from concrete dust.[3] Tests carried out on with both $CaCl_2$ and $MgCl_2$ mixed with $CaSO_4$ solutions indicated that, due to its low solubility, the presence of $CaSO_4$ is unlikely to lead to inhibition under a wide range of atmospheric conditions.

Table VII summarizes data for the effects of magnesium sulfate on the inhibition of corrosion for both logarithmic variation tests (CDDs between 0.85–850 μg/cm^2) and linear variation tests (CDD fixed at 1230 μg/cm^2). Magnesium sulfate was not clearly seen to act as a corrosion inhibitor at humidity of either 36% RH or 46% RH on either 304L or 316L. At 58% RH inhibition was observed on both alloys.

On 304L, the critical SDD:CDD ratio (on a deposition density basis) was between ~0.3–1 and was only observed at high CDD (250–1230 μg/cm^2). The reason for the effect of CDD on the inhibiting effects of sulfate on 304L is unclear, though it is important to note that these levels of CDD are higher than those expected to develop in storage facilities for the majority of their service.[3] At high SDD:CCD ratios (>2). precipitation of magnesium sulfate removed any inhibiting effects (Figure 13e and Figure 15).

On 316L, comparison of control tests with tests containing sulfate indicated that, like in 304L, some inhibition was obtained at the highest RH tested (58%). At this RH, the SDD:CDD inhibition ratio was between ~0.1–0.3, which is slightly lower than that estimated for 304L. In this case, however, inhibition was also observed at lower CDD values and almost no corrosion was seen to occur under droplets containing magnesium sulfate precipitates at high SDD:CDD ratios (1 corrosion site in 40 droplets, Figure 13f), indicating that precipitation had little effect on the inhibition provided (notwithstanding the limited inherent reliability of tests on 316L).

Examples of inhibition ratios for sulfate on 304 reported in other studies in bulk solution are presented in Table VIII. On a concentration (molar) basis, typical inhibition ratios are of the order of 0.2–10 for sulfate, which are very scattered and substantially higher than those found in this study. One reason for this may be the definitions used for 'inhibition' in some of the electrochemical tests in the literature, being a condition under which no pitting was observed up to the largest applied potential (e.g. ~800 mV vs. Ag-AgCl).[13] In compar-

Table VI. Summary of literature data on pitting inhibition ratios on 304 stainless steel and similar alloys for nitrate – chloride solutions.[43]

Alloy	Temperature (°C)	NO_3^-:Cl^-	$\{NO_3^-\}$:$\{Cl^-\}$	Maximum $[Cl^-]$(mol/L)	Reference
18Cr-8Ni	25	0.4	–	0.56	Rosenfeld and Danilov 1967[12]
304	25	–	0.24	1.0	Leckie and Uhlig 1966[11]
304	25	0.2	–	0.5	Yashiro et al. 1997[13]
304*	25	0.2	–	0.2	Bobić and Jedić 2005[14]
18Cr–8Ni	–	–	0.2	3.12	Uhlig and Gilman 1964[7]

*= an alloy similar to Type 304.

Table VII. Summary of sulfate:chloride inhibition ratios for both logarithmic (CDDs between 0.85–850 μg/cm^2, 316L and 304L separately) and linear (CDD of 1230 μg/cm^2, 304L) variation tests (Figure 13 and Figure 15). Both tests give the range in which the inhibition ratio lies. Values where an inhibition range was only observed at high CDD conditions (250 – 850 μg/cm^2 on logarithmic tests, 1230 μg/cm^2 on linear tests) are marked with an asterisk (*). SO_4^{2-}:Cl^- ratios are calculated from deposited solution composition. Activity ratios could not be calculated as several solution compositions were thermodynamically over-saturated.

	SDD:CDD			SO_4^{2-}:Cl^-		
Relative humidity	35%	46%	58%	35%	46%	58%
Logarithmic variation (316L)	X	X	0.1–0.3	X	X	0.04–0.11
Logarithmic variation (304L)	X	X	0.3–1*	X	X	0.11–0.37*
Linear variation (304L)	X	X	0–0.5*	X	X	0-0.18*

X = No inhibition observed.
*= Inhibition only observed at high CDDs (>250 μg/cm^2).

ison, in this work all that may be required to inhibit corrosion is the raising of the pitting potential above that able to be supplied by the droplet. As such the upper values given in Table VIII may be overestimates for a droplet system. Furthermore the pH of the electrolyte solutions may have an effect on the critical inhibitor ratio, as suggested by Rosenfeld and Danilov (though it is interesting to note that Leckie and Uhlig disagree that there is any effect from neutral to low pH).[11,12] Not all studies report the pH of their testing solutions, which may introduce some uncertainty in interpreting the current literature data.

According to studies in bulk electrolytes,[11] the critical activity ratio for inhibition of sulfate to chloride increases with increasing chloride activity (the opposite to what was predicted in nitrate systems, but the same relation as has been found for nitrate systems in the current work), suggesting that the higher chloride concentrations obtained at low humidities would require higher SDD:CDD ratios.[34] This was observed in the current work, where sulfate:chloride ratios which had inhibited corrosion at 58% RH did not inhibit at 47% RH. Given the limited solubility of sulfate salts, there is therefore a more limited range of humidities where inhibition can be expected to occur, as a solution in equilibrium with a low humidity cannot hold sufficient sulfate in the aqueous phase as would be required to inhibit corrosion. If the values listed in Table VIII are indeed representative of a sulfate:chloride inhibition ratio, then it is likely that such solution ratios are only achievable under conditions of high humidity, where both chloride and sulfate species can remain in solution without precipitating.[34]

There were indications that corrosion product coverage was reduced in droplets with sulfate contents close to the inhibition/precipitation ratio. This was most clearly seen on the linear tests. This suggests that sulfate may affect the propagation of active pits.[42] However, the limited statistics of these tests suggests further work should be done in order to deliver robust ratios.

Solution precipitation.—Additional complexity in the interpretation of these tests is associated with the case of corrosion following precipitation of salts. In static humidity tests (such as those presented here) in which precipitation was observed to develop over time, precipitation occurs as a result of solution supersaturation. In mixed salt solutions, precipitation depends on both the humidity and the ratio of salts (it does not depend on the total deposition density of different salts). These factors will affect whether, when precipitation starts, salts containing inhibitor or chloride will form, followed, at the efflorescence point, by precipitation of both inhibitor-containing and chloride-containing salts (see below). For a given IDD:CDD ratio (where IDD is "inhibitor deposition density", representing either nitrate or sulfate), the effect of precipitation in removing ions from solution should be independent of the deposition density of each salt.

For $MgCl_2 + Mg(NO_3)_2$ mixtures, in droplets at NDD:CDD ratios $\gtrsim$3, precipitation was observed at 36% RH and 46% RH, though two instances of precipitation at NDD:CDD ratios <3 were observed (Figure 6b). At 36% RH on 304L corrosion was observed under some of these droplets. This indicates that, even when saturated in inhibitor, a solution containing a solid salt phase can undergo corrosion. In the case of nitrate salts, corrosion under precipitates was only observed at low humidities (36% RH) and may affect the corrosion behavior of stainless steel in relatively dry conditions.

Much more substantial precipitation was observed in sulfate solutions. In the case of $MgSO_4$ on 304L, inhibition was only observed at relatively high humidities (58% RH) and CDDs (>250 μg/cm^2) but was effectively lost at higher SDD:CDD ratios when precipitation occurred. In a droplet containing both aqueous and solid sulfate phases, the aqueous phase must be at saturation. It is notable that inhibiting effects were lost when saturation was observed, even though the solution concentration of sulfate was theoretically at its maximum value, and had shown inhibiting effects previously. This suggests that either (a) a greater inhibition ratio is required to prevent corrosion underneath solid deposits or (b) the systems which showed evidence of sulfate inhibition were in fact super-saturated, and the precipitation brought the aqueous solution sulfate content down below inhibiting levels.

Thermodynamic modelling of these binary salt systems does indicate that super-saturation of droplets was occurring in systems just beyond thermodynamic saturation. Figure 6a shows experimental data overlaid with the theoretical saturation point of $Mg(NO_3)_2$ under these conditions. While precipitation was observed in some cases in systems above this threshold, it was not seen in all cases, suggesting

Table VIII. Summary of literature data on pitting inhibition ratios on 304 stainless steel and similar alloys for sulfate – chloride solutions.[43]

Alloy	Temperature (°C)	SO_4^{2-}:Cl^-	{SO_4^{2-}}:{Cl^-}	Maximum [C^-](mol/L)	Reference
18Cr-8Ni	25	2,10*	–	0.56	Rosenfeld and Danilov 1967[12]
304	25	–	1.15	1.0	Leckie and Uhlig 1966[11]
304	25	0.2–5	–	0.5	Yashiro et al. 1997[13]
304**	25	5	–	0.2	Bobić and Jedić 2005[14]

*Inhibition ratios varied with pH, with ratios of 2 observed for pHs of 2 and 12, and a ratio for 10 observed for a pH of 7.
**an alloy similar to type 304.

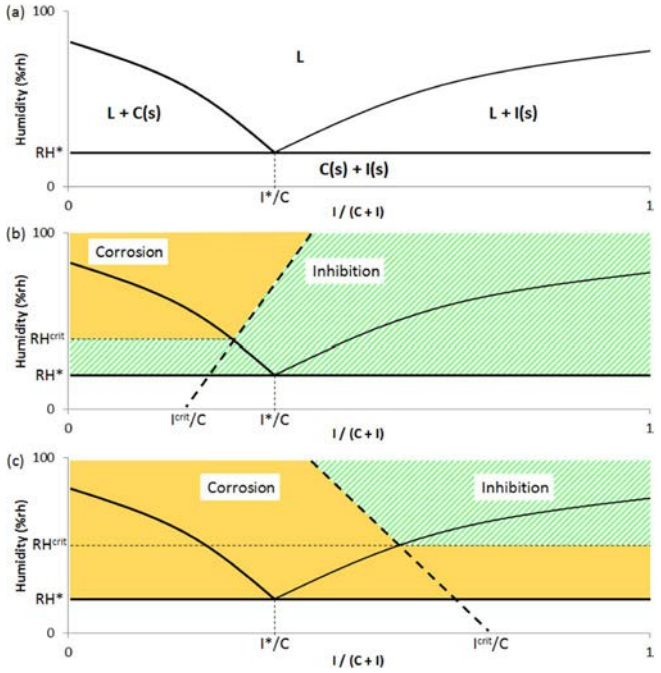

Figure 18. Schematics of the (a) phase and (b,c) possible corrosion behaviors of a general mixed salt system, composed of salts I (inhibitor) and C (chloride), in relation to the equilibrium ambient humidity. I^*/C is the eutectic point of the system; the I^{crit}/C line (b,c) is defined as the solution ratio over which corrosion is inhibited, for which two specific dependences on RH are assumed for illustrative purposes.

that some droplets were maintaining a thermodynamically unstable concentration of salts.

Mixed salt phases at variable humidities.—In single salt systems, the humidity and deposition density together control the extent/continuity of any moisture film or droplet developed on exposed surfaces, which controls the overall amount of cathodic surface able to drive corrosion damage and hence the extent of damage (as noted in other studies as well as in this study).[2,21,36] In studies with mixed salts, however, the relative deposition density of different salts also affects the wetting behavior of the system.

Figure 18a shows a schematic phase diagram of a binary system containing salts I (inhibiting salt) and C (chloride salt), which have no mutual solubility in the solid phase, as a function of composition. The eutectic point is at RH^* and a concentration fraction I^*/C. This is the lowest RH at which a liquid phase can be found. To the left of this composition (an overall composition rich in C), in the L+C(s) region, solid C will be found, with a solution concentration (given by the tie line to the liquidus) that is richer in I than the overall composition. To the right of the eutectic composition (overall composition richer in I), in the L+I(s) region, solid I will be found with a solution composition given by the tie line that is richer in C than the overall composition. However, in the liquid region (L), the composition of the solution is identical to the overall composition.

The corrosion behavior of a mixed salt droplet can be considered by assuming that there is a critical ratio of inhibitor:chloride, I^{crit}/C, required to inhibit corrosion (this value may vary with RH). Two systems with different example inhibitors (and inhibitor behaviors) are shown in Figure 18. In general, it is the absolute I/C ratio on the surface and its relationship with I^{crit}/C which is of prime importance in predicting corrosion behavior. Depending on the variation of I^{crit}/C with RH, however, the humidity may still need to be taken into account, both in terms of changes in inhibition ratios as a function of concentration/activity (as seen in this work for nitrate) and, at relatively low RH, in terms of any precipitation effects that may occur.

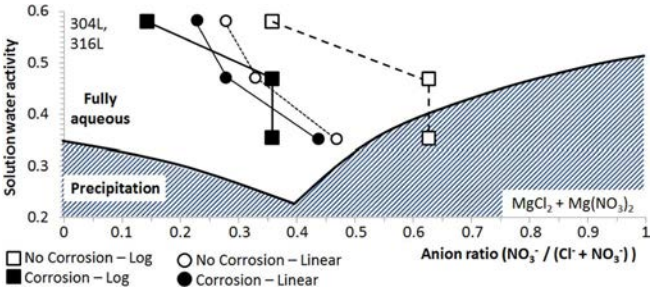

Figure 19. Saturation conditions for a $MgCl_2 + Mg(NO_3)_2$ mixed salt system. Calculated at 30°C using OLI Analyser 9.2, MSE database. Corrosion and inhibition data on both 304L and 316L alloys has been overlaid (data from Figure 9). Solution water activity is equivalent to equilibrium relative humidity, i.e. water activity x 100 = RH%.

Figure 18b shows a system where I^{crit}/C crosses the liquidus line to the left of the eutectic (I^*/C). In such a system, variations in humidity will never cause sufficient inhibitor salt to be precipitated, and thus removed, from the liquid phase to allow corrosion (i.e. to bring I/C below I^{crit}/C). In this case, the dependence of the corrosion behavior on the RH may be limited, though the variation of I^{crit}/C with RH in this example does allow the system to become uninhibited for certain values of I/C at higher RHs. Figure 18c, conversely, shows an inhibitor with I^{crit}/C crossing the liquidus to the right of the eutectic point. In this system, even in inhibitor-rich systems (i.e. $I/C > I^{crit}/C$), sufficiently low RH may cause I (the inhibitor salt) to precipitate, removing it from solution and potentially allowing the solution composition to decrease below I^{crit}/C. In such a case, both the salt ratios and the humidity are of key importance in predicting the corrosion behavior of the system.

These considerations illustrate a simple I^{crit}/C dependence on RH, and it should be highlighted that any real dependence may be more complex than a simple linear relation. It also assumes that the formation of precipitates has no effect on the value of I^{crit}/C. If this is not the case, the system will display additional complexity, displaying a larger number of possible behaviors but also becoming more difficult to generalize (i.e. the complexity will depend on the functional form of the solution concentration (I/C), and inhibition ratio (I^{crit}/C), with the relative humidity).

Figure 19 and Figure 20 show thermodynamic saturation curves for $MgCl_2 + Mg(NO_3)_2$, and $MgCl_2 + MgSO_4$ systems, respectively, together with the experimental data obtained in this work. For the nitrate system, the data points show experimental findings for corrosion and inhibition as a function of water activity (determined from RH) and anion fraction taken from Figure 9 (largely based on 304L, but considered applicable to 316L). For the sulfate system, results from the linear tests on 304L and the logarithmic tests on 316L have been shown.

The nitrate system in Figure 19 shows similarities with the model system suggested in Figure 18c, with I^{crit}/C increasing with decreasing RH, and crossing the liquidus to the right of the eutectic point. In the

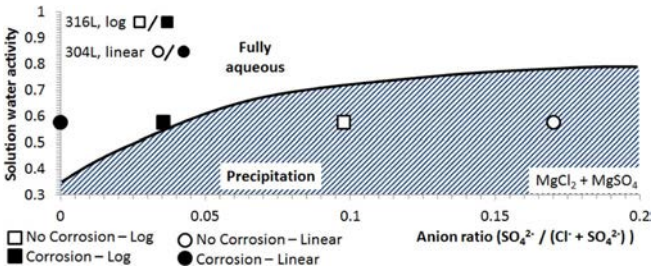

Figure 20. Saturation conditions for a $MgCl_2 + MgSO_4$ mixed salt system. Calculated at 30°C using OLI Analyser 9.2, MSE database. Corrosion and inhibition data for 316L (logarithmic tests, squares) and 304L (linear tests, circles) have been overlaid. Solution water activity is equivalent to equilibrium relative humidity, i.e. water activity x 100 = RH%.

conditions tested, any dependence of the inhibition effect from the relative humidity is likely to be associated with changes in anion activity as a function of RH rather than precipitation effects, although precipitation effects may be expected to potentially play a role at particularly low RH.

The sulfate system in Figure 20, conversely, lacks sufficient data to establish an I^{crit}/C trend, although it is interesting to see that inhibition was observed in conditions where sulfate precipitation was expected (based on thermodynamic calculations) but not observed. As such, one may conclude that inhibition was only seen in cases of supersaturation, and not in thermodynamically stable conditions.

It is clear that, in order to fully assess atmospheric systems consisting of mixed salts, thermodynamic modelling is a key tool to predict and interpret the appearance of different chemical phases from solution, and to give insight as to the evolution of corrosion behavior when the exposure conditions of these systems changes. In this work, thermodynamic calculations (in line with the well-established theory of phase separation) and experimental work have shown that a liquid phase containing a corrosion inhibitor (either nitrate or sulfate in this work) may be present in mixed salts below the saturation point (i.e. at lower RH) of the inhibiting salt, thus affording some corrosion protection. Precipitation/dissolution of either corrosive and/or inhibiting salts as the RH varies will change the chemistry of the aqueous solution, with the potential to increase or decrease the amount of inhibitor present in solution, and so affect whether or not corrosion will occur.

Combinatorial droplet tests have been shown in this study to be an excellent method for investigating such atmospheric systems, allowing a large range of variables (absolute deposition densities, inhibitor:chloride ratios, alloy, inhibitor type, exposure RH) to be combined with high levels of statistical robustness in order to deliver results with confidence.

Conclusions

Experiments were carried out on 304L and 316L stainless steels to assess the ability of nitrate and sulfate to act as corrosion inhibitors for atmospheric corrosion in chloride-containing environments. Tests were carried out at 31°C in a range of humidities (between 35–75% RH) with mixtures of chloride salts ($MgCl_2$ and $CaCl_2$) and inhibiting salts ($MgNO_3$, $MgSO_4$ and $CaSO_4$) as well as in the absence of inhibiting salt (control experiments). Deposition densities of chloride tested ranged between ~8 and 1,200 $\mu g/cm^2$, compared with levels up to 100 $\mu g/cm^2$ expected to be relevant to the specific problem studied (the storage of ILW containers). The results of this study indicate that:

- Magnesium nitrate acts as a corrosion inhibitor on both 304L and 316L at all humidities tested (between 35% to 58% RH), when the ratio between the nitrate deposition density and the chloride deposition density (NDD:CDD, anion mass per unit area) is above a critical value. This critical value generally decreases as the relative humidity increases, and is similar for both 304L and 316L. The critical inhibition ratio on a mass basis was in the range ~1–3 at 36% RH and 46% RH, and ~0.3–1 for 58% RH, judged across a range of CDDs (0.85–850 $\mu g/cm^2$).
- Magnesium sulfate does not act as a corrosion inhibitor for either 304L or 316L at humidities of 36% RH or 46% RH. At 58% RH sulfate inhibited corrosion of 316L at a critical sulfate:chloride deposition density ratio (SDD:CDD, anion mass per unit area) within the range ~0.1–0.3. Sulfate also inhibited pitting of 304L at 58% RH at a critical SDD:CDD ratio between ~0.3 and 0.5, though only when the CDD was high, between 250 and 1230 $\mu g/cm^2$. In general, the behavior of magnesium sulfate in these tests was not straightforward to ascertain, given its tendency to precipitate and indications that, when achieved, inhibition was associated with supersaturated solutions (see below).
- Precipitation of nitrate and particularly sulfate salts occurred in high IDD:CDD systems, depending on humidity, and under some droplets caused a loss of corrosion inhibition. This is suggested to be caused by either the formation of a more stable corrosion environment under precipitates (i.e. crevice or under-deposit corrosion), or as evidence of previous super-saturation of inhibitor in solution.
- A model for the interaction and development of chloride/inhibitor systems under varying humidities was developed based on thermodynamic calculations, for use in predicting the behavior of such systems under conditions close to and beyond saturation.
- Preliminary work on the role of calcium sulfate deposits on atmospheric corrosion did not give any indication that their presence influenced pitting susceptibility of 316L stainless steel in the presence of either magnesium or calcium chloride, but further work is required to confirm this.

Acknowledgments

The authors thank Fraser King (Integrity consulting Ltd.), Kevin Christie and Cliff Harris (Amec Foster Wheeler) and Trevor Rayment (Diamond Light Source Ltd.) for useful discussions. The work was funded by EPSRC (grant EP/I036397/1) and Radioactive Waste Management Ltd. (Contract NPO004411A-EPS02). Supplementary data may be accessed via http://epapers.bham.ac.uk/2952/.

References

1. Nuclear Decomissioning Authority, *Geological Disposal: Package Evolution Status Report*, NDA/RWMD/031, 2010.
2. C. Padovani, O. E. Albores-Silva, and E. A. Charles, *Corrosion*, **71** (3), 292 (2015).
3. C. Padovani, R. J. Winsley, N. R. Smart, P. A. H. Fennell, C. Harris, and K. Christie, *Corrosion*, **71** (5), 646 (2015).
4. R. P. V. Cruz, A. Nishikata, and T. Tsuru, *Corrosion Science*, **38** (8), 1397 (1996).
5. R. P. V. Cruz, A. Nishikata, and T. Tsuru, *Corrosion Science*, **40** (1), 125 (1998).
6. T. Prosek, A. Le Gac, D. Thierry, S. Le Manchet, C. Lojewski, A. Fanica, E. Johansson, C. Canderyd, F. Dupoiron, T. Snauwaert, F. Maas, and B. Droesbeke, *Corrosion*, **70** (10), 1052 (2014).
7. H. H. Uhlig and J. R. Gilman, *Corrosion*, **20** (9), 289t (1964).
8. G. O. H. Whillock, T. J. Binks, and C. J. Donohoe, *Corrosion*, **68** (11), (2012).
9. R. S. Lillard, G. Vasquez, and D. F. Bahr, *Corrosion*, **66** (7), (2010).
10. S. R. Street, W. C. Xu, M. Amri, L. Y. Guo, S. J. M. Glanvill, P. D. Quinn, J. F. W. Mosselmans, J. Vila-Comamala, C. Rau, T. Rayment, and A. J. Davenport, *Journal of the Electrochemical Society*, **162** (9), C457 (2015).
11. H. P. Leckie and H. H. Uhlig, *Journal of the Electrochemical Society*, **113** (12), 1262 (1966).
12. I. L. Rosenfeld and I. S. Danilov, *Corrosion Science*, **7** (3), 129 (1967).
13. H. Yashiro, A. Oyama, and K. Tanno, *Corrosion*, **53** (4), 290 (1997).
14. B. Bobić and B. Jegdić, *Scientific-Technical Review*, **55** (3), 3 (2005).
15. C. S. Brossia and R. G. Kelly, *Corrosion*, **54** (2), 145 (1998).
16. R. C. Newman and M. A. A. Ajjawi, *Corrosion Science*, **26** (12), 1057 (1986).
17. R. C. Newman and T. Shahrabi, *Corrosion Science*, **27** (8), 827 (1987).
18. OLI Systems, 2015.
19. T. V. Nam, E. Tada, and A. Nishikata, *Journal of the Electrochemical Society*, **162** (9), C419 (2015).
20. Y. Tsutsumi, A. Nishikata, and T. Tsuru, *Corrosion Science*, **49** (3), 1394 (2007).
21. N. Mi, M. Ghahari, T. Rayment, and A. J. Davenport, *Corrosion Science*, **53** (10), 3114 (2011).
22. S. Hastuty, Y. Tsutsumi, A. Nishikata, and T. Tsuru, *ISIJ Int.*, **52** (5), 863 (2012).
23. X. X. Fu, J. H. Dong, E. H. Han, and W. Ke, *Sensors*, **9** (12), 10400 (2009).
24. G. S. Frankel, M. Stratmann, M. Rohwerder, A. Michalik, B. Maier, J. Dora, and M. Wicinski, *Corrosion Science*, **49** (4), 2021 (2007).
25. E. Schindelholz and R. G. Kelly, *Electrochemical and Solid State Letters*, **13** (10), C29 (2010).
26. B. E. Risteen, E. Schindelholz, and R. G. Kelly, *Journal of the Electrochemical Society*, **161** (14), C580 (2014).
27. S. Shoji and N. Ohnaka, *Corrosion Engineering*, **38** (2), 92-7 (1989).
28. M. Gunther, N. P. C. Stevens, G. McFiggans, and A. B. Cook, *Corrosion Engineering Science and Technology*, **49** (6), 509 (2014).
29. B. Maier and G. S. Frankel, *Journal of the Electrochemical Society*, **157** (10), C302 (2010).
30. F. King, P. Robinson, C. Watson, J. Burrow, and C. Padovani, *NACE International*, **Corrosion/2013** (paper no. 2717), (2013).
31. AMEC, *Investigation Into the Atmospheric Corrosion of Stainless Steel ILW containers – Tests With Salt Mixtures and in Conditions of Cyclic Relative Humidity*, 17391/TR/0009-4, 2016.
32. ASTM, *E104-02(2007) "Standard Practice for Maintaining Constant Relative Humidity by Means of Aqueous Solutions"*, 2007.
33. S. R. Street, N. Mi, A. J. M. C. Cook, H. B. Mohammed-Ali, L. Guo, T. Rayment, and A. J. Davenport, *Faraday Discuss.*, **180** (0), 251 (2015).
34. P. Pohjanne, L. Carpén, T. Hakkarainen, and P. Kinnunen, *Journal of Constructional Steel Research*, **64** (11), 1325 (2008).
35. Y. Tsutsumi, A. Nishikata, and T. Tsuru, *Journal of The Electrochemical Society*, **152** (9), B358 (2005).
36. Z. Y. Chen and R. G. Kelly, *Journal of The Electrochemical Society*, **157** (2), C69 (2010).
37. R. H. Jung, H. Tsuchiya, and S. Fujimoto, *ISIJ Int.*, **52** (7), 1356 (2012).

38. C. Clayton and O. lngemar, in *Corrosion Mechanisms in Theory and Practice*, Third Edition, p. 327, CRC Press, (2011).
39. R. C. Newman, *Corrosion Science*, **25** (5), 331 (1985).
40. R. S. Lillard, G. Vasquez, and D. F. Bahr, *Journal of the Electrochemical Society*, **158** (6), C194 (2011).
41. P. C. Pistorius and G. T. Burstein, *Philos. Trans. R. Soc. Lond. Ser. A-Math. Phys. Eng. Sci.*, **341** (1662), 531 (1992).
42. P. C. Pistorius and G. T. Burstein, *Corrosion Science*, **33** (12), 1885 (1992).
43. F. King, e-mail to A. Cook, (26/02/2014).

8 GENERAL CONCLUSIONS

Experiments with mixed composition electrolytes have shown that the addition of other salt species to chloride containing droplets, and even different species of chlorides, can drastically alter the corrosion behaviour of stainless steels under atmospheric conditions. Such complex mixtures are more representative of actual conditions within stores, and indeed in other atmospheric environments; while simpler model systems comprising single species are useful in order to understand fundamental aspects of a system, the differences between model and real systems may be really quite pronounced. In general the amount of corrosion observed under pure $MgCl_2$ droplets (for example) in a laboratory testing environment is likely to be very much greater than that observed in realistic conditions, where solid phases and inhibiting species are likely to be also present.

As such it is clear that, in order to more accurately predict the evolution of corrosion over time, a full understanding of the chemical species present on a given surface and their interaction both with each other and their environment is important; it is insufficient to rely solely on single metrics, such as the level of chloride contamination, to predict corrosion behaviour.

Thermodynamic calculations can prove a useful tool in assessing the environmental regimes in which given species are likely to be present, in what phases (i.e. aqueous, solid), and in what concentrations. These calculations can highlight circumstances where corrosion may occur or be inhibited, and at the very least indicate which systems are worth further experimental exploration.

The automated deposition of electrolyte droplets onto stainless steel samples has provided a useful method to test the atmospheric corrosion of stainless steels under

multiple electrolyte thin-films. This has been key in both gathering statistically significant amounts of data, as well as altering multiple experimental parameters in parallel for high-throughput experiments, a feature which is extremely useful when testing multivariate systems such as those found in ILW stores. Alongside this, the utility of an equally high-throughput monitoring technique allows useful insights into the corrosion processes to be gained with comparatively little experimental overhead. It is worth highlighting, however, that the automated generation of large datasets still requires the development of automated analytical techniques to fully utilise the potential capability.

Where experiments directly compared the behaviour of 304L and 316L stainless steels, 316L was seen to be generally more resistant to the initiation of corrosion, with fewer droplets exhibiting corrosion on 316L than on 304L, for a given experimental condition. When corrosion did initiate on 316L, however, the propagation of pitting was seen to be comparable to that on 304L. Further, the critical inhibition ratio for nitrate:chloride deposits was found to be the same for both 304L and 316L, within experimental resolution.

9 FUTURE WORK

All experiments discussed in this thesis have been conducted over a period of seven or fewer days. There is an opportunity, therefore, to investigate corrosion under droplets for extended periods, in order to verify and validate the results gathered for the week-long tests. The chloride:inhibitor ratios for the inhibition of corrosion, for example, may also have a time dependence, whereby corrosion was not fully inhibited but delayed to a point beyond the seven day test period. Longer testing periods would allow any time-dependence of this nature to be better explored.

Surveys of chemicals found on ILW store surfaces found detectable levels of oxalate, formate and bicarbonate.[10] The effect of both a range of carboxylic acids likely to be present in stores, as well as the effect of electrolyte pH on the atmospheric corrosion of stainless steels are of interest in order to build a more complete understanding of the interplay between the ILW containers and the chemical species found on them.

The tests conducted in this thesis used droplets to simulate thin electrolyte layers, which are indicative of an interconnected atmospheric deposit which has been developed over a period of time. In more realistic situations the chemical deposits will build up from gradual aerosol deposition, and so a patchy, disconnected electrolyte is likely to be more representative of the earlier stages of atmospheric exposure. As such, the development of a technique to deposit aerosol-like particles in a repeatable, high-throughput manner (akin to the automated droplet deposition system discussed in this thesis) would be of benefit.

Lastly, despite the benefit of the generation of large data-sets from automated and high-throughput techniques, the generation of such large amounts of data requires

corresponding high-throughput analytical techniques. The automated image analysis, for example, of in-situ scanner data to detect the onset of pitting, or the propagation of corrosion products would allow the full utility of these techniques to come to the fore.

10 REFERENCES

1. Shelley, P.B., *Ozymanidas*. Miscellaneois and Posthumour Poems of Percy Bysshe Shelley. 1826, London.

2. Smith, H., *Ozymanidas*. Amarynthis, The Nympholet: A Pastoral Drama, In Three Acts. With Other Poems. 1821, London: Longman, Hurst, Rees, Orme, & Brown.

3. *Implementing Geological Disposal - A Framework for the long-term management of higher activity radioactive waste*, Department of Energy & Climate Change UK, 2014, Department of Energy & Climate Change UK, https://www.gov.uk/government/uploads/system/uploads/attachment_data/file/332890/GDF_White_Paper_FINAL.pdf

4. *Meeting the Energy Challange - a Whitepaper on Nuclear Power*, Department for Business, Enterprise & Regulatory Reform, 2008, Department for Business, Enterprise & Regulatory Reform, http://webarchive.nationalarchives.gov.uk/+/http:/www.berr.gov.uk/files/file43006.pdf

5. Nuclear Decomissioning Authority, *Geological Disposal: An overview of the generic Disposal System Safety Case*, Radioactive Waste Management Limited, 2010,

6. Nuclear Decomissioning Authority, *UK Radioactive Higher Activity Waste Storage Review March 2009*, 2009,

7. Nuclear Decomissioning Authority, *Industry Guidance: Interim Storage of Higher Activity Waste Packages - Intgrated Approach*, I.W. Management, 2012,

8. R. J. Winsley, N.R.S., B. Reddy, A. P. Rance, P. A. H. Fennell, *4 Metre Box Monitoring Programme – Final Report for the Period 2007-2010*, Serco, 2011, NR3219/011 NPO2279

9. Harris, C., *Current Environmental Conditions Within Interim Stores and GDF Analogues*, Amec, 2012, 17391/TR/0007

10. Padovani, C., R.J. Winsley, N.R. Smart, P.A.H. Fennell, C. Harris, and K. Christie, *Corrosion Control of Stainless Steels in Indoor Atmospheres—Practical Experience (Part 2).* Corrosion, 2015. **71**(5): p. 646-666.

11. Harris, C., *A Survey of Current Environmental Conditions Within ILW Interim Stores and Potential GDF Analogues*, AMEC, 2015, 17391/TR/0007

12. P.A.H. Fennell, N.R.S., M. Izzo, N.A. Turner, *Characterisation of Environmental Conditions in an ILW Store*, Amec, 2012, D.005265/001

13. Bhadeshia, H.K.D.H. and R. Honeycombe, *Steels - Microstructure and Properties*. 3rd ed. 2006, Oxford: Butterworth-Heinemann.

14. Clayton, C., R and O. Ingemar, *Passivity of Austenitic Stainless Steels*, in *Corrosion Mechanisms in Theory and Practice, Third Edition*. 2011, CRC Press. p. 327-347.

15. Ryan, M.P., D.E. Williams, R.J. Chater, B.M. Hutton, and D.S. McPhail, *Why stainless steel corrodes.* Nature, 2002. **415**(6873): p. 770-774.

16. Webb, E.G. and R.C. Alkire, *Pit initiation at single sulfide inclusions in stainless steel - I. Electrochemical microcell measurements.* Journal of the Electrochemical Society, 2002. **149**(6): p. B272-B279.

17. Webb, E.G. and R.C. Alkire, *Pit initiation at single sulfide inclusions in stainless steel - II. Detection of local pH, sulfide, and thiosulfate.* Journal of the Electrochemical Society, 2002. **149**(6): p. B280-B285.

18. Webb, E.G. and R.C. Alkire, *Pit initiation at single sulfide inclusions in stainless steel - III. Mathematical model.* Journal of the Electrochemical Society, 2002. **149**(6): p. B286-B295.

19. Wranglen, G., *Pitting and sulphide inclusions in steel.* Corrosion Science, 1974. **14**(5): p. 331-349.

20. Dieter, L., *Introduction to Surface Reactions*, in *Corrosion Mechanisms in Theory and Practice*. 2002, CRC Press. p. 1-17.

21. Thibeau, R.J., C.W. Brown, and R.H. Heidersbach, *Raman Spectra of Possible Corrosion Products of Iron.* Applied Spectroscopy, 1978. **32**(6): p. 532-535.

22. Pourbaix, M.J.N., *Thermodynamique des solutions aqueuses diluées: Représentation graphique du rôle du pH et du potentiel* [P.hD Thesis thesis]. Delft: Delft Technical University; 1945

23. Pourbaix, M., *Some Applications of Potential – pH Diagrams to the Study of Localized Corrosion.* Journal of The Electrochemical Society, 1976. **123**(2): p. 25C-36C.

24. Barry, M. and G. Michael, *Growth and Stability of Passive Films*, in *Corrosion Mechanisms in Theory and Practice*. 2002, CRC Press. p. 189-216.

25. Williams, D.E., C. Westcott, and M. Fleischmann, *Stochastic-models of pitting corrosion of stainless-steels .2. Measurement and interpretation of data at constant potential.* Journal of the Electrochemical Society, 1985. **132**(8): p. 1804-1811.

26. Frankel, G.S., *Pitting corrosion of metals - A review of the critical factors.* Journal of the Electrochemical Society, 1998. **145**(6): p. 2186-2198.

27. Michel, K., *Anodic Dissolution*, in *Corrosion Mechanisms in Theory and Practice*. 2002, CRC Press. p. 97-169.

28. Strehblow, H.H. and B. Titze, *Pitting potentials and inhibition potentials of iron and nickel for different aggressive and inhibiting anions.* Corrosion Science, 1977. **17**(6): p. 461-472.

29. Williams, G., H.A.L. Dafydd, R. Subramanian, and H.N. McMurray, *The Influence of Chloride Ion Concentration on Passivity Breakdown in Magnesium.* Corrosion, 2017. **73**(5): p. 471-481.

30. Chen, Z.Y. and R.G. Kelly, *Computational Modeling of Bounding Conditions for Pit Size on Stainless Steel in Atmospheric Environments.* Journal of The Electrochemical Society, 2010. **157**(2): p. C69-C78.

31. Soltis, J., *Passivity breakdown, pit initiation and propagation of pits in metallic materials – Review.* Corrosion Science, 2015. **90**(0): p. 5-22.

32. Asami, K., K. Hashimoto, and S. Shimodaira, *Xps study of passivity of a series of iron-chromium alloys in sulfuric-acid.* Corrosion Science, 1978. **18**(2): p. 151-160.

33. Galvele, J.R., *Transport processes and mechanism of pitting of metals.* Journal of the Electrochemical Society, 1976. **123**(4): p. 464-474.

34. Strehblow, H., *Mechanisms of Pitting Corrosion*, in *Corrosion Mechanisms in Theory and Practice*, P. Marcus, Editor. 2002, Marcel Dekker, Inc.: New York, NY.

35. Greene, N.D. and M.G. Fontana, *A Critical Analysis of Pitting Corrosion.* CORROSION, 1959. **15**(1): p. 41-47.

36. Hoar, T.P., D.C. Mears, and G.P. Rothwell, *The relationships between anodic passivity, brightening and pitting.* Corrosion Science, 1965. **5**: p. 279.

37. Sato, N., *A theory for breakdown of anodic oxide films on metals.* Electrochimica Acta, 1971. **16**(10): p. 1683-1692.

38. Kolotyrkin, J.M., *Pitting Corrosion of Metals.* CORROSION, 1963. **19**(8): p. 261t-268t.

39. Hoar, T.P. and W.R. Jacob, *Breakdown of Passivity of Stainless Steel by Halide Ions.* Nature, 1967. **216**(5122): p. 1299-1301.

40. Eklund, G.S., *Initiation of pitting at sulfide inclusions in stainless-steel.* Journal of the Electrochemical Society, 1974. **121**(4): p. 467-473.

41. Stewart, J. and D.E. Williams, *The initiation of pitting corrosion on austenitic stainless-steel - on the role and importance of sulfide inclusions.* Corrosion Science, 1992. **33**(3): p. 457-&.

42. Galvele, J., *Transport processes in passivity breakdown—II. Full hydrolysis of the metal ions.* Corrosion Science, 1981. **21**(8): p. 551-579.

43. Williams, D.E., M.R. Kilburn, J. Cliff, and G.I.N. Waterhouse, *Composition changes around sulphide inclusions in stainless steels, and implications for the initiation of pitting corrosion.* Corrosion Science, 2010. **52**(11): p. 3702-3716.

44. Philippe, M., *Sulfur-Assisted Corrosion Mechanisms and the Role of Alloyed Elements*, in *Corrosion Mechanisms in Theory and Practice*. 2002, CRC Press. p. 287-310.

45. Castle, J.E. and R. Ke, *Studies by auger-spectroscopy of pit initiation at the site of inclusions in stainless-steel.* Corrosion Science, 1990. **30**(4-5): p. 409-428.

46. Laitinen, T., *Localized corrosion of stainless steel in chloride, sulfate and thiosulfate containing environments.* Corrosion Science, 2000. **42**(3): p. 421-441.

47. Meng, Q., G.S. Frankel, H.O. Colijn, and S.H. Goss, *Metallurgy - Stainless-steel corrosion and MnS inclusions.* Nature, 2003. **424**(6947): p. 389-390.

48. Ryan, M.P., D.E. Williams, R.J. Chater, B.M. Hutton, and D.S. McPhail, *Metallurgy - Stainless-steel corrosion and MnS inclusions - Reply.* Nature, 2003. **424**(6947): p. 390-390.

49. Isaacs, H.S., *Behavior of resistive layers in localized corrosion of stainless-steel.* Journal of the Electrochemical Society, 1973. **120**(11): p. 1456-1462.

50. Beck, T.R. and R.C. Alkire, *Occurrence of salt films during initiation and growth of corrosion pits.* Journal of the Electrochemical Society, 1979. **126**(10): p. 1662-1666.

51. Alkire, R.C. and K.P. Wong, *The corrosion of single pits on stainless-steel in acidic chloride solution.* Corrosion Science, 1988. **28**(4): p. 411-&.

52. Laycock, N.J. and R.C. Newman, *Localised dissolution kinetics, salt films and pitting potentials.* Corrosion Science, 1997. **39**(10-11): p. 1771-1790.

53. Frankel, G.S., L. Stockert, F. Hunkeler, and H. Bohni, *Metastable pitting of stainless steel.* Corrosion 1987. **43**: p. 429-436.

54. Pistorius, P.C. and G.T. Burstein, *Metastable pitting corrosion of stainless-steel and the transition to stability.* Philosophical Transactions of the Royal Society of London Series a-Mathematical Physical and Engineering Sciences, 1992. **341**(1662): p. 531-559.

55. Isaacs, H.S., *The localized breakdown and repair of passive surfaces during pitting.* Corrosion Science, 1989. **29**(2-3): p. 313-323.

56. Williams, D.E., J. Stewart, and P.H. Balkwill, *The nucleation, growth and stability of micropits in stainless steel.* Corrosion Science, 1994. **36**(7): p. 1213-1235.

57. Tester, J.W. and H.S. Isaacs, *Diffusional Effects in Simulated Localized Corrosion.* Journal of The Electrochemical Society, 1975. **122**(11): p. 1438-1445.

58. Ghahari, M., D. Krouse, N. Laycock, T. Rayment, C. Padovani, M. Stampanoni, F. Marone, R. Mokso, and A.J. Davenport, *Synchrotron X-ray radiography studies of pitting corrosion of stainless steel: Extraction of pit propagation parameters.* Corrosion Science, 2015. **100**: p. 23-35.

59. Ryan, M.P., N.J. Laycock, H.S. Isaacs, and R.C. Newman, *Corrosion pits in thin films of stainless steel.* Journal of the Electrochemical Society, 1999. **146**(1): p. 91-97.

60. Ernst, P. and R.C. Newman, *Pit growth studies in stainless steel foils. I. Introduction and pit growth kinetics.* Corrosion Science, 2002. **44**(5): p. 927-941.

61. Ernst, P. and R.C. Newman, *Pit growth studies in stainless steel foils. II. Effect of temperature, chloride concentration and sulphate addition.* Corrosion Science, 2002. **44**(5): p. 943-954.

62. Pierre, C., *Crevice Corrosion of Metallic Materials*, in *Corrosion Mechanisms in Theory and Practice, Third Edition*. 2011, CRC Press. p. 449-498.

63. Brossia, C.S. and R.G. Kelly, *Influence of Alloy Sulfur Content and Bulk Electrolyte Composition on Crevice Corrosion Initiation of Austenitic Stainless Steel.* Corrosion, 1998. **54**(2): p. 145-154.

64. Nishimoto, M., J. Ogawa, I. Muto, Y. Sugawara, and N. Hara, *Simultaneous visualization of pH and Cl− distributions inside the crevice of stainless steel.* Corrosion Science, 2016. **106**: p. 298-302.

65. Aoki, S., *Optical Microscopic In-situ Observation of Crevice Corrosion of a Duplex Stainless Steel*, in *Electrochem*2017: Birmingham.

66. Frankel, G., J. Mauzeroll, G. Thornton, H. Bluhm, J. Morrison, V. Maurice, T. Rayment, D. Williams, A. Cook, G. Joshi, A. Davenport, S. Gibbon, D. Kramer, M. Acres, M. Tautschnig, H. Habazaki, P. Marcus, D. Shoesmith, C. Wren, T. Majchrowski, R. Lindsay, M. Wood, M. Todorova, J. Scully, F. Renner, A. Kokalj, C. Taylor, S. Virtanen, and J. Wharton, *Corrosion scales and passive films: general discussion.* Faraday Discussions, 2015. **180**(0): p. 205-232.

67. Frankel, G., G. Thornton, S. Street, T. Rayment, D. Williams, A. Cook, A. Davenport, S. Gibbon, D. Engelberg, C. Ornek, A. Mol, P. Marcus, D. Shoesmith, C. Wren, K. Yliniemi, G. Williams, S. Lyon, R. Lindsay, T. Hughes, J. Lutzenkirchen, S.-T. Cheng, J. Scully, S.F. Lee, R. Newman, C. Taylor, R. Springell, J. Mauzeroll, S. Virtanen, S. Heurtault, and J. Sullivan, *Localised corrosion: general discussion.* Faraday Discussions, 2015. **180**(0): p. 381-414.

68. Maurice, V., H. Peng, L.H. Klein, A. Seyeux, S. Zanna, and P. Marcus, *Effects of molybdenum on the composition and nanoscale morphology of passivated austenitic stainless steel surfaces.* Faraday Discussions, 2015. **180**(0): p. 151-170.

69. Tan, M.W., E. Akiyama, A. Kawashima, K. Asami, and K. Hashimoto, *The effect of air exposure on the corrosion behavior of amorphous Fe-8Cr-Mo-13P-7C alloys in 1 M HCl.* Corrosion Science, 1995. **37**(8): p. 1289-1301.

70. Olefjord, I., *The passive state of stainless steels.* Materials Science and Engineering, 1980. **42**: p. 161-171.

71. Clayton, C.R. and Y.C. Lu, *A Bipolar Model of the Passivity of Stainless Steel: The Role of Mo Addition.* Journal of The Electrochemical Society, 1986. **133**(12): p. 2465-2473.

72. Lu, Y.C., C.R. Clayton, and A.R. Brooks, *A bipolar model of the passivity of stainless steels—II. The influence of aqueous molybdate.* Corrosion Science, 1989. **29**(7): p. 863-880.

73. Castle, J.E. and J.H. Qiu, *A co-ordinated study of the passivation of alloy steels by plasma source mass spectrometry and x-ray photoelectron spectroscopy—1. characterization of the passive film.* Corrosion Science, 1989. **29**(5): p. 591-603.

74. Elbiache, A. and P. Marcus, *The role of molybdenum in the dissolution and the passivation of stainless steels with adsorbed sulphur.* Corrosion Science, 1992. **33**(2): p. 261-269.

75. Marcus, P. and M. Moscatelli, *The Role of Alloyed Molybdenum in the Dissolution and the Passivation of Nickel‐Molybdenum Alloys in the Presence of Adsorbed Sulfur.* Journal of The Electrochemical Society, 1989. **136**(6): p. 1634-1637.

76. Olefjord, I. and B.-O. Elfstrom, *The Composition of the Surface during Passivation of Stainless Steels.* CORROSION, 1982. **38**(1): p. 46-52.

77. Hashimoto, K., K. Asami, and K. Teramoto, *An X-ray photo-electron spectroscopic study on the role of molybdenum in increasing the corrosion resistance of ferritic stainless steels in HC1.* Corrosion Science, 1979. **19**(1): p. 3-14.

78. OGAWA, H., H. OMATA, I. ITOH, and H. OKADA, *Auger Electron Spectroscopic and Electrochemical Analysis of the Effect of Alloying Elements on the Passivation Behavior of Stainless Steels.* CORROSION, 1978. **34**(2): p. 52-60.

79. Yang, W., R.-C. Ni, H.-Z. Hua, and A. Pourbaix, *The behavior of chromium and molybdenum in the propagation process of localized corrosion of steels.* Corrosion Science, 1984. **24**(8): p. 691-707.

80. Newman, R.C., *The dissolution and passivation kinetics of stainless alloys containing molybdenum .1. Coulometric studies of Fe-Cr and Fe-Cr-Mo alloys.* Corrosion Science, 1985. **25**(5): p. 331-339.

81. Tomashov, N.D., *Development of electrochemical theory of metallic corrosion.* Corrosion, 1964. **20**(1): p. T7-&.

82. Tsutsumi, Y., A. Nishikata, and T. Tsuru, *Pitting corrosion mechanism of Type 304 stainless steel under a droplet of chloride solutions.* Corrosion Science, 2007. **49**(3): p. 1394-1407.

83. Williams, G. and H.N. McMurray, *Pitting Corrosion of Steam Turbine Blading Steels: The Influence of Chromium Content, Temperature, and Chloride Ion Concentration.* Corrosion, 2006. **62**(3): p. 231-242.

84. Evans, U.R., *The Ferroxyl Indicator in Corrosion Research With special Reference to the Controversey Regarding the Cause of Pitting.* The Metal Industry, 1926. **11**.

85. Wang, Y.H., Y.Y. Liu, W. Wang, L. Zhong, and J. Wang, *Influences of the three-phase boundary on the electrochemical corrosion characteristics of carbon steel under droplets.* Materials and Corrosion-Werkstoffe Und Korrosion, 2013. **64**(4): p. 309-313.

86. Jiang, J., J. Wang, W.W. Wang, and W. Zhang, *Modeling influence of gas/liquid/solid three-phase boundary zone on cathodic process of soil corrosion.* Electrochimica Acta, 2009. **54**(13): p. 3623-3629.

87. Tan, Y.-J., *Wire beam electrode: a new tool for studying localised corrosion and other heterogeneous electrochemical processes.* Corrosion Science, 1998. **41**(2): p. 229-247.

88. Nishikata, A., Y. Ichihara, Y. Hayashi, and T. Tsuru, *Influence of Electrolyte Layer Thickness and pH on the Initial Stage of the Atmospheric Corrosion of Iron.* Journal of The Electrochemical Society, 1997. **144**(4): p. 1244-1252.

89. Cook, A.B., S.B. Lyon, N.P.C. Stevens, R.C. Newman, M. Gunther, G. McFiggans, and D.L. Engelberg, *Under-Deposit Chloride-Induced Stress Corrosion Cracking in Austenitic Stainless Steels: Aspects Associated with Deposit Type, Size and Composition.* ECS Transactions, 2014. **58**(29): p. 25-39.

90. Agarwal, A.S., U. Landau, and J.H. Payer, *Modeling Particulates Effects on the Cathode Current Capacity in Crevice Corrosion.* Journal of The Electrochemical Society, 2008. **155**(5): p. C269-C278.

91. Tada, E. and G.S. Frankel, *Effects of particulate silica coatings on localized corrosion behavior of AISI 304SS under atmospheric corrosion conditions.* Journal of the Electrochemical Society, 2007. **154**(6): p. C318-C325.

92. Maier, B. and G.S. Frankel, *Pitting Corrosion of Silica-Coated Type 304 Stainless Steel Under Thin Electrolyte Layers.* CORROSION, 2011. **67**(3): p. 035004-1-035004-10.

93. Cruz, R.P.V., A. Nishikata, and T. Tsuru, *AC impedance monitoring of pitting corrosion of stainless steel under a wet-dry cyclic condition in chloride-containing environment.* Corrosion Science, 1996. **38**(8): p. 1397-1406.

94. Cruz, R.P.V., A. Nishikata, and T. Tsuru, *Pitting corrosion mechanism of stainless steels under wet-dry exposure in chloride-containing environments.* Corrosion Science, 1998. **40**(1): p. 125-139.

95. Tsutsumi, Y., A. Nishikata, and T. Tsuru, *Initial Stage of Pitting Corrosion of Type 304 Stainless Steel under Thin Electrolyte Layers Containing Chloride Ions.* Journal of The Electrochemical Society, 2005. **152**(9): p. B358-B363.

96. Tsutsumi, Y., A. Nishikata, and T. Tsuru, *Monitoring of rusting of stainless steels in marine atmospheres using electrochemical impedance technique.* Journal of the Electrochemical Society, 2006. **153**(7): p. B278-B282.

97. Hastuty, S., A. Nishikata, and T. Tsuru, *Pitting corrosion of Type 430 stainless steel under chloride solution droplet.* Corrosion Science, 2010. **52**(6): p. 2035-2043.

98. Hastuty, S., Y. Tsutsumi, A. Nishikata, and T. Tsuru, *Pitting Corrosion of Type 430 Stainless Steel in the Process of Drying of Chloride Solution Layer.* Isij International, 2012. **52**(5): p. 863-867.

99. Prosek, T., A. Iversen, C. Taxen, and D. Thierry, *Low-Temperature Stress Corrosion Cracking of Stainless Steels in the Atmosphere in the Presence of Chloride Deposits.* Corrosion, 2009. **65**(2): p. 105-117.

100. Cheng, C.-Q., L.-I. Klinkenberg, Y. Ise, J. Zhao, E. Tada, and A. Nishikata, *Pitting corrosion of sensitised type 304 stainless steel under wet–dry cycling condition.* Corrosion Science, 2017. **118**: p. 217-226.

101. Mi, N., M. Ghahari, T. Rayment, and A.J. Davenport, *Use of inkjet printing to deposit magnesium chloride salt patterns for investigation of atmospheric corrosion of 304 stainless steel.* Corrosion Science, 2011. **53**(10): p. 3114-3121.

102. Street, S.R., N. Mi, A.J.M.C. Cook, H.B. Mohammed-Ali, L. Guo, T. Rayment, and A.J. Davenport, *Atmospheric pitting corrosion of 304L stainless steel: the role of highly concentrated chloride solutions.* Faraday Discussions, 2015. **180**(0): p. 251-265.

103. Maier, B. and G.S. Frankel, *Pitting Corrosion of Bare Stainless Steel 304 under Chloride Solution Droplets.* Journal of the Electrochemical Society, 2010. **157**(10): p. C302-C312.

104. Shoji, S.O., N., *Effects of Relative Humidity and Chloride type on Stainless-Steel Room-Temperature Atmospheric Corrosion Cracking.* Corrosion Engineering, 1989. **1989**(38): p. 111-119.

105. Prosek, T., A. Le Gac, D. Thierry, S. Le Manchet, C. Lojewski, A. Fanica, E. Johansson, C. Canderyd, F. Dupoiron, T. Snauwaert, F. Maas, and B. Droesbeke, *Low-Temperature Stress Corrosion Cracking of Austenitic and Duplex Stainless Steels Under Chloride Deposits.* Corrosion, 2014. **70**(10): p. 1052-1063.

106. Örnek, C., X. Zhong, and D.L. Engelberg, *Low-Temperature Environmentally Assisted Cracking of Grade 2205 Duplex Stainless Steel Beneath a MgCl2:FeCl3 Salt Droplet.* CORROSION, 2016. **72**(3): p. 384-399.

107. Padovani, C., O.E. Albores-Silva, and E.A. Charles, *Corrosion Control of Stainless Steels in Indoor Atmospheres—Laboratory Measurements Under MgCl2 Deposits at Constant Relative Humidity (Part 1).* Corrosion, 2015. **71**(3): p. 292-304.

108. N.G. Needham, P.F.F., J. Wilkinson, J. Chapman. *The Atmpshoeric Corrosion Resistance of Stainless Steels*. in *Stainless Steels '87*. 1987. Univesity of York.

109. C. Liang, W.H., *Twelve Year Atmospheric Exposure Study of Stainless Steels in China.* Outdoor Atmospheric Corrosion, ASTM STP 1421, 2002.

110. Yamashita, M., H. Miyuki, Y. Matsuda, H. Nagano, and T. Misawa, *The long-term growth of the protective rust layer formed on weathering steel by atmospheric corrosion during a quarter of a century.* Corrosion Science, 1994. **36**(2): p. 283-299.

111. R.M. Hudson, P.F.F., G.K. Allan, *Corrosion of Stainless Steel Above and Below Ground Level*, in *4th Stainless Steel Science and Market Congress*2002: Paris.

112. Cheng, Y.L., Z. Zhang, F.H. Cao, J.F. Li, J.Q. Zhang, J.M. Wang, and C.N. Cao, *A study of the corrosion of aluminum alloy 2024-T3 under thin electrolyte layers.* Corrosion Science, 2004. **46**(7): p. 1649-1667.

113. Zhong, X., G. Zhang, Y. Qiu, Z. Chen, X. Guo, and C. Fu, *The corrosion of tin under thin electrolyte layers containing chloride.* Corrosion Science, 2013. **66**: p. 14-25.

114. Nam, T.V., E. Tada, and A. Nishikata, *Pit Initiation and Repassivation of Stainless Steels Exposed to Cyclic Relative Humidity Changes.* Journal of the Electrochemical Society, 2015. **162**(9): p. C419-C425.

115. Tsuru, T., K.I. Tamiya, and A. Nishikata, *Formation and growth of micro-droplets during the initial stage of atmospheric corrosion.* Electrochimica Acta, 2004. **49**(17-18): p. 2709-2715.

116. Schindelholz, E. and R.G. Kelly, *Application of Inkjet Printing for Depositing Salt Prior to Atmospheric Corrosion Testing.* Electrochemical and Solid State Letters, 2010. **13**(10): p. C29-C31.

117. Schindelholz, E., B.E. Risteen, and R.G. Kelly, *Effect of Relative Humidity on Corrosion of Steel under Sea Salt Aerosol Proxies.* Journal of the Electrochemical Society, 2014. **161**(10): p. C450-C459.

118. Schindelholz, E., B.E. Risteen, and R.G. Kelly, *Effect of Relative Humidity on Corrosion of Steel under Sea Salt Aerosol Proxies.* Journal of the Electrochemical Society, 2014. **161**(10): p. C460-C470.

119. Oltra, R., L. Colard, and R. Bonzom, *A novel methodology to study localized corrosion under atmospheric simulated corrosion conditions: Toward a continuous monitoring of the corrosion damage on AA2024.* Materials and Corrosion, 2017. **68**(3): p. 311-315.

120. Tsuru, T., A. Nishikata, and J. Wang, *Electrochemical studies on corrosion under a water film.* Materials Science and Engineering: A, 1995. **198**(1–2): p. 161-168.

121. Williams, G. and H.N. McMurray, *The Kinetics of Chloride-Induced Filiform Corrosion on Aluminum Alloy AA2024-T3.* Journal of The Electrochemical Society, 2003. **150**(8): p. B380-B388.

122. Stratmann, M. and H. Streckel, *On the atmospheric corrosion of metals which are covered with thin electrolyte layers—I. Verification of the experimental technique.* Corrosion Science, 1990. **30**(6-7): p. 681-696.

123. Wang, J.S., X. Tang, Y. Li, and X.Q. Qiu, *Observation and micro-electrochemical characterisation for micro-droplets in initial marine atmospheric corrosion.* Corrosion Engineering, Science and Technology, 2016. **51**(4): p. 308-312.

124. Cook, A.B., Z. Barrett, S.B. Lyon, H.N. McMurray, J. Walton, and G. Williams, *Calibration of the scanning Kelvin probe force microscope under controlled environmental conditions.* Electrochimica Acta, 2012. **66**: p. 100-105.

125. Geary, S., H.N. McMurray, and A.C.A. de Vooys, *High Resolution Characterization of Pitting Corrosion Using a Novel Environmental SVET and White Light Interferometry.* ECS Transactions, 2013. **50**(47): p. 37-51.

126. Wint, N., S. Geary, H.N. McMurray, G. Williams, and A.C.A. de Vooys, *The Kinetics and Mechanism of Atmospheric Corrosion Occurring on Tin and Iron-Tin Intermetallic Coated Steels: I. Cathodic Delamination.* Journal of The Electrochemical Society, 2015. **162**(14): p. C775-C784.

127. Wint, N., H.N. McMurray, G. Williams, and A.C.A. de Vooys, *The Kinetics and Mechanism of Atmospheric Corrosion Occurring on Tin and Iron-Tin Intermetallic Coated Steels: II. Filiform Corrosion.* Journal of The Electrochemical Society, 2016. **163**(2): p. C1-C6.

128. Rafla, V., A.D. King, S. Glanvill, A. Parsons, A. Davenport, and J.R. Scully, *Operando Observation of Galvanic Corrosion Between Aluminum Alloy 7050-T7451 and 304 Stainless Steel in a Simulated Fastener Arrangement Using X-Ray Tomography.* CORROSION, 2015. **71**(10): p. 1171-1176.

129. Guo, L., *Atmospheric localised corrosion of type 304 austenitic stainless steels* [PhD thesis]. Birmingham (UK): University of Birmingham; 2016

130. Mi, N., *Synchrotron x-ray studies of atmospheric pitting corrosion of stainless steel* [Ph.D thesis]. Birmingam: University of Birmingham; 2014

131. Frankel, G.S., M. Stratmann, M. Rohwerder, A. Michalik, B. Maier, J. Dora, and M. Wicinski, *Potential control under thin aqueous layers using a Kelvin Probe.* Corrosion Science, 2007. **49**(4): p. 2021-2036.

132. Ilevbare, G.O. and G.T. Burstein, *The inhibition of pitting corrosion of stainless steels by chromate and molybdate ions.* Corrosion Science, 2003. **45**(7): p. 1545-1569.

133. Street, S.R., W.C. Xu, M. Amri, L.Y. Guo, S.J.M. Glanvill, P.D. Quinn, J.F.W. Mosselmans, J. Vila-Comamala, C. Rau, T. Rayment, and A.J. Davenport, *The Effect of Nitrate on Salt Layers in Pitting Corrosion of 304L Stainless Steel.* Journal of the Electrochemical Society, 2015. **162**(9): p. C457-C464.

134. Uhlig, H.H. and J.R. Gilman, *Pitting of 18-8 Stainless Steel in Ferric Chloride Inhibited by Nitrates.* Corrosion, 1964. **20**(9): p. 289t-292t.

135. Eichinger, E., J. Osborne, and T. Van Cleave, *Hexavalent chromium elimination: An aerospace industry progress report.* Metal Finishing, 1997. **95**(3): p. 36-36.

136. Morales-Gil, P., G. Negron-Silva, M. Romero-Romo, C. Angeles-Chavez, and M. Palomar-Pardave, *Corrosion inhibition of pipeline steel grade API 5L X52 immersed in a 1 M H2SO4 aqueous solution using heterocyclic organic molecules.* Electrochimica Acta, 2004. **49**(26): p. 4733-4741.

137. Leckie, H.P. and H.H. Uhlig, *Environmental factors affecting critical potential for pitting in 18-8 stainless steel.* Journal of the Electrochemical Society, 1966. **113**(12): p. 1262.

138. Whillock, G.O.H., T.J. Binks, and C.J. Donohoe, *Localized Corrosion of Stainless Steel in a Nuclear Waste Cooling Water System-Part 4: Artificial Pit Investigation of Nitrate Inhibition.* Corrosion, 2012. **68**(11).

139. Lillard, R.S., G. Vasquez, and D.F. Bahr, *Influence of Nitrate on Pit Stability in Austenitic Stainless Steel.* Corrosion, 2010. **66**(7).

140. Rosenfeld, I.L. and I.S. Danilov, *Electrochemical aspects of pitting corrosion.* Corrosion Science, 1967. **7**(3): p. 129-142.

141. Yashiro, H., A. Oyama, and K. Tanno, *Effects of temperature and potential on the inhibitive action of oxoacid salts for pitting in high-temperature chloride solutions.* Corrosion, 1997. **53**(4): p. 290-297.

142. Bobić, B. and B. Jegdić, *Pitting corrosion of stainless steels in chloride solutions.* Scientific-Technical Review, 2005. **55**(3-4): p. 3-7.

143. Newman, R.C. and M.A.A. Ajjawi, *A microelectrode study of the nitrate effect on pitting of stainless-steels.* Corrosion Science, 1986. **26**(12): p. 1057-1063.

144. Newman, R.C. and T. Shahrabi, *The effect of alloyed nitrogen or dissolved nitrate ions on the anodic behavior of austenitic stainless-steel in hydrochloric-acid.* Corrosion Science, 1987. **27**(8): p. 827-838.

145. British Standards Institution. BS EN 10028-7: Flat products made of steels for pressure purposes. Stainless steels [cited 12 July, 2017]. Available from: https://shop.bsigroup.com/ProductDetail/?pid=000000000030133804

146. ASTM. E104-02(2007) "Standard Practice for Maintaining Constant Relative Humidity by Means of Aqueous Solutions" [cited 08/06/2011]. Available from: www.astm.org

147. J. Schindelin, I.A.-C., E. Frise, V. Kaynig, M. Longair, T. Pietzsch, S. Preibisch, C. Rueden, S. Saalfeld, B. Schmid, J. Tinevez, D.J. White, V. Hartenstein, K. Eliceiri, P. Tomancak, A. Cardona, *Fiji: an open-source platform for biological-image analysis.* Nature Methods, 2012. **9**(7): p. 7.

148. Preibisch, S., S. Saalfeld, and P. Tomancak, *Globally optimal stitching of tiled 3D microscopic image acquisitions.* Bioinformatics, 2009. **25**(11): p. 1463-1465.